Synthesis and Complexes of Bridging Heterocyclic Ligands

A thesis submitted in partial fulfillment of the requirements for the degree of **Doctor of Philosophy** in **Chemistry** at the **University of Canterbury**

SIJI RAJAN

Supervisor: ***Prof. Peter J. Steel***

University of Canterbury

Christchurch

New Zealand 8041.

UNIVERSITY OF CANTERBURY
Te Whare Wānanga o Waitaha
CHRISTCHURCH NEW ZEALAND

2014

Acknowledgements

It gives me immense pleasure in expressing my gratitude to all the people without whom this thesis would not have been possible to accomplish. Firstly, I would like to acknowledge my supervisor Prof. Peter J. Steel for his incredible guidance, encouragement and advice over the past few years. I am grateful for his patience, support and lots of ideas throughout the writing of this thesis. I greatly appreciate the financial support from the Marsden Fund through my entire study program and I am indebted to Peter for initiating this.

My sincere thanks to Prof. Richard Keene for his scientific advice and constructive suggestions during the course of my research which helped me a lot and also for reviewing my thesis at very short notice. The academic and technical members of the Chemistry Department have been tremendously helpful, in particular Dr. Chris Fitchett for his valuable suggestions over the years and also for proofreading my thesis. Thanks to Dr. Matt Polson for generously sharing his time and expertise in X–ray crystallography, as well as many long insightful discussions. Thanks to Dr. Jan Wikaira for her advice on X–ray crystallography. I am very grateful to Dr. Marie Squire for her excellent assistance with NMR and mass spectrometry. I would also like to thank Dr. Justine Cottam for editing countless pages of this thesis and her valuable comments are greatly appreciated. Thanks to Nathan Wain from the Learning Skill Centre at the University of Canterbury for the formatting tips.

The support and contributions from many student colleagues is also greatly acknowledged, especially Lita Lee for her significant contributions to the electrochemical measurements. I would like to thank the past and present members of the Steel group, Solomon, Rakesh, Ryan, Tom, King and Team Fitchett especially Jayne, Robbie, Samantha, Will and Nick for the wonderful time I had in both the lab and office. I am extremely grateful to Kajitha, Gurpreet, Davey, Janadari and Fatemeh for their endless support and friendship and thanks to all the members of labs 655, 831 and 839 for the loan of chemicals and help on a regular basis.

Travel grants from the Marsden Fund and the New Zealand Institute of Chemistry (NZIC) for attending conferences were very much appreciated.

Away from chemistry, I am very grateful to Pragya for everything and for being there in good and rough times. Big heartfelt thanks to Ravi and Kamiya for providing the much needed escape from studies and for all the memorable times.

Finally, and most importantly, I would like to express my deepest thanks to my parents for their unconditional love and support as I would not have come this far without them. I am extremely grateful to Patel uncle and family for their generosity and moral support. I would also like to thank my sisters and Anil for always being part of my support army and for their constant encouragement.

Contents

Abstract

Ligand–mediated coupling between metal centres is of fundamental importance in inorganic and materials chemistry. Bridging ligands involving azo groups as coordinating π–acceptors can yield complexes with interesting properties.

This thesis describes the synthesis of a series of N–heterocyclic compounds containing the azo functionality, designed for potential coordination to the metal through the azo nitrogen and a N–heterocyclic ring. The azo ligands are divided into four categories; ligands based on azobispyridines, ligands containing pyrimidine and fused aromatic azine groups and ligands capable of coordinating in a bis–tridentate fashion to the metal centre. Ligands containing flexible imine subunits connected directly, or through different spacers, are also discussed. Overall twenty one ligands were synthesised, six of which are new compounds.

The coordination and metallosupramolecular chemistry of these ligands with ruthenium(II) and silver(I) metal atoms was investigated. A total of thirty five ruthenium(II) and eleven silver(I) complexes were prepared, of which thirty eight were characterised by X–ray crystallography. Mononuclear and dinuclear ruthenium(II) complexes of the type $[(TL)_2Ru(L)]^{2+}$ and $[(TL)_2Ru(\mu–L)Ru(TL)_2]^{4+}$ (L = azo ligand and TL = bpy or terpy), were synthesised and characterised by a combination of spectroscopic and structural techniques. UV/Visible absorption studies and electrochemical methods were used to investigate the nature of metal–ligand and metal–metal interactions.

In the mononuclear Ru(II) complexes, N–heterocyclic azo ligands act as chelating ligands forming five–membered chelate rings involving azo–N and heterocyclic–N atoms. The non–coordinated pyridine ring of the azo ligand is twisted with respect to the azo–N atom and is directed towards the adjacent bipyridine rings. Studies reveal that these azo ligands posses extremely low–lying π*–orbitals and are electron deficient. X–Ray structural analysis of the dinuclear complexes revealed short inter–metal separations of *ca.* 4.9 Å and electrochemical studies indicate that these ligands mediate very strong interactions between the metal centres (comproportionation constant, $K_c \sim 10^8 – 10^9$), due to the excellent π*–acceptor properties of the azo functionality.

Varying the pyridine ring of the azo ligand to pyrimidines and fused N–aromatic rings has a considerable effect on the electronic properties of these complexes. Incorporation of a

pyrimidine ring facilitates the stabilisation of azo anion radicals and leads to the formation of diruthenium(II) species, $[(bpy)_2Ru^{II}(\mu\text{–}\mathbf{3.1})Ru^{II}(bpy)_2](PF_6)_3$, **3.10** and $[(bpy)_2Ru^{II}(\mu\text{–}\mathbf{3.2})Ru^{II}(bpy)_2](PF_6)_3$, **3.12**, bridged by radical species. The X–ray crystal structures of both these complexes were determined.

The use of the hexadentate ligands azobis[6–(2,2'–bipyridine)], **4.1**, and azobis[2–(1,10–phenanthroline)], **4.2**, coordinating in a bis–tridentate manner mediate even stronger communication between the two ruthenium centres with K_c values greater than 10^{13}.

Ligands containing bis–pyridylimines result in weaker coupling between the metal centres in dinuclear ruthenium(II) species. A complete absence in the inter–metal communication was observed with increasing the distance and/or flexibility between the two pyridylimine units, contrary to a previous reported claim.

Reaction with different silver(I) salts afforded an array of one–dimensional coordination polymers and a discrete dinuclear complex depending on the coordination strengths of the anions. The metallosupramolecular assemblies obtained were characterised mainly by X–ray crystallography, elemental analysis and mass spectrometry.

Abbreviations

BL	bridging ligand
bpy	2,2’–bipyridine
bpym	2,2’–bipyrimidine
CIS	coordination induced shift
2,3–dpp	2,3–di(2’–pyridyl)pyrazine
2,5–dpp	2,5–di(2’–pyridyl)pyrazine
DPV	differential pulse voltammetry
ESI–MS	electron spray ionisation mass spectrometry
eV	electron volts
gCOSY	gradient correlation spectroscopy
HMBC	heteronuclear multiple–bond correlation spectroscopy
HOMO	highest occupied molecular orbital
HSQC	heteronuclear single–quantum correlation spectroscopy
K_c	comproportionation constant
LUMO	lowest unoccupied molecular orbital
MLCT	metal–to–ligand charge transfer
mV	millivolts
NMR	nuclear magnetic resonance
NOE	nuclear overhauser effect
NOESY	nuclear overhauser spectroscopy
phen	1,10–phenanthroline
ROESY	rotating frame overhauser spectroscopy
SCE	standard calomel electrode
terpy	2,2’:6’,2’’–terpyridine
TL	terminal ligands
TOCSY	total correlation spectroscopy

Atom Colour Scheme

- Silver
- Ruthenium
- Bromine
- Chlorine
- Sulfur
- Fluorine
- Oxygen
- Nitrogen
- Carbon
- Hydrogen

Chapter 1

Introduction

1. Introduction

Ruthenium(II) polypyridyl complexes have received continuous attention for several decades.[1–3] Due to their combination of chemical inertness in different oxidation states, photophysical characteristics and redox properties,[4–7] they are widely used in photochemical molecular devices,[8–11] solar energy conversion schemes[12–16] and molecular recognition.[10],[17–19]

The tris(2,2'–bipyridine)ruthenium(II) dication, $[Ru(\mathbf{1.1})_3]^{2+}$ (Figure 1.1a) is one of the most well known and extensively studied compounds due to its important redox, photophysical and photochemical properties.[7],[10],[20–22] Since the early discovery of $[Ru(\mathbf{1.1})_3]^{2+}$ to act as a photocatalyst in the splitting of water into hydrogen and oxygen,[23] there has been considerable interest in ruthenium(II)–bipyridine type complexes.[1],[10],[11],[24] Replacement of ligand **1.1** by 1,10'–phenanthroline (**1.2**) in $[Ru(\mathbf{1.2})_3]^{2+}$, showed new excited state transitions for the reduced phen ligand and also profoundly modifies the coupling conditions.[25],[26]

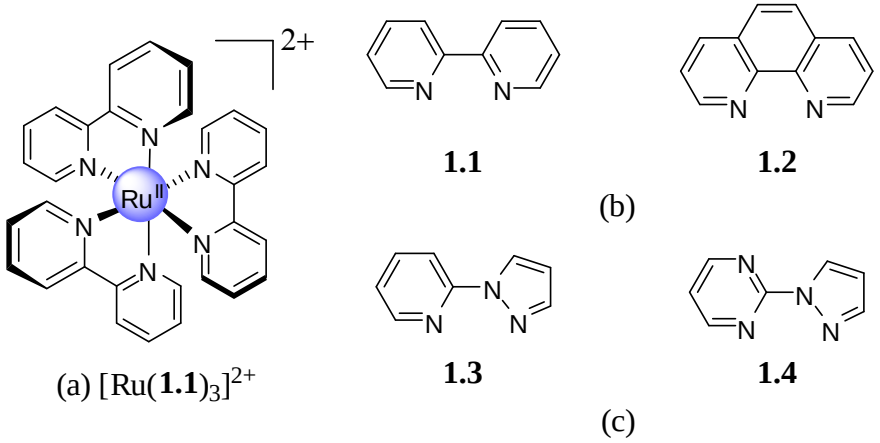

(a) $[Ru(\mathbf{1.1})_3]^{2+}$

Figure 1.1. (a) $[Ru(\mathbf{1.1})_3]^{2+}$, (b) six–membered chelating bidentate ligands and (c) chelating ligands containing other heterocycles.

The ground and excited–state properties of such complexes can be systematically tuned by varying the structures of the chelating ligands.[13],[27],[28] Replacement of the pyridine rings by other heterocycles further modifies the properties of the resulting complexes due to the different donor–acceptor properties of the ligands involved. For example, homoleptic complexes of 2–(1'–pyrazolyl)pyridine, **1.3** ($[Ru(\mathbf{1.3})_3]^{2+}$) and 2–(1'–pyrazolyl)pyrimidine,

1.4 ($[Ru(\mathbf{1.4})_3]^{2+}$), as shown in Figure 1.1, show significant changes in the absorption spectroscopy and electrochemical measurements in comparison to $[Ru(\mathbf{1.1})_3]^{2+}$.[29],[30]

Ligands with multiple nitrogen donor sites that can coordinate to more than one metal have been used to bridge two or more metals with the emphasis on the nature and magnitude of metal–metal interactions in such complexes. Since the discovery of the mixed–valence Creutz–Taube ion $[(H_3N)_5Ru(\mu\text{–pyz})Ru(NH_3)_5]^{5+}$ **1.5** (Figure 1.2),[31] there has been an increased interest towards the study of electronic interactions between multinuclear metal centres linked by a bridging ligand.[32–35] The interactions between the metal centres are of interest for both fundamental and application reasons.

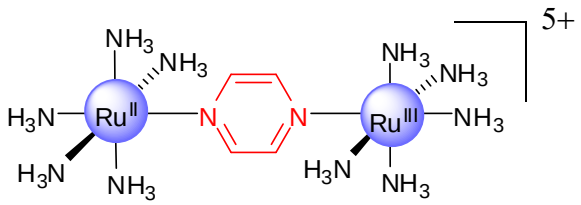

1.5

Figure 1.2. The Creutz–Taube Ion.

In a symmetrical dinuclear system, the two metal centres undergo oxidation at the same potential in the absence of electronic coupling; however, the existence of two different oxidation redox potentials is a clear indication of a metal–metal interaction. The magnitude of separation between the two successive oxidation potentials (ΔE_{ox}), gives a direct measure of the comproportionation constant (K_c) for the equilibrium (1) between the mixed–valence form ($Ru^{II}Ru^{III}$) and the fully–reduced ($Ru^{II}Ru^{II}$) and fully–oxidised ($Ru^{III}Ru^{III}$) forms.[36]

$$(Ru^{II}Ru^{II}) \quad + \quad (Ru^{III}Ru^{III}) \quad \underset{}{\overset{K_c}{\rightleftharpoons}} \quad 2\,(Ru^{II}Ru^{III}) \qquad \text{.....(1)}$$

$$K_c = \exp\frac{nF(\Delta E_{ox})}{RT} = \exp\frac{\Delta E_{ox}}{25.69} \quad \text{at 298K} \qquad \text{.....(2)}$$

The equilibrium constant K_c can be measured spectroscopically or electrochemically and may be related to thermodynamic parameters and can be obtained from the electrochemical data as shown above.[37] If there is no interaction between the metal centres, at a statistical level $K_c = 4$ and it will be higher if there is a reasonable interaction between the metal centres. The values are often found to be sensitive to the solvent and the electrolyte

used.[38],[39] Spectral measurements of the IVCT transitions, if observed, serve as a better indicator to probe the degree of electronic coupling.[33],[40] In spite of this, electrochemically–derived K_c and ΔE_{ox} values for a homodinuclear system are often used to measure the extent of communication between the metal centres.[37],[41–43]

1.1. Binucleating Ligands

Bridging aromatic N–heterocyclic ligands are well known to facilitate communication between the metal centres *via* the π–system of the ligand.[36],[37],[44] The degree of these interactions can be controlled by varying (i) the electronic properties of the ligand, (ii) the distance between the metal centres, and (iii) the degree of conjugation between the metal centres.[44],[45] The π–deficient six–membered aromatic N–heterocycles have relatively low–lying π*–orbitals and are good acceptors of metal d–orbital electron density. In contrast, five–membered N–heterocycles are good π–donors and the removal of the proton of an acidic N–hydrogen generates an N–anion.[46] The interactions between the metal and the ligand are governed by the specific metal and the ligand involved. Therefore, the design of the bridging ligand is one of the key steps in the spatial organisation and electronic interaction between the active metal components.

1.1.1. Monodentate ligands

The majority of early work on diruthenium complexes involved symmetrical monodentate azine–bridges such as pyrazine **1.6**,[31],[47],[48] pyrimidine **1.7**, and 4,4'–bipyridine **1.8**, as shown in Figure 1.3.[49],[50]

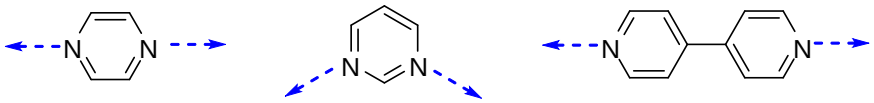

1.6 **1.7** **1.8**

Figure 1.3. Monodentate ligands.

The Creutz–Taube ion **1.5** is perhaps the most well–studied binuclear azine–bridged complex and thus still has considerable attention. Structural analogues of the Creutz–Taube ion such as substitution of the monodentate ammine groups with pyridine, bipyridine, chloro or aqua groups have provided substantial understanding of the factors governing internuclear

interactions in Ru(II) complexes.[51–55] Many X–ray crystallographic structures of pyrazine–bridged complexes including the Creutz–Taube ion have been reported.[49],[56–59]

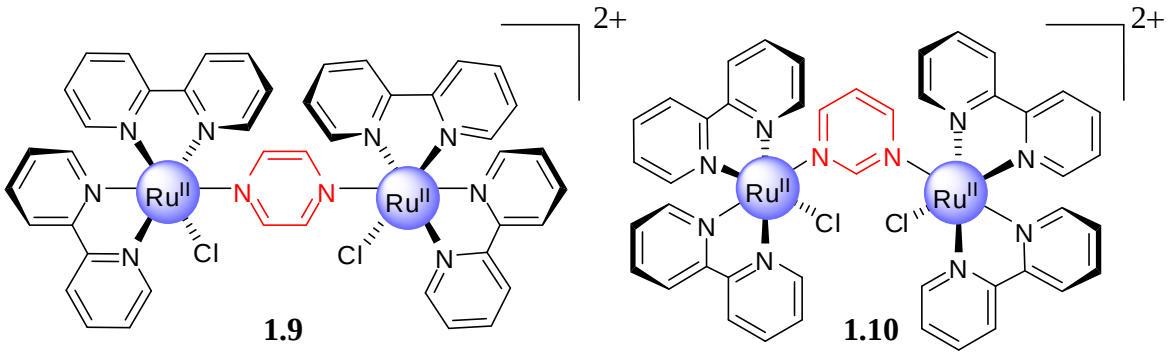

Figure 1.4. Structural analogues of the Creutz–Taube ion involving pyrazine **1.9** and pyrimidine **1.10**.

Studies on pyrimidine–bridged complexes by Taube *et al.*[60] indicate weaker metal–metal interactions, despite being closer in space (*ca.* 6.0 Å) than in pyrazine–bridged complexes (*ca.* 6.9 Å).[49],[50] Meyer *et al.* observed electrochemically equal interactions for $[(bpy)_2ClRu(\mathbf{1.6})RuCl(bpy)_2]^{2+}$ (**1.9**), and the corresponding pyrimidine–bridged complex $[(bpy)_2ClRu(\mathbf{1.7})RuCl(bpy)_2]^{2+}$ (**1.10**), as shown in Figure 1.4.[61] Molecular orbital calculations on the free ligand display the lowest π*–level at a lower energy for pyrazine compared to pyrimidine and this difference might account for equal electronic coupling. Similarly, studies on the 4,4'–bipyridine **1.8**, bridged analogue of the Creutz–Taube ion exhibit a reduced level of interaction for symmetric systems.[62],[63] The replacement of a pyrazine **1.6** bridge by a 4,4'–bipyridine **1.8** increases the metal–metal separation to *ca.* 11.2 Å.[50]

1.1.2. Bidentate Ligands

The binuclear complexes bridged by monodentate ligands are often unstable. On the other hand, bidentate coordination improves stability at each metal coordination site because of the chelate effect and also imparts conformational rigidity to the complex. 2,2'–Bipyrimidine **1.11**, is a classic example of a doubly–chelating bridging ligand. Numerous homobinuclear and heterobinuclear ruthenium(II) complexes have been described where **1.11** bridges two metals at a distance of *ca.* 5.5 Å and this mediates a very strong communication between the metal centres.[64–69]

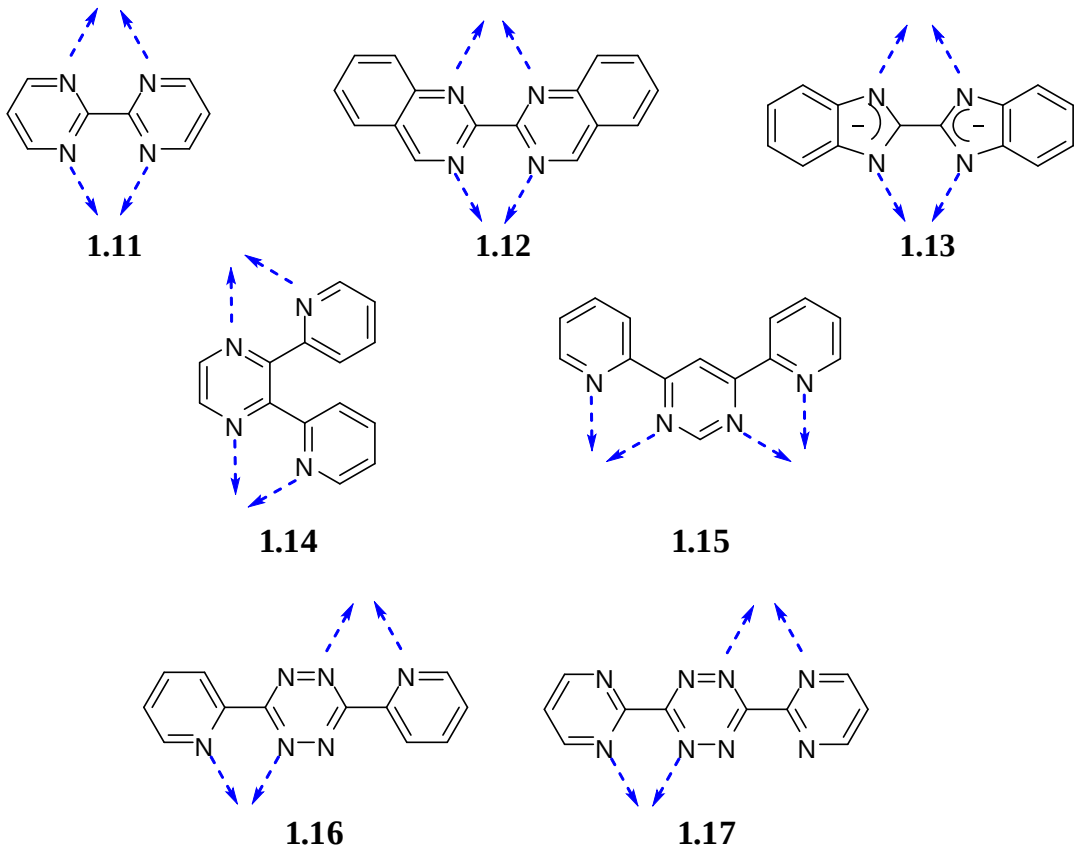

Figure 1.5. Examples of bridging bidentate ligands.

There have been no reports of diruthenium complexes of 2,2'–biquinazoline **1.12**, however, metallosupramolecular assemblies with late transition metals have been reported recently.[70] The complexes of the bibenzimidazolate ligand **1.13** were more stable than the corresponding complexes of **1.11**, due to the π–excessive donor properties of the ligand and the reduction of electrostatic repulsion between the positively charged metal centres.[71],[72] In spite of structural similarities, ruthenium(II) complexes of the binucleating ligand 2,3–bis(2'–pyridyl)pyrazine **1.14**[73] exhibit excellent inter–metal communication, compared to the pyrimidine ligand 4,6–bis(2'–pyridyl)pyrimidine **1.15**,[74] since pyrazine is a better π–acceptor than pyrimidine. Tetrazine derivatives 3,6–bis(2'–pyridyl)–1,2,4,5–tetrazine **1.16** and 3,6–(2'–pyrimidyl)–1,2,4,5–tetrazine **1.17**, bridge metal centres in a transoid manner and have very low–lying π*–orbitals, which therefore make them excellent π–acceptors.[75]

1.2. Stereochemistry of Ruthenium(II) Complexes

Polypyridyl ligands coordinated to octahedral metal centres such as Ru^{II} and Os^{II} have been of great interest because of their favourable photophysical and redox properties. However, when bidentate ligands are involved, stereochemical complexity exists which influences the photophysical properties of the assemblies.[41],[76–80]

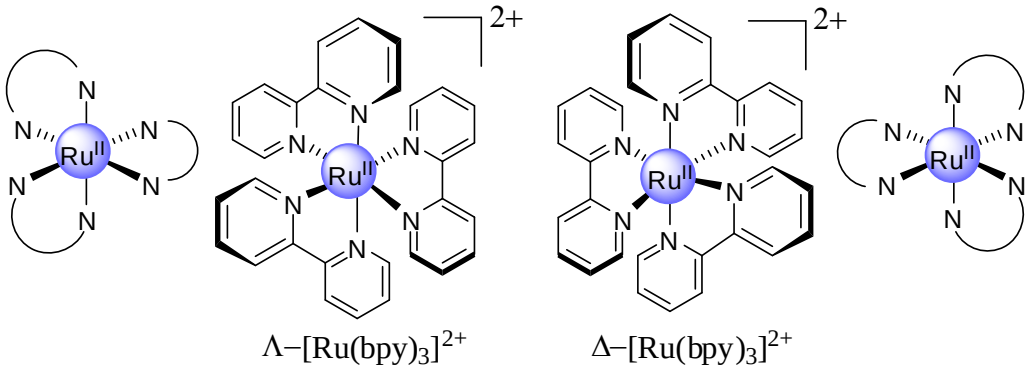

Figure 1.6. Enantiomers of $[Ru(bpy)_3]^{2+}$ with symmetrical bidentate ligands.

A tris(bidentate) complex cation, such as $[Ru(bpy)_3]^{2+}$, exists in two enantiomeric forms i.e. Λ and Δ forms, as shown in Figure 1.6. If the bpy ligands are unsymmetrically substituted, then additional isomers, i.e. *facial* and *meridional* geometrical isomers are found as shown in Figure 1.7. Furthermore, each of these can exist as two enantiomers.[79],[81],[82]

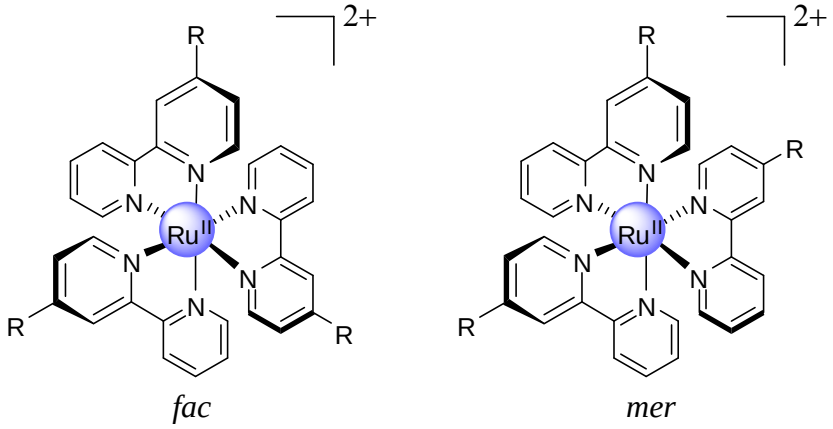

Figure 1.7. Geometrical isomers in unsymmetrical $[Ru(bpy^R)_3]^{2+}$ complexes.

In dinuclear complexes, where the metal centres are tris(bidentate) in nature, each centre may possess left–handed (Λ) or right–handed (Δ) chirality giving rise to diastereoisomeric forms; *meso* (ΔΛ) and *racemic* (consisting of ΔΔ/ΛΛ enantiomeric pairs) isomers, as shown in Figure 1.8.[79],[83]

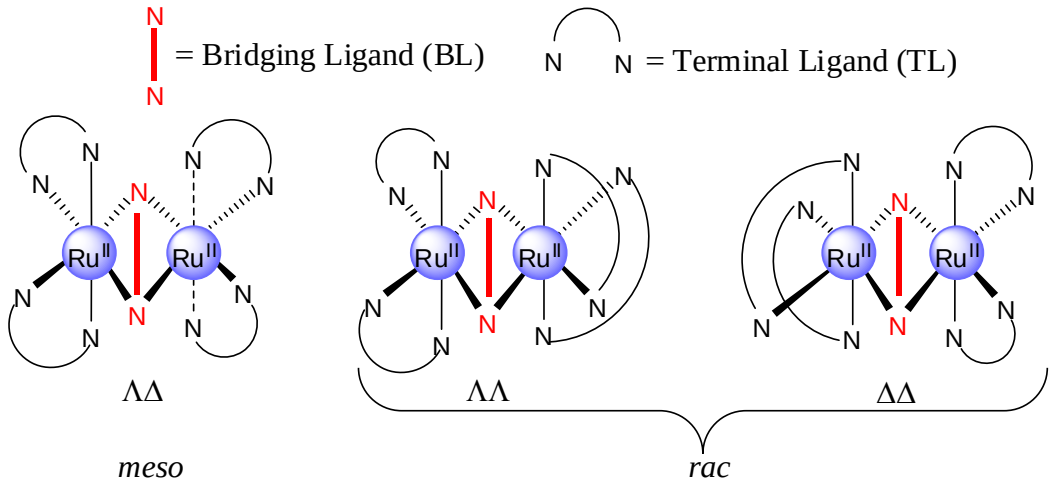

Figure 1.8. Diastereoisomeric forms of $[(TL)_2Ru(\mu–BL)Ru(TL)_2]^{n+}$.

In symmetrical dinuclear complexes such as $[(TL)_2Ru(\mu–BL)Ru(TL)_2]^{4+}$, where BL is a symmetrical bridging ligand and TL is a bidentate terminal ligand, the *meso* and *racemic* isomer differ only in the orientation of the terminal ligands above and below the plane. Figure 1.9 shows examples of bridging ligands which can be categorised as linear (**1.11**), stepped–parallel (2,5–bis(2'–pyridyl)pyrazine, **1.17**) and angular (**1.15**) on the basis of the arrangement about their coordination sites.[65],[80],[84]

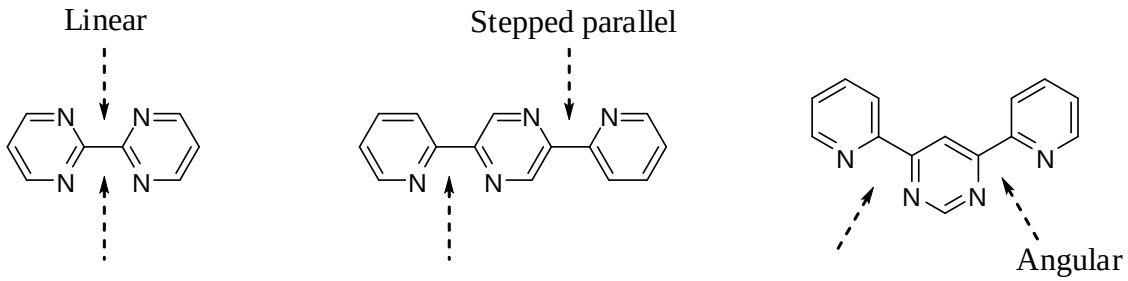

Figure 1.9. Bridging ligands exhibiting different arrangements about the coordination sites.

In the case of bridging ligands having a linear or stepped–parallel relationship between the axes of the bites of the two coordination sites, the terminal ligands above and below the plane of the bridge are orthogonal in the *meso* (ΔΛ) isomer and approximately parallel in the *racemic* (ΔΔ/ΛΛ) diastereoisomer. However, if the bites are angular, terminal ligands are approximately parallel and orthogonal for the *meso* and *racemic* forms, respectively. The diaseteroisomeric (*meso* and *rac*) forms of the dinuclear Ru(II) complex of **1.11** are shown in Figure 1.10.

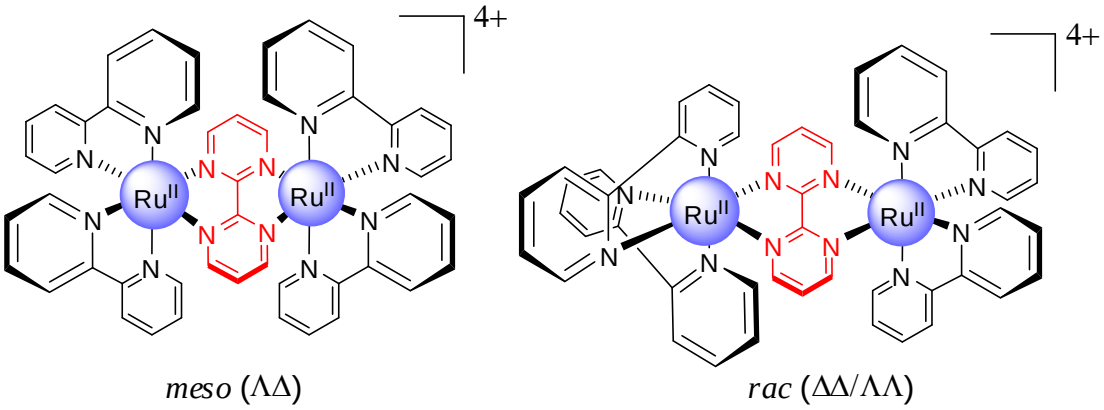

meso (ΛΔ) *rac* (ΔΔ/ΛΛ)

Figure 1.10. Diastereoisomeric forms of $[(bpy)_2Ru(\mu\text{–}\mathbf{1.11})Ru(bpy)_2]^{4+}$.

1.2.1. Strategies to control the stereochemistry

In general, the number of isomers increases with the number of metals involved and, therefore, the formation of polynuclear complexes becomes a real issue. A number of different approaches have been employed to address this stereochemical problem.[80],[84–86] The enantiomerically pure building blocks such as $[Ru(bpy)_2(py)_2]^{2+}$, $[Ru(phen)_2(py)_2]^{2+}$ and $[Ru(bpy)_2(CO)_2]^{2+}$ (resolved using O,O'–dibenzoyltartrate, arsenyl–(+)–tartrate and antimony(+) tartrate anions, respectively) have been used to synthesise polynuclear species with predetermined stereochemistry (such as ΔΔ, ΛΛ, ΔΛ).[87–89] A second strategy by von Zelewsky and coworkers involves the use of ligands called chiragens **1.18** and **1.19** in which two bidentate ligands are linked by a chiral connecting group, as shown in Figure 1.11.[90–92] These ligands predetermine the chirality at the metal centre, which promotes the synthesis of stereospecific oligomers.

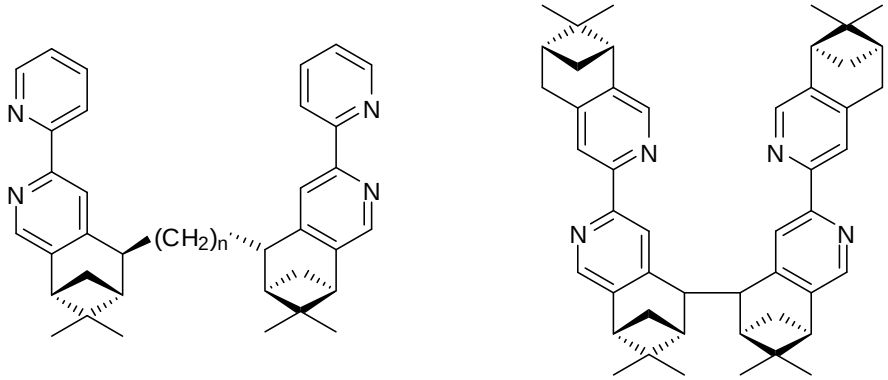

Chiragen[n] {n = 0,3–7} **1.18**

Chiragen[0] **1.19**

Figure 1.11. Chiragen ligands used for stereospecific synthesis.

Another approach pioneered by Keene and coworkers, has been extensively used in our laboratory, and involves the use of cation exchange chromatography on a SP Sephadex C–25 support using sodium chloride or sodium tosylate as the eluent.[83],[84],[93–100] The separation of stereoisomers is based on the differential interaction of the eluent anions with the relative orientation of the heterocyclic ligands in the diastereoisomers.[65],[69]

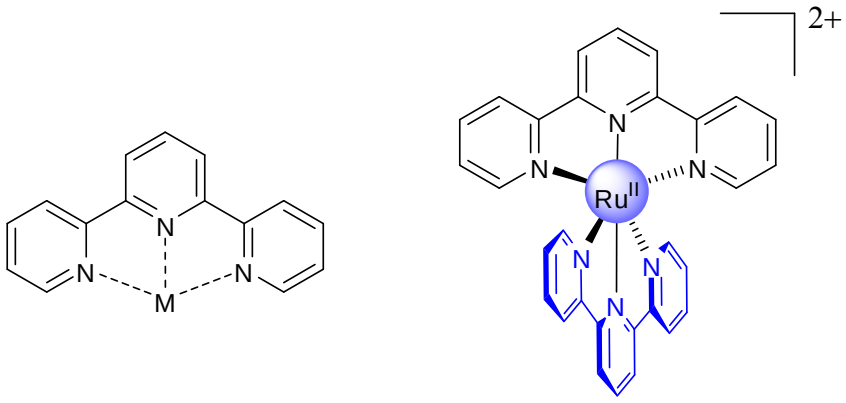

1.20 **1.21**

Figure 1.12. Mode of coordination in 2,2':6',2''–terpyridine **1.20** and the Ru(II) complex containing terpy units **1.21**.

The stereochemical problem may also be avoided by the use of tridentate ligands of the type 2,2':6'2''–terpyridine (terpy) **1.20**, which coordinates to an octahedral metal centre in a meridional manner creating a single isomer of the achiral $[Ru(terpy)_2]^{2+}$ **1.21** complex cation, as shown in Figure 1.12.[6],[101] The use of two symmetrical tridentate ligand components coordinated to metal centres eliminates the possibility of stereoisomerism. In addition, the presence of two chelate rings per ligand makes $[Ru(terpy)_2]^{2+}$ more stable than $[Ru(bpy)_3]^{2+}$. Examples of some commonly used bridging doubly–tridentate ligands are shown in Figure 1.13.

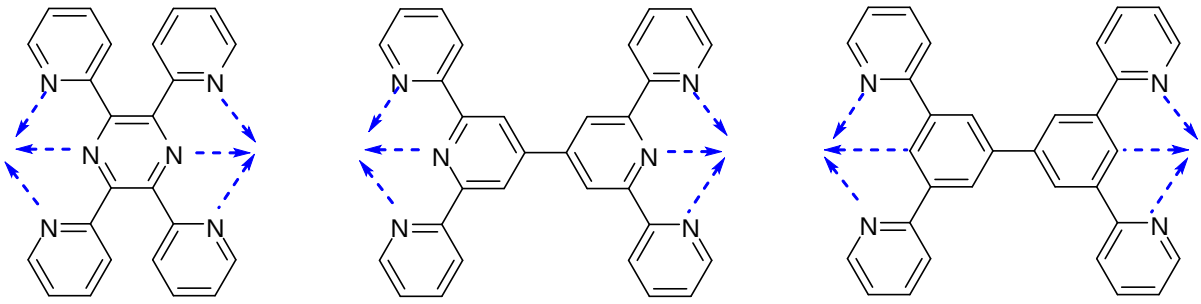

1.22 **1.23** **1.24**

Figure 1.13. Examples of commonly used doubly–tridentate ligands.

The bischelating ligand 2,3,5,6–tetrakis(2–pyridyl)pyrazine, **1.22** has been extensively used as a bridging ligand to prepare homo– and hetero–nuclear complexes with a range of terminal ligands such as bpy and terpy.[102–104] Complexes of this ligand with octahedral transition metal ions, such as Ru(II) and Os(II), have been studied for their redox, luminescence and mixed–valence properties by several groups.[105–111] In these complexes the metal centres are extremely close and exhibit a high degree of electronic coupling and mediate electron transfer through multiple redox states of the metal ions. A series of dinuclear complexes with bridging ligands containing two terpy units joined by different spacers, as in **1.23**, gives rise to a linear connectivity and display well defined control over the geometry.[112],[113] While terpy ligands enable the synthesis of defined polymetallic complexes, $[Ru(terpy)_2]^{2+}$ is not as luminescent as $[Ru(bpy)_3]^{2+}$.[7] A number of different strategies have been used to increase the photophysical properties of Ru–terpy complexes.[114–117] For example, cyclometallated ligands, such as **1.24**, where one of the pyridine ring is replaced by a phenyl ring, increases the σ–donating properties of the ligand and therefore coordinates strongly to the metal centre, which subsequently increases the lifetime of the excited state.[118],[119]

These ligands, therefore, offer great potential for the preparation of polymetallic complexes. However, to fully understand the influence of stereochemistry on the intramolecular electron and energy transfer, the use of tris(bidentate) species is required.

1.3. Azobispyridines as Bridging Ligands

Aromatic azo compounds have extensive applications in materials chemistry due to their unique combination of electronic and geometrical structures, which lead to intriguing properties.[120–125] This class of compounds possesses extremely low–lying azo–centred π*–orbitals, which result in intense long–wavelength absorptions responsible for making them ideal for their use in dyes and pigments.[126],[127] Their efficient and fully reversible *cis–trans* isomerisation under appropriate radiation also makes them excellent candidates to function as molecular switches.[128],[129] In addition, azo compounds have recently been targeted for potential applications in drug delivery,[130–132] optical storage media,[133],[134] sensors,[135],[136] and nanotubes.[137],[138]

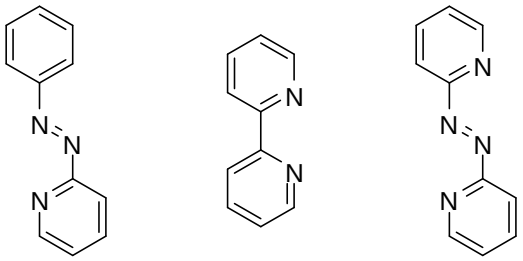

1.25 **1.1** **2.1**

Figure 1.14. Structural representation of three bidentate ligands.

Azo compounds based on N–containing heterocycles, such as 2–phenylazopyridine **1.25** (Figure 1.14) and its analogues are extensively studied bidentate ligands,[139–145] involving coordination to the metal centre through the pyridine and azo nitrogen atoms forming a stable five–membered chelate ring.[146–148] The weak σ–donor and intermediate π–acceptor properties of the pyridine nitrogen atoms of **1.25** make it similar to 2,2'–bipyridine, **1.1**, in its coordination properties. However, the π–acceptor ability of the azo nitrogen atom is much stronger than the bpy–N atoms. The symmetrical azobispyridine ligand, 2,2'–azobispyridine, **2.1**, is related to **1.25** by replacing the phenyl ring with a pyridine ring and **1.1** by insertion of an azo bridge between the two pyridine rings (Figure 1.14). As a matter of fact, the mononuclear complexes of **2.1** are similar to the corresponding compounds with **1.25**.[143],[144],[149]

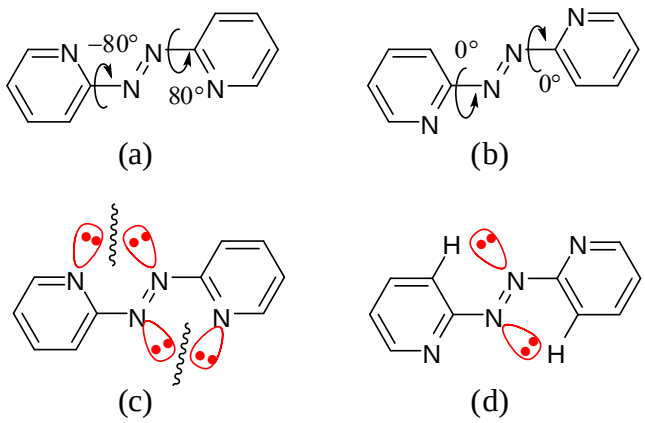

Figure 1.15. Structure of **2.1** in (a) gas–phase; (b) solid–state; (c) and (d) interactions responsible for the preferred solid state conformation.

In both solution[150] and the gas phase,[151] the free ligand **2.1** exists in a twisted conformation, however, the single crystal X–ray structure of **2.1** displays s–*trans*/*E*/s–*trans* conformation,[151] as shown in Figure 1.15a and b, respectively. In the solid state structure the stabilising C–H···:N azo–N lone pair interaction is preferred over the destabilising pyridyl–N

and azo–N lone pairs N:···:N (Figure 1.15c and d). There are also a number of other factors which are responsible for planar conformations with colinear adjacent nitrogen atoms.[152]

Ligand **2.1** was first described in 1927 by Kirpal *et al.*[153] and later in 1969 was recognised by Baldwin *et al.*[154] to exhibit strong interactions with low–valent metal centres such as iron(II). The presence of two equivalent metal centres in the **2.1**–bridged ruthenium complex, $[(bpy)_2Ru(\mu\text{–}\mathbf{2.1})Ru(bpy)_2]^{4+}$ enables the formation of two diastereoisomers, *meso* and *racemic*. This feature was exploited by Kelso *et al.*,[93] who have reported the synthesis of a series of dinuclear α–azodiimine bridged ruthenium(II) complexes and their separation into diastereoisomers, i.e. *meso* (ΔΛ) and *racemic* (ΔΔ/ΛΛ) forms, as shown in Figure 1.16. Electronic spectral and electrochemical studies indicated differences in the communication between the metal centres in the two diastereoisomeric forms.[93]

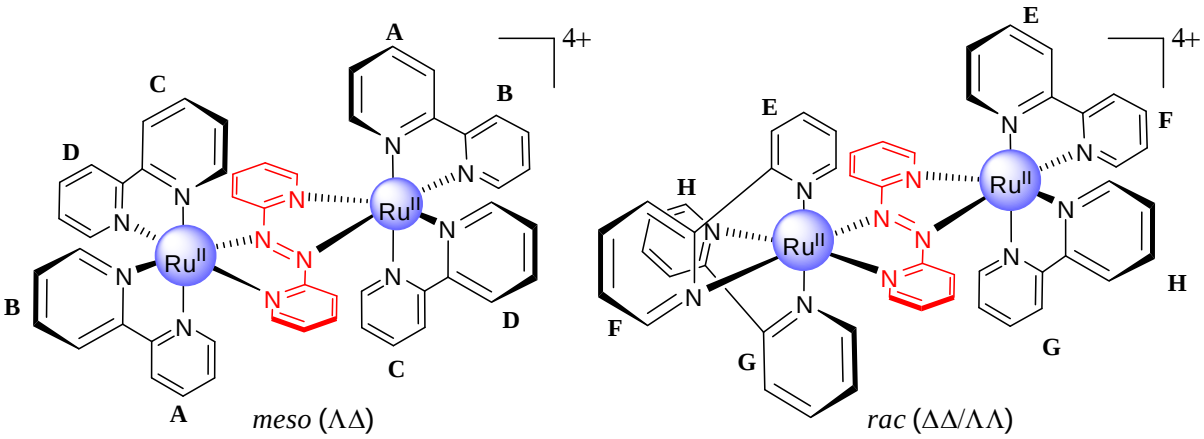

Figure 1.16. Diastereoisomers of $[(bpy)_2Ru(\mu\text{–}\mathbf{2.1})Ru(bpy)_2]^{4+}$.

As reviewed by Kaim *et al.*,[155] the ability of **2.1** and its analogues to bridge two metal centres at a distance of about 5 Å *via* two five–membered chelate rings and relatively low–lying π*–orbitals makes it a suitable ligand to study interactions between metal centres across an unsaturated molecular bridge.[150],[155],[156] A more detailed investigation of this ligand will be discussed in Chapter 2.

1.4. The Model System

The coordination chemistry of **2.1** has been of interest mainly to develop an understanding of ligand–mediated intramolecular metal–to–metal communication. As seen from the literature studies and previous work in the group,[74],[99],[100],[157],[158] subtle changes in the ligand structure can have a dramatic effect on the physicochemical properties of the subsequent complex. Accordingly, we were drawn towards the investigation of substituted azo–based compounds as potential candidates for ligand–mediated intramolecular metal–to–metal communication.

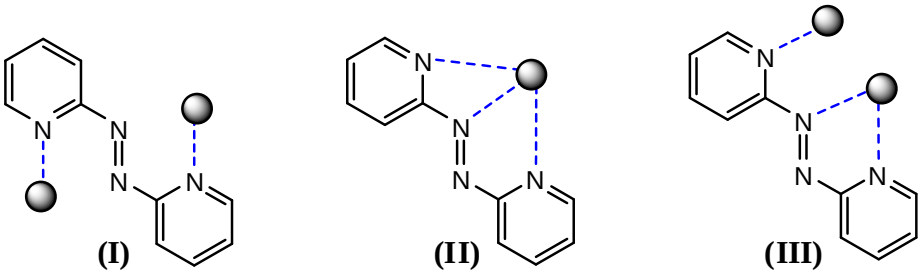

Figure 1.17. Other possible coordination modes of **2.1**.

Ligands with multiple binding sites have led to the formation of coordination networks with greater structural diversity.[159],[160] Multinodal ligands have been used to prepare a large array of discrete one–, two– and three–dimensional metallosupramolecular assemblies.[161] The azo N–aromatic ligands, in addition to the bis(chelating) coordination mode, are also capable of several other possible coordination modes, as shown in Figure 1.17.[162–164] Interest in silver(I) complexes of azo aromatic compounds as building blocks for coordination polymers[165],[166] and our interest in silver(I) chemistry,[167–173] inspired us to also explore the metallosupramolecular self–assembly of azo N–aromatic ligands.

1.5. Metallosupramolecular Chemistry

The concepts of complex formation may be extended to form one of the central principles in supramolecular chemistry.[174] Metallosupramolecular chemistry is considered to represent a "generalized coordination chemistry extending beyond the coordination of transition metal ions by organic and inorganic ligands" to "the chemistry of molecular assemblies and of intermolecular bonds."[175],[176] In general, supramolecular chemistry concerns non–covalent bonding interactions like ion–ion interactions, ion–dipole interactions,

dipole–dipole interactions, hydrogen bonding, cation–π interactions, anion–π interactions, π–π interactions and van der Waals forces etc.[177],[178]

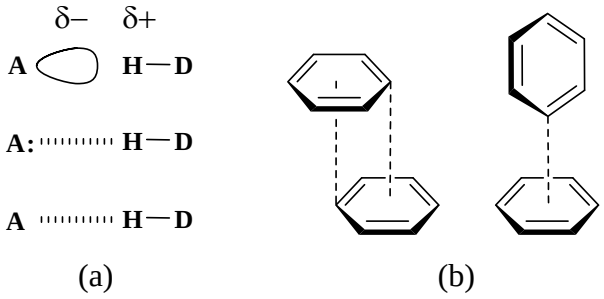

Figure 1.18. Two of the most common non–covalent interactions (a) Hydrogen bonding between acceptor atom (A) and hydrogen atom of the donor atom (D). (b) The π–π interactions between two benzene molecules face–to–face (left) and edge–to–face (right).

Hydrogen bonding interactions, shown in Figure 1.18a, are commonly encountered in supramolecular assemblies between the hydrogen donor atoms and the electronegative or electron–deficient acceptor atoms.[179–181] These interactions are relatively weak (5–50 kJ mol^{-1}) and are generally directional.[179],[180] Other interactions commonly observed in supramolecular species involve face–to–face and edge–to–face π–π stacking interactions, as shown in Figure 1.18b.[182] These are categorised as weak electrostatic interactions[177] with energies ranging between 0–20 kJ mol^{-1}. Typically, these interactions are relatively weak individually; however, a combination of multiple interactions can act as a 'glue' to build up large supramolecular aggregates.

The construction of supramolecular architectures from a combination of organic ligands and metal ions is described as metallosupramolecular chemistry, a term first introduced by Constable,[183],[184] which makes use of the interactions between metal ions and donor groups in the organic molecule. A diverse range of discrete and polymeric aggregates can be obtained by simply mixing metal and ligand building blocks.[185]

Transition metal ions have characteristic and preferred coordination numbers and geometries. Some of the common metal geometries are shown in Figure 1.19. Therefore, the choice of metal can have a large effect on the structure of the metallosupramolecular system. Silver(I) is a d^{10} transition metal with a flexible coordination number and geometry, with a preference for two–coordinate (linear or bent), three–coordinate (trigonal) and four–coordinate (tetrahedral) geometries.[186] Unlike the robust Ru(II) complexes, due to the weak

nature of the silver–ligand interactions, such complexes are often influenced by weaker supramolecular interactions and crystal packing forces in the solid state structure.[187–189]

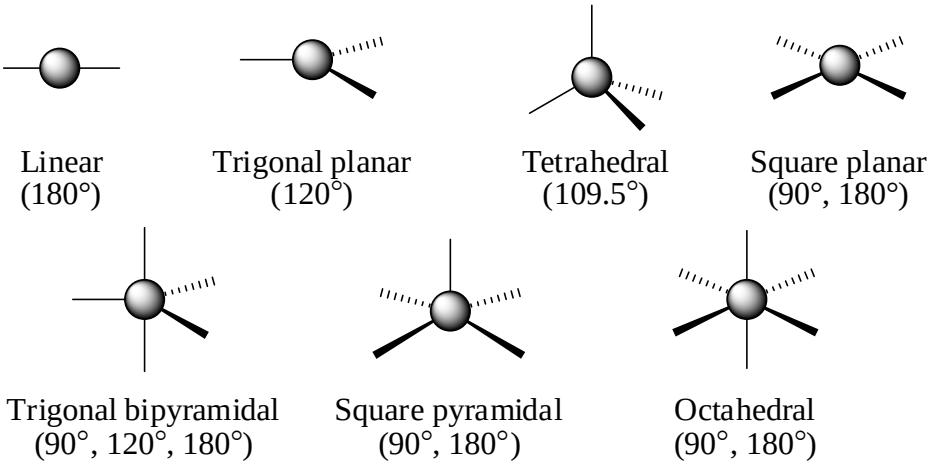

Figure 1.19. Some of the common coordination geometries and the angles for metals.

The ligand design also plays an important role in determining the shape of the overall structure. Aromatic N–heterocycles are commonly used for the construction of metallosupramolecular assemblies as the spatial arrangement, the spacing between the donor atoms, electronic and steric properties can easily be modified.[167],[190–195] The two commonly used ligands 2,2'–bipyridine **1.1**[196] and 4,4'–bipyridine **1.8**[197–201] behave as 'convergent' and 'divergent' donor atoms, respectively, as shown in Figure 1.20. Ligands such as 2,2'–bipyrazine **1.26**[161],[202] and 2,2'–bi–1,5–naphthyridine **1.27**[159] can interact with metals in both these ways and are therefore described as ambivergent ligands.

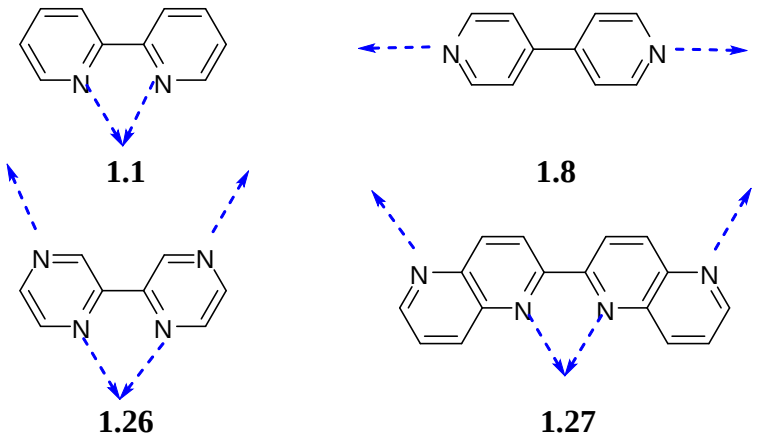

Figure 1.20. Potential coordination modes for symmetrical N–heterocycles.

The coordination requirements of the metal ions are matched with the bonding properties of the polydentate ligands to build a wide range of novel supramolecular species ranging from polygons,[193],[200],[203–205] helicates,[206–209] interlocked rings,[210–212] coordination polymers and networks.[190],[213],[214] The combination of bidentate ligands and two–coordinate metal ions can often lead to one–dimensional coordination polymers,[190] where the ligands have a linear geometry (pyrazine **1.6**, [199],[215],[216] 4,4'–bipyridine **1.8**,[198],[217–220] 1,4–bis(4–pyridyl)benzene **1.28**),[221],[222] and the donor groups are linked by a rigid spacer group.

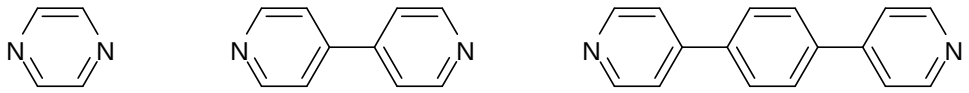

1.6 7 Å **1.8** 11 Å **1.28** 15 Å

Figure 1.21. Some common linear bridging ligands and their corresponding M–M separations.

The coordination of rigid ligand **1.8** to linear bridging metal ions such as silver(I) as shown in Figure 1.22a, leads to a one–dimensional coordination polymer.[219],[223] Fujita *et al.'s* two–dimensional molecular square, as shown in Figure 1.22b, comprises of square planar *cis*–coordinated platinum(II) or palladium(II) centres with **1.8** as the rigid linear bridges.[200] A three–dimensional polyhedron, such as a molecular cube (Figure 1.22c), can be constructed by using **1.8** and a facially capped ruthenium precursor.[201] The dimensionality of the metallosupramolecular structure, therefore, can be altered by modifying the components involved.[184]

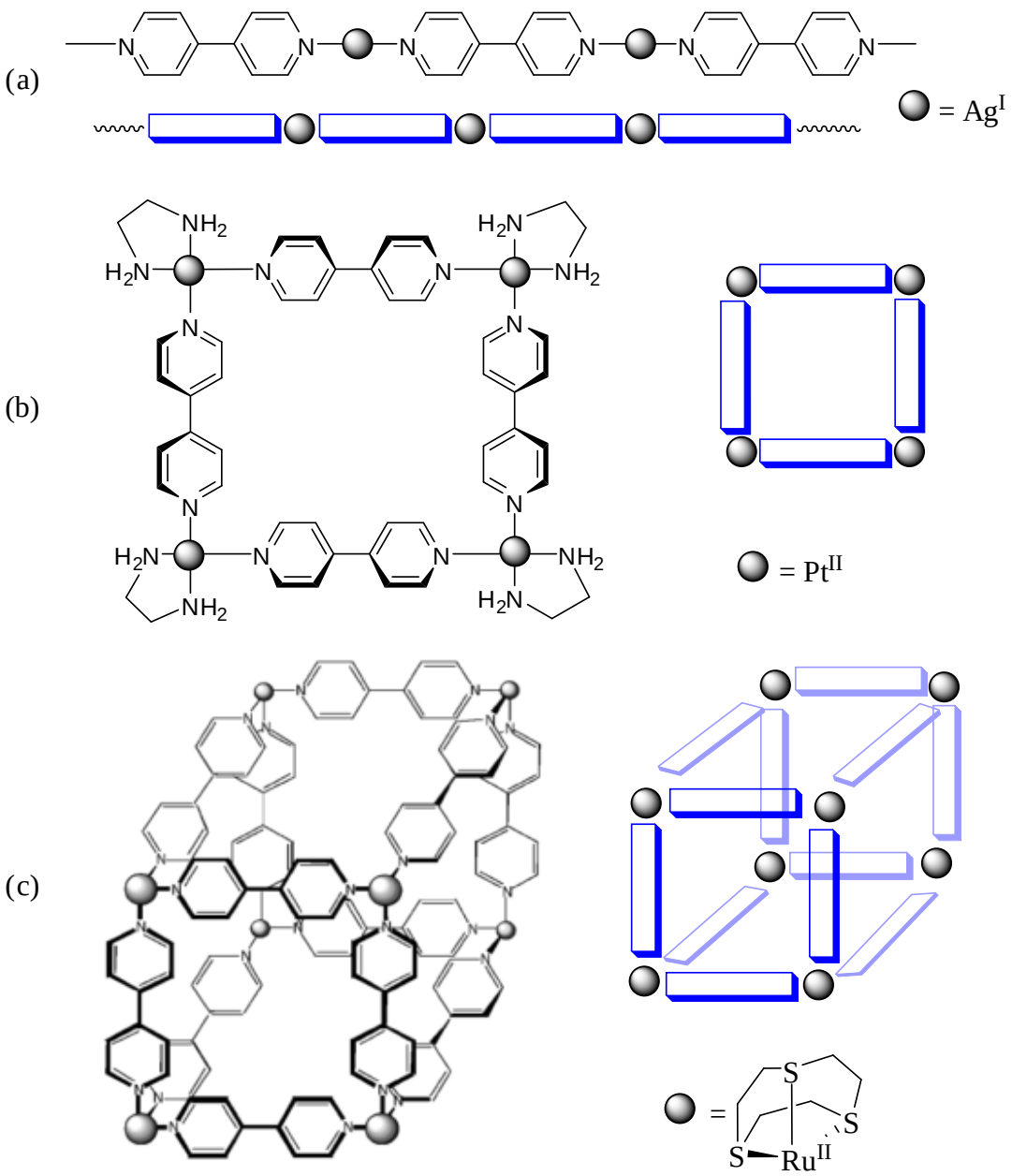

Figure 1.22. Structural representation of (a) 1D coordination polymer; (b) 2D molecular square and (c) 3D molecular cube.[201]

In addition to these, the choice of anion and solvent used can also influence the formation and type of the metallosupramolecular assembly.[189] Non–coordinating anions, such as hexafluorophosphate (PF_6^-) and tetrafluoroborate (BF_4^-) anions, occupy the free sites around the metal centre and allow maximum interaction between the ligand and the metal ions. Coordinating anions, such as nitrate (NO_3^-), triflate ($CF_3SO_3^-$) and trifluoroacetate ($CF_3CO_2^-$), affect the coordination number and geometry of the metal by interacting with the metal centre in a chelating, bridging or terminating manner. As a result, the choice of anions can template the formation of supramolecular assemblies.[172],[224–228]

1.6. Thesis Coverage

Ligand–bridged dinuclear complexes have been the subject of extensive research with considerable attention on the nature and magnitude of metal–metal interactions in such complexes. These interactions are mediated by the bridging ligand and in the case of N–heterocyclic rings, communication between the metal centres takes place through the π–system of the ligand. Therefore, this project involves the synthesis and study of bridging ligands, capable of mediating strong communication between the metal centres. The high degree of metal–metal interaction within the dinuclear complexes of azobispyridine **2.1**, prompted us towards the investigation of dinuclear ruthenium(II) complexes with N–heterocyclic azo compounds as the bridge.

Chapter 2 investigates the synthesis and coordination chemistry of azobispyridine, **2.1**, and its substituted derivatives. The ligands vary by substitution in the pyridine ring. A range of mono– and dinuclear Ru(II) complexes were synthesised and will be discussed in detail. The nature of the metal–ligand and metal–metal interactions was probed by UV/Visible spectroscopy and electrochemistry.

Chapter 3 concentrates on the synthesis and Ru(II) complexes of ligands with azo units between different N–heterocyclic cores. The ligands were classified into two groups, depending on the core structure. The first class of ligands contain pyrimidine–based azo compounds and the second one involves azo compounds based on fused N–heterocyclic rings such as quinoline, quinazoline, quinoxaline and naphthyridines. These ligands were used to investigate the effect of different rings on the electronic coupling between the metal centres.

The synthesis and coordination chemistry of hexadentate azo compounds coordinating in a bis(tridentate) manner are discussed in Chapter 4. The complexes were characterised by ^{1}H, ^{13}C NMR spectroscopy and X–ray structure analysis.

Chapter 5 involves the synthesis of bis–pyridylimine ligands, where the two pyridylimine units are connected either directly or through a spacer of variable length, between the two imine units. The influence of these flexible imine moieties on the electronic coupling between the metal centres in dinuclear ruthenium complexes is probed using electrochemistry.

In Chapter 6, different coordination modes of the azo ligands with a range of different silver(I) salts are discussed. Depending on the coordinating strength of the anions a variety of discrete or polymeric chains were obtained. The structures were confirmed by X–ray crystallographic analysis.

Characterisation of the ligands and ruthenium(II) complexes were achieved by ^{1}H and ^{13}C NMR spectroscopy, mass spectrometry, elemental analysis and infrared spectroscopy. Ruthenium(II) complexes were also characterised by UV/Visible spectroscopy, electrochemistry and X–ray crystallography where possible. The structures of silver(I) complexes were determined mainly from X–ray crystallography and elemental analysis.

Chapter 2

Bidentate ligands based on azobis(pyridines)

2. Bidentate ligands based on azobis(pyridines)

2.1. Introduction

Azo compounds based on N–containing heterocycles, such as 2–phenylazopyridine (pap), **1.25**, and its analogues are extensively studied ligands,[139–142],[144],[145] in which an additional donor substituent allows a stabilising chelate coordination mode.[146–148] The mononuclear complexes of azobispyridine are similar to the corresponding compounds with pap ligands.[143],[144],[149] The symmetrical azobispyridine ligands, such as 2,2'–azobispyridine, **2.1**, is related to the widely studied 2,2'–bipyridine, **1.1**, by insertion of an azo bridge between the two pyridine rings (Figure 2.1).[149]

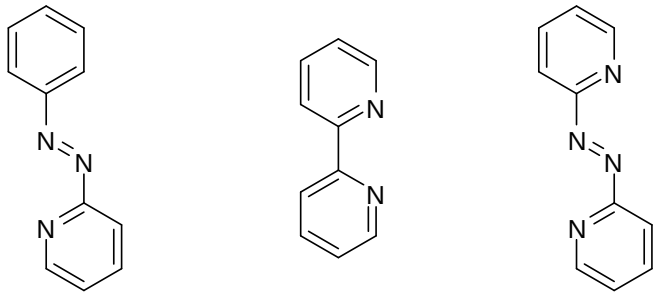

1.25 **1.1** **2.1**

Figure 2.1. Three closely related ligands that form five–membered chelate rings.

2,2'–Azobispyridine, **2.1**, was recognized by Baldwin *et al.*[154] to exhibit strong interaction with low–valent metal centers such as iron(II) and to have a potential for several different coordination modes. The structurally established alternatives include mono– and dinuclear coordination situations with five–membered (NNCNM) chelate ring formation, as illustrated in Figure 2.2.

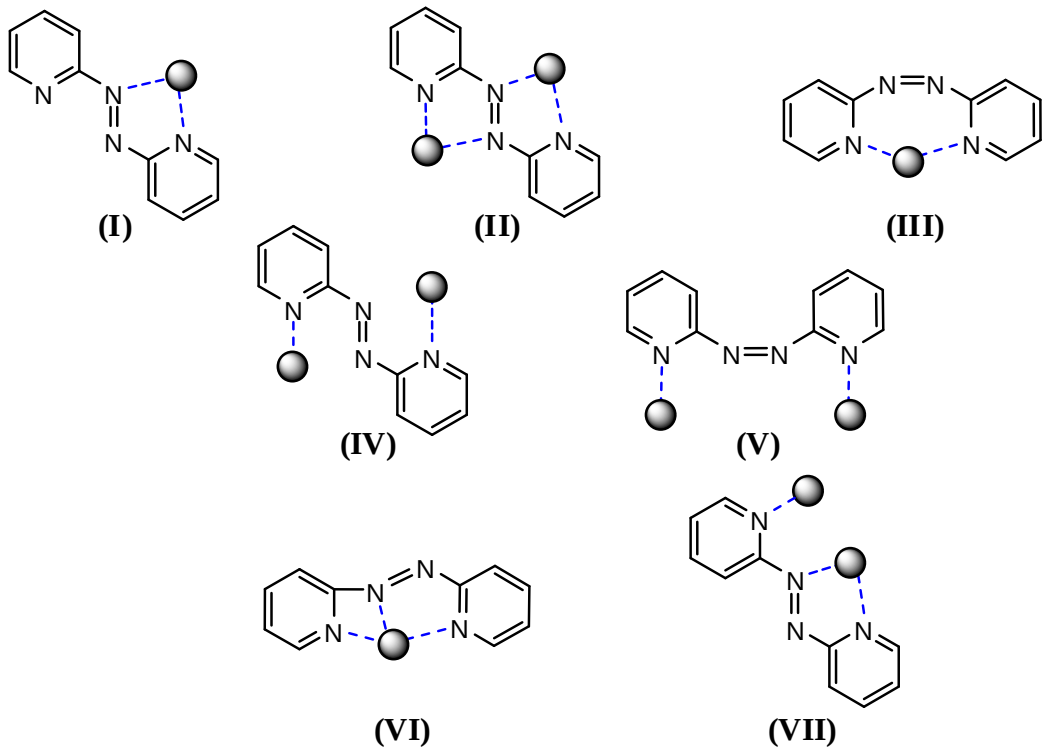

Figure 2.2. Different coordination modes of **2.1**.

The modes of coordination **(I)** and **(II)** possess the most favourable five–membered chelate rings that are preferred over the seven–membered possibility **(III)**. The non–chelate bonding of bis–monodentate **2.1 (IV)** and **(V)** are feasible, however, evidence for only **(IV)**, shown in Figure 2.3 has been documented to date.[162] Although, the ligand cannot function as a tridentate ligand without experiencing considerable strain, Tsurugi *et al.*[229] have shown that a tungsten(IV) complex can form as shown in Figure 2.4.

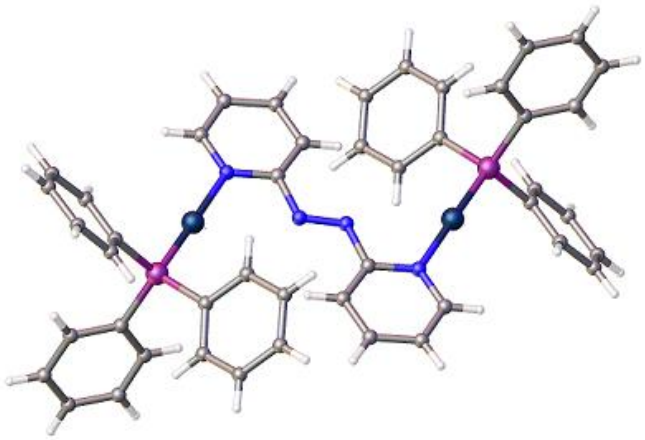

Figure 2.3. The X–ray crystal structure of $[(PPh_3)_2Au(\mathbf{2.1})]^{2+}$ displaying coordination mode (**IV**).[162]

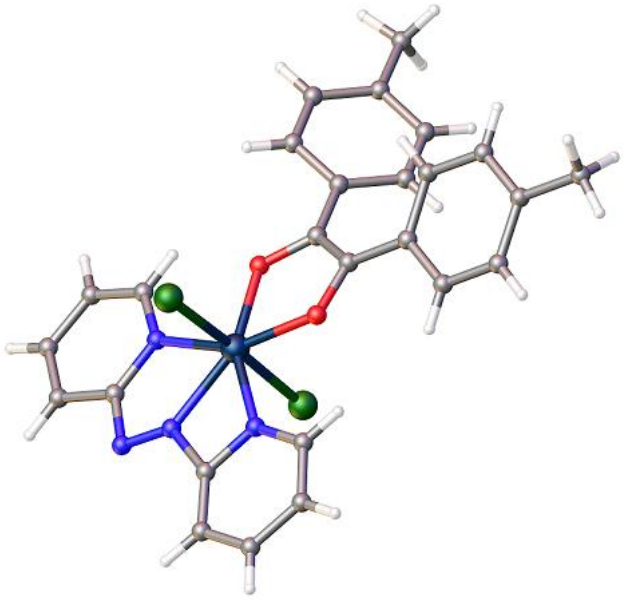

Figure 2.4. An example of a $[(C_6H_{14}O_2)W(\mathbf{2.1})Cl_2]$ complex where **2.1** adopts structure (**VI**).[229]

Interestingly, in the $[Os_4(\mu\text{–}H)_2(CO)_{10}\{\mu\text{–}\eta^3\text{–}(\mathbf{2.1})]$ cluster, both pyridine and azo nitrogens were found to coordinate to the cluster core, as shown in Figure 2.5a.[230] Dogan *et al.*[164] showed that in the dinuclear complex, $[(\mathbf{2.1})PtCl](ZnCl_4)$, two platinum(II) centres are bridged in an unsymmetrical fashion due to the $\mu,\eta^2\text{:}\eta^1$–coordination mode of **2.1**, as shown in Figure 2.5b with the counterions removed for clarity.

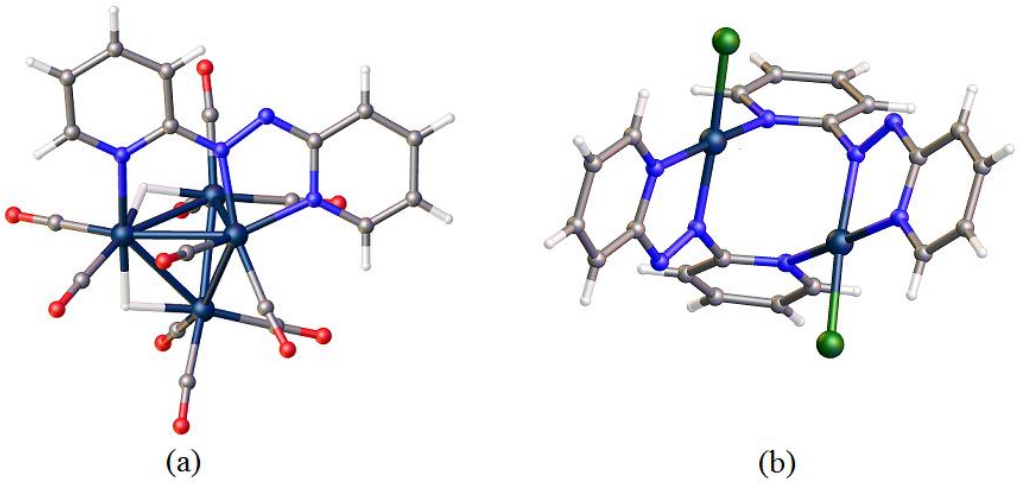

Figure 2.5. The X–ray crystal structures of complexes where **2.1** exhibits coordination mode (**VII**).[230],[164]

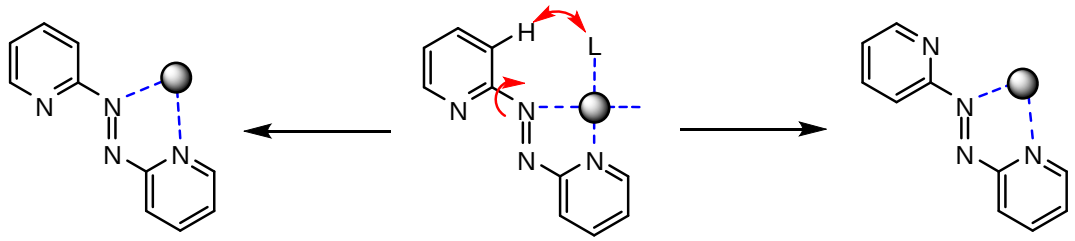

(Ia) **(I)** **(Ib)**

Scheme 2.1

In mononuclear complexes, where one of the 2–pyridyl rings remains non–coordinated, two conformations **(Ia)** and **(Ib)** are possible (Scheme 2.1). Due to the repulsion effects between the azo N–atom lone pairs, twisting of the 2–pyridyl ring from **(Ia)** to **(Ib)** occurs. This diminishes the non–bonding contacts between the terminal ligands (L) on the metal and the pyridyl group and also the destabilising repulsion between the azo–N and pyridine–N atoms.[152],[156],[231]

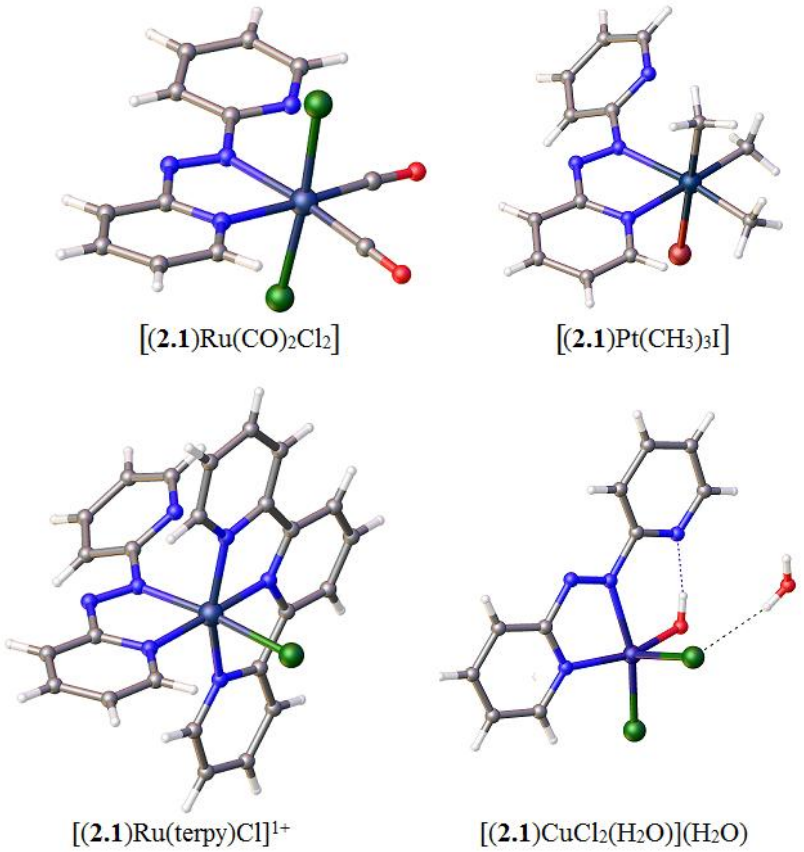

Figure 2.6. The X–ray crystal structures of some mononuclear complexes showing the **Ib** form as reported in previous studies.[232–235]

The X–ray structure data available for the mono–chelate complexes such as [(**2.1**)Ru(CO)$_2$Cl$_2$],[232] [(**2.1**)Pt(CH$_3$)$_3$I],[233] [(**2.1**)Ru(terpy)L^{n-}](ClO$_4$)$_{2-n}$, L = Cl, H$_2$O, CH$_3$CN,[234] and [(**2.1**)Cu(Cl$_2$)(H$_2$O)][235] are closer to the structure **(Ib)** with the pyridyl–N directed towards the metal centre, as shown in Figure 2.6. An example of the rare s–*cis/E*/s–*trans* (**Ia**) form for **2.1** was observed in the complex [(**2.1**)Pt(CH$_3$)$_3$Br], as illustrated in Figure 2.7.[233]

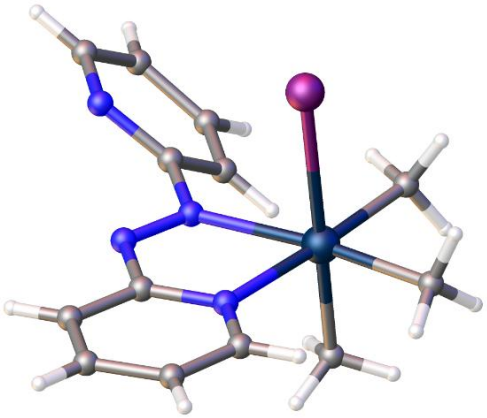

Figure 2.7. An example of an **Ia** conformation of the **2.1** ligand in a mononuclear complex.[233]

However, in the dinuclear complexes, such interactions are inevitable and the μ–**2.1** ligand twists in order to chelate to both metals. The "S–frame" conformation of the ligand (Scheme 2.2), with the two five–membered chelate rings sharing a common bridge enables a short intramolecular distance between the metal centres.[155]

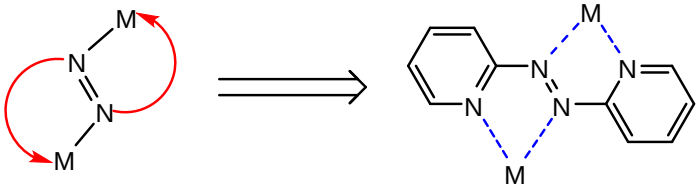

Scheme 2.2

The X–ray crystal structure for (μ–**2.1**)[Re(CO)$_3$Cl]$_2$ reported by Hartmann *et al.*,[231] exhibits a Re–Re distance of 5.033(7) Å, which is considerably shorter than the inter–metal separation observed in conventional bridging ligands, such as 2,2'–bpym (*ca.* 5.6 Å) and pyrazine (*ca.* 6.9 Å).[65],[236–238] The π–molecular orbital perturbation calculation carried out by Kaim *et al.*[156] on the complex (μ–**2.1**)[Mo(CO)$_4$]$_2$ indicates substantial stabilisation of the π* (LUMO) levels in **2.1**, which strongly facilitates reduction of the complexes and causes

intense shifts in the MLCT absorption bands to the near–infrared region. These spectral results strongly suggest the use of **2.1** as a useful bridging ligand for studies relevant to the ligand mediated electronic interactions between metal centres.

The capability of **2.1** to bridge two metals at a rather close distance has proven exceptional in stabilizing mixed–valent dimetal configurations, as well as radical intermediates of the multistep reduction process.[150] As an abundantly studied example, the step–wise metal–centered one–electron oxidation of $[(bpy)_2Ru(\mu\text{–}\mathbf{2.1})Ru(bpy)_2]^{4+}$ occurs with a potential separation of ~0.5 V, translating to a comproportionation constant, K_c of 10^8 – 10^9 and hence it exhibits a very high degree of metal–metal interaction.[93],[150] The K_c values for other commonly used bridging ligands such as 2,2'–bpym or 2,5–dpp are much lower for the dinuclear $(bpy)_2Ru^{2+/3+}$ system.[39],[73],[239],[240] The fact that the diosmium analogue $[(bpy)_2Os(\mu\text{–}\mathbf{2.1})Os(bpy)_2]^{4+}$ has a K_c value greater than 10^{17}, further supports the mediating nature of the π^*–acceptor orbital of the **2.1** ligand.[241]

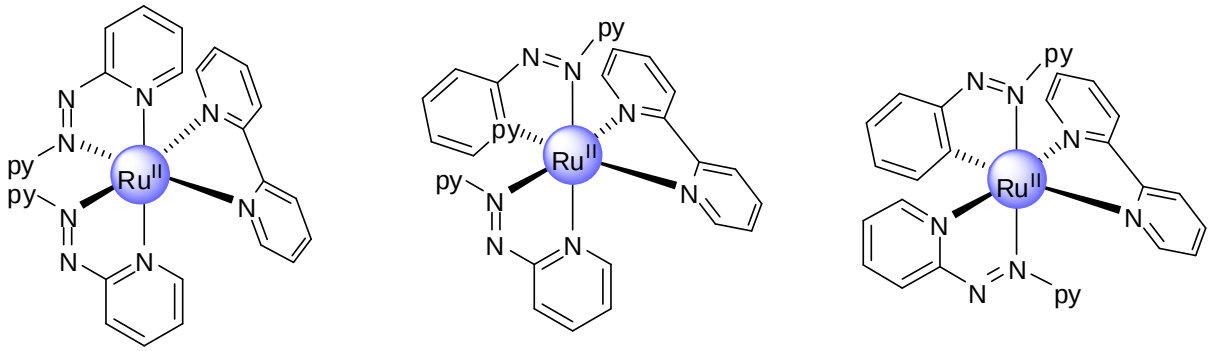

Figure 2.8. Diastereoisomers of $[(bpy)Ru(\mathbf{2.1})_2]^{2+}$.

The unsymmetrical nature of the five–membered chelate rings formed by ligand **2.1** and its capability to bind to two metal centres gives rise to different kinds of isomerism in complexes with octahedral metal centres. The three diastereoisomers of $[(bpy)Ru(\mathbf{2.1})_2]^{2+}$, were identified by Heilmann *et al.*,[242] using ^{1}H NMR spectroscopy and the crystal structure information from precursor complexes (Figure 2.8).

The absence of a centre or plane of symmetry for the metal sites in complexes such as $[(bpy)_2Ru(\mu\text{–}\mathbf{2.1})Ru(bpy)_2]^{4+}$ enable the formation of two diastereoisomers, *meso* and *racemic* forms. This feature was exploited by Kelso *et al.*,[93] who have also reported the synthesis of a series of dinuclear α–azodiimine bridged ruthenium(II) complexes and their

separation into diastereoisomers, i.e. *meso* (ΔΛ) and *racemic* (ΔΔ/ΛΛ) forms, shown in Figure 2.9. Electronic spectral and electrochemical studies indicate differences in the communication between the metal centres in the two diastereoisomeric forms.

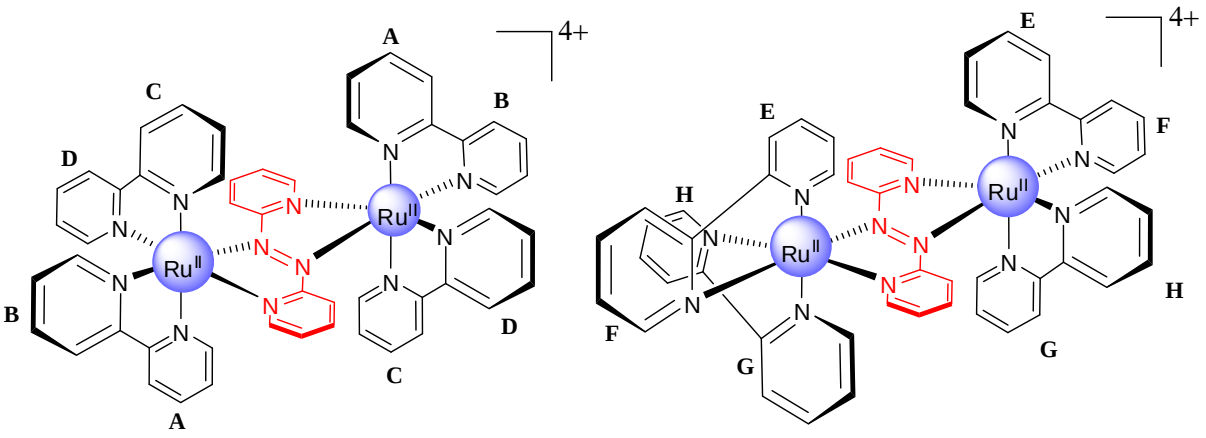

meso (ΛΔ) *rac* (ΔΔ/ΛΛ)

Figure 2.9. Diastereoisomeric forms of $[(bpy)_2Ru(\mu\text{–}\mathbf{2.1})Ru(bpy)_2]^{4+}$.[93]

The Steel group has considerable expertise in the study of metal–metal interactions.[74],[98],[100],[243],[244] Examples of some ligands previously synthesised in the group are shown in Figure 2.10. These ligands were complexed with ruthenium(II) metal to investigate the inter–metal interactions. It is clearly evident from the comproportionation constant K_c, that small modifications in the bridging ligands can drastically alter the communication between the metal centres.

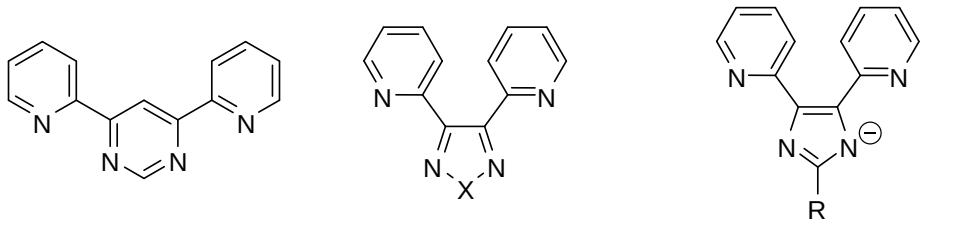

K_c = 500

X = O (K_c = 800,000)
S (K_c = 25,000)
N$^-$ (K_c = 1,200,000)

R = H (K_c = 750,000)
Ph (K_c = 46,000)

Figure 2.10. Examples of ligands synthesised previously in the Steel group.

Therefore, we were interested in investigating the dinuclear ruthenium(II) complexes with azobispyridine ligands as the bridge. This chapter details the synthesis of a series of mono– and dinuclear complexes containing ligands based on azobispyridine, as shown in Figure 2.11. The influence of different substituents in the bridging ligand on the metal–metal

and metal–ligand interactions is assessed using UV/Vis absorption spectroscopy and electrochemical studies

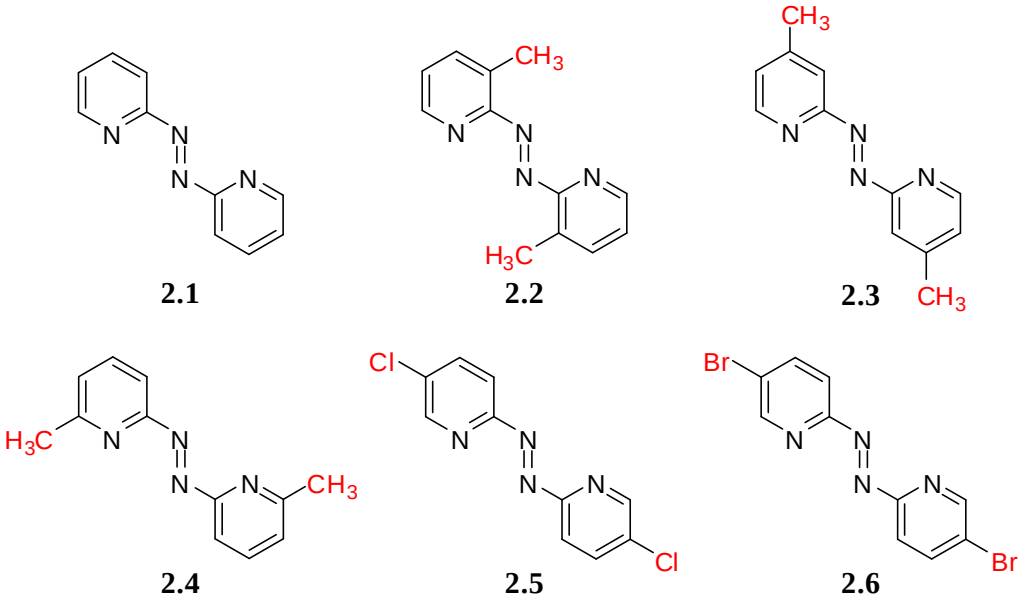

Figure 2.11. The ligands based on symmetrical azobispyridine.

2.2. Syntheses of the ligands

To analyse the influence of different substituents on the inter–metal communication, the parent ligand **2.1** with no substituent and three methyl substituted derivatives **2.2** – **2.4** were synthesised. These ligands were all synthesised starting from commercially available amine precursors. The precursor amines required for the synthesis of electron–donating halogen substituted derivatives **2.5** and **2.6** were synthesised in the laboratory and are discussed below.

Oxidative coupling of the corresponding aminopyridines using sodium hypochlorite, as outlined in Scheme 2.3, gave the required azo ligands **2.1** – **2.4**.[93] The *trans* isomer is thermodynamically preferred, and in ^{1}H NMR studies no evidence for the *cis* product was found.

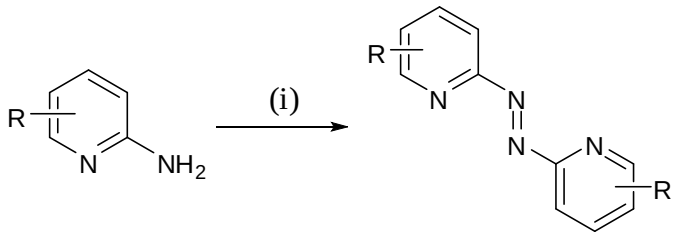

(i) NaOCl, 0 to -20 °C, 15 - 30%

R	**Ligand**
H	**2.1**
3–CH_3	**2.2**
4–CH_3	**2.3**
6–CH_3	**2.4**

Scheme 2.3

Commercially available, 2–aminopyridine was first converted to the chloro amine precursor using N–chlorosuccinimide.[245] This was then subjected to oxidative coupling using sodium hypochlorite to give the corresponding ligand **2.5** in moderate yield, as shown in Scheme 2.4.

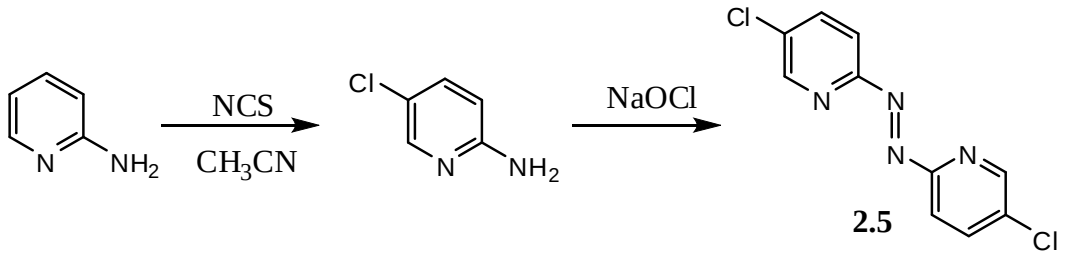

Scheme 2.4

The bromo–substituted ligand **2.6**, was similarly synthesised, as outlined in Scheme 2.5. The synthesis involves reaction of 2–aminopyridine with N–bromosuccinimide,[246] followed by coupling using NaOCl to give the desired ligand **2.6**.

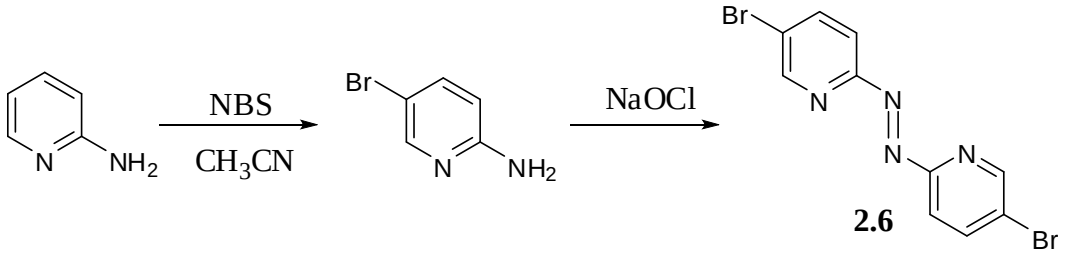

Scheme 2.5

2.3. Coordination chemistry of azobis(pyridines)

The ruthenium(II) complexes were synthesised by reaction of the bridging ligand with a ruthenium(II) precursor in 50% aqueous methanol/ethanol solution. The complexes were isolated as the hexafluorophosphate salts. The purification techniques used involved either silica gel column chromatography using 7:1 acetonitrile/saturated potassium nitrate as the eluent or ion exchange chromatography on SP Sephadex C–25 *via* a gradient elution process using 0.1–0.5 mol L^{-1} sodium chloride solution as the eluent.

2.3.1. Complexes of 2.1

The mono– and dinuclear ruthenium(II) complexes of ligand **2.1** have been previously synthesised and characterised by Kelso *et al.*[93] and Kaim *et al.*[155] using solution studies; however, at the time this work was carried out the crystal structures were not known. Thus, to elucidate the crystal structures of the complexes **2.7** and **2.8**, the ligand **2.1** was refluxed with three equivalents of $[Ru(bpy)_2Cl_2]$ in 50% aqueous methanol for 3 days, as shown in Scheme 2.6.

The crude product was loaded onto a SP Sephadex C–25 column and separation of the mononuclear and dinuclear products from the crude mixture was achieved *via* a gradient elution procedure using aqueous 0.1–0.5 mol L^{-1} sodium chloride as the eluent.[93] Three bands were eluted: Band 1 (dark red, 0.1 mol L^{-1} NaCl), Band 2: (purple, 0.2 mol L^{-1}) and Band 3: (green, 0.3 mol L^{-1}). The fractions were precipitated by addition of a saturated solution of ammonium hexafluorophosphate to each band. The resultant products were extracted into dichloromethane and the solvent was removed under reduced pressure. The solid residues were recrystallised from acetone/diethyl ether. The composition of Bands 1, 2 and 3 were established by electrospray mass spectrometry and ^1H NMR. Analysis of Band 1 revealed the presence of a mononuclear ruthenium species, Band 2 as unreacted ruthenium(II) precursor and Band 3 as a dinuclear ruthenium species.

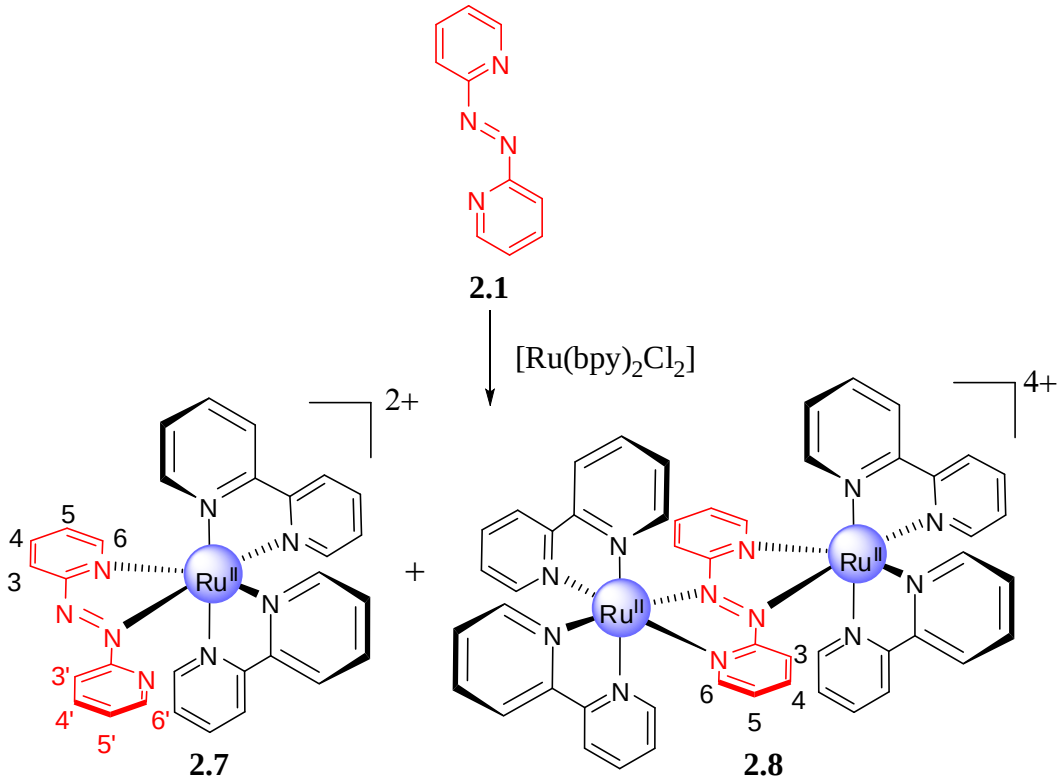

Scheme 2.6

When a ligand forms a transition metal complex, subtle or drastic differences in the NMR spectra of the ligand and complex are seen. The differences are described as the coordination induced shifts (*CIS* = $\delta_{complex} - \delta_{ligand}$). A number of factors have been previously identified that are responsible for the sign and magnitude of *CIS* values in ruthenium(II) complexes, such as ligand–to–metal σ donation, metal–to–ligand π donation, conformational changes due to chelation and through–space ring–current anisotropy effects.[247] The contribution of these factors is included in the discussion which follows.

The ^{1}H NMR spectrum of **2.7** shows 24 non–equivalent proton signals, some of which are overlapping, as shown in Figure 2.12. Six different pyridine ring environments exist within the complex. Since the ligand **2.1** is unsymmetrical after coordination, its two pyridine rings are non–equivalent. The remaining four rings correspond to the bipyridine rings, which were easily identified by a gCOSY experiment. The pyridine rings corresponding to the bpy ligands were identified by 1D TOCSY and ROESY experiments. The H3' proton (8.88 ppm) corresponding to the free pyridyl ring of the ligand **2.1** is highly deshielded by the nearby azo nitrogen, whereas the H3 proton (7.59 ppm) of the coordinated ring is in a strongly shielded environment due to metal–to–ligand π back–donation. The H6 protons of the ligand **2.1** in the coordinated as well as the free pyridyl ring (7.92 and 7.91 ppm, respectively) are strongly

shielded when compared to the H6 proton (8.75 ppm) in the free ligand **2.1**, due to through–space ring–current effects, which is also evident from the crystal structure shown in Figure 2.13. The *CIS* values, given in Table 2.1, are also in accordance with this observation.

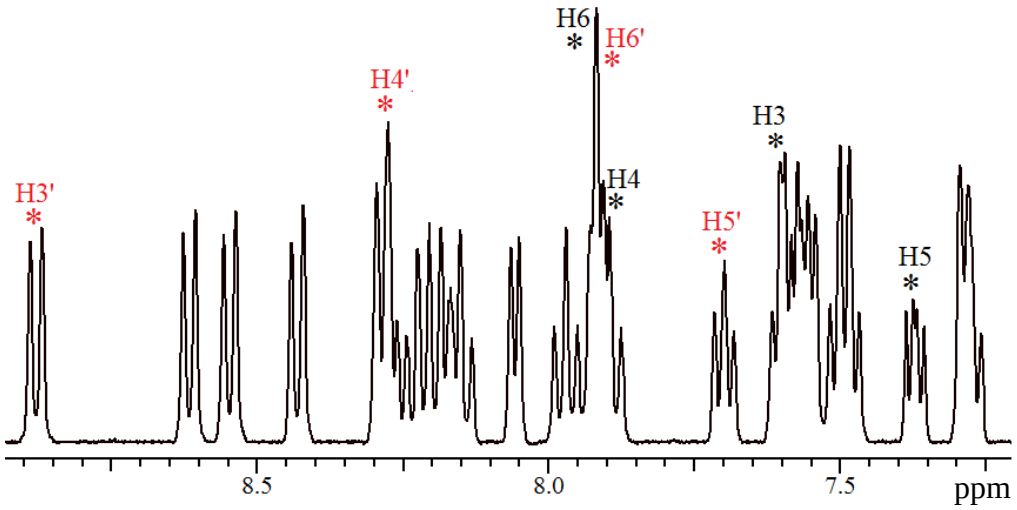

Figure 2.12. The ^{1}H NMR spectrum of complex **2.7**.

Table 2.1. The ^{1}H NMR chemical shifts[a] and *CIS* values[b] (italics) for **2.1** and **2.7**.

	H3	**H4**	**H5**	**H6**
2.1	8.00	8.01	7.54	8.75
2.7[c]	7.59	7.90	7.38	7.92
CIS	*–0.41*	*–0.11*	*–0.16*	*–0.83*
2.7[d]	8.88	8.28	7.70	7.91
CIS	*+0.88*	*+0.27*	*+0.16*	*–0.84*

[a]In acetonitrile–d_3.
[b]$CIS = \delta_{complex} - \delta_{ligand.}$
[c]Coordinated pyridyl ring of **2.1**.
[d]Free pyridyl ring of **2.1**.

*Crystal Structure of **2.7***

A single crystal suitable for X–ray analysis was grown by diffusing petroleum ether into a solution of the complex in acetone. The complex **2.7** crystallises in the triclinic space group *P*–1 with three bidentate ligands, one ruthenium atom, two hexafluorophosphate anions and one acetone molecule in the asymmetric unit, as shown in Figure 2.13.

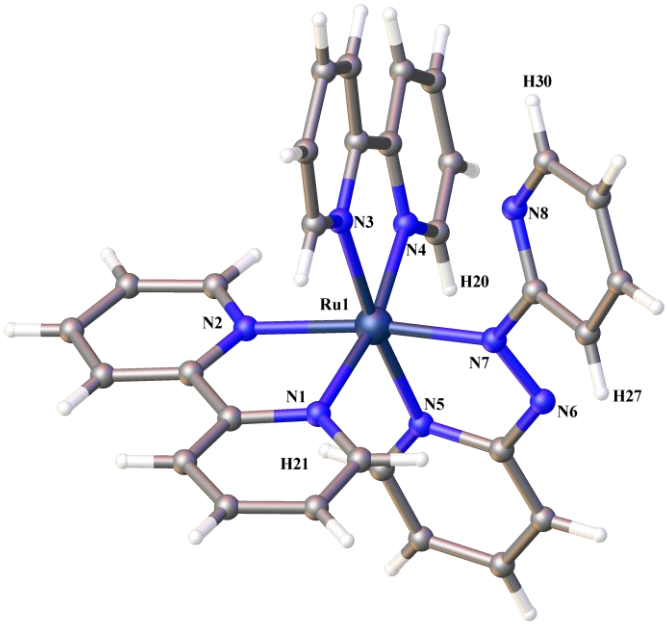

Figure 2.13. The asymmetric unit of compound **2.7**. The counterions and solvate molecules are omitted for clarity. Selected bond distances (Å) and bond angles (°): Ru1–N1 2.072(4), Ru1–N2 2.099(4), Ru1–N3 2.066(4), Ru1–N4 2.065(4), Ru1–N5 2.034(4), Ru1–N7 1.993(4), N6–N7 1.288(5), N1–Ru1–N2 78.16(14), N3–Ru1–N1 93.13(16), N3–Ru1–N2 87.84(14), N4–Ru1–N1 168.18(14), N4–Ru1–N2 92.55(14), N4–Ru1–N3 79.08(16), N5–Ru1–N1 90.24(15), N5–Ru1–N2 98.35(15), N5–Ru1–N3 173.45(15), N5–Ru1–N4 98.41(15), N7–Ru1–N1 96.05(15), N7–Ru1–N2 172.35(15), N7–Ru1–N3 97.54(15), N7–Ru1–N4 93.81(15), N7–Ru1–N5 76.51(15).

The ruthenium(II) atom binds to ligand **2.1** using the azo nitrogen atom N7 and the pyridine ring nitrogen atom N5, forming a stable five–membered chelate ring, with the chelate bite angles being 76.51(15)° (N5–Ru1–N7), 78.16(14)° (N1–Ru1–N2), and 79.08(16)° (N3–Ru1–N4). The ruthenium atom possesses a distorted octahedral geometry. The Ru–N_{azo} distance of 1.993(4) Å (Ru1–N7), is shorter than that of the Ru–N_{py} distance of 2.034(4) Å (Ru1–N5), due to the ability of the azo functionality to act as a π−acceptor unit with effective π−backbonding, Ru(dπ) → azo(π*). The azo bond is almost in the same plane as the coordinated pyridine ring with the torsion angle being 2.0(6)^o (N7−N6−C25−N5), while that of the non–coordinated pyridine ring is –35.3(6)^o (N6−N7−C26−C27). This implies that the non–coordinated pyridine ring is significantly rotated, adopting a structure closer to the **Ib** form discussed previously in Scheme 2.1.

The N_{azo}–N_{azo} distance in this complex is 1.288(5) Å (N6–N7), comparable to those in structurally related complexes.[164],[232–234],[248] Since this structure was determined, the X–ray structure of the corresponding perchlorate salt has been reported,[249] with almost identical structural features. The crystal structure also gives a better understanding of the ^{1}H NMR spectrum of complex **2.7**, shown in Figure 2.12. The H3 proton (H27) of the free pyridyl ligand is highly deshielded due to the twist. The H6 proton (H21 and H30) of ligand **2.1** lies directly over or in the plane of the pyridyl ring of an ancillary bipyridine. The H6 proton (H20) from one of the bipyridine ligands is strongly shielded since it is positioned over the pyridyl ring of **2.1**, and hence experiences ring–current anisotropic interacions from the adjacent ring.

*^{1}H NMR of **2.8***

The ^{1}H NMR spectrum for the dinuclear complex **2.8** (Figure 2.14) shows 20 non–equivalent proton signals, corresponding to five different pyridine rings. Compared to **2.7**, the number of signals for the bridging ligand is halved in **2.8** due to the higher symmetry of the dinuclear complex. Thus, both the pyridine rings corresponding to the ligand **2.1** are equivalent. The signals corresponding to the bridging ligand and the bipyridines are easily identified by a combination of gCOSY, 1D TOCSY and NOESY experiments.

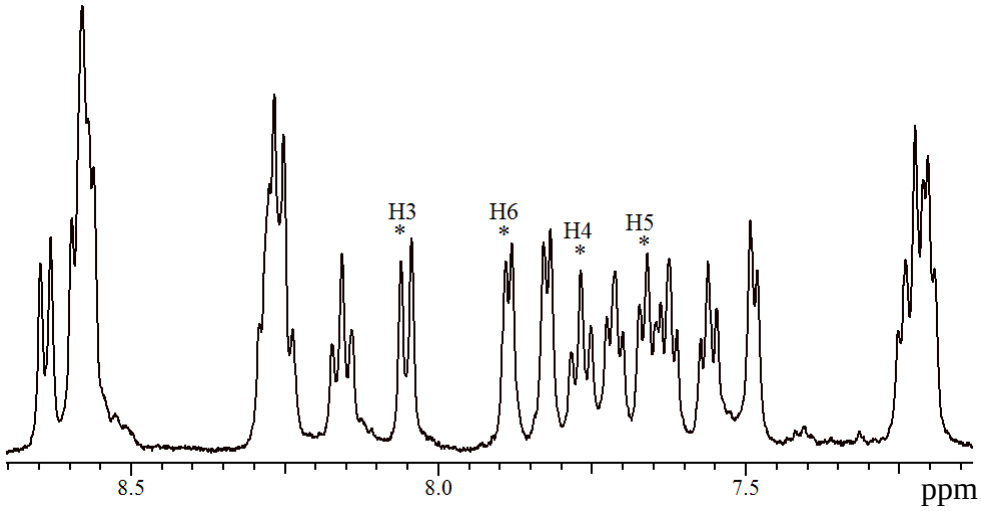

Figure 2.14. The ^{1}H NMR spectrum for complex **2.8**.

Table 2.2 lists the ^{1}H NMR chemical shifts and the *CIS* values in acetonitrile for **2.1** and **2.8**. The *CIS* value for the H3 proton (8.00 ppm) indicates the presence of strong metal–to–ligand π back–donation into the low lying π*–orbital of the ligand. This reduces the strong

positive *CIS* effect of ligand–to–metal σ donation as seen in **2.7**. The H6 proton (7.83 ppm) is strongly shielded due to the through–space ring–current anisotropic effects, as it lies over the pyridyl ring of a bipyridine ligand.

Table 2.2. The ^{1}H NMR chemical shifts[a] and *CIS* values[b] (italics) for **2.1** and **2.8**.

	H3	**H4**	**H5**	**H6**
2.1	8.00	8.01	7.54	8.75
2.8	8.05	7.77	7.66	7.89
CIS	*+0.05*	*–0.24*	*+0.10*	*–0.86*

[a] In acetonitrile–d_3.
[b] $CIS = \delta_{complex} - \delta_{ligand.}$

*Crystal Structure of **2.8***

Crystals of **2.8** were obtained by vapour diffusion of diethyl ether into an acetonitrile solution of the complex. The complex crystallised in the triclinic centrosymmetric space group *P*−1. The asymmetric unit contains half a ligand **2.1**, two bpy ligands and one ruthenium atom, along with two hexafluorophosphate anions and two molecules of acetonitrile. This confirms the formation of the complex in a 1:2 (ligand to metal) ratio. The structure, as determined by X−ray crystallography, is depicted in Figure 2.15.

The complex possesses a crystallographic inversion symmetry about the azo bridge, in such a way that the terminal bipyridine ligands ‘above’ and ‘below’ the plane of the azo ligand are approximately orthogonal indicating the formation of the *meso* diastereoisomer, as illustrated in Figure 2.16. The chelate bite angles are 78.40(9)° (N1–Ru1–N12), 78.42(9)° (N13–Ru1–N24) and 76.42(8)° (N25–Ru1–N31A). The Ru–Ru bond distance is 4.883(4) Å (Ru31–Ru31A) which is shorter than the distance reported for the dinuclear complexes (μ–**2.1**)$[ReCl(CO)_3]_2$ [5.033(7) Å] and $[(\mu\text{–}\mathbf{2.1})\{Cu(PPh_3)_2\}_2](BF_4)_2$ [4.937 Å].[231],[250]

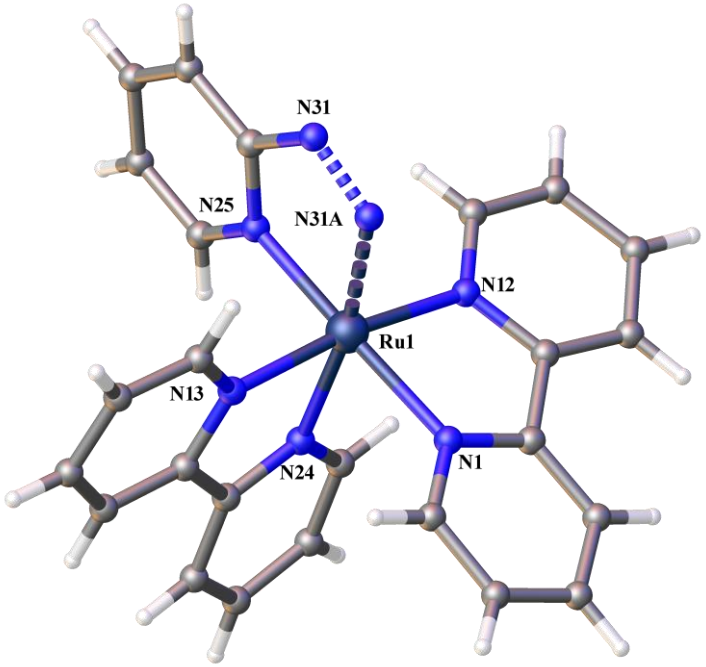

Figure 2.15. The asymmetric unit of complex **2.8**. The counterions and the solvate molecules are omitted for clarity. Selected bond distances (Å) and bond angles (°): Ru1–N1 2.094(2), Ru1–N12 2.063(2), Ru1–N13 2.066(2), Ru1–N24 2.072(2), Ru1–N25 2.021(2), Ru1–N31A 2.049(2), N31–N31A 1.343(4), N25–Ru1–N31A 76.42(8), N25–Ru1–N12 96.63(9), N25–Ru1–N1 173.75(9), N25–Ru1–N13 88.73(9), N25–Ru1–N24 95.90(8), N31A–Ru1–N12 91.98(8), N31A–Ru1–N1 107.31(8), N31A–Ru1–N13 95.29(9), N31A–Ru1–N24 170.29(9), N12–Ru1–N1 78.40(9), N12–Ru1–N13 171.83(8), N12–Ru1–N24 94.84(9), N13–Ru1–N24 78.42(9), N13–Ru1–N1 95.82(9), N24–Ru1–N1 80.88(8).

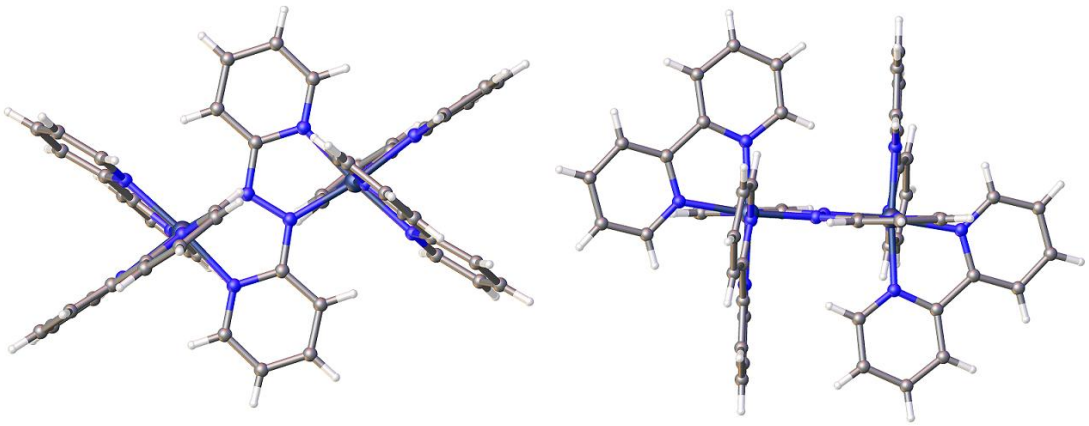

Figure 2.16. Two perspective views of **2.8** indicating the formation of the *meso* isomer. Counterions and solvent molecules are omitted for clarity.

The Ru–N_{azo} bond distance 2.049(2) Å (Ru1–N31) is shorter than the bond length for Ru–N_{py} 2.072(2) Å (Ru1–N25), similar to **2.7**. The N_{azo}–N_{azo} distance in the dinuclear complex N31–N31A is 1.343(4) Å, which is slightly longer than the value observed for **2.7** [1.286(6) Å]. This lengthening might be due to the increased backbonding into the N=N π*–orbital. The average Ru–N bond lengths (*ca.* 2.063 Å) are similar and correlate with those published for related structures.[232],[234] The X–ray crystal structure of the corresponding perchlorate salt has been reported recently and the structural features are almost identical to those discussed above.[249]

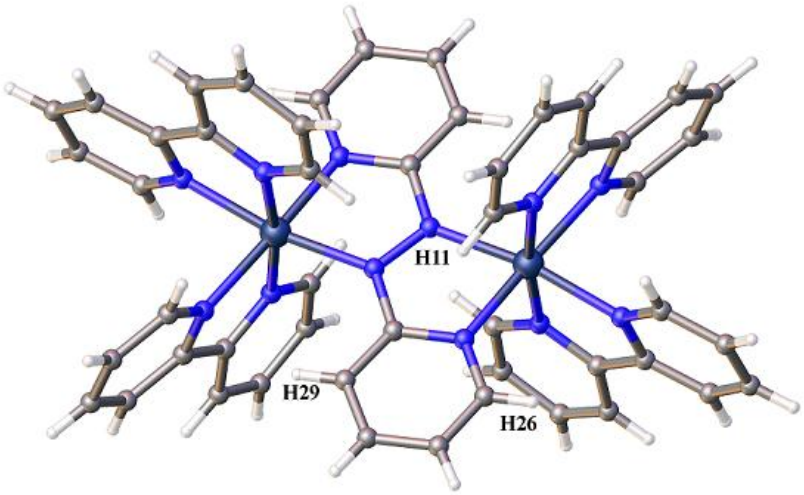

Figure 2.17. A perspective view of **2.8** with three hydrogen atoms being labelled and the counterions and solvent molecules omitted for clarity.

As discussed for the previous complex **2.7**, the X–ray analysis unambiguously allows the establishment of the exact structure. If we correlate the previously shown ^{1}H NMR (Figure 2.10), with the crystal structure, shown in Figure 2.17, the H3 proton (H29) of the bridging ligand is considerably deshielded compared to the mononuclear complex **2.7**, however, the H6 proton (H26) experiences similar ring–current effects. The H6 proton (H11) of the pyridine ring from one of the bipyridines lies directly over the pyridyl ring of **2.1**, and is strongly shielded.

2.3.2. Complex of 2.2

Ligand **2.2**, a potentially doubly–bidentate ligand, reacts with $[Ru(bpy)_2Cl_2]$, as shown in Scheme 2.7, to form only the mononuclear complex **2.9**, which was characterised as $[(bpy)_2Ru(\mathbf{2.2})](PF_6)_2$ by ^1H NMR and mass spectrometry.

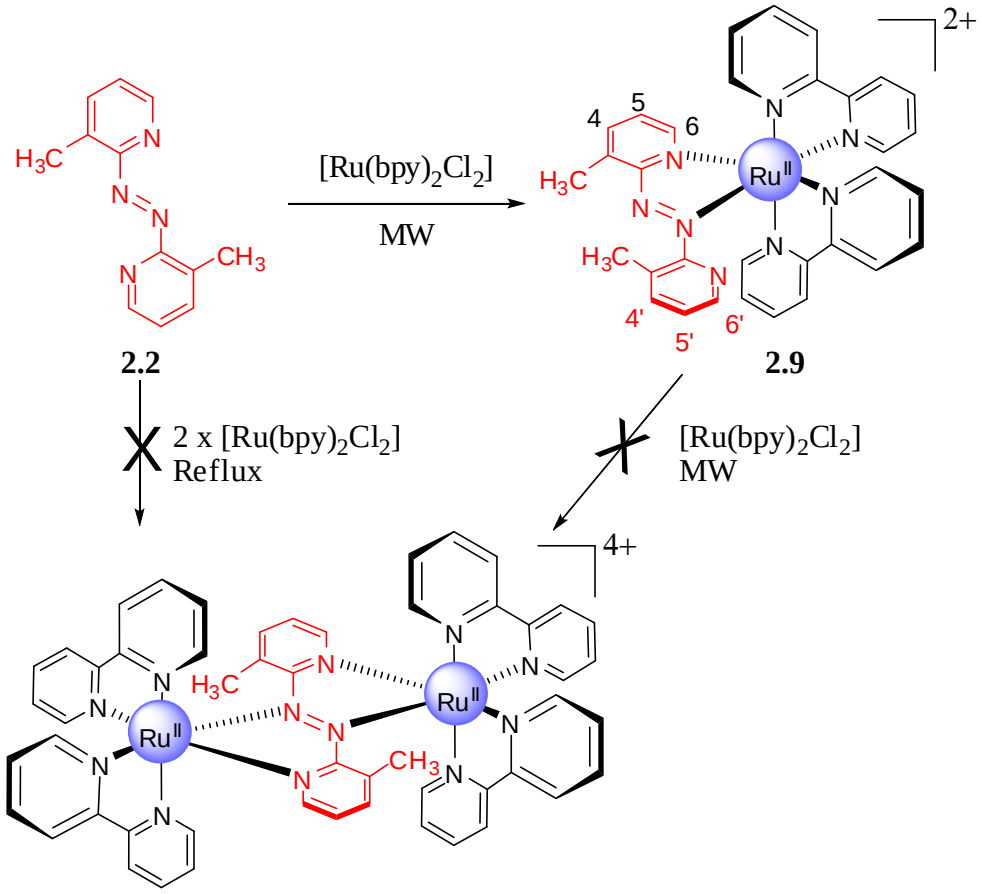

Scheme 2.7

All attempts to synthesise the dinuclear complex, with increased equivalents of the ruthenium precursor or different reaction conditions, such as heating at a higher temperature, were unsuccessful. The use of the microwave assisted synthesis with the isolated mononuclear complex **2.9**, also did not show any evidence of the dinuclear complex. This is almost certainly due to the steric bulk of the methyl group at the 3–position. Unfortunately, attempts to grow crystals of the complex **2.9** were also unsuccessful.

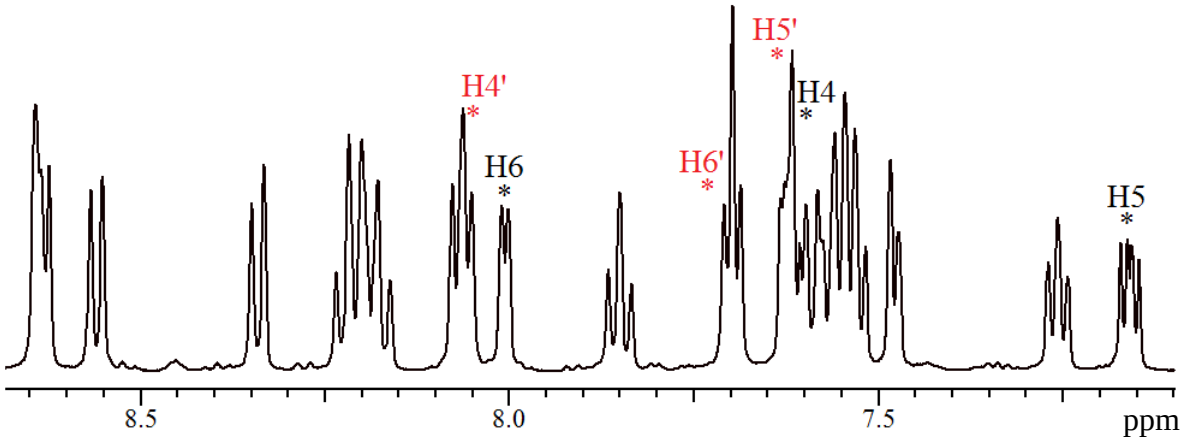

Figure 2.18. The ^{1}H NMR spectrum of complex **2.9**.

The aromatic region of the ^{1}H NMR spectrum of **2.9** is shown in Figure 2.18. The ^{1}H NMR chemical shifts and the *CIS* values for **2.2** and **2.9** are summarised in Table 2.3. The spectrum shows 22 non–equivalent aromatic proton signals, corresponding to six different pyridine ring environments. When compared to complex **2.7**, the addition of a methyl substituent to the bridging ligand **2.2**, simplifies the spin–spin coupling for the ligand in complex **2.9**. Hence, the identification of the pyridine ring system corresponding to the ligand **2.2** was readily made by a gCOSY experiment, shown in Figure 2.19.

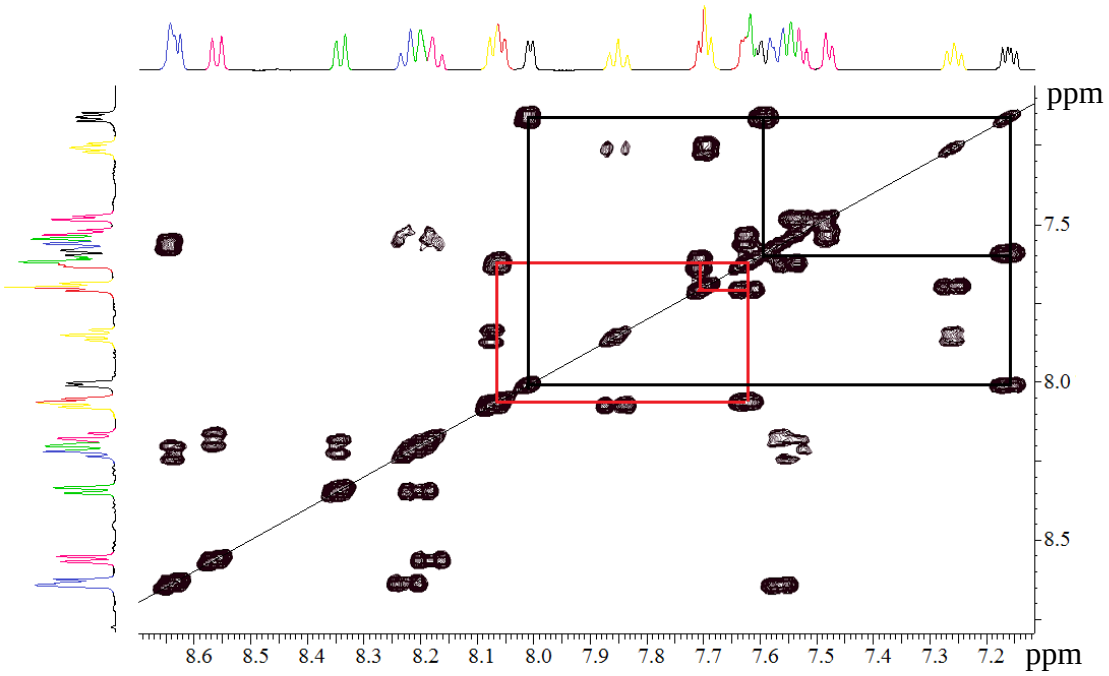

Figure 2.19. The gCOSY spectrum for the complex **2.9**, with the ring systems corresponding to the ligand **2.2** being identified.

The methyl group (1.43 ppm) corresponding to the coordinated pyridyl ligand of ligand **2.2** is strongly shielded due to the chelation induced conformational change. A bpy–H6 proton (7.48 ppm) is strongly shielded, whilst the H6 proton of the same bipyridine is strongly deshielded. A similar, strongly shielded proton is observed in complex **2.7** and **2.8**, but the strongly deshielded proton was not observed in the previous complexes.

Table 2.3. The ^{1}H NMR chemical shifts[a] and *CIS* values[b] (italics) for **2.2** and **2.9.**

	3–CH$_3$	**H4**	**H5**	**H6**
2.2	2.60	7.87	7.44	8.46
2.9[c]	1.43	7.59	7.16	8.01
CIS	*–1.17*	*–0.28*	*–0.28*	*–0.45*
2.9[d]	2.90	8.06	7.63	7.70
CIS	*+0.30*	*+0.19*	*+0.19*	*–0.76*

[a]In acetonitrile–d_3.
[b]*CIS* = $\delta_{complex} - \delta_{ligand.}$
[c]Coordinated pyridyl ring of **2.2**.
[d]Free pyridyl ring of **2.2**.

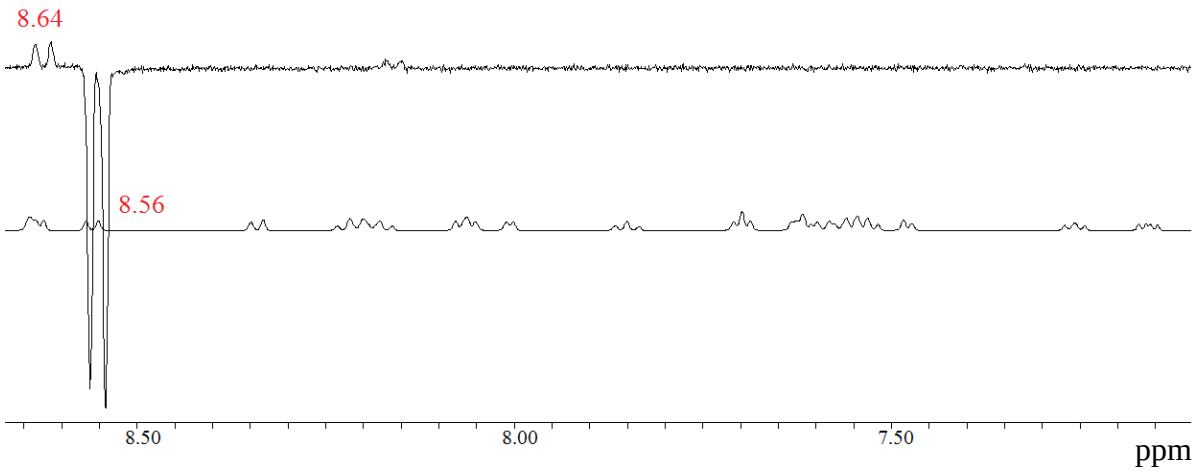

Figure 2.20. The ROESY spectrum for complex **2.9**, showing connectivity between the adjacent H3 protons of the same bipyridine.

The connectivity between the pyridyl ligands of the same bipyridine was confirmed by ROESY (Rotating Frame Overhauser Effect SpectroscopY) experiment, which was extensively used throughout this research project. This technique is similar to NOESY (Nuclear Overhauser Effect SpectroscopY), and is useful in determining signals which arise from protons that are close to each other in space even if they are not bonded. The irradiation

of the H3 proton at 8.56 ppm shows a correlation to the adjacent H3 proton at 8.63 ppm on the connected pyridyl ligand of the same bipyridine, as shown in Figure 2.20.

2.3.3. Complexes of 2.3

Ligand **2.3** reacts with $[Ru(bpy)_2Cl_2]$ in a methanol/water (1:1) mixture to give the mononuclear complex **2.10**. The complex was isolated as the hexafluorophosphate salt and characterised as $[(bpy)_2Ru(\mathbf{2.3})](PF_6)_2$ by ^1H NMR and mass spectrometry. This was then used as the precursor for synthesis of the dinuclear complex **2.11**. This complex was purified by ion exchange chromatography by the gradient elution technique using 0.1–0.5 mol L^{-1} sodium chloride as the eluent. The dinuclear complex was characterised as $[\{Ru(bpy)_2\}_2(\mu\text{–}\mathbf{2.3})](PF_6)_4$. The schematic route used for the synthesis of **2.10** and **2.11** is illustrated in Scheme 2.8.

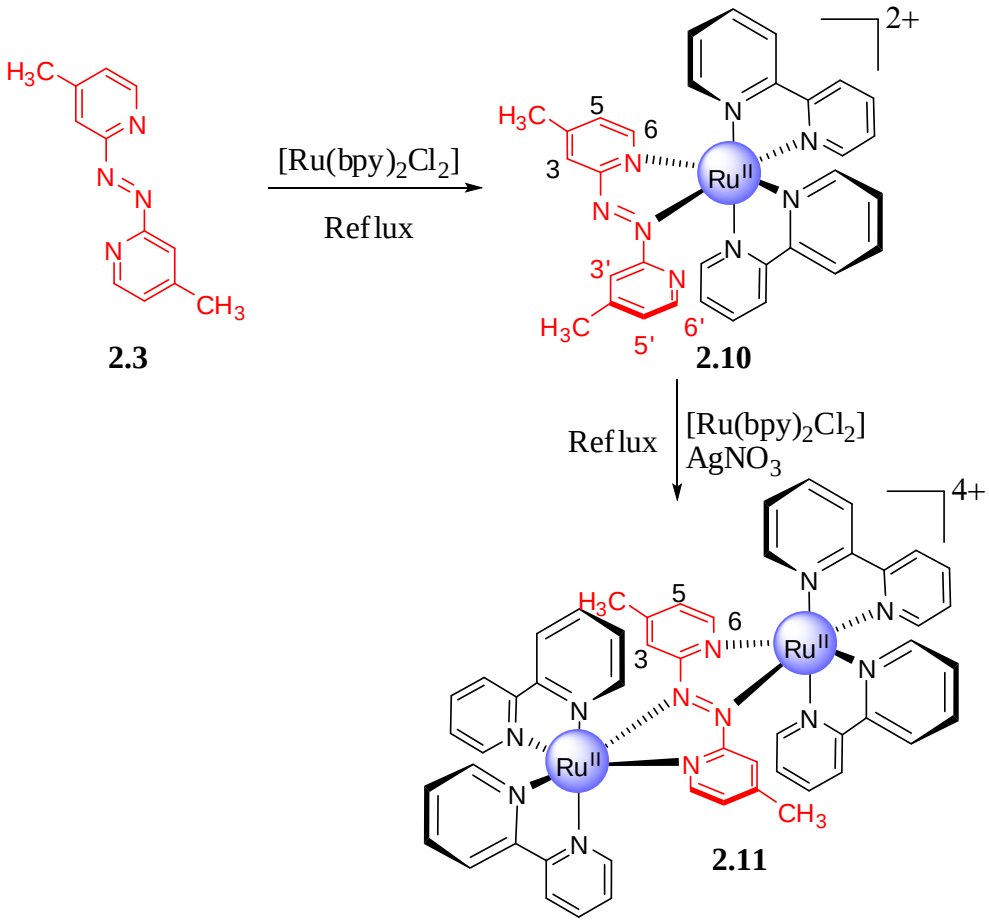

Scheme 2.8

The aromatic region of the ^{1}H NMR spectrum of complex **2.10**, shown in Figure 2.21, displays six pyridine ring environments, four for the bipyridine pyridyl rings and two for the ligand **2.3**. The substitution at the 4–position simplified the interpretation of the pyridyl rings of **2.3**. The strong positive *CIS* value for the H3' proton (8.71 ppm) of ligand **2.3** arises due to conformational changes on chelation with the metal centre. The H6 protons (7.77 ppm) and H6' proton (7.72 ppm) show *CIS* values of –0.83 and –0.88, respectively, due to reasons already discussed. The ^{1}H NMR chemical shifts and the *CIS* values for **2.3** and **2.10**, are given in Table 2.4.

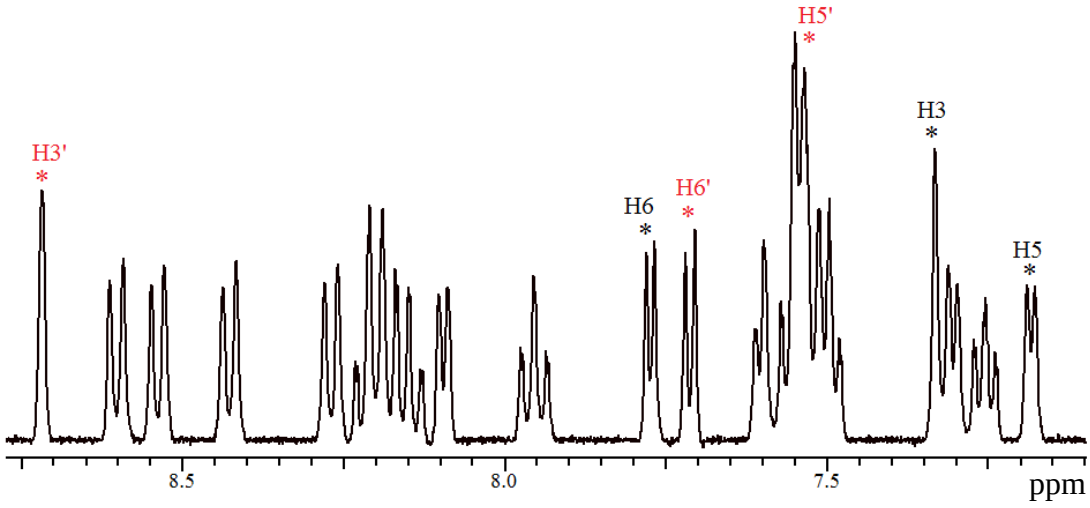

Figure 2.21. A section of the ^{1}H NMR spectrum for the complex **2.10**.

Table 2.4. The ^{1}H NMR chemical shifts[a] and *CIS* values[b] (italics) for **2.3** and **2.10**.

	H3	**4–CH$_3$**	**H5**	**H6**
2.3	7.64	2.48	7.40	8.60
2.10[c]	7.33	2.31	7.18	7.77
CIS	*–0.31*	*–0.17*	*–0.22*	*–0.83*
2.10[d]	8.71	2.67	7.54	7.72
CIS	*+1.07*	*+0.19*	*+0.14*	*–0.88*

[a]In acetonitrile–d_3.
[b]$CIS = \delta_{complex} - \delta_{ligand}$.
[c]Coordinated pyridyl ring of **2.3**.
[d]Free pyridyl ring of **2.3.**

The pyridine rings corresponding to the bipyridine ligand were identified by the selective 1D–TOCSY experiment, shown in Figure 2.22. The selective 1D–TOCSY (One Dimensional Total Correlated SpectroscopY) experiment has also been widely used during

this research. This experiment is useful for dividing the proton signals into individual spin systems, especially when the signals overlap. In this technique, irradiation of a single resolved proton can show correlations among the spins that are not directly connected but exist within the same spin system. The experiment was done by irradiating the H3 or H6 proton for 5 relays with a mixing pulse of 35 msec, i.e., 0 s, 0.035 s, 0.07 s, 0.105 s and 0.14 s. As shown in Figure 2.17, in this way the excited bipyridine H_3 proton at 8.61 ppm transfers its magnetisation first to its ^{3}J–coupled partner H_4 at 8.21 ppm and then to their ^{3}J–coupled partners H_5 (7.56 ppm) and H_6 at (7.60 ppm) until all the members of the spin system are excited.

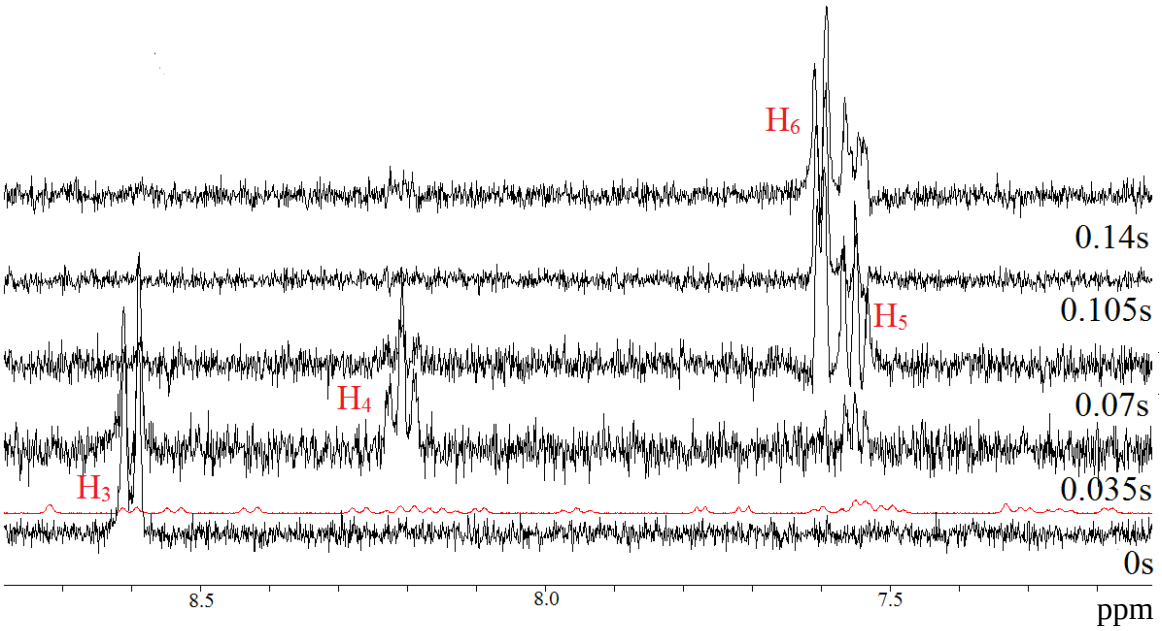

Figure 2.22. Stacked plot TOCSY spectrum for complex **2.10**.

*Crystal Structure of **2.10***

Crystals of **2.10** were grown by diffusing petroleum ether into an acetone solution of the complex. It crystallises in the monoclinic space group $P2_1/c$ with a full cation and two hexafluorophosphate anions in the asymmetric unit, as shown in Figure 2.23. The *trans* N–Ru–N angles greater than 171° indicate distorted octahedral geometry of the ruthenium. The Ru–N_{py} bond lengths are consistent (*ca.* 2.06 Å) with the Ru–N_{py} bond distance of the bridging ligand being the shortest at 2.047(2) Å (Ru1–N8). Once again, one $Ru(bpy)_2$ fragment coordinates to the ligand **2.3** through the azo nitrogen atom N6 and pyridine

nitrogen atom N8. The coordinated pyridine ring of **2.3** lies in the plane of the azo group, while the non–coordinated pyridine ring adopts a twisted conformation.

The structure supports the previously assigned ^{1}H NMR signals, the H3' proton (H22) of the free 2–pyridyl ring is deshielded by the lone pair of an azo nitrogen whereas, due to chelation induced conformation changes, the H3 proton (H28) of the coordinated ring is no longer deshielded by the azo nitrogen and moves upfield. The H6 protons of both the coordinated and the free pyridyl ring (H31 and H25) lie over the pyridyl ring of the terminal bipyridine, thus experiencing similar through–space ring–current anisotropy effects.

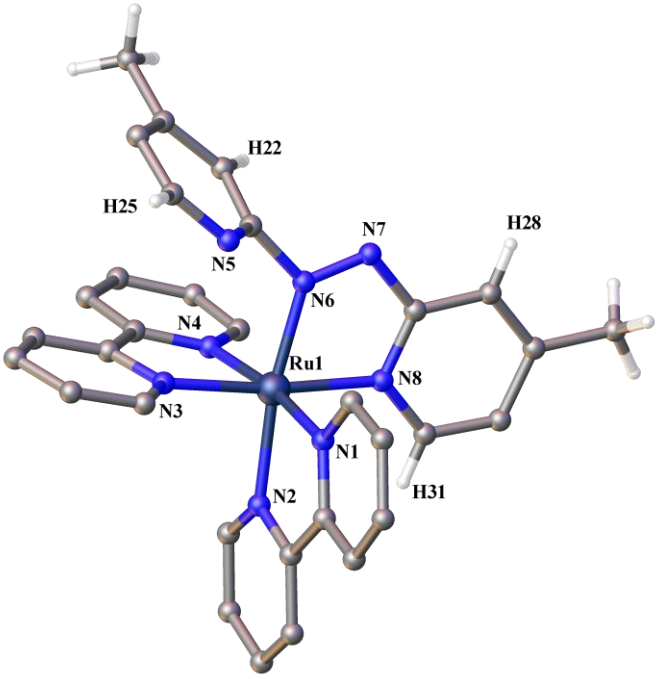

Figure 2.23. The crystal structure of the complex **2.10**. The counterions, solvate molecules and the hydrogen atoms of the bpy ligands are omitted for clarity. Selected bond distances (Å) and bond angles (°): Ru1–N1 2.054(2), Ru1–N2 2.082(2), Ru1–N3 2.068(2), Ru1–N4 2.072(2), Ru1–N6 1.963(2), Ru1–N8 2.047(2), N6–N7 1.288(2), N2–Ru1–N1 78.35(6), N3–Ru1–N1 94.99(6), N3–Ru1–N2 91.28(6), N4–Ru1–N1 171.74(6), N4–Ru1–N2 96.41(6), N3–Ru1–N4 78.63(6), N6–Ru1–N1 98.15(6), N6–Ru1–N2 171.23(6), N6–Ru1–N3 97.07(6), N6–Ru1–N4 87.92(6), N8–Ru1–N1 87.97(6), N8–Ru1–N2 95.29(6), N8–Ru1–N3 173.23(6), N8–Ru1–N4 98.94(6), N6–Ru1–N8 76.46(6).

*^{1}H NMR of **2.11***

The aromatic region of the ^{1}H NMR spectrum for the dinuclear complex **2.11** is shown in Figure 2.24. The ^{1}H NMR chemical shifts and the *CIS* values for **2.3** and **2.11** are given in Table 2.5. The negative value for the H6 proton is from the inter–ligand through–space ring–current anisotropic interactions, since these protons lie over the plane of an adjacent bipyridine ligand. The positive *CIS* values are due to the donation of electron density from ligand **2.3** to the metal.

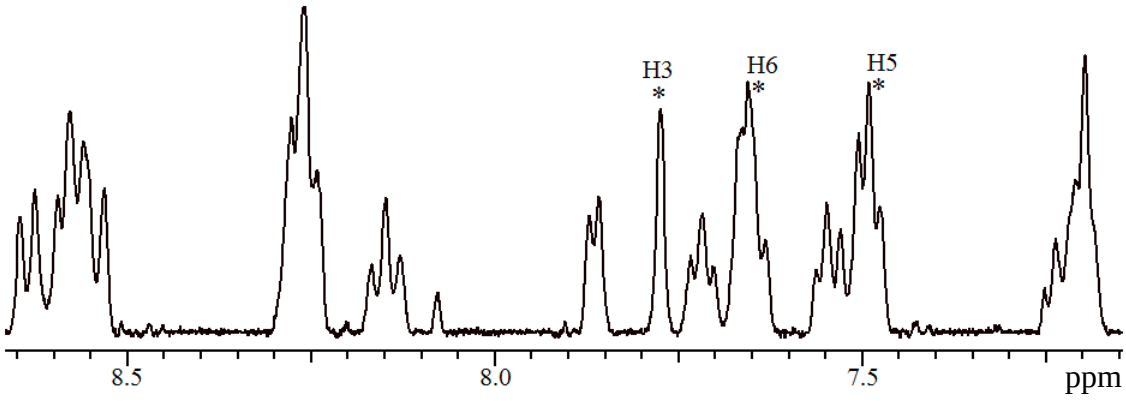

Figure 2.24. The ^{1}H NMR spectrum for complex **2.11**.

Table 2.5. The ^{1}H NMR chemical shifts[a] and *CIS* values[b] (italics) for **2.3** and **2.11**.

	H3	**4–CH_3**	**H5**	**H6**
2.3	7.64	2.48	7.40	8.46
2.11	7.77	2.10	7.45	7.64
CIS	*+0.13*	*–0.38*	*+0.05*	*–0.82*

[a] In acetonitrile–d_3.
[b] $CIS = \delta_{complex} - \delta_{ligand.}$

*Crystal Structure of **2.11***

Green crystals of complex **2.11** obtained by diffusing diisopropyl ether into an acetonitrile solution of the complex were suitable for X–ray analysis. The structure solved in the orthorhombic space group $P2_12_12_1$, to reveal a dinuclear complex, as shown in Figure 2.25. The asymmetric unit contains one full dinuclear cation with four hexafluorophosphate anions and five acetonitrile solvate molecules. The structure unambiguously confirms the formation of the complex in a 1:2 ligand–to–metal ratio.

The coordination sphere of the ruthenium(II) ion is similar to complex **2.8**. This is a *meso* isomer (ΛΔ), in which the azo ligand **2.3** acts as a planar bridge between the two ruthenium atoms separated by 4.863(3) Å (Ru1–Ru2). The average Ru–N bond distances are (*ca.* 2.069 Å) similar and consistent with the earlier complex **2.8**. The N_{azo}–N_{azo} bond distance [1.334(4) Å (N2–N3)] is consistent with the previously described dinuclear complex **2.8**.

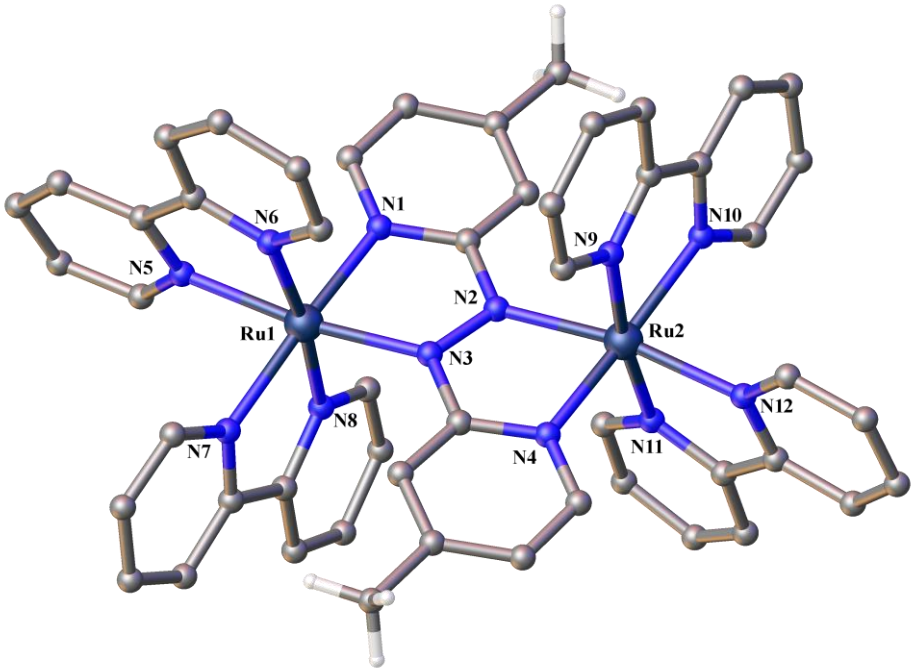

Figure 2.25. A perspective view of the structure of complex **2.11**. Selected hydrogen atoms, counterions and solvate molecules are omitted for clarity. Selected bond distances (Å) and bond angles (°): Ru1–N1 2.032(4), Ru1–N3 2.038(4), Ru1–N5 2.081(4), Ru1–N6 2.085(4), Ru1–N7 2.094(4), Ru1–N8 2.086(4), Ru2–N4 2.031(4), Ru2–N2 2.049(4), Ru2–N12 2.077(4), Ru2–N11 2.080(4), Ru2–N10 2.086(4), Ru2–N9 2.094(4), N2–N3 1.334(5), N1–Ru1–N3 76.03(16), N5–Ru1–N6 78.15(16), N8–Ru1–N7 78.29(16), N4–Ru1–N2 75.83(16), N12–Ru1–N11 78.35(16), N10–Ru1–N9 77.91(16), N11–Ru2–N9 172.87(16), N4–Ru2–N10 172.24(16), N2–Ru2–N12 169.56(16), N1–Ru1–N7 171.92(16), N6–Ru1–N8 173.01(16), N3–Ru1–N5 172.01(16).

2.3.4. Complex of 2.4

Ligand **2.4**, similar to the ligand **2.2**, gave only the mononuclear complex **2.12**, when refluxed with $[Ru(bpy)_2Cl_2]$, as outlined in Scheme 2.9. The mononuclear complex **2.12**, was characterised as $[(bpy)_2Ru\mathbf{(2.4)}](PF_6)_2$ by ^1H NMR and mass spectrometry. All attempts to synthesise the dinuclear complex were unsuccessful, presumably due to steric effects of the 6–methyl as was seen with **2.2**. All attempts to grow crystals of **2.12** were also unsuccessful.

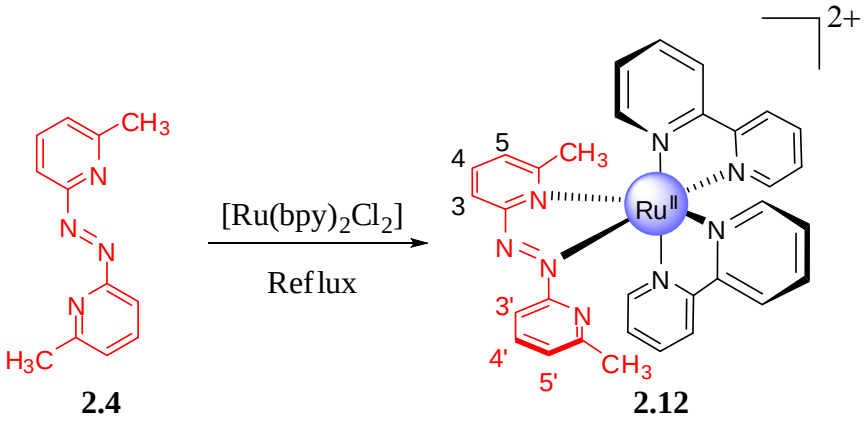

2.4 **2.12**

Scheme 2.9

The aromatic region of the ^1H NMR spectrum of complex **2.12**, is shown in Figure 2.26. The spectrum shows four pyridine ring environments corresponding to the ancillary bipyridine ligands and two ring environments corresponding to ligand **2.4**. The pyridine ring systems for the bipyridines were identified easily, however, the connectivity between the rings could not be determined due to the overlapping of signals. The ^1H NMR chemical shift and *CIS* values for **2.4** and **2.12** are given in Table 2.6. A bpy–H6 proton (7.22 ppm) lies in a strongly shielded environment. A similar, strongly shielded bpy–H6 proton is seen for the complexes **2.9** and **2.10**. However, the strongly deshielded bpy–H6 proton observed in **2.9** is missing in both **2.10** and **2.12**.

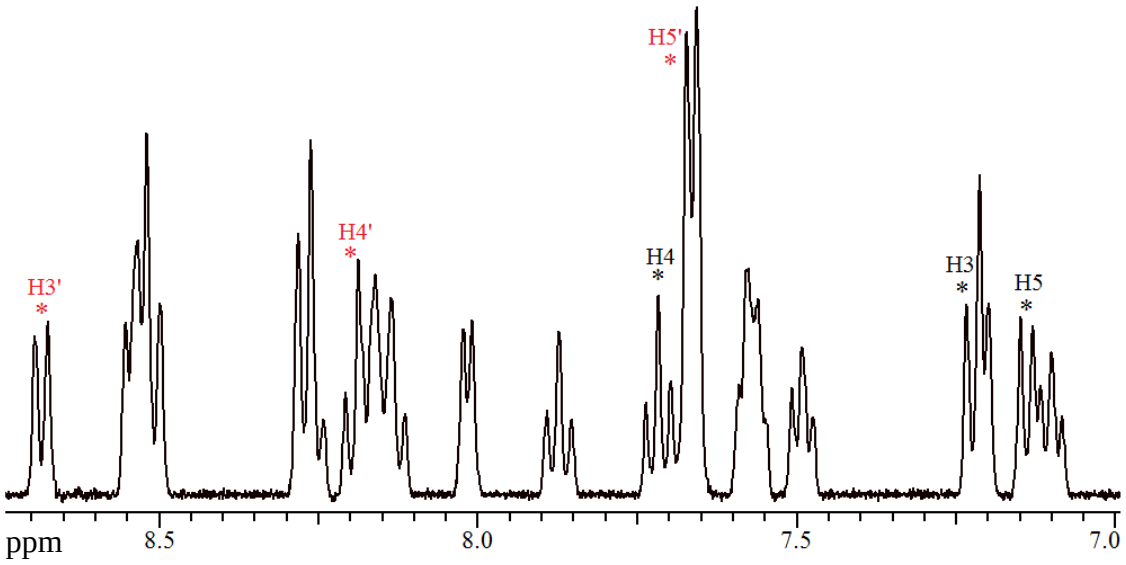

Figure 2.26. The ^{1}H NMR of complex **2.12**.

Table 2.6. The ^{1}H NMR chemical shifts[a] and *CIS* values[b] (italics) for **2.4** and **2.12**.

	H3	**H4**	**H5**	**6–CH$_3$**
2.4	7.61	7.93	7.43	2.66
2.12[c]	7.23	7.73	7.15	2.04
CIS	*–0.38*	*–0.20*	*–0.28*	*–0.62*
2.12[d]	8.68	8.20	7.67	2.04
CIS	*+1.07*	*+0.27*	*+0.24*	*–0.62*

[a]In acetonitrile–d_3.
[b]$CIS = \delta_{complex} - \delta_{ligand}$.
[c]Coordinated pyridyl ring of 2.4.
[d]Free pyridyl ring of 2.4.

2.3.5. Complexes of 2.5

The reaction of **2.5** with one equivalent of [Ru(bpy)$_2$Cl$_2$] in 50% aqueous methanol gave the mononuclear complex, **2.13**, which was characterised as [(bpy)$_2$Ru(**2.5**)](PF$_6$)$_2$ by ^{1}H NMR and mass spectrometry. The dinuclear complex **2.14** was synthesised by reacting ligand **2.5** with a ruthenium(II) precursor in a 1:2 ligand to metal stoichiometric ratio.

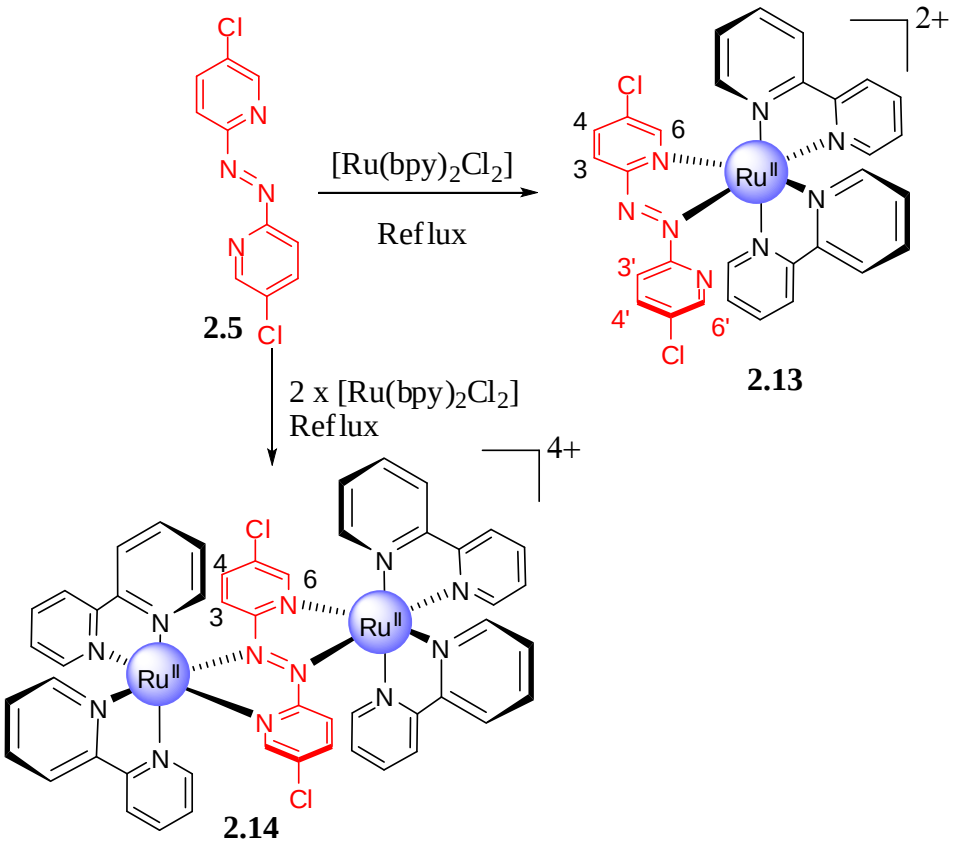

Scheme 2.10

The crude product was purified by silica gel chromatography using acetonitrile:saturated potassium nitrate (7:1) as the eluent. The isolated complex **2.14** was precipitated as the hexafluorophosphate salt and characterised as $[\{Ru(bpy)_2\}_2(\mu\text{–}\mathbf{2.5})](PF_6)_4$. (Scheme 2.10)

The ^{1}H NMR spectra for complexes **2.13** and **2.14** are shown in Figure 2.27. The spectra show six distinguishable pyridine ring environments for **2.13** and five different pyridine rings for **2.14**, which are colour coded. The unsymmetrical nature of the mononuclear complex **2.13** gives rise to 23 non–equivalent proton signals, whereas the C_i point group symmetry in **2.14** leads to 19 different aromatic proton signals. Despite the complexity of the spectra, the ^{1}H NMR chemical shifts for the ligand **2.5** and the ancillary bipyridine ligands in **2.13** and **2.14**, were assigned by using a combination of spin coupling information from the ^{1}H NMR spectrum, gCOSY, 1–D TOCSY and 1–D ROESY experiments. The assignment of the various pyridine rings are given in Table 2.7.

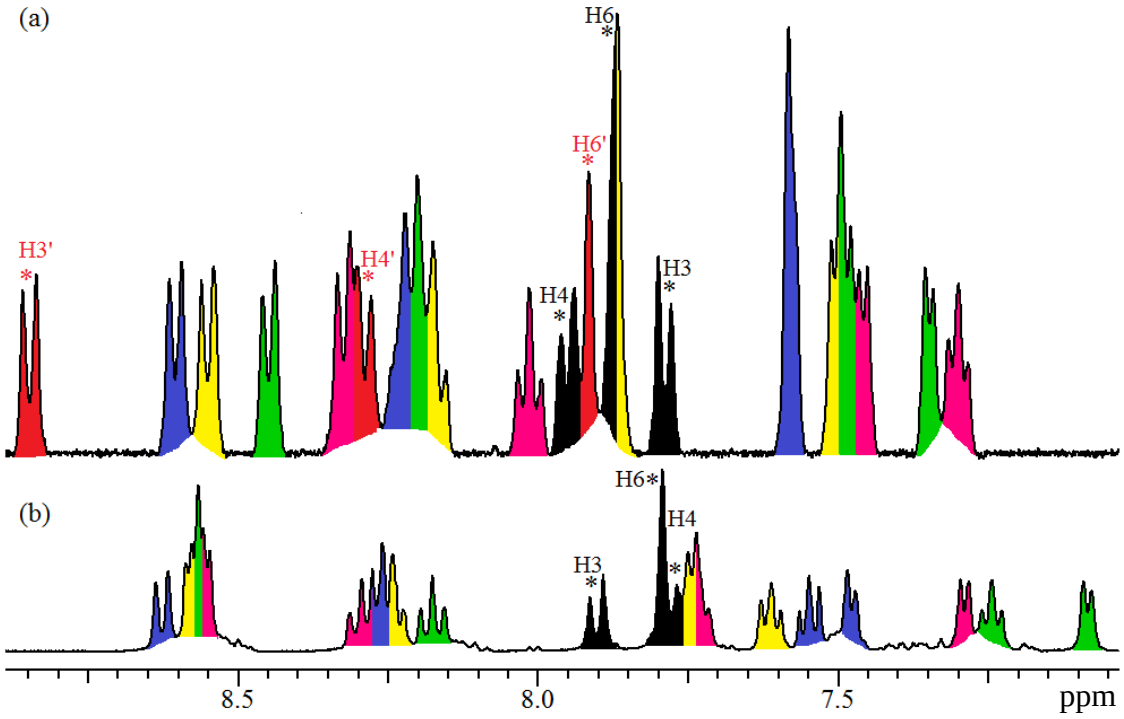

Figure 2.27. The ^{1}H NMR spectra of (a) **2.13** and (b) **2.14**. The various pyridine rings were assigned into groups and are colour coded.

Table 2.7. The ^{1}H NMR chemical shifts[a] for **2.13** and **2.14** in CD_3CN.

	H3 (d)	**H4 (t)**	**H5 (t)**	**H6 (d)**
[b]**2.13**–py (red)[c]	8.84	8.29	–Cl	7.92
[d]**2.13**–py (black)	7.78	7.95	–Cl	7.87
^{A}bpy–py (blue)[e]	8.60	8.21	7.57	7.58
$^{A'}$bpy–py (yellow)	8.55	8.16	7.50	7.86
^{B}bpy–py (green)[f]	8.44	8.18	7.48	7.35
$^{B'}$bpy–py (pink)	8.32	8.01	7.30	7.46
2.14–py (black)	7.90	7.76	–Cl	7.79
^{A}bpy–py (blue)	8.62	8.25	7.55	7.48
$^{A'}$bpy–py (yellow)	8.58	8.24	7.61	7.75
^{B}bpy–py (green)	8.56	8.18	7.24	7.09
$^{B'}$bpy–py (pink)	8.55	8.30	7.72	7.29

[a] For atom labelling, see Scheme 2.10.
[b] Free pyridine ring of **2.5**.
[c] The colours relate to Figure 2.27.
[d] Coordinated pyridine ring of **2.5**.
[e] ^{A}bpy and $^{A'}$bpy are part of the same bpy ligand.
[f] ^{B}bpy and $^{B'}$bpy are part of the same bpy ligand.

The ^{1}H NMR chemical shifts in acetonitrile for ligand **2.5** and the ruthenium complexes **2.13** and **2.14**, along with the *CIS* values are shown in Table 2.8. The sign and magnitude of the *CIS* values observed for **2.13** and **2.14** indicate that the effects of coordination are similar for both the mononuclear and dinuclear complexes.

Table 2.8. The ^{1}H NMR chemical shifts[a] and *CIS* values[b] (italics) for **2.5**, **2.13** and **2.14**.

	H3	**H4**	**H6**	**H3'**	**H4'**	**H6'**
2.5	7.85	8.06	8.76			
2.13	7.78	7.95	7.87	8.84	8.29	7.92
CIS	*–0.41*	*–0.11*	*–0.89*	*0.88*	*0.27*	*–0.84*
2.14	7.90	7.76	7.79			
CIS	*0.00*	*–0.30*	*–0.92*			

[a] In acetonitrile–d_3.
[b] $CIS = \delta_{complex} - \delta_{ligand.}$

*Crystal Structure of **2.13***

Vapour diffusion of petroleum ether into a solution of **2.13** in acetone gave red coloured crystals suitable for X–ray analysis. The complex crystallises in the triclinic space group *P*–1, as shown in Figure 2.28, with one complete cation, two hexafluorophosphate counterions and three acetone solvate molecules in the asymmetric unit. The crystal structure unambiguously confirms the mononuclear nature of **2.13**.

The ruthenium atom possesses distorted octahedral geometry with five pyridine nitrogen atoms and one azo nitrogen atom completing the coordination sphere. The Ru–N (*ca.* 2.053 Å) and N_{azo}–N_{azo} [1.295(3) Å] bond distances are similar to the mononuclear complexes **2.7** and **2.10**. Once again, the Ru–N_{py} bond distance of the ligand **2.5** is shorter than the bpy Ru–N_{py} bond distance. The azo bond is in the same plane as the coordinated pyridine ring with the torsion angle being –0.6(3)^{o} (N7−N6−C26−N8), while that of the non–coordinated pyridine ring is 29.5(3)^{o} (N7−N6−C26−C27), indicating a significant rotation to the free pyridyl ring of the ligand **2.5**. Similar observations were seen in the X–ray crystal structures of **2.7** and **2.10**. The crystal packing shows numerous weak short contacts such as F···HC and Cl···HC which further stabilises the overall crystal structure.

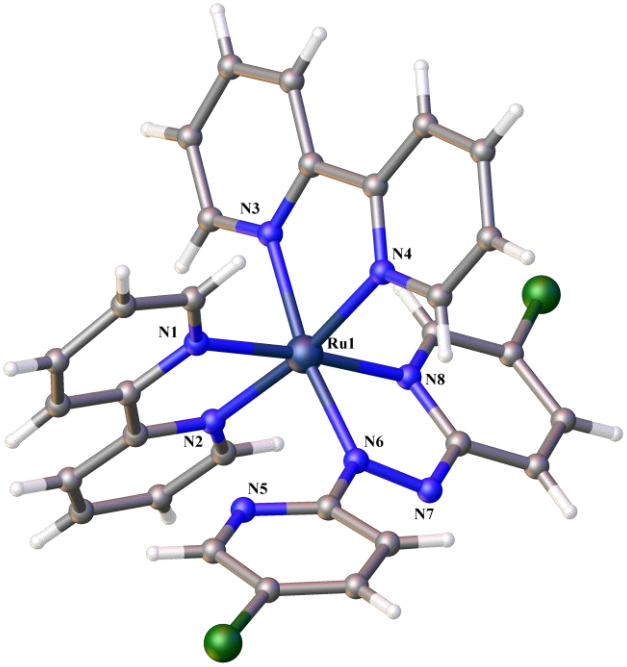

Figure 2.28. The X–ray crystal structure of compound **2.13**. The counterions and solvent molecules, are omitted for clarity. Selected bond distances (Å) and bond angles (°): Ru1–N1 2.068(2), Ru1–N2 2.060(2), Ru1–N3 2.085(2), Ru1–N4 2.070(3), Ru1–N8 2.043(2), Ru1–N6 1.993(2), N6–N7 1.295(3), N2–Ru1–N1 78.54(9), N1–Ru1–N3 86.85(8), N2–Ru1–N3 94.55(8), N1–Ru1–N4 95.99(9), N2–Ru1–N4 171.47(8), N4–Ru1–N3 78.51(8), N6–Ru1–N1 99.37(8), N6–Ru1–N2 93.73(8), N6–Ru1–N3 170.49(8), N6–Ru1–N4 93.61(8), N8–Ru1–N1 174.86(8), N8–Ru1–N2 98.42(9), N8–Ru1–N3 97.57(8), N8–Ru1–N4 87.49(8), N6–Ru1–N8 76.59(9).

*Crystal Structure of **2.14***

Crystals of **2.14** were obtained by diffusing diisopropyl ether into an acetonitrile solution of the complex. The structure solved in the monoclinic space group $P2_1/c$ to reveal one ruthenium atom, half a ligand **2.5**, two bipyridine ligands, two hexafluorophosphate anions and three acetonitrile solvate molecules in the asymmetric unit, as shown in Figure 2.29.

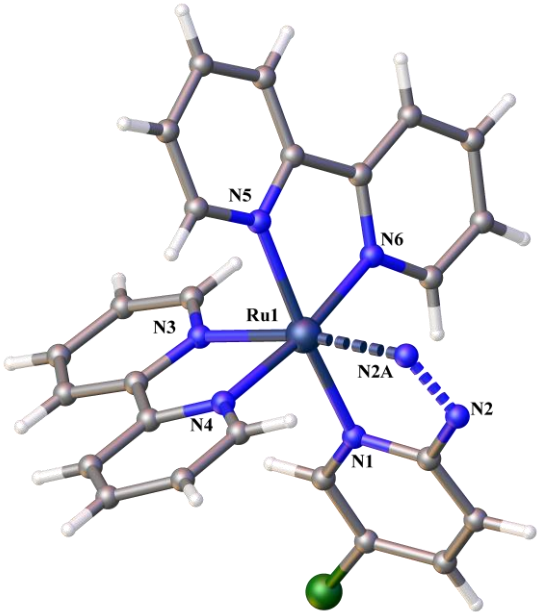

Figure 2.29. The asymmetric unit of compound **2.14** with counterions and solvent molecules omitted for clarity. Selected bond distances (Å) and bond angles (°): Ru1–N1 2.024(2), Ru1–N2A 2.047(2), Ru1–N3 2.071(2), Ru1–N4 2.067(2), Ru1–N5 2.086(2), Ru1–N6 2.078(2), N2–N2A 1.340(3), N1–Ru1–N2 76.14(7), N1–Ru1–N3 95.09(7), N1–Ru1–N4 92.23(7), N1–Ru1–N5 172.00(7), N1–Ru1–N6 93.94(7), N2A–Ru1–N3 169.80(7), N2A–Ru1–N4 96.53(7), N2A–Ru1–N5 105.43(7), N2A–Ru1N6 89.43(7), N3–Ru1–N5 83.98(7), N3–Ru1–N6 96.46(7), N4–Ru1–N3 78.38(7), N4–Ru1–N5 95.35(7), N4–Ru1–N6 172.30(7), N6–Ru1–N5 78.30(7).

The crystal structure confirms the formation of the complex in a 1:2 ligand–to–metal ratio. The terminal ligands ‘above’ and ‘below’ the plane of the azo bridge are orthogonal indicating the formation of the *meso* diastereoisomer, as illustrated in Figure 2.30. The ruthenium(II) geometry is distorted octahedral with the bridging ligand **2.5** acting as a bridge with an inter–metal separation of 4.882(2) Å (Ru1···Ru2). The chelate bite angles are consistent with the previously described binuclear complexes **2.8** and **2.11**. The average Ru–N bond distances (*ca.* 2.062 Å) are within the expected range.

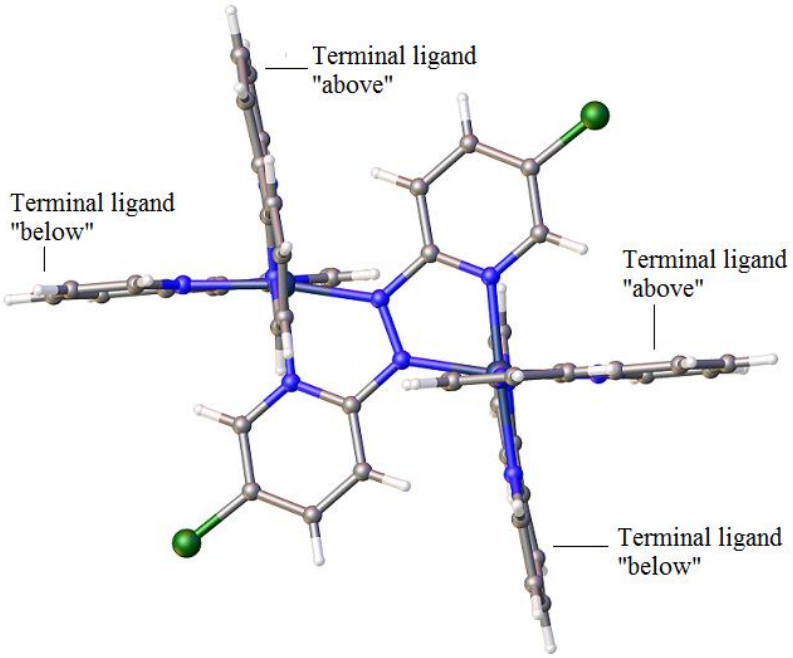

Figure 2.30. A perspective view of complex **2.14**, showing the approximately orthogonal orientation of the terminal bipyridine 'above' and 'below' the azo bridge.

2.3.6. Complexes of 2.6

Reaction of **2.6** with $[Ru(bpy)_2Cl_2]$ in 50% aqueous methanol, as shown in Scheme 2.11, gave a brownish green solution, which was separated into the mononuclear and dinuclear products by silica gel column chromatography using acetonitrile:saturated potassium nitrate (7:1) as the eluent. The aqueous solution was precipitated as hexafluorophosphate salts and extracted with dichloromethane. The organic layer was separated, dried over anhydrous magnesium sulfate and concentrated under vacuum. The red solid was characterised as the mononuclear complex **2.15**, $[(bpy)_2Ru(\mathbf{2.6})](PF_6)_2$, by ESI–MS and ^{1}H NMR.

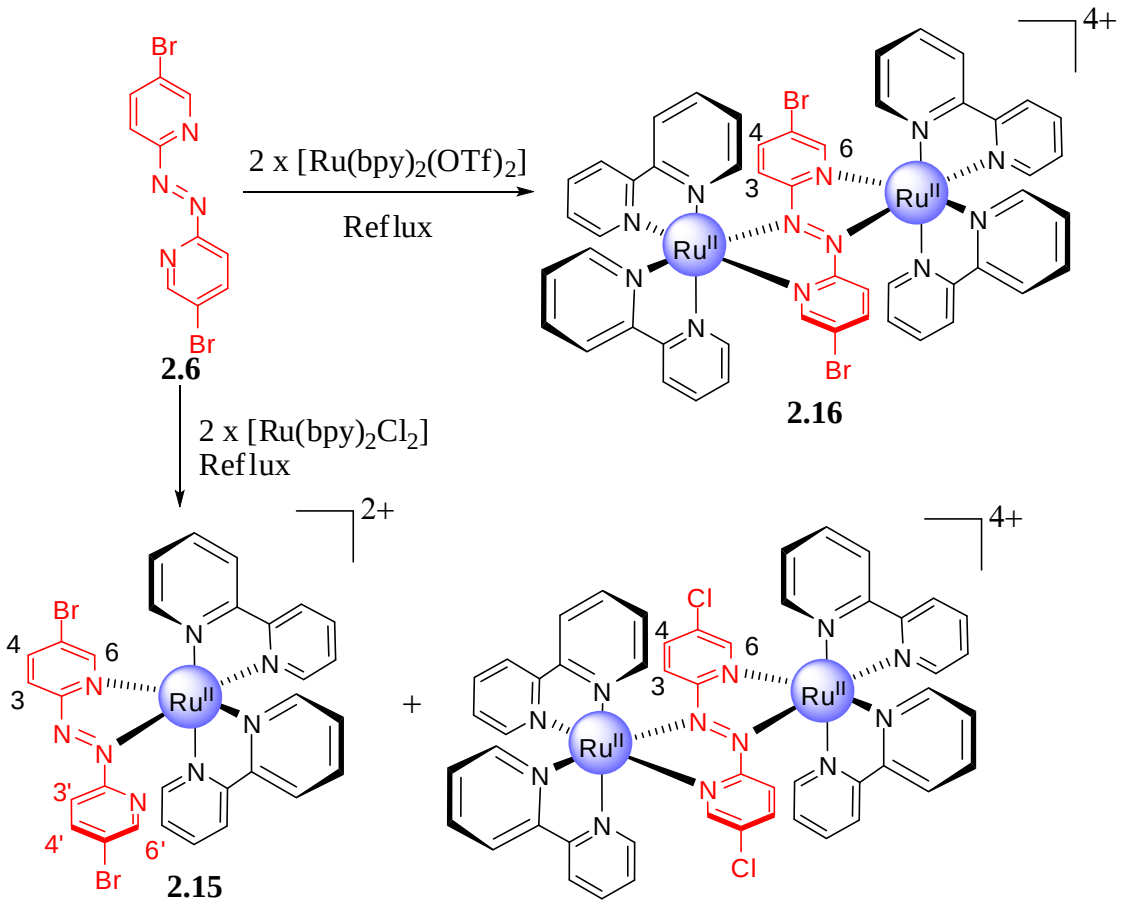

Scheme 2.11

The green solid was, however, characterised by ESI–MS and X–ray analysis, as the dinuclear complex [{Ru(bpy)$_2$}$_2$(μ–**2.5**)](PF$_6$)$_4$ instead of [{Ru(bpy)$_2$}$_2$(μ–**2.6**)](PF$_6$)$_4$. The bromo substituents on the bridging ligand **2.6** were replaced by the chloride ion present in the reaction mixture. The mass spectrum did not show any evidence for the bromo–substituted dinuclear complex, shown in Figure 2.31a.

This was a highly surprising result. We are unaware of any literature example where a chloride anion released from the [Ru(bpy)$_2$Cl$_2$] precursor effects an aromatic nucleophilic substitution (S$_N$Ar) on a coordinated ligand. Reactions of coordinated ligands are common in coordination chemistry, but not of this type.[251] Clearly the coordination of the ruthenium to the dibromo ligand **2.6** facilitates this reaction. A possible reason for this comes from inspection of the NMR *CIS* values for the dinuclear complex of the parent unsubstituted ligand **2.1**. The H5 proton of its dinuclear complex **2.8** experiences a significant downfield shift upon coordination, indicating that C5 is more electropositive and hence more

susceptible to a S_NAr reaction at this site in the dibromo derivative, *via* an addition–elimination mechanism.

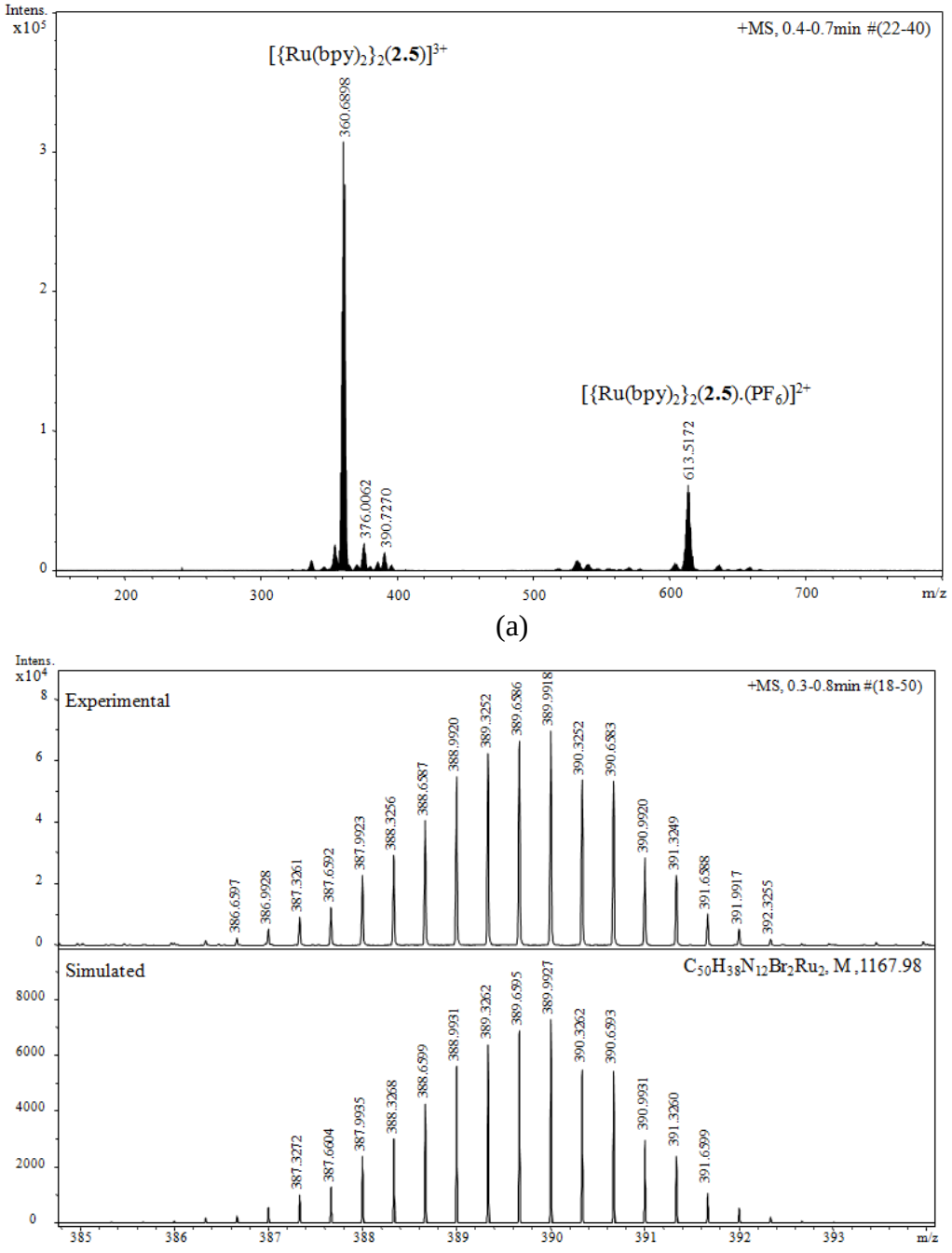

Figure 2.31. ESI–MS spectra for the (a) chloro–substituted dinuclear by–product, and (b) isotopic pattern for **2.16.**

In order to circumvent this complication, a different approach was employed using $[Ru(bpy)_2(OTf)_2]$ as the precursor instead of $[Ru(bpy)_2Cl_2]$. The reaction of **2.6** with two equivalents of $[Ru(bpy)_2(OTf)_2]$ in ethylene glycol gave the dinuclear bromo–substituted complex **2.16**. This was characterised as $[\{Ru(bpy)_2\}_2(\mu$–**2.6**$)](PF_6)_4$ by ESI–MS, ^{1}H NMR

and X–ray analysis. The mass spectrum was consistent with **2.16** and no evidence for the chloro–substituted dinuclear complex was observed, as shown in Figure 2.31b. A similar observation was made with ligand **3.2**, which will be discussed later in Chapter 3.

Table 2.9. ^{1}H NMR chemical shifts[a] and *CIS* values[b] (italics) for **2.6**, **2.15** and **2.16**.

	H3	**H4**	**H6**	**H3'**	**H4'**	**H6'**
2.6	7.79	8.20	8.86			
2.15	7.72	8.09	7.97	8.76	8.42	7.98
CIS	*–0.07*	*–0.11*	*–0.89*	*+0.97*	*+0.22*	*–0.88*
2.16	7.92	7.81	7.87			
CIS	*+0.13*	*–0.39*	*–0.99*			

[a] In acetonitrile–d_3.
[b] $CIS = \delta_{complex} - \delta_{ligand.}$

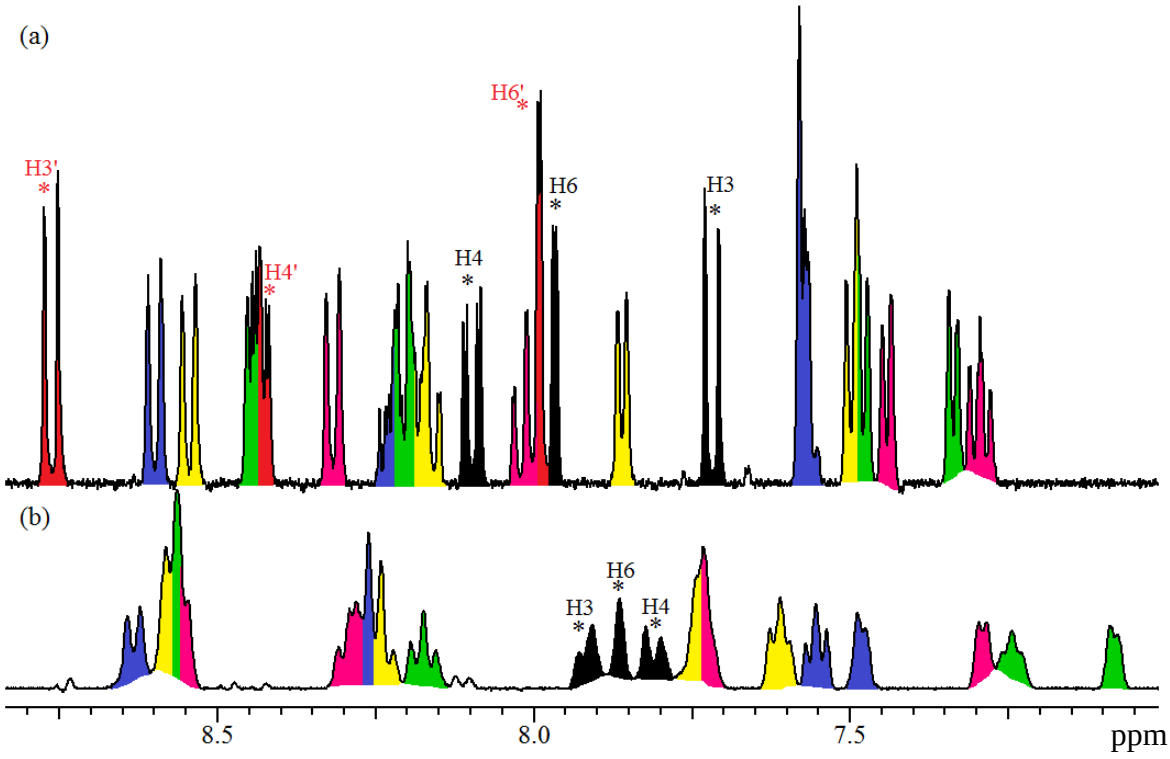

Figure 2.32. The ^{1}H NMR spectra for (a) **2.15** and (b) **2.16**. The pyridine rings are assigned into groups, which are colour coded.

The ^{1}H NMR spectra of **2.15** and **2.16** are illustrated in Figure 2.32. The spectra show distinguishable pyridine ring environments in both the complexes and are colour coded. The assignments were made by using spin–spin coupling information, gCOSY and 1D–ROESY experiments. The ^{1}H NMR chemical shifts for ligand **2.6** and the ruthenium complexes **2.15** and **2.16** in acetonitrile, are given in Table 2.9, along with the *CIS* values.

*Crystal Structure of **2.15***

Crystals of **2.15** were grown by diffusing petroleum ether into an acetone solution of the complex. The complex crystallises in the triclinic space group *P*–1 with one full cation, two hexafluorophosphate anions and two and a half acetone solvate molecules in the asymmetric unit, as shown in Figure 2.33. The crystal structure determination confirms the mononuclear nature of the complex. The free pyridyl ligand is twisted at an angle of 29.7(3)° to avoid the non–bonding contact with the ancillary bipyridine ligand, similar to the mononuclear complexes **2.7**, **2.10** and **2.13**. The coordination geometry of the ruthenium atom is distorted with the *trans* N–Ru–N greater than 170°. The average Ru–N bond (*ca.* 2.052 Å) distances are similar and consistent with **2.7**, **2.10** and **2.13**.

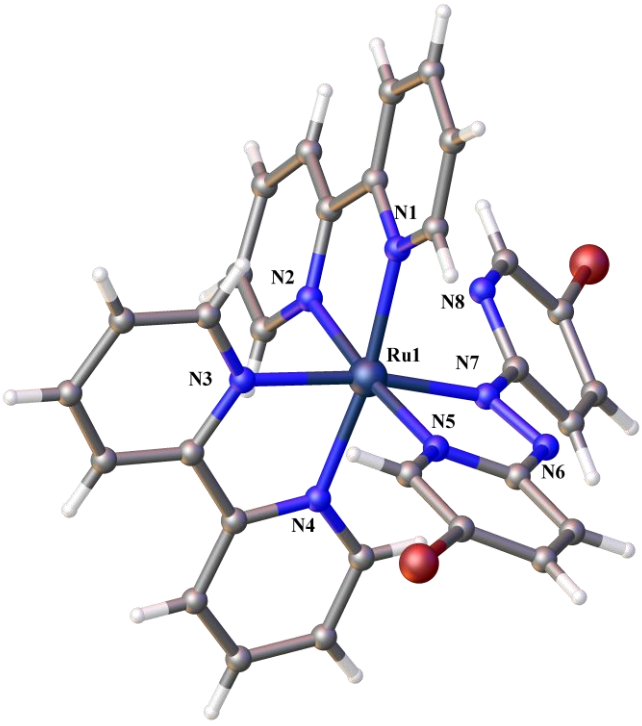

Figure 2.33. The X–ray crystal structure of compound **2.15**. The counterions and solvate molecules are omitted for clarity. Selected bond distances (Å) and bond angles (°): Ru1–N1 2.060(2), Ru1–N2 2.071(2), Ru1–N3 2.086(2), Ru1–N4 2.067(2), Ru1–N5 2.042(2), Ru1–N7 1.991(2), N6–N7 1.301(3), N1–Ru1–N2 78.29(8), N1–Ru1–N3 94.40(8), N2–Ru1–N3 86.81(8), N1–Ru1–N4 171.26(8), N4–Ru1–N2 96.15(8), N4–Ru1–N3 78.44(8), N5–Ru1–N1 98.61(8), N5–Ru1–N2 174.54(8), N5–Ru1–N3 97.96(8), N5–Ru1–N4 87.45(8), N7–Ru1–N1 94.00(8), N7–Ru1–N2 99.09(8), N7–Ru1–N3 170.57(8), N7–Ru1–N4 93.54(8), N7–Ru1–N5 76.53(8).

*Crystal Structure of **2.16***

Crystals of **2.16** were obtained by diffusing diisopropyl ether into an acetonitrile solution of the complex. The complex crystallises in the monoclinic space group $P2_1/c$. The asymmetric unit contains one ruthenium atom, half a ligand **2.6**, two bipyridine ligands, two hexafluorophosphate anions and three acetonitrile solvate molecules, confirming the formation of the complex in a 1:2 ligand to metal stoichiometric ratio. The other half of the molecule is related by a crystallographic centre of inversion at the centre of the bridge. The complex is the *meso* isomer with two $[Ru(bpy)_2]^{2+}$ moieties bridged by **2.6,** which acts as a doubly–chelating ligand, as shown in Figure 2.34. Each ruthenium atom possesses a slightly distorted octahedral geometry with a separation of 4.882(4) Å between the ruthenium atoms.

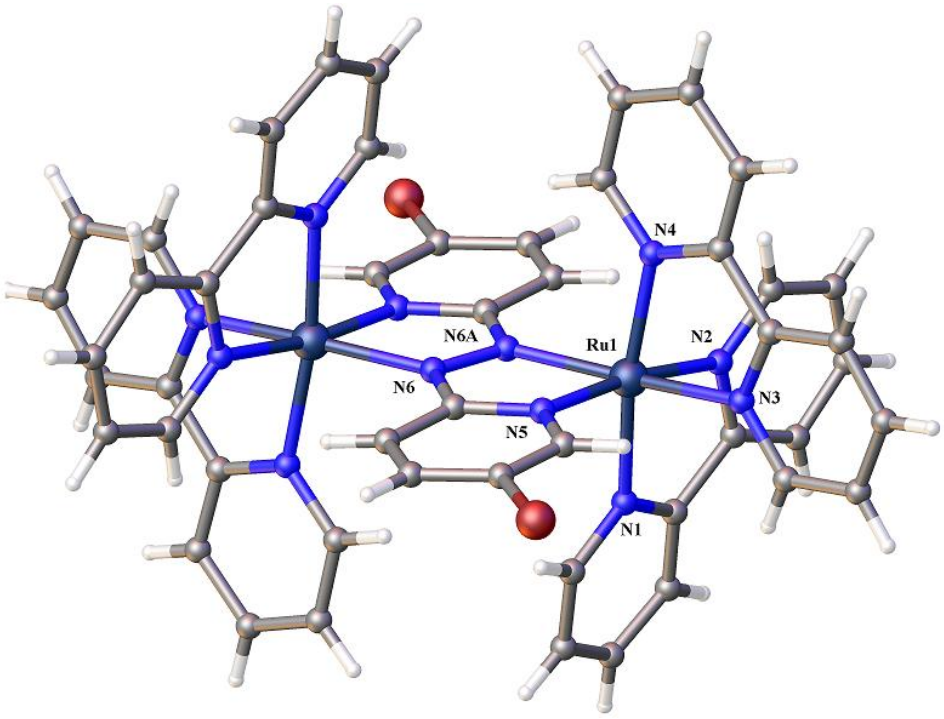

Figure 2.34. The X–ray crystal structure of compound **2.16**. Hydrogen atoms, counterions and solvate molecules are omitted for clarity. Selected bond distances (Å): Ru1–N1 2.072(2), Ru1–N2 2.070(2), Ru1–N3 2.092(2), Ru1–N4 2.080(2), Ru1–N5 2.080(2), Ru1–N6A 2.046(2), N6–N6A 1.401(3). Selected bond angles (°): N1–Ru1–N3 94.90(9), N1–Ru1–N4 171.88(9), N2–Ru1–N1 78.38(9), N2–Ru1–N4 96.23(9), N2–Ru1–N3 83.85(9), N4–Ru1–N3 78.38(9), N5–Ru1–N1 92.60(9), N5–Ru1–N2 95.30(9), N5–Ru1–N3 172.11(9), N5–Ru1–N4 93.95(9), N5–Ru1–N6A 75.97(9), N6A–Ru1–N1 96.47(9), N6A–Ru1–N2 169.77(9), N6A–Ru1–N3 105.53(9), N6A–Ru1–N4 89.77(9).

2.4. Electronic Absorption Spectroscopy and Electrochemistry

The UV/Visible absorption spectra and redox potentials give information about the metal–ligand interactions in mononuclear complexes and metal–metal interactions in dinuclear complexes. The complexes exhibit strong absorption bands in the UV region which is attributed to the ligand–centered ($\pi \rightarrow \pi^*$) transition, while bands in the visible region are most likely metal–to–ligand ($d\pi \rightarrow \pi^*$) transitions.

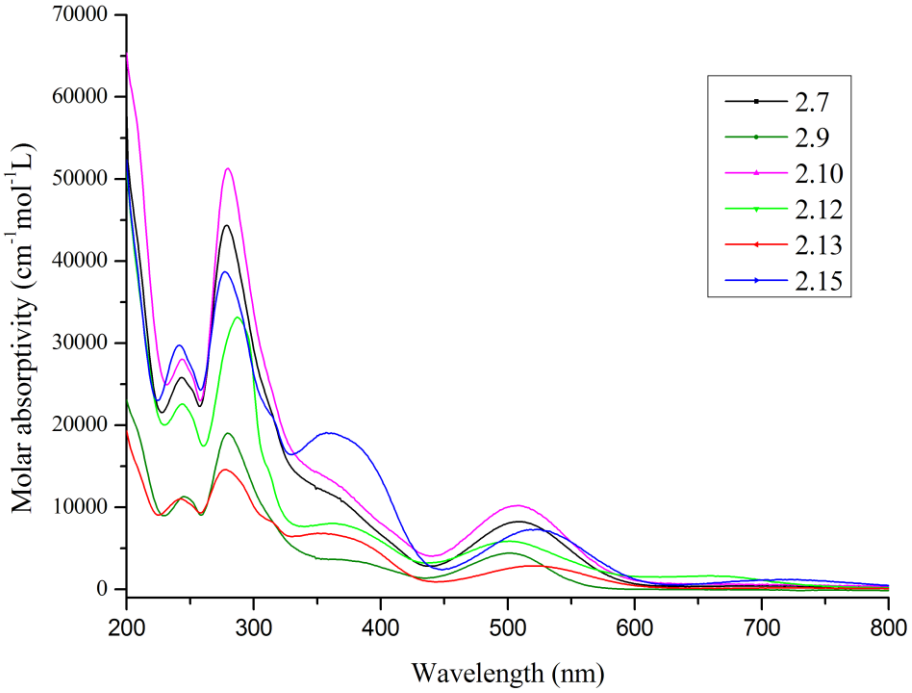

Figure 2.35. The UV/Visible spectra for the mononuclear complexes **2.7**, **2.9**, **2.10**, **2.12**, **2.13** and **2.15**.

The mononuclear complexes all exhibit lowest–energy maxima at *ca.* 510 nm, with an associated shoulder at *ca.* 370 nm, as shown in Figure 2.35. The electronic absorption spectra and redox potentials for the mononuclear complexes in acetonitrile solution are listed in Table 2.10. Previous studies have confirmed that the azo ligand is more π–accepting than the terminal bpy ligands[156] and, therefore, the lowest energy transition is assigned as the Ru($d\pi$) → azo(π^*) transition.

Based on the similarity to $[Ru(bpy)_3]^{2+}$,[1] the higher energy absorption is associated with the Ru($d\pi$) → bpy(π^*) charge transfer. Thus, mononuclear ruthenium complexes of azobispyridine posses small HOMO–LUMO energy gaps. The energy corresponding to the MLCT transition into the bridging ligand (E_{MLCT}) increases with electron–donating

substituents on the bridging ligand, while it decreases in the presence of electron–withdrawing substituents.

Table 2.10. Absorption maxima[a] and redox potentials[b,c] for the mononuclear complexes.

Mononuclear complexes	**λ nm (log ε)**	E_{MLCT}[d] **eV**	$\Delta E_{ox/red}$[e] **V**	$E_{1/2ox1}$	$E_{1/2red1}$	$E_{1/2red2}$	$E_{1/2red3}$
2.7	508 (3.91) 368 (4.04) 279 (4.64) 243 (4.41)	2.44	1.95	+1.24	–0.71	–1.42	–2.03
2.9	503 (3.64) 382 (3.53) 280 (4.27) 245 (4.05)	2.46	2.08	+1.23	–0.85	–1.56	–2.07
2.10	508 (3.79) 280 (4.63) 244 (4.28)	2.44	1.96	+1.19	–0.77	–1.46	–1.77
2.12	505 (3.76) 364 (3.90) 287 (4.52) 244 (4.35)	2.45	1.96	+1.21	–0.75	–1.44	–2.05
2.13	517 (3.45) 355 (3.83) 277 (4.16) 243 (4.04)	2.40	1.90	+1.32	–0.58	–1.25	–2.00
2.15	523 (3.86) 361 (4.28) 277 (4.58) 242 (4.47)	2.37	1.88	+1.31	–0.57	–1.23	–2.00

[a] In acetonitrile (±2 nm).
[b] In V *vs*. $Ag/AgNO_3$ in CH_3CN/0.1M $[(n\text{–}C_4H_9)_4]ClO_4$.
[c] Calculated from DPV measurements.
[d] Energy for the lowest MLCT absorption.
[e] Difference between the first oxidation and first reduction potentials.

The electrochemical studies give additional insights into the electron–transfer processes in such complexes. An example of a differential pulse voltammogram for complex **2.15** is shown in Figure 2.36. The mononuclear complexes all displayed one reversible metal–centered oxidation, Ru(II)/Ru(III), and at least three well resolved reversible reductions of the ligands. Compared to $[Ru(bpy)_3]^{2+}$ (+1.26 V *vs* SCE),[1] these complexes are significantly easier to reduce, indicative of a relatively low–energy π*–orbital (LUMO) of the azobispyridine. Thus, the first reduction occurs on the azo bridging ligand, with the second and third reductions corresponding to the ancillary bpy ligands.[93] The potential difference

between the first ligand–based reduction couple and the metal–based oxidation couple, $\Delta E_{ox/red}$, correlates well with the energy associated with the lowest MLCT absorption, E_{MLCT}, as these processes involve the same HOMO–LUMO orbitals.[252],[253]

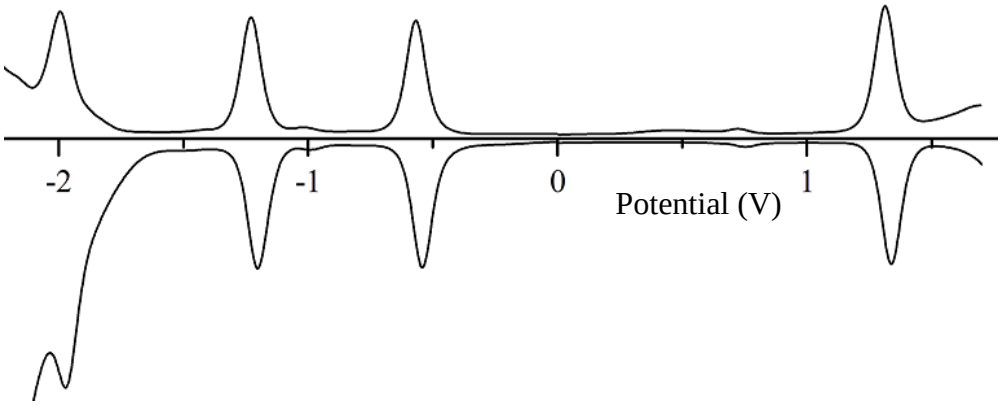

Figure 2.36. The differential pulse voltammogram of **2.15**.

Substituting the parent ligand with electron–donating methyl groups, as in **2.9**, **2.10** and **2.12**, shifts the reduction potential by 40–140 mV compared to **2.7**. For complexes **2.13** and **2.15**, the ruthenium oxidation potentials are shifted *ca.* 75 mV more positive and the ligand becomes *ca.* 130 mV easier to reduce.

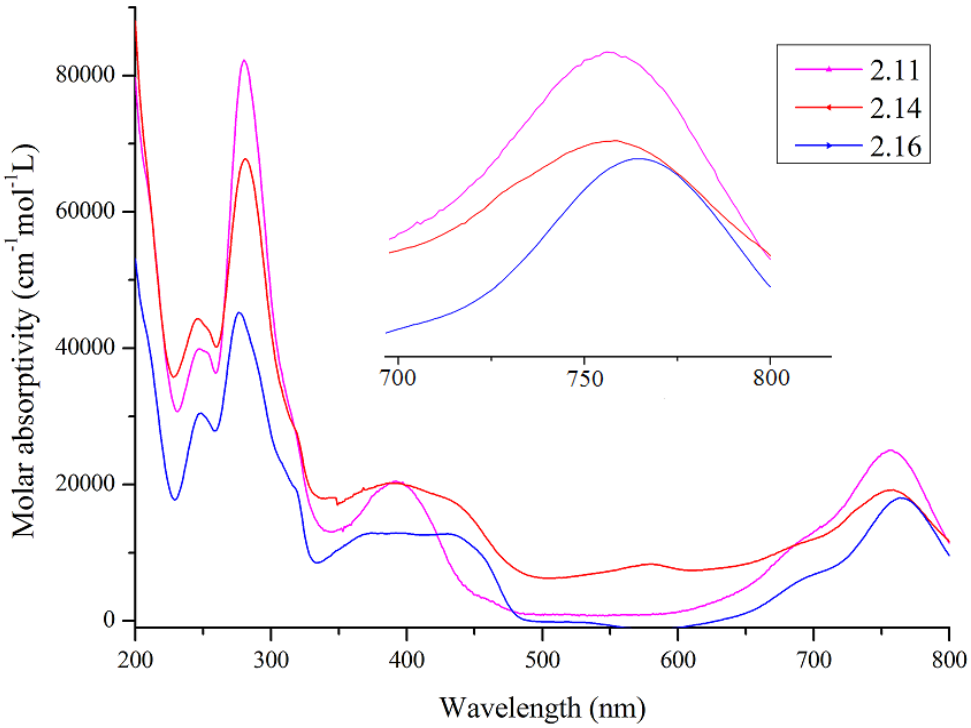

Figure 2.37. The UV/Visible spectra of **2.8, 2.11, 2.14** and **2.16.**

Table 2.11. Absorption maxima[a] and electrochemical[b,c] data for the dinuclear complexes.

Dinuclear complexes	λ nm (log ε)	E_{MLCT},[d] eV	$\Delta E_{ox/red}$,[e] V	ΔE_{ox},[f] V	log K_c[g]
([{Ru(bpy)$_2$}$_2$(bpym)]$^{4+}$)[6]	594 540 412	2.09	1.94	0.16	2.70
2.8	757 (4.38) 375 (4.18) 283 (4.89) 247 (4.59)	1.64	1.42	0.49	8.28
2.11	761 (3.64) 392 (3.53) 280 (4.27) 247 (4.05)	1.63	1.42	0.48	8.11
2.14	758 (3.79) 427 (4.26) 393 (4.30) 281 (4.63) 246 (4.28)	1.64	1.39	0.48	8.11
2.16	764 (3.76) 431 (4.10) 373 (3.90) 276 (4.52) 243 (4.35)	1.62	1.40	0.50	8.45

[a] In acetonitrile (±2 nm).
[b] In V *vs*. Ag/$AgNO_3$ in CH_3CN/0.1M $[(n\text{–}C_4H_9)_4]ClO_4$.
[c] Calculated from DPV measurements.
[d] Energy for the lowest MLCT absorption.
[e] Difference between the first oxidation and first reduction potential.
[f] Difference between the two successive oxidation potentials.
[g] Comproportionation constant, $K_c = \exp\{\Delta E_{ox}F/RT\}$, where F/RT = 38.92 V^{-1} at 298 K.

The dinuclear complexes **2.8**, **2.11**, **2.14** and **2.16** all exhibit strong ligand–centered absorptions at *ca.* 280 nm and 247 nm and metal–to–ligand charge transfer bands at λ>350 nm. Figure 2.37 shows the electronic absorption spectra of the dinuclear complexes. The lowest energy absorptions at *ca.* 760 nm are assigned as the MLCT transition into the bridging ligand [Ru(dπ) → BL(π*)] and represent relatively low HOMO–LUMO energy gaps. The large bathochromic shift (~ 250 nm) of these absorptions, compared to the mononuclear ruthenium(II) complexes, has been observed regularly for dinuclear complexes.[1],[6],[156] This red shift is due to the lowering of the π*–orbital of the bridging ligand on coordination of a second $[Ru(bpy)_2]^{2+}$ moiety. The other bands in the visible region are assigned as the MLCT transitions into the ancillary bpy ligands [Ru(dπ) → bpy(π*)]. The large red–shift of the lowest–energy MLCT absorptions indicates very strong interactions between the metal centres in these dinuclear complexes. The extent of these interactions is

revealed by electrochemical studies using differential pulse voltammetry. Table 2.11 lists the absorption maxima and electrochemical data for the dinuclear complexes **2.8**, **2.11**, **2.14** and **2.16**.

The dinuclear complexes all exhibit two separate reversible metal–centered one–electron oxidations and four reversible ligand–based reductions. The splitting between the two metal–centered oxidation potentials measures the metal–metal interaction across the bridge. The difference in the two successive oxidation potentials (ΔE_{ox}) gives a direct measure of the comproportionation constant (K_c), which has been extensively used to quantify the extent of communication between two metal centres.[33],[41],[244]

The dinuclear complexes each display ΔE_{ox} values of approximately 500 mV equivalent to K_c values of ~ 2 x 10^9 and hence exhibit a very high degree of metal–metal communication compared to bpym[39] and 2,5–dpp.[73] X–ray crystal structure analysis of the binuclear complexes (Section 2.3) indicates an inter–metal distance of *ca.* 4.9 Å in these complexes, whereas the distances in complexes of bpym[65] and 2,5–dpp[41],[254] are 5.6 Å and 6.2 Å, respectively. Short internuclear metal–metal distances along with a number of other important factors, such as the electronic properties of the ligand and the metal, electron density of the LUMO at the coordinating sites, have been proposed as governing factors responsible for the interaction between the metal centres. More recently, it has been shown that the nature of the counterion also plays a role.[39],[40] In the present work the anion was maintained constant.

Table 2.12. Redox potentials[a] for **2.8**, **2.11**, **2.14** and **2.16**.

Dinuclear complexes	$E_{1/2ox2}$	$E_{1/2ox1}$	$E_{1/2red1}$	$E_{1/2red2}$	$E_{1/2red3}$	$E_{1/2red4}$	$E_{1/2red5}$
([{Ru(bpy)$_2$}$_2$(bpym)]$^{4+}$)[6]	+1.69	+1.53	–0.41	–1.08			
2.8	+1.85	+1.36	–0.06	–0.71	–1.83[b]		
2.11	+1.74	+1.26	–0.16	–0.81	–1.85	–1.91	
2.14	+1.84	+1.36	–0.03	–0.65	–1.19	–1.73	–1.86
2.16	+1.87	+1.37	–0.03	–0.63	–1.84	–2.14	–2.23

[a] Calculated from DPV measurements.
[b] Two electron reduction.

The redox potentials for the dinuclear complexes are listed in Table 2.12. The first oxidation potential for the dinuclear complexes occurs at a slightly more positive potential than the corresponding mononuclear complexes, since coordination of a second ruthenium ion reduces the electron density on the bridging ligand and as a result on the coordinated

metal. For example, the dinuclear complex **2.16** exhibits two separate one–electron metal–centered oxidation potentials at +1.37 and +1.87, whereas the mononuclear complex **2.15** oxidises at +1.31 V. Figure 2.38 shows differential pulse voltammogram for **2.16**.

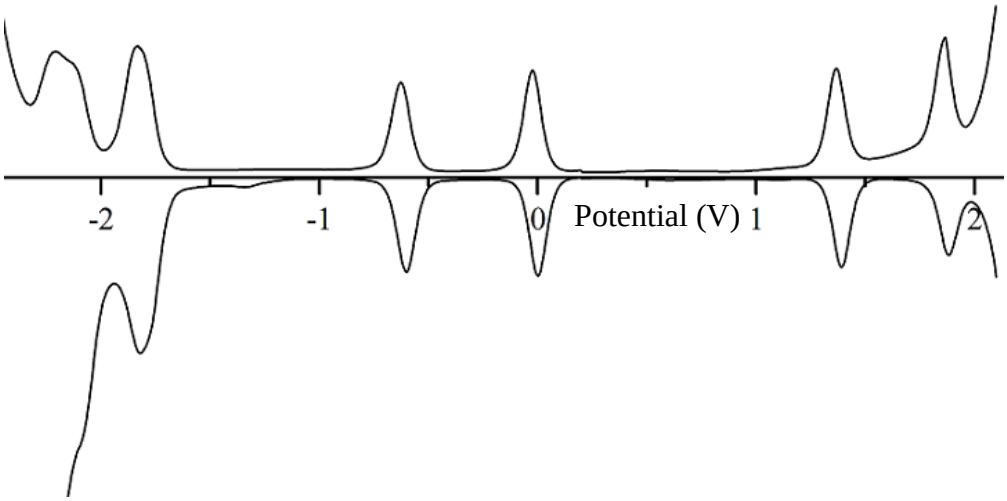

Figure 2.38. Differential pulse voltammogram for **2.16**.

Earlier work on **2.8** has assigned the first two reductions as bridge–centered and the subsequent reductions are bpy–centered.[93] The potential shift of the first reduction potential in the binuclear complexes when compared to the mononuclear complexes is due to the lowering of the π*–orbital of the bridging ligand through double $[Ru(bpy)_2]^{2+}$ coordination, which facilitates the electron uptake.

Substituents on the bridging ligand have similar effects on the redox couple as observed for the mononuclear complexes. The electron–donating methyl substituents donate electron density to the Ru–centre making them easier to oxidise but more difficult to reduce as they raise the π*–orbital of the bridging ligand, as seen in **2.11**. Conversely, electron–withdrawing halide substituents, in **2.14** and **2.16**, destabilise the Ru(III) in comparison to Ru(II) making them difficult to oxidise but easier to reduce, due to the lowering of the π*–orbital of the bridging ligand.

2.5. Summary

This chapter has described the synthesis and characterization of a series of bidentate bridging ligands based on azobispyridine. Ligand **2.1** was prepared by oxidative coupling of 2–aminopyridine using sodium hypochlorite. Ligands **2.2**, **2.3** and **2.4** were synthesised from methyl–substituted amines to study the effect of electron–donating groups on the bridge. This

chapter also describes the synthesis of electron–withdrawing halogen substituted ligands **2.5** and **2.6**.

The coordination chemistry of these bidentate ligands with ruthenium(II) metal ions was investigated by synthesising mononuclear and binuclear complexes with $[Ru(bpy)_2Cl_2]$. All the doubly–bidentate ligands readily bridged two ruthenium metal atoms, except **2.2** and **2.4**, which is probably due to the steric interference of the methyl group at the 3– and 6–positions. Surprisingly, reaction of ligand **2.6** with $[Ru(bpy)_2Cl_2]$ resulted in the chloro–substituted dinuclear product, which was avoided by using $[Ru(bpy)_2(OTf)_2]$ to give the corresponding bromo–substituted complex **2.16**. These complexes were characterised by NMR spectroscopy and X–ray crystallography. Crystal structures of the mononuclear complexes show that the ruthenium atom binds to the azobispyridine ligand using the azo nitrogen atom and the pyridine ring nitrogen atom, forming a stable five–membered chelate ring. In all cases the $Ru–N_{azo}$ bond is the shortest Ru–N bond and the $Ru–N_{py}$ bond of the bridging ligand is shorter than those to the bpy ligands. The visible absorption spectroscopy and differential pulse voltammetry reveal that these complexes possess small HOMO–LUMO energy gaps.

In the dinuclear complexes selective formation of only one diastereoisomer, the *meso* form, was observed. The X–ray crystal structures indicate that the azo ligand acts as a planar bridge between the two ruthenium atoms separated by *ca.* 4.9 Å. Electronic absorption spectroscopy in acetonitrile exhibit MLCT absorption bands extending to *ca.* 760 nm indicating a low–lying π^*–orbital in the bridging ligand. The electrochemical measurements reveal two widely separated one–electron metal–centred oxidation processes, indicating very strong communication between the metal centres.

Chapter 3

Bidentate ligands based on azobis(N–heterocycles)

3. Bidentate ligands based on azobis(N–heterocycles)

3.1. Introduction

Ruthenium(II) complexes involving polypyridyl ligands have attracted extensive attention with emphasis on their stereochemical, electrochemical and photophysical properties. In such complexes, the ground and excited–state properties can be tuned by varying the structure of the ligand.[13],[28] Replacement of the pyridine rings of bpy with different heterocycles can have significant effects on the physical properties of the resulting ruthenium complexes.[27],[196] Previous investigations in the Steel group has shown that certain heterocycles can have quite dramatic effects on the physicochemical properties of the metal complexes.[195] As shown in Figure 3.1, replacement of the pyrazine ring in 2,3'–dpp[73] by a pyrimidine ring as in 4,6–di(2'–pyridyl)pyrimidine (dppm)[74] slightly reduces the interaction between the metal centres. However, electrochemical studies of dinuclear ruthenium complexes involving an imidazolate bridge (dpim) exhibit remarkably strong metal–metal interactions.[100]

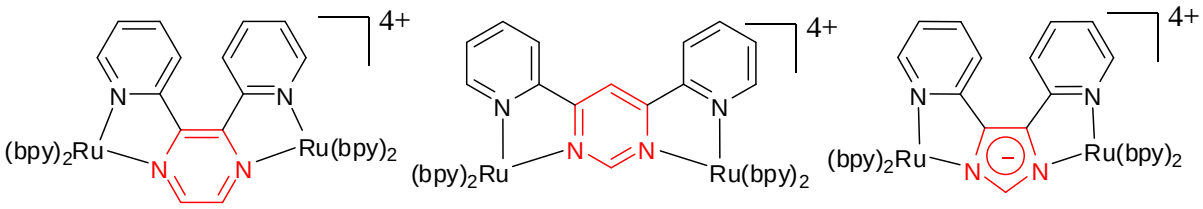

2,3'−dpp	**dppm**	**dpim**
K_c = 747	506	188 000 (*meso*) 652 000 (*rac*)

Figure 3.1. Ruthenium complexes with varying heterocyclic groups and their corresponding K_c values.

This chapter describes a series of polydentate ligands containing metal–binding substituents at the N=N unit, as shown in Figure 3.2. The ligands are divided into two categories: (i) ligands in which the pyridine ring of the azobispyridines, as discussed in Chapter 2, is replaced by a pyrimidine ring; (ii) ligands involving increased delocalisation through fused aromatic rings.

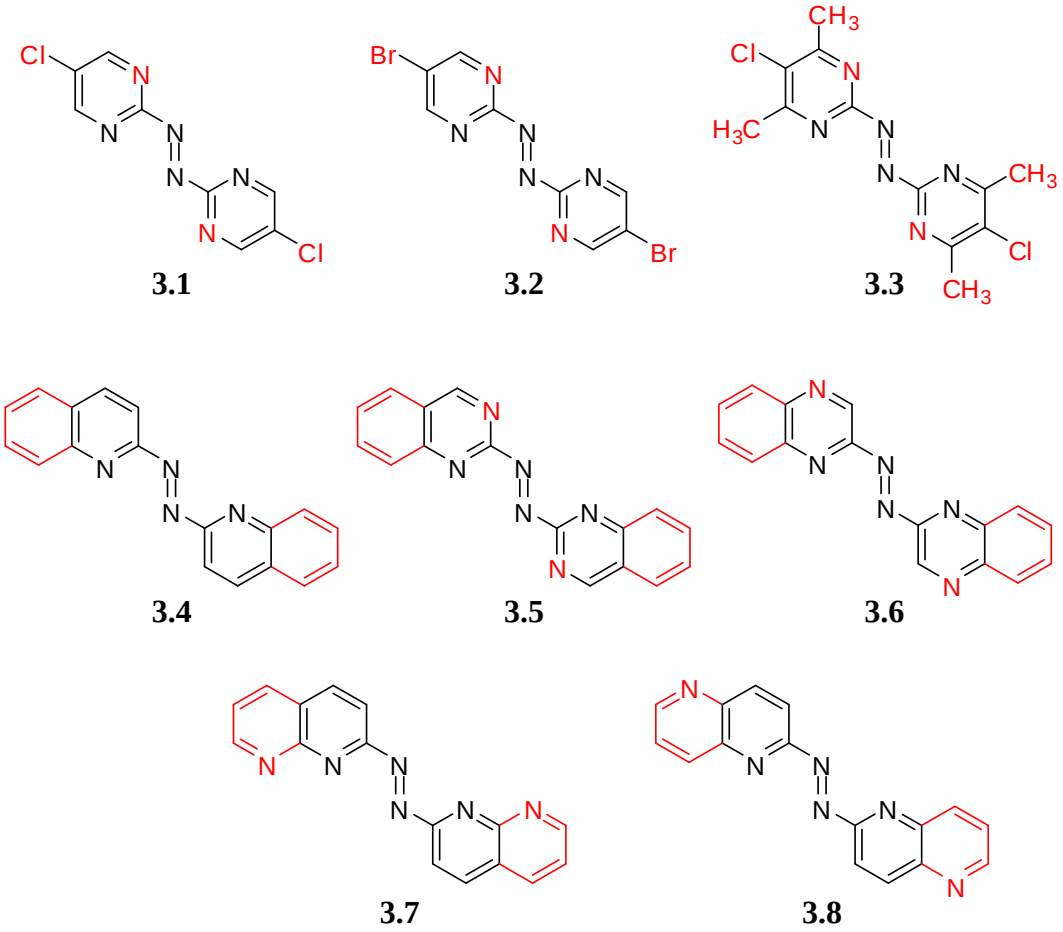

Figure 3.2. The series of ligands discussed in this chapter.

3.2. Pyrimidine–based ligands

The ability of azobispyridine–based ligands to mediate strong metal–metal interactions has been discussed in Chapter 2. The replacement of the pyridine ring with a pyrimidine ring and the introduction of electron withdrawing substituents on the ligand was done to lower the energy of the π*–orbital of the ligand. In addition, the pyrimidine ligands also possess additional sites for coordination. The ruthenium chemistry of pyrimidine–based ligands **3.1** – **3.3** and their effect on the communication between the metal centres is investigated in this chapter. The supramolecular chemistry of these ligands with silver(I) was also investigated and is discussed in Chapter 6.

Ligand **3.1**, first described by Doslik *et al.*,[255] is an exceptionally strong π–accepting bidentate ligand, when compared to the well studied ligand **2.1**. The spectroelectrochemistry and high–field EPR studies of ruthenium, rhodium and copper complexes of **3.1** indicate high metal/ligand orbital mixing in these complexes.[256] The most unexpected result is the

formation and high stability of the dinuclear complexes containing the ligand **3.1** as a radical anion. The introduction of chlorine substituents and additional nitrogen functionalities further lowers the π*–level of the bridging ligand. Ye *et al.*[257] established a synthetic approach for the preparation of low valence triruthenium clusters by substituting the acetate bridge in the $Ru_3(OAc)_6$ core with **3.1**. This substitution dramatically modifies the electronic and redox properties in the triruthenium derivatives. A recent study by Jana *et al.*[258] involves the structural characterization of a **3.1**–bridged oligonuclear Fe_2Cu_2 complex.

There have been numerous investigations on the structural and spectroscopic properties for complexes containing ligand **3.1**, however, pyrimidine–based azo ligands containing substituents other than chlorine are not known. In an attempt to design new azo ligands based on pyrimidine units, we synthesised a ligand containing electron–withdrawing bromo substituents **3.2**, and an example of a ligand containing both electron–withdrawing chloro and electron–donating methyl substituents, **3.3**.

3.2.1. Syntheses of the ligands

The pyrimidine–based ligands **3.1** and **3.3** were synthesised by chlorinating oxidative coupling of the precursor amines, while **3.2** was obtained by oxidative coupling of the bromo amine using sodium hypochlorite. The starting material for **3.1** was commercially available, whereas the precursors for **3.2** and **3.3** were synthesised as discussed below.

Ligand **3.1** has been previously prepared by chlorinating oxidative coupling of 2–aminopyrimidine using lithium hypochlorite.[255] In this case, **3.1** was synthesised by oxidative coupling using sodium hypochlorite, as shown in Scheme 3.1.

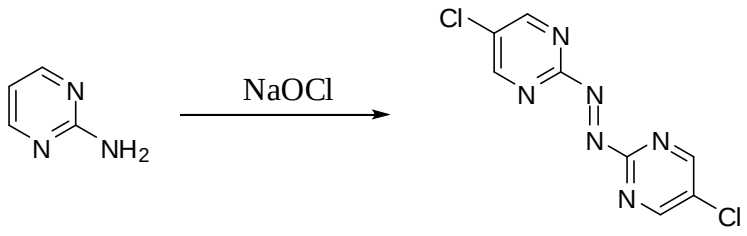

3.1

Scheme 3.1

Ligand **3.2** was synthesised by oxidative coupling of 2–amino–5–bromo pyrimidine using sodium hypochlorite as shown in Scheme 3.2. The bromo precursor was synthesised using the method of Nara *et al.*[246]

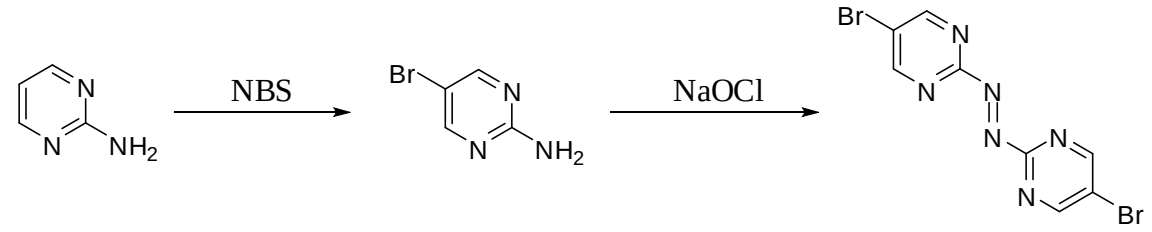

3.2

Scheme 3.2

A microwave–assisted cyclisation reaction, following the method of Goswami *et al.*,[259] gave the precursor dimethyl aminopyrimidine, which on coupling using sodium hypochlorite gave the corresponding new ligand **3.3** in moderate yield, as shown in Scheme 3.3.

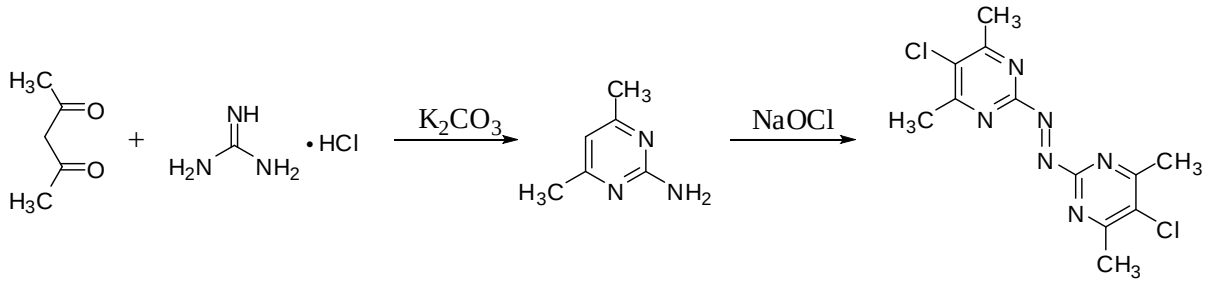

3.3

Scheme 3.3

3.2.2. Ruthenium(II) Complexes of 3.1

Ligand **3.1** reacted with $[Ru(bpy)_2Cl_2]$ in aqueous ethanol to give the mononuclear complex **3.9**, which was characterised as $[(bpy)_2Ru(\mathbf{3.1})](PF_6)_2$. The dinuclear complex **3.10** was obtained by refluxing an ethanolic mixture of **3.1** and $[Ru(bpy)_2Cl_2]$ in a 1:2 stoichiometric ratio, as shown in Scheme 3.4. The precipitation of complex **3.10** as hexafluorophosphate salts gave a paramagnetic 3+ complex indicating the formation of a radical anion. The ^{1}H NMR spectrum was able to be obtained by addition of a small amount of oxidising agent, *m*–chloroperbenzoic acid to the acetonitrile–d_3 solution.

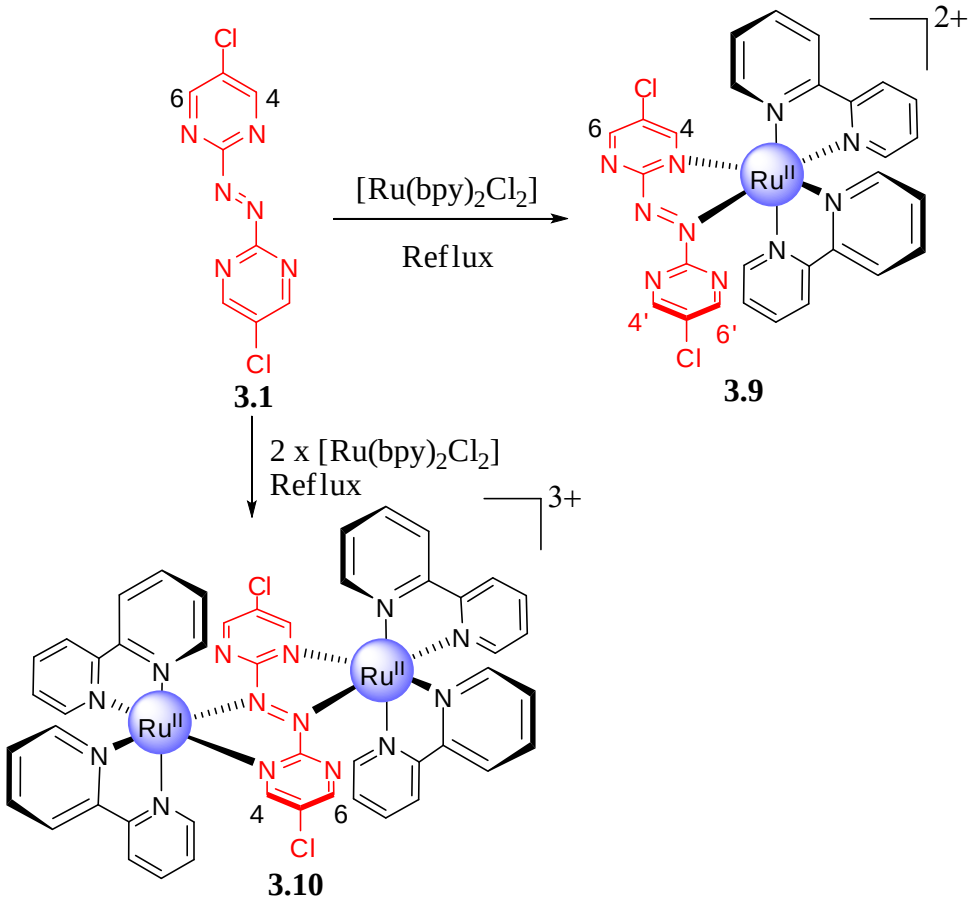

Scheme 3.4

The ^{1}H NMR spectrum of **3.9**, shown in Figure 3.3, exhibits 20 proton signals with the signals corresponding to **3.1** identified easily due to the chloride substituents and additional N–atom in the pyrimidine ring. The four pyridine rings corresponding to the terminal bpy units were also identified and are color coded into groups; however, due to overlapping of signals, individual bpy rings could not be identified. Table 3.1 lists the ^{1}H chemical shifts and *CIS* values for the free ligand **3.1** and complex **3.9**. The coordinated pyrimidine ring of **3.1** shows two different proton environments for the H4 and H6 protons. Based on the strong negative *CIS* value for the H6 proton it could be concluded that it must be shielded due to the through–space ring–current effects from the adjacent bpy ring. Unfortunately, all attempts to grow crystals of **3.9** were unsuccessful.

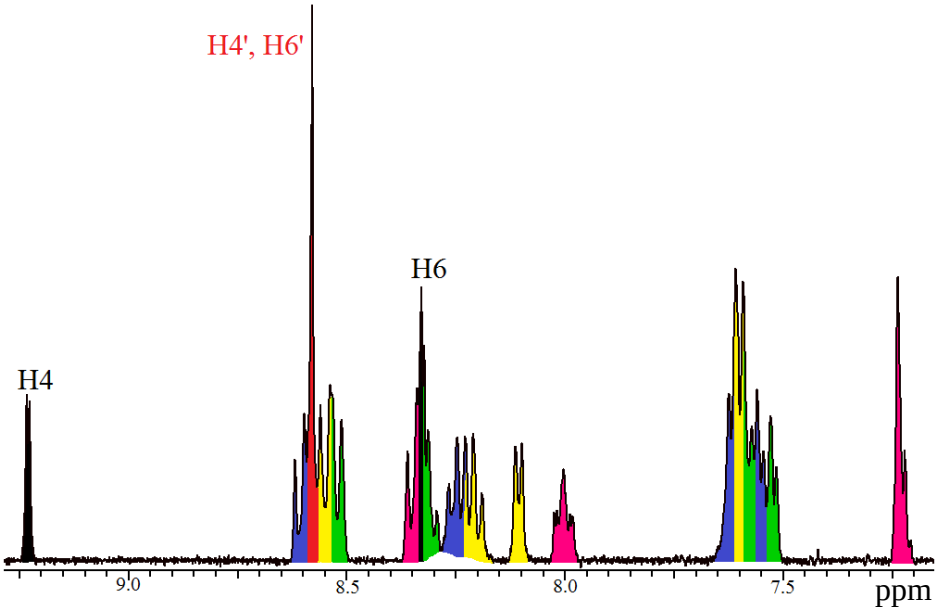

Figure 3.3. The ^{1}H NMR spectrum of **3.9**.

Table 3.1. The ^{1}H NMR chemical shifts[a] and *CIS* values[b] for **3.1** and **3.9**.

	H4	**H6**
3.1	9.02	9.02
3.9[c] (black)	9.23	8.33
CIS	*+0.21*	*–0.69*
3.9[d] (red)	8.58	8.58
CIS	*–0.44*	*–0.44*

[a]In acetonitrile–d_3.
[b]$CIS = \delta_{complex} – \delta_{ligand}$.
[c]Coordinated pym ring of **3.1**.
[d]Free pym ring of **3.1**.

*Crystal Structure of **3.10***

Vapour diffusion of diisopropyl ether into an acetonitrile solution of the complex gave green crystals of complex **3.10**, which were suitable for X–ray analysis. The complex crystallises in the monoclinic space group *C*2/c with one Ru(bpy)$_2$ fragment, half of ligand **3.1**, one and a half hexafluorophosphate anions and one acetonitrile molecule in the asymmetric unit, as shown in Figure 3.4.

The overall structure of **3.10** grows into the dinuclear complex in which the ligand **3.1** forms five–membered chelate rings with two Ru(bpy)$_2$ fragments separated at a distance of

4.881(5) Å. The *trans* N–Ru–N angles are ~ 173° which indicate a slight distortion in the ruthenium octahedral geometry. The Ru–N_{py} bond lengths are similar (*ca.* 2.06 Å) and consistent with those found in Chapter 2.

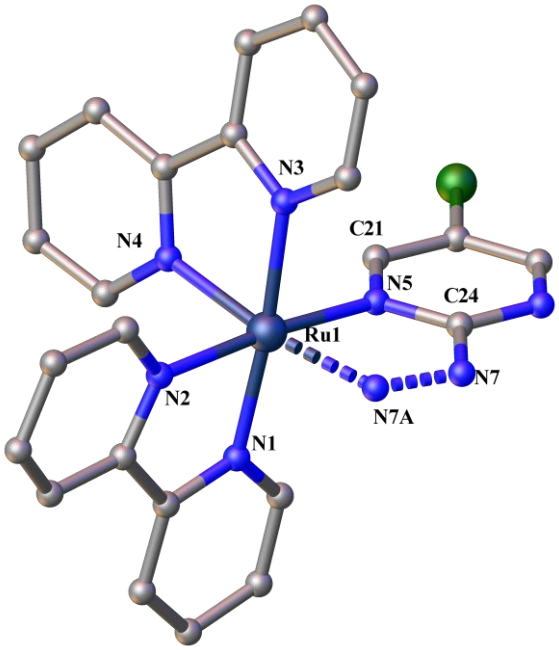

Figure 3.4. The asymmetric unit of complex **3.10** with atom–labelling. Counterions and solvate molecules are omitted for clarity. Selected bond lengths (Å): Ru1–N1 2.053(3), Ru1–N2 2.057(3), Ru1–N3 2.067(4), Ru1–N4 2.074(3), Ru1–N5 2.035(3), Ru1–N7A 2.050(3), N7–N7A 1.373(6), N7–C24 1.362(4), N5–C24 1.364(5), N6–C24 1.344(5), N5–C21 1.341(4), N6–C23 1.326(6). Selected bond angles (°): N1–Ru1–N2 78.41(17), N1–Ru1–N3 174.52(13), N1–Ru1–N4 96.37(13), N2–Ru1–N3 99.05(15), N2–Ru1–N4 85.85(12), N3–Ru1–N4 78.54(13), N5–Ru1–N1 97.17(14), N5–Ru1–N2 174.65(14), N5–Ru1–N3 85.60(13), N5–Ru1–N4 97.73(12), N5–Ru1–N7 76.82(12), N7A–Ru1–N1 90.52(13), N7A–Ru1–N2 100.04(12), N7A–Ru1–N3 94.72(13), N7A–Ru1–N4 171.74(12).

The charge state in ruthenium complexes containing azo ligands can be correlated to the N_{azo}–N_{azo} bond length. As reviewed by Kaim *et al.*[249] the N=N bond length (*ca.* 1.25 Å) tends to increase to about 1.36 Å in the azo anion radical form. Further reduction of the azo function to hydrazine/hydrazo results in a further lengthening of the N–N distance to about 1.40 Å. In the previously reported dicopper(I) complex of **3.1**, the non–reduced azo ligand exhibits a N=N bond length of 1.248(11) Å in [{$Cu(PPh_3)_2$}$_2$(**3.1**)]$(PF_6)_2$, whereas the reduced azo–aromatic ligand in [($Cu(PPh_3)_2$}$_2$(**3.1**)](PF_6) displays a longer N_{azo}–N_{azo} bond

length of 1.345(7) Å and shorter C–N(–N) bond length of 1.360(5) Å.[250],[255] Interestingly, **3.10** also displays a longer N–N bond length [N7–N7A 1.373(6) Å] and shorter C–N_{azo} bond length [N7–C24 1.362(4) Å]. This indicates that the ligand **3.1** exists as a reduced anion radical. The presence of three hexafluorophosphate anions and the electrochemical studies (Section 3.5) further support this observation.

3.2.3. Ruthenium(II) Complexes of 3.2

Reaction of ligand **3.2** with $[Ru(bpy)_2Cl_2]$ in aqueous methanol gave the mononuclear complex **3.11**, which was characterised as $[(bpy)_2Ru(\mathbf{3.2})](PF_6)_2$, as shown in Scheme 3.5. Ligand **3.2** reacts with two equivalents of $[Ru(bpy)_2Cl_2]$ in aqueous methanol to give a chloro substituted dinuclear complex, as was also seen with ligand **2.6** in Chapter 2.

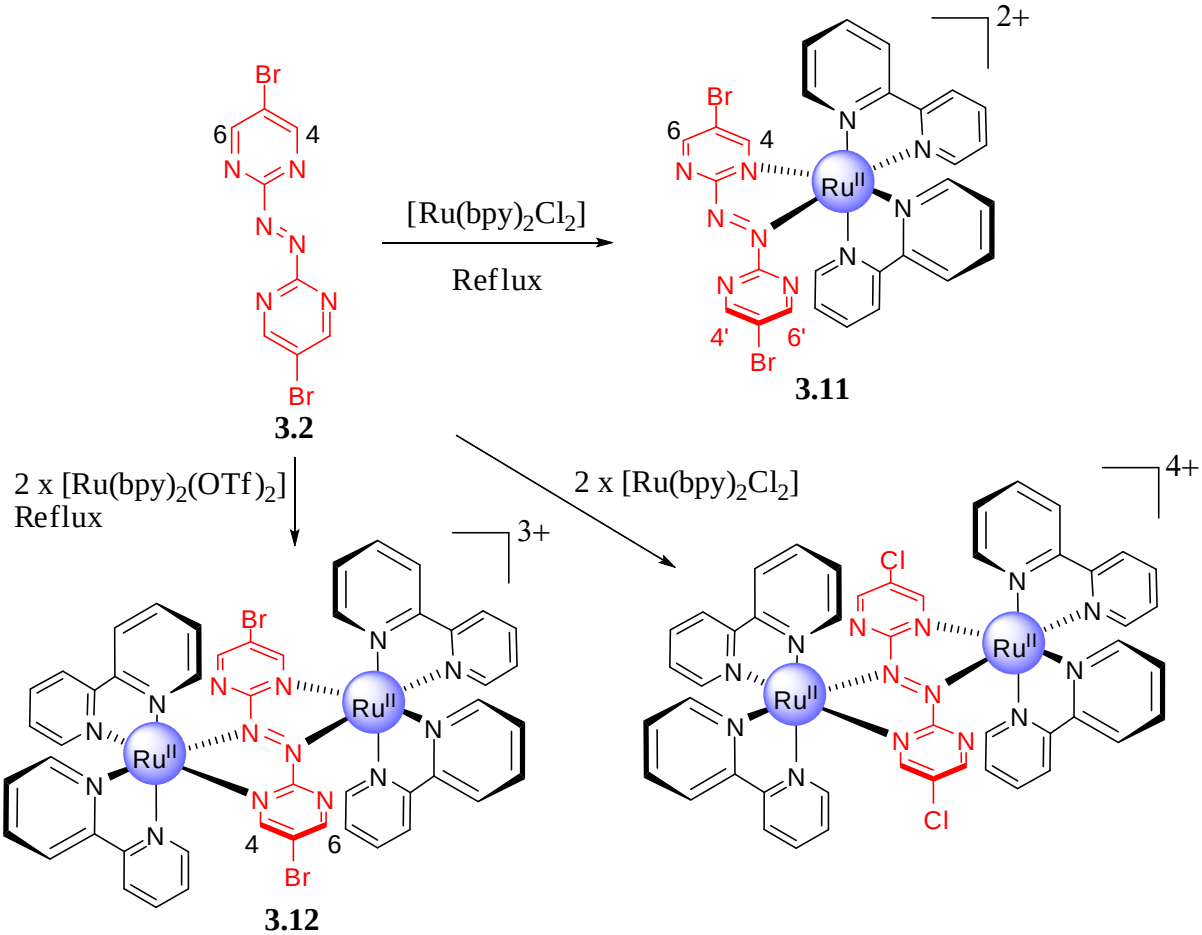

Scheme 3.5

The product was characterised as $[\{Ru(bpy)_2\}_2(\mu\text{–}\mathbf{3.1})](PF_6)_4$ by ESI–MS as shown in Figure 3.5. No evidence for the bromo substituted dinuclear species was obtained. Interestingly, the dinuclear chloro–product obtained by this method was a diamagnetic 4+

charged compound, unlike the paramagnetic 3+ charged dinuclear complex **3.10** obtained from ligand **3.1**.

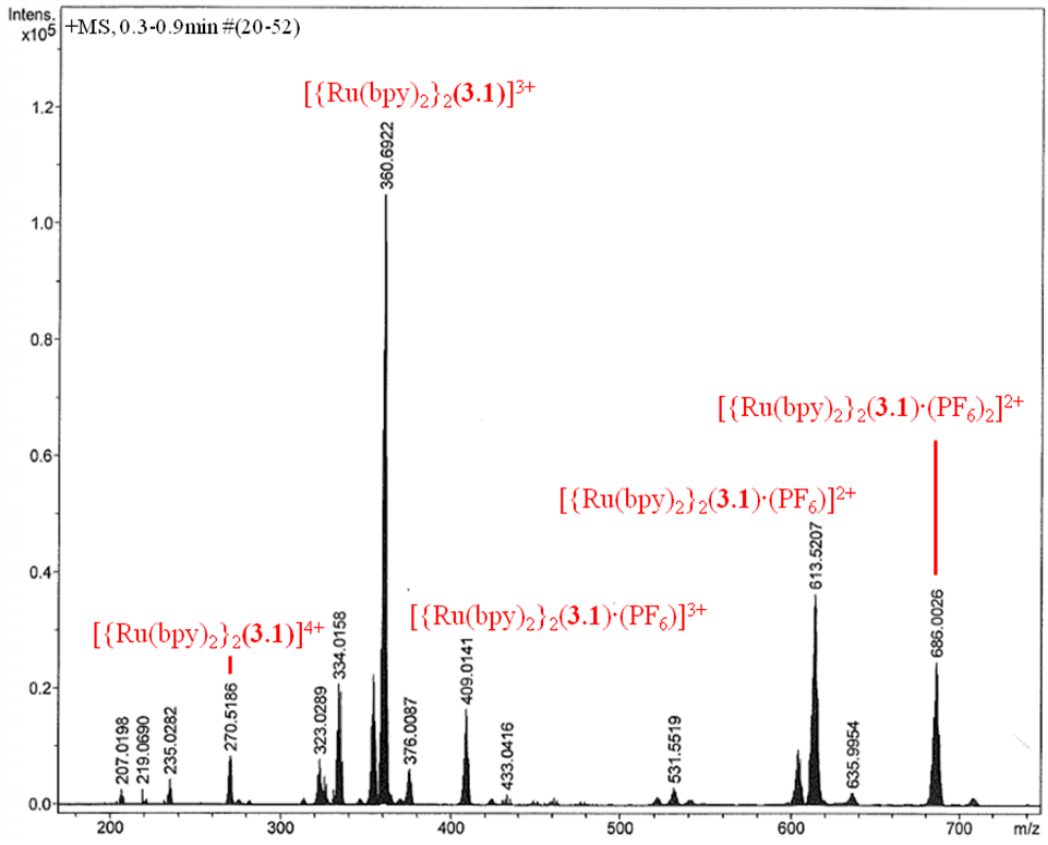

Figure 3.5. The mass spectrum of the chloro–substituted dinuclear product.

Reaction of the free ligand **3.2** with an excess of LiCl did not show any evidence for the chloro–substituted ligand **3.1**. Furthermore, the presence of only the mononuclear bromo product **3.11** on reacting **3.2** and $[Ru(bpy)_2Cl_2]$ suggests that the dibromo pyrimidine ligand **3.2** promotes aromatic nucleophilic substitution only after coordination to two metals. Like **2.6** discussed in Chapter 2, this is possibly due to the increased electropositive character of the C5 atom in the dinuclear complex. Therefore to overcome this substitution reaction $[Ru(bpy)_2Cl_2]$ was replaced with $[Ru(bpy)_2(OTf)_2]$. The reaction of **3.2** with two equivalents of $[Ru(bpy)_2(OTf)_2]$ in ethylene glycol gave the dinuclear bromo–substituted complex **3.12**. This was characterised as a singly reduced complex $[\{Ru(bpy)_2\}_2(\mu\text{–}\mathbf{3.2})](PF_6)_3$ by X–ray analysis. The mass spectrum was consistent with **3.12** and no evidence for the chloro–substituted dinuclear complex was observed, as shown in Figure 3.6.

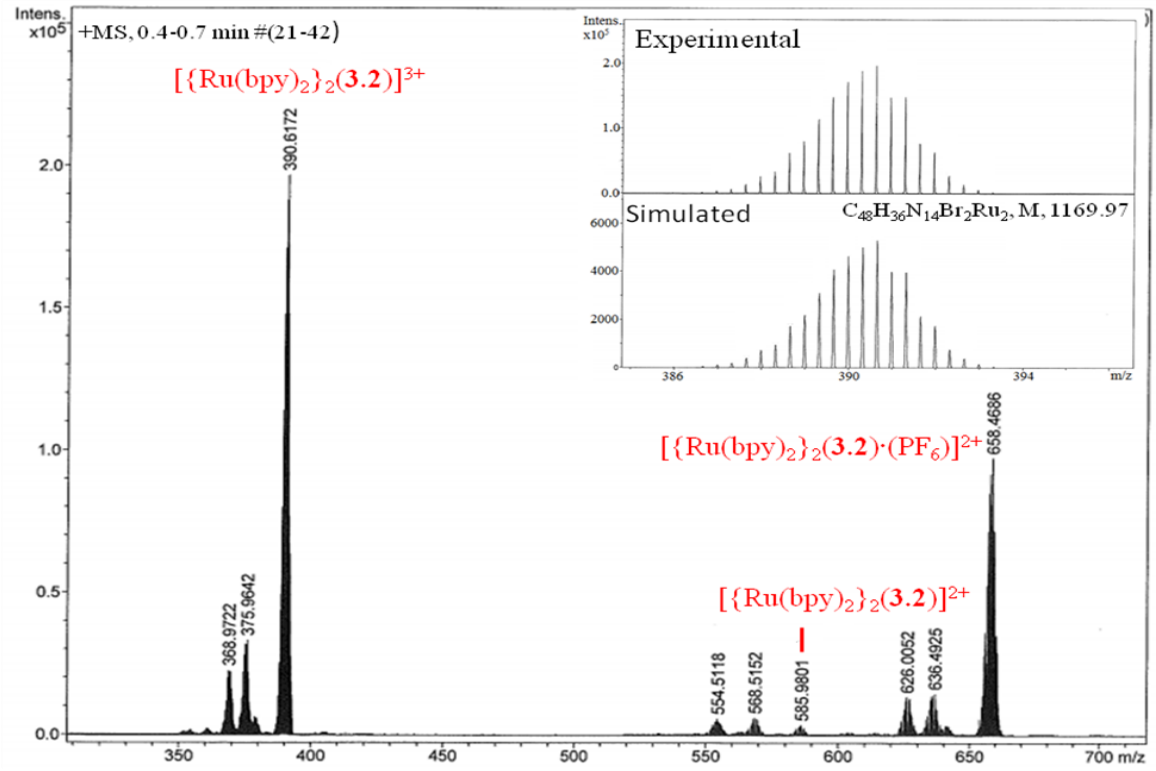

Figure 3.6. The mass spectrum and the isotopic pattern of **3.12**.

*^{1}H NMR of **3.11***

Figure 3.7 shows the ^{1}H NMR spectrum for **3.11,** which shows chemical shifts similar to **3.9**. The spectrum shows 20 aromatic proton signals with four pyridine ring environments corresponding to the bpy ligands. The individual bipyridine rings were identified by 1D ROESY experiments, where the H3 protons of the pyridyl rings connected on the same bpy show an NOE. In the bridging ligand, the peak corresponding to the H6 proton (8.41 ppm) is more shielded when compared to the H4 proton (9.31 ppm), since it is close in space to the adjacent bpy rings and hence experiences through–space ring–current effects. Contrary to this, the H6' and H4' protons (8.87 ppm) of the free pyrimidine ring experience similar shifts as they are not effected much by the coordination. Attempts to grow crystals of the complex were unsuccessful.

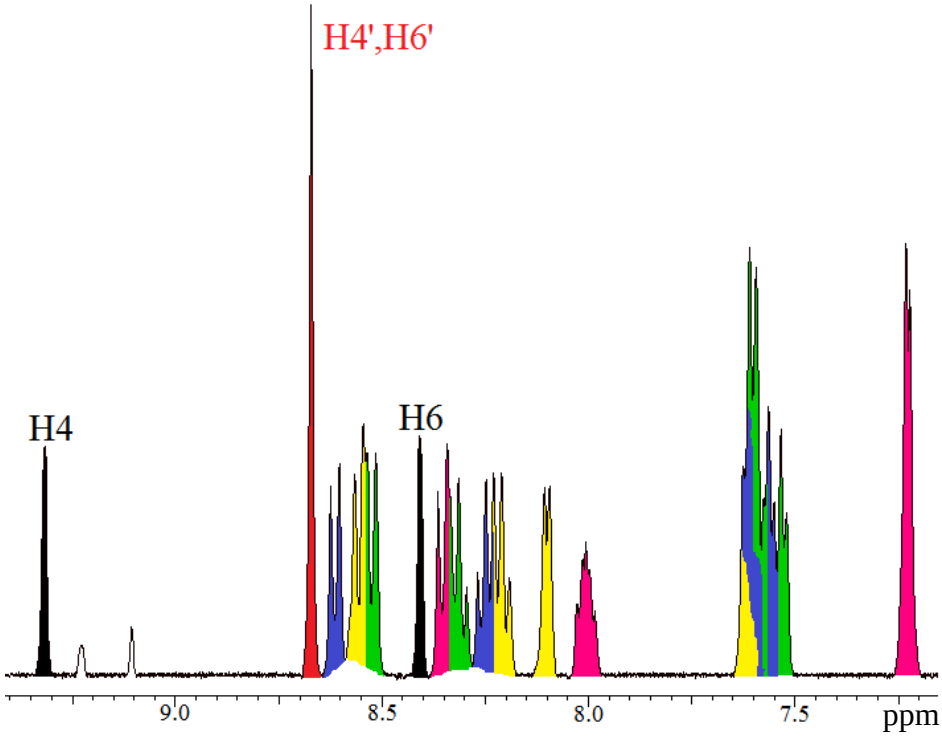

Figure 3.7. The ^{1}H NMR spectrum of **3.11**.

*Crystal Structure of **3.12***

Crystals of **3.12** were obtained by diffusion of diisopropyl ether into an acetonitrile solution of the complex. The complex crystallised in the triclinic space group *P*–1, with half a cation, one and a half hexafluorophosphate anions and one acetonitrile solvate molecule in the asymmetric unit. The one and half hexafluorophosphate anions indicates that the complex exists as the reduced complex $[\{Ru(bpy)_2\}_2(\mu\text{–}\mathbf{3.2})](PF_6)_3$. The complex lies on a crystallographic centre of inversion and is the *meso* isomer.

The complex adopts an "S–frame" coordination mode with the Ru–coordination sphere being unexceptional, as shown in Figure 3.8. The azo bridge acts as a planar bridge with a separation of 4.882(4) Å between the metals. Interestingly, **3.12** also displays a longer N_{azo}–N_{azo} [N7–N7A 1.374(5) Å] bond length and shorter C–N_{azo} [C21–N7 1.366(4) Å] bond length, indicative of a reduced azo–aromatic ligand.[255] The coordination geometry of ruthenium is normal with consistent Ru–N bond lengths. The formation of the anion radical ligand is also supported by the oxidation state of the ligand which is discussed further in Section 3.5.

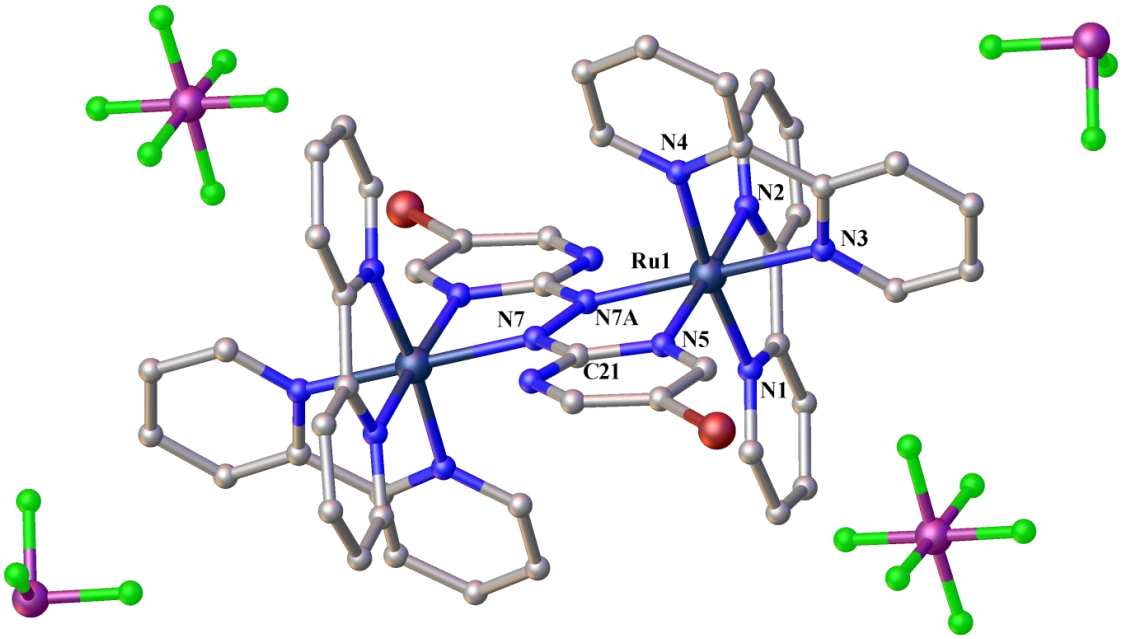

Figure 3.8. X–ray crystal structure of **3.12** showing three PF_6^- anions. All hydrogen atoms and solvate molecules are omitted for clarity. Selected bond distances (Å): Ru1–N1 2.051(3), Ru1–N2 2.065(3), Ru1–N3 2.061(3), Ru1–N4 2.067(3), Ru1–N5 2.042(3), Ru1–N7A 2.054(3), N7–N7A 1.374(5), N7–C21 1.366(4). Selected bond angles (°): N1–Ru1–N2 79.01(11), N1–Ru1–N3 96.63(11), N1–Ru1–N4 173.61(10), N1–Ru1–N7A 89.18(11), N2–Ru1–N4 96.72(11), N3–Ru1–N2 88.83(10), N3–Ru1–N4 78.43(11), N5–Ru1–N1 99.91(11), N5–Ru1–N2 176.00(10), N5–Ru1–N3 95.13(10), N5–Ru1–N4 84.67(11), N5–Ru1–N7A 76.65(10), N7A–Ru1–N2 99.45(10), N7A–Ru1–N3 170.68(10), N7A–Ru1–N4 96.25(11).

3.2.4. Ruthenium(II) Complexes of 3.3

Ligand **3.3** was refluxed with $[Ru(bpy)_2Cl_2]$ in aqueous methanol to give **3.13** and **3.14**, characterised as $[(bpy)_2Ru(\mathbf{3.3})](PF_6)_2$ and $[\{Ru(bpy)_2\}_2(\mu\text{–}\mathbf{3.3})](PF_6)_4$ respectively, as shown in Scheme 3.6.

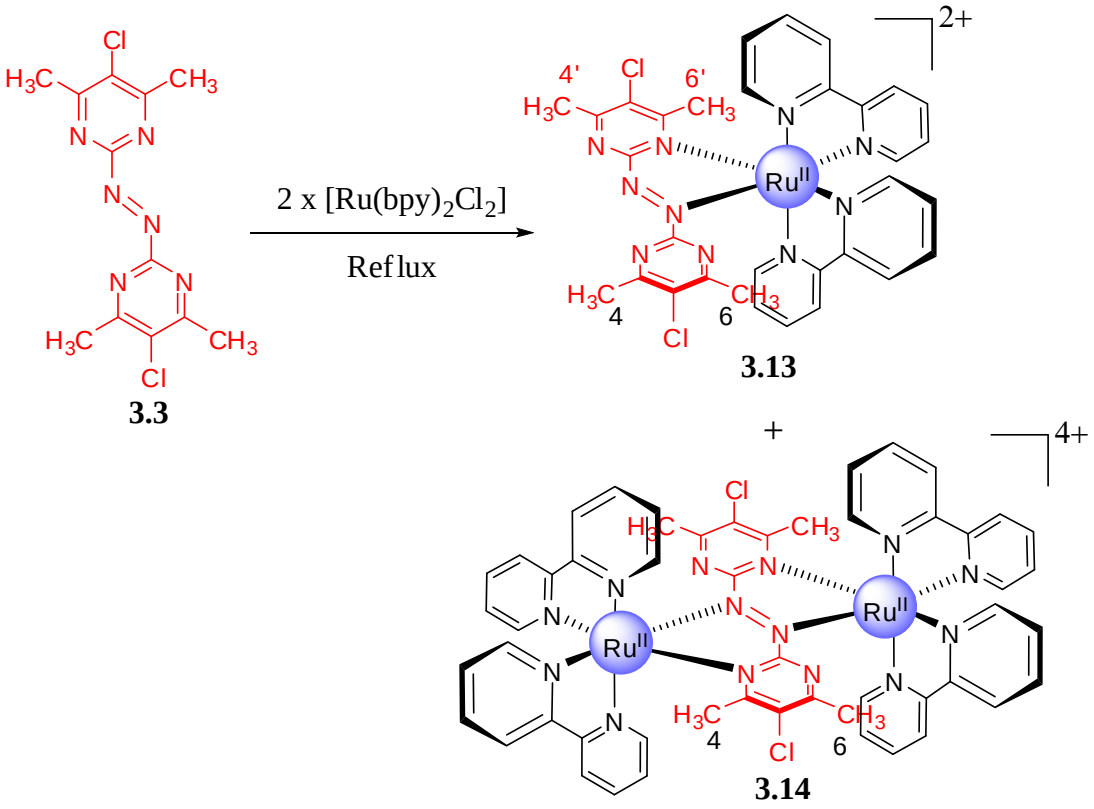

Scheme 3.6

Due to the substituents on **3.3**, complex **3.13** shows aromatic proton signals corresponding to the bpy pyridine rings only, as shown in Figure 3.9a. The individual pyridine rings were identified by gCOSY experiments as shown in Figure 3.9b. Unfortunately, due to overlapping of signals the individual pyridine rings could not be identified. One of the bpy–H6 protons (7.01 ppm) experiences strong ring–current effects as it is positioned directly over an adjacent pyrimidine ring, which correlates with the X–ray structure discussed below. The methyl substituents on the bridging ligand **3.3** exhibit three different signals for the coordinated and the free pym ring. The 6–CH_3 of the coordinated ring is shifted upfield since it is in close proximity to an adjacent bpy ring,

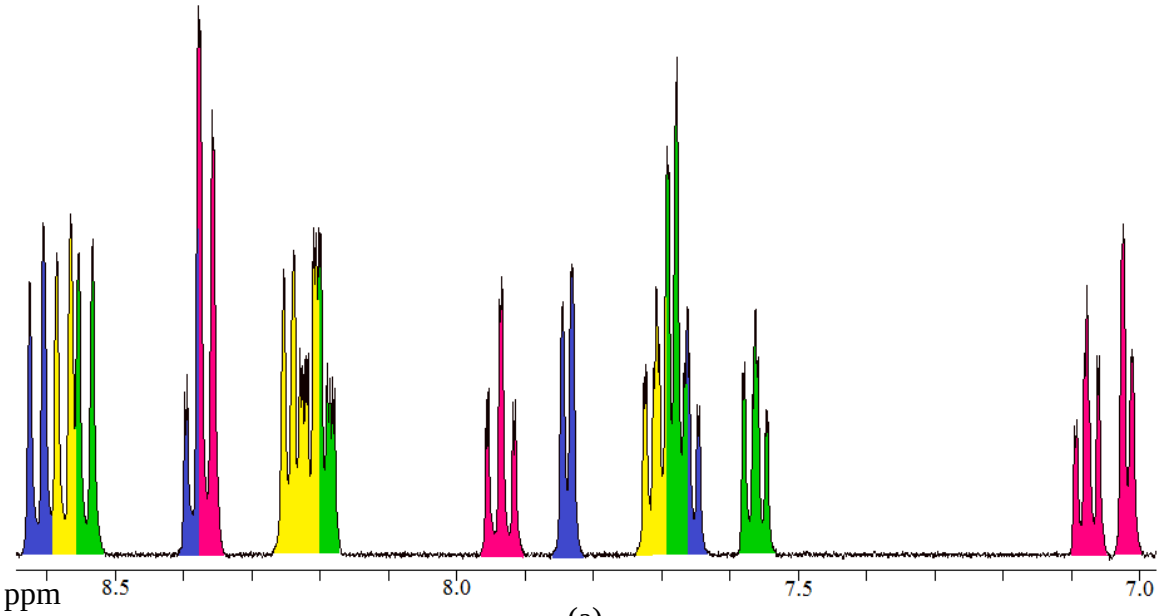

(a)

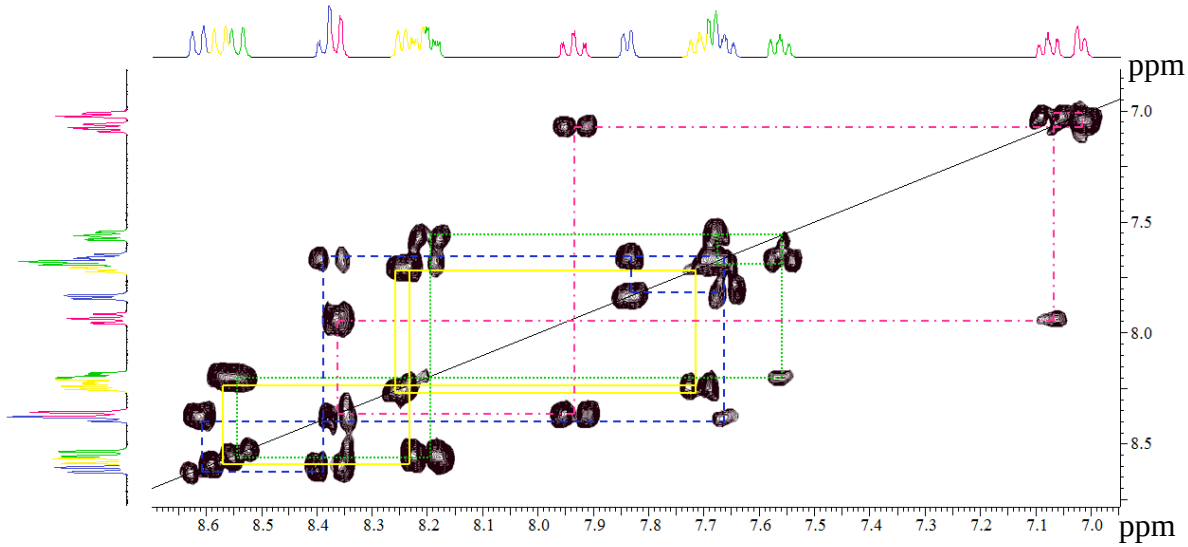

(b)

Figure 3.9. The ^{1}H NMR (a) and gCOSY (b) spectra of **3.13** displaying the bpy pyridine rings, color–coded in groups.

*Crystal Structure of **3.13***

Red needles of **3.13** suitable for X–ray analysis were obtained by diffusing petroleum ether into an acetone solution of the complex. The complex crystallised in the monoclinic space group $P2_1/c$, with one full cation and two hexafluorophosphate anions in the asymmetric unit, as shown in Figure 3.10. The X–ray crystal structure confirms the mononuclear nature of the complex.

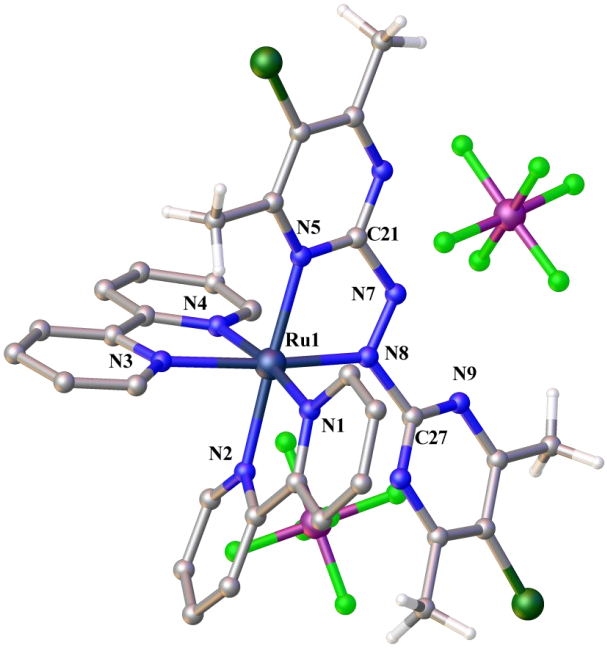

Figure 3.10. The X–ray crystal structure of **3.13**. The bipyridine hydrogen atoms are omitted for clarity. Selected bond distances (Å): Ru1–N1 2.053(3), Ru1–N2 2.062(3), Ru1–N3 2.103(3), Ru1–N4 2.080(3), Ru1–N5 2.079(3), Ru1–N8 1.972(3), N7–N8 1.291(4). Selected bond angles (°): N8–Ru1–N4 93.69(12), N1–Ru1–N4 171.99(12), N8–Ru1–N1 92.99(12), N5–Ru1–N4 86.43(12), N8–Ru1–N5 75.97(13), N1–Ru1–N5 99.48(12), N2–Ru1–N4 95.31(12), N8–Ru1–N2 102.12(12), N1–Ru1–N2 78.95(12), N2–Ru1–N5 177.52(12), N4–Ru1–N3 77.76(12), N8–Ru1–N3 171.16(12), N1–Ru1–N3 95.70(12), N5–Ru1–N3 100.95(12), N2–Ru1–N3 81.17(12).

Ligand **3.3** forms a five–membered chelate ring involving a pyrimidine N–atom (N5) and an azo N–atom (N8). The ruthenium atom possesses a distorted octahedral geometry with the average Ru–N_{py} bond distances (*ca.* 2.07 Å) consistent with similar complexes. Once again the Ru–N_{azo} bond distance [Ru1–N8 1.972(3)] is shorter than the Ru–N_{pym} bond distance [Ru1–N5 2.079(3)] indicating the better π*–accepting ability of the azo group when compared to the pyrimidine ring. However, unlike the pyrimidine–based dinuclear complexes **3.10** and **3.12**, the N_{azo}–N_{azo} bond length [N7–N8 1.291(4) Å] in **3.13** is within the range of d_{NN} values (1.23–1.32 Å) for compounds containing an unreduced azo ligand.[249] As seen in the mononuclear complexes in Chapter 2, the free pyrimidine ring is considerably twisted with the torsion angle (N7–N8–C27–N9) being –21.2(5)° and the coordinated ring is in the same plane as the azo with a torsion angle (N8–N7–C21–N5) of 4.2(5)°. The crystal packing shows numerous weak interactions, such as F···HC and N···HC, at a range > 2.4 Å.

*Crystal Structure of **3.14***

Crystals of **3.14** were obtained by vapour diffusion of diisopropyl ether into an acetonitrile solution of the complex. The complex crystallises in the triclinic space group *P*–1. The asymmetric unit contains one ruthenium atom, half of ligand **3.3** and two bpy ligands with two hexafluorophosphate anions and two acetonitrile molecules, as shown below.

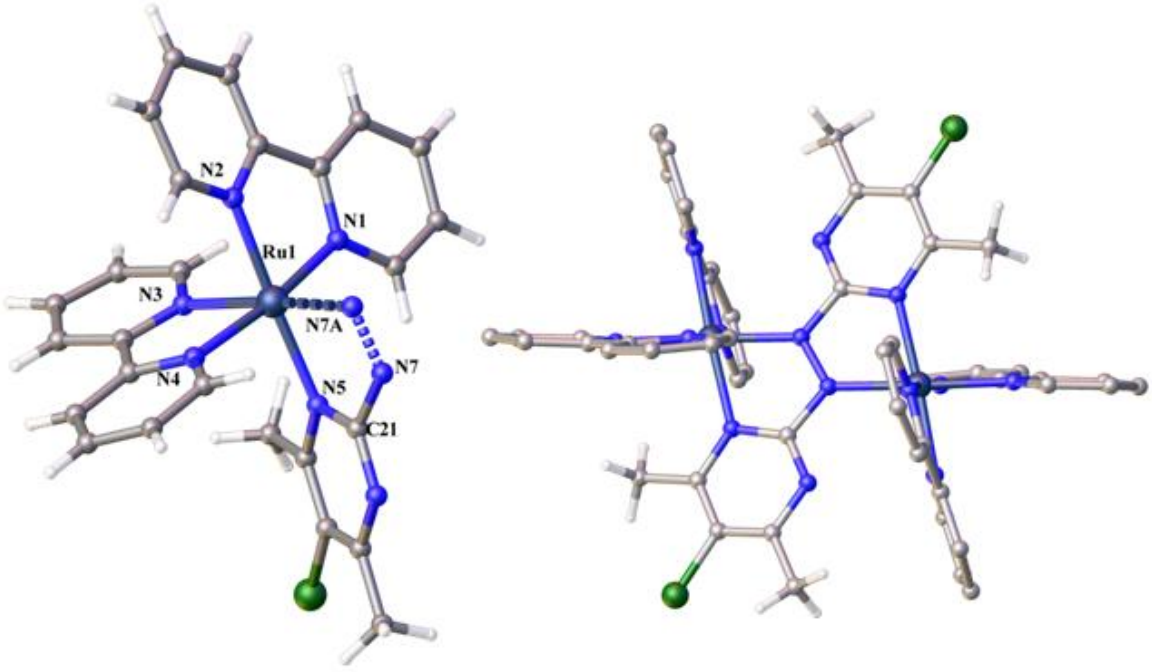

(a) (b)

Figure 3.11. (a) Asymmetric unit of **3.14**. (b) A perspective view of the X–ray structure of **3.14**. Selected bond lengths (Å): Ru1–N1 2.053(5), Ru1–N2 2.049(6), Ru1–N3 2.089(5), Ru1–N4 2.079(5), Ru1–N5 2.076(6), Ru1–N7A 1.995(5), N7–N7A 1.355(10), N7–C21 1.414(8). Selected bond angles (°): N1–Ru1–N3 94.4(2), N1–Ru1–N4 171.7(2), N1–Ru1–N5 100.8(2), N2–Ru1–N1 78.6(2), N2–Ru1–N3 81.9(2), N2–Ru1–N4 96.7(2), N2–Ru1–N5 177.2(2), N4–Ru1–N3 78.1(2), N5–Ru1–N3 100.9(2), N5–Ru1–N4 84.3(2), N7A–Ru1–N1 91.8(2), N7A–Ru1–N2 100.4(2), N7A–Ru1–N3 173.7(2), N7A–Ru1–N4 95.8(2), N7A–Ru1–N5 76.8(2).

The X–ray crystal structure unambiguously confirms the crystallised complex as the *meso* isomer with the terminal ligands above and below the plane of the bridge, as shown in Figure 3.11b. The *trans* angles of 177.2(2)° (N2–Ru1–N5), 171.7(2)° (N1–Ru1–N4), 173.7(2)° (N3–Ru1–N7) indicate a slightly distorted octahedral geometry at the metal centre. As expected, ligand **3.3** exhibits the conventional "S–frame" conformation with each

$Ru(bpy)_2$ coordinated through the N_{azo} atom and N_{pym} atom on either sides. The bridge separates the two metal centres at a distance of 4.790(1) Å [Ru···Ru]. The Ru–N_{py} bond lengths are consistent with those found in structurally related compounds. Contrary to complexes **3.10** and **3.12**, the shorter N_{azo}–N_{azo} bond distance [N7–N7A 1.355(10) Å] and longer C–N_{pym} bond distance [N7–C21 1.414(8) Å], along with four hexafluorophosphate anions indicate the presence of the azopyridyl ligand **3.3** as a non–reduced species.

3.3. Ligands based on fused aromatic azines

The metallosupramolecular chemistry of symmetrical aromatic bibenzodiazines has been previously investigated in our group.[70],[159] Although ligand **3.4** has been known for a long time,[260–262] its coordination chemistry has been ignored. In this section, a series of ligands **3.4** – **3.8** based on azo linked fused aromatic azines are described. These ligands were designed to introduce delocalisation in the ligand backbone through fused aromatic rings, which could be used to tune redox properties and absorption spectra.

3.3.1. Syntheses of the ligands

The fused aromatic azo ligands **3.4** – **3.8** were synthesised from their precursor amines by oxidative coupling using sodium hypochlorite. The required amines, 2–aminoquinoline (Scheme 3.7), 2–aminoquinazoline (Scheme 3.8) and 2–aminoquinoxaline (Scheme 3.9), 2–amino–1,8–naphthyridine (Scheme 3.10) and 2–amino–1,5–naphthyridine (Scheme 3.11) were not readily available and were synthesised from literature procedures.

Ligand **3.4** has previously been synthesised by oxidation of the hydrazo compound using $FeCl_3$[262] or oxides of nitrogen, obtained by the action of nitric acid on copper.[261] Instead, **3.4** was conveniently synthesised by oxidative coupling of 2–aminoquinoline, as shown in Scheme 3.7. The precursor amine was synthesised by heating 2–chloroquinoline with acetamide and potassium carbonate under solvent free conditions using the method of Ferenc Kóródi[263] in reasonably good yield (78%). The chloro derivative was prepared in two steps starting from quinoline using a literature procedure.[264],[265]

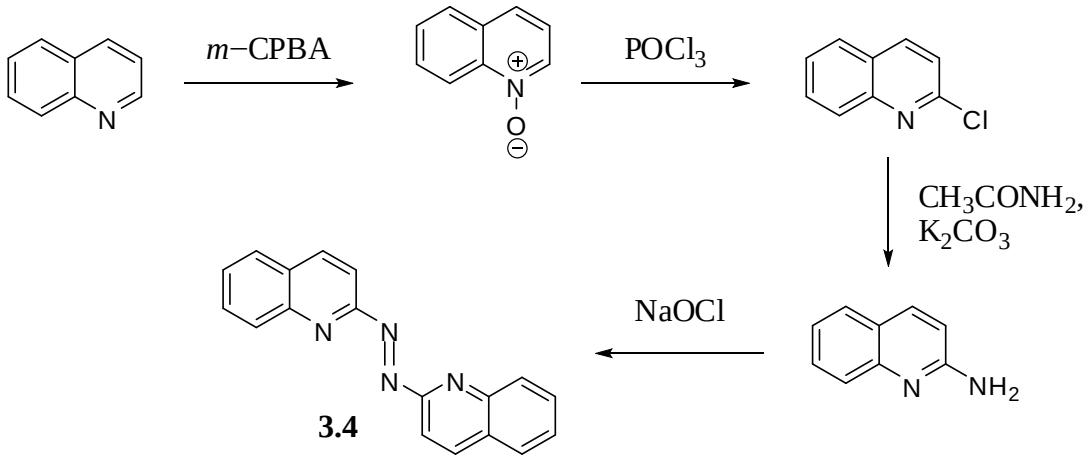

Scheme 3.7

Copper–catalysed coupling of 2–bromobenzaldehyde with guanidine hydrochloride, following a method by Huang *et al.*[266] gave the 2–aminoquinazoline in moderate yield (53%). This was then subjected to oxidative coupling using sodium hypochlorite to give the new ligand **3.5** in 39% yield, as shown in Scheme 3.8.

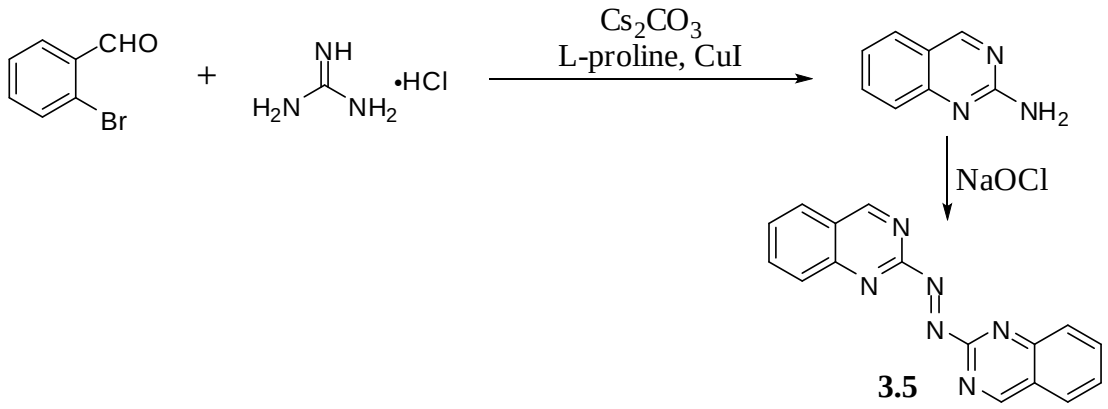

Scheme 3.8

Ligand **3.6** has been reported by Krieger *et al.*[267] as the product obtained from 2(1H)–quinoxalinone oxime by the template effect of Co(II) and Ni(II) ions. Alternatively, **3.6** was synthesised by oxidative coupling of the precursor amine in moderate yield, as shown in Scheme 3.9. The 2–amino quinoxaline precursor was prepared by aminolysis of 2–chloroquinoxaline[268] using the method of Rawua *et al.*[269]

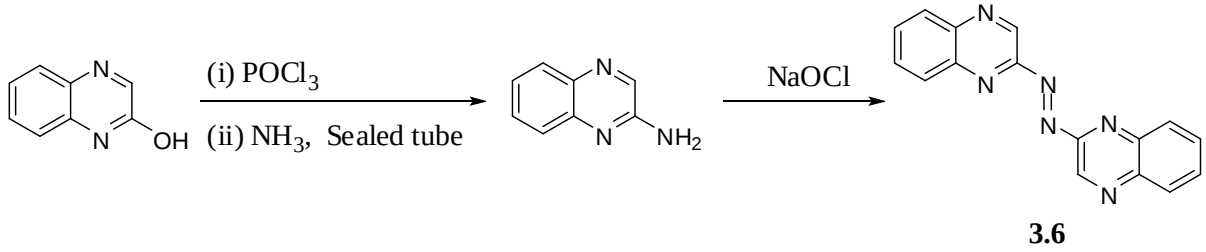

3.6

Scheme 3.9

The naphthyridine–based ligands **3.7** and **3.8** were also synthesised by oxidative coupling of their precursor naphthyridine amines. The starting amines were synthesised *via* Skraup reactions of the corresponding diamines using methods from Campbell *et al.*[270] The condensation of commercially available pyridine–2,6–diamine with sodium *m*–nitrobenzenesulfonate and glycerol gave 2–amino–1,8–naphthyridine in 19% yield, which then undergoes coupling to give ligand **3.7**, as shown in Scheme 3.10.

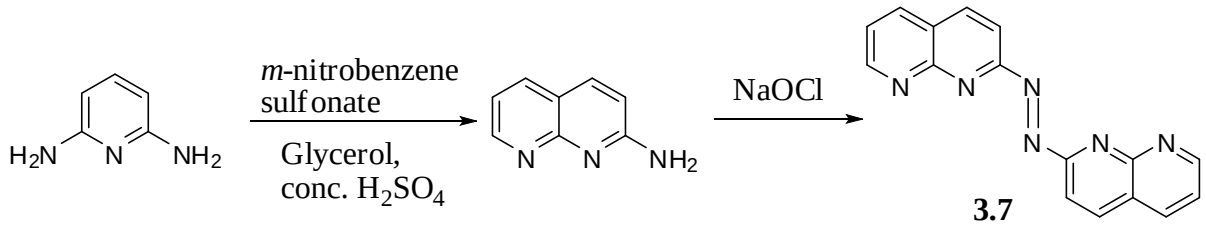

3.7

Scheme 3.10

Ligand **3.8** was synthesised by oxidative coupling of 2–amino–1,5–naphthyridine using sodium hypochlorite in moderate yield. The precursor amine, as shown in Scheme 3.11, was prepared following the method of Campbell *et al.*[270]

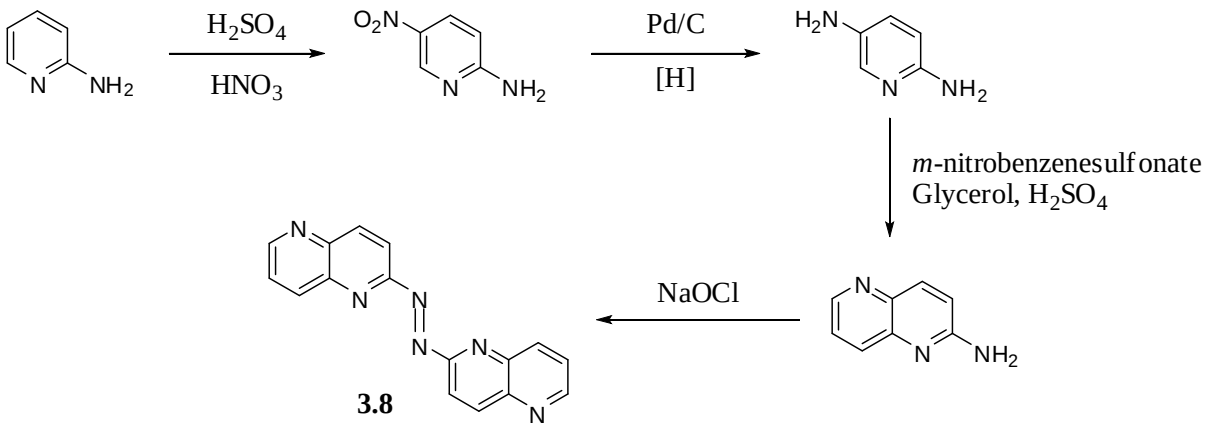

3.8

Scheme 3.11

3.3.2. Ruthenium(II) Complexes of 3.4

Ligand **3.4** is structurally similar to azobis(2–pyridine) **2.1**, however, the fused benzene ring should increase the delocalisation of electrons as well as the steric effects in the region of the N–atom (Figure 3.12).

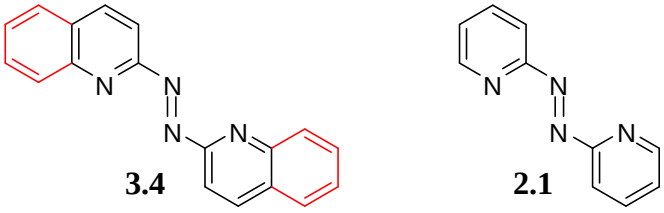

Figure 3.12. The structural similarity between **3.4** and **2.1**.

The mononuclear complex **3.15** was obtained by refluxing **3.4** with $[Ru(bpy)_2Cl_2]$ in aqueous methanol. The complex was precipitated as the hexafluorophosphate salts to give a red powder, which was characterised as $[(bpy)_2Ru(\mathbf{3.4})](PF_6)_2$. The dinuclear complex **3.16** was obtained as a green powder by refluxing a suspension of ligand **3.4** with two equivalents of $[Ru(bpy)_2Cl_2]$ in aqueous methanol (Scheme 3.12).

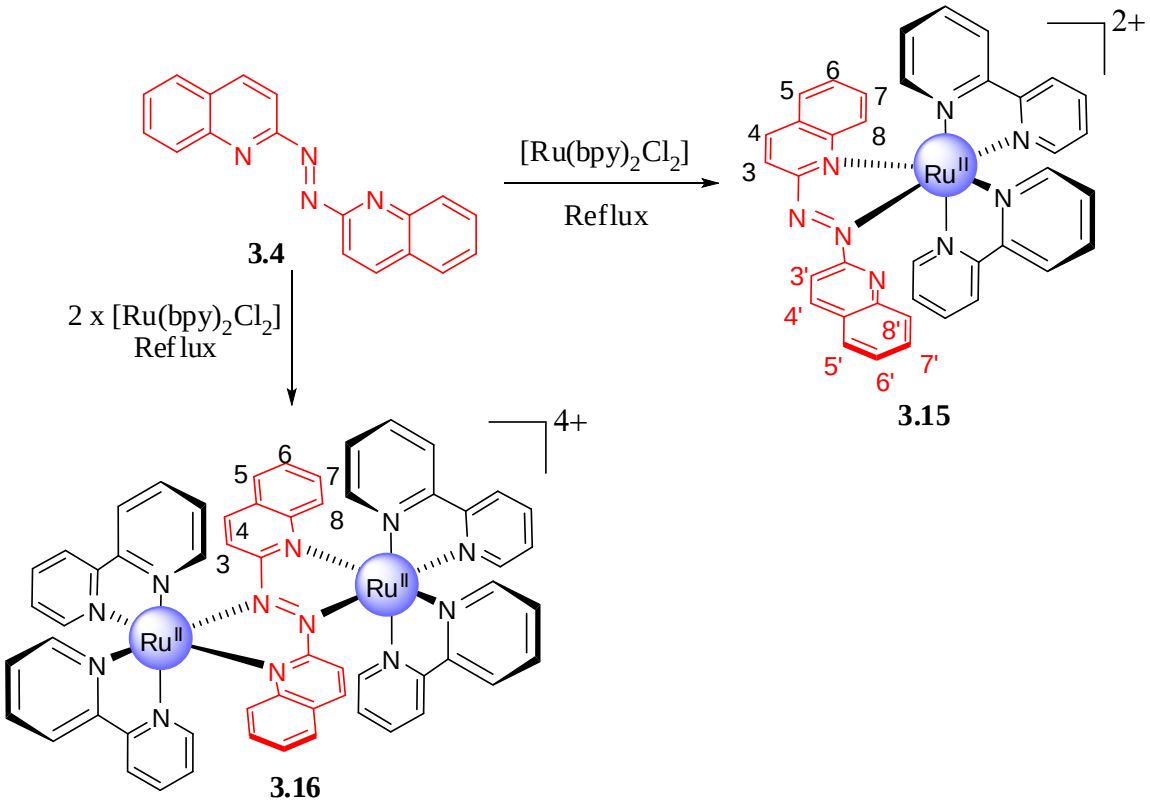

Scheme 3.12

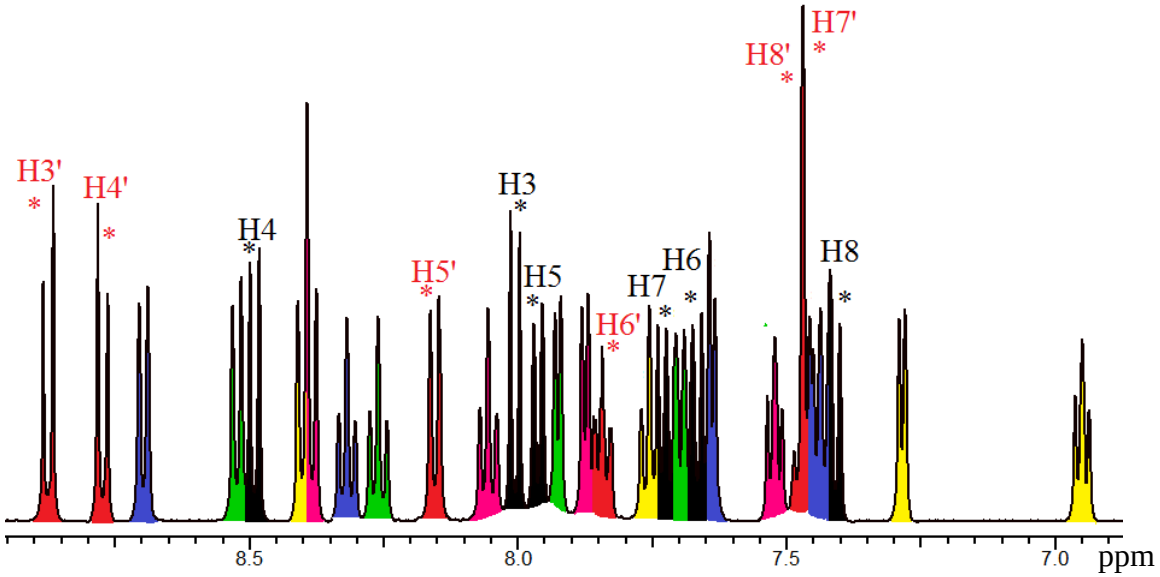

Figure 3.13. The ^{1}H NMR spectrum of **3.15** with the ring systems being identified**.**

The ^{1}H NMR spectrum of **3.15** displays 28 non–equivalent proton signals, as shown in Figure 3.13, corresponding to four pyridine rings and two quinoline ring environments. Due to the unsymmetrical nature of the coordinated ligand **3.4** the two quinoline rings are different. The quinoline ring systems were identified using a combination of gCOSY and 1D ROESY, as shown in Figure 3.14. Table 3.2 summarises the ^{1}H NMR chemical shifts and *CIS* values for **3.4** and **3.15** in acetonitrile. The negative values for the H8 protons of the coordinated ring (–0.68 ppm) and free ring (–0.63 ppm) indicate similar through–space ring–current effects. It can be clearly seen from the crystal structure described below that both these protons are positioned over adjacent bpy rings. However, the H8 proton (H28A) of the coordinated ring lies directly over the pyridyl N–atom and hence experiences stronger ring–current effect when compared to the free ring (H34A). The H3 proton (8.16 ppm) of the coordinated ring is deshielded due to chelation induced conformational change, whereas the H3' proton (8.87 ppm) (H31A) of the non–coordinated ring is deshielded by the azo N–atom. Similar to the previous complexes, a strongly shielded bpy–H6 proton (7.29 ppm) (H1A) is observed in **3.15** also.

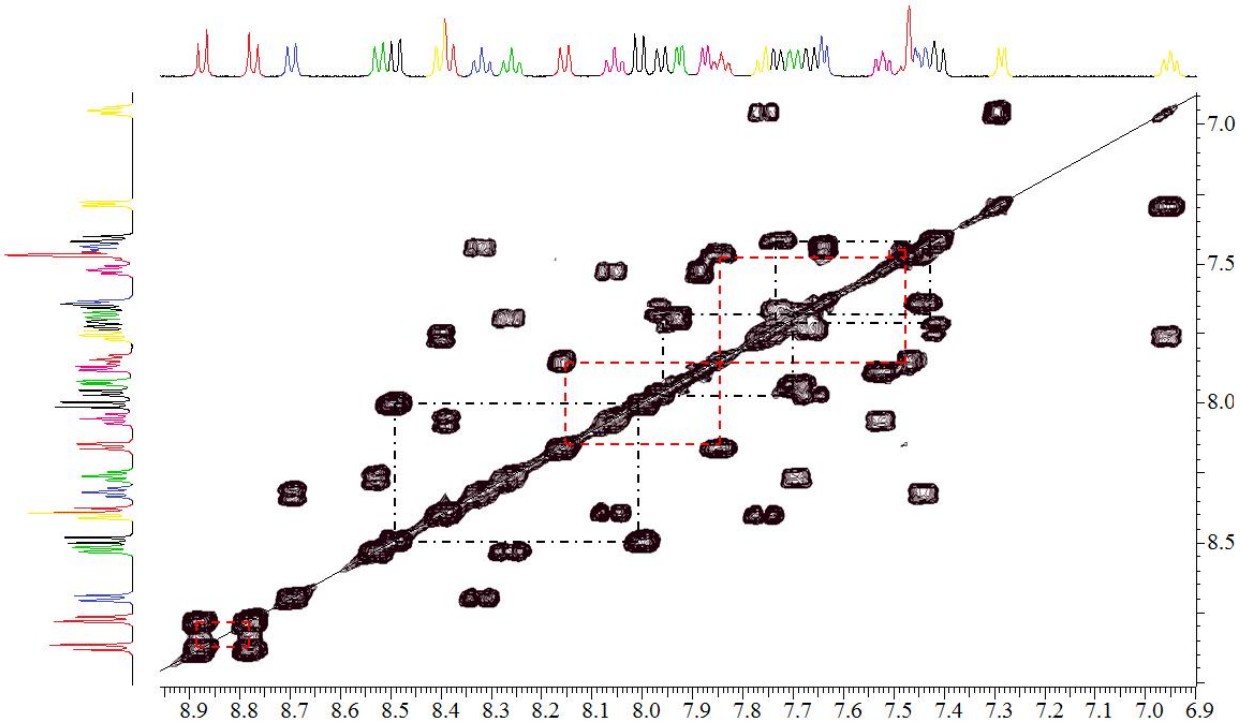

(a)

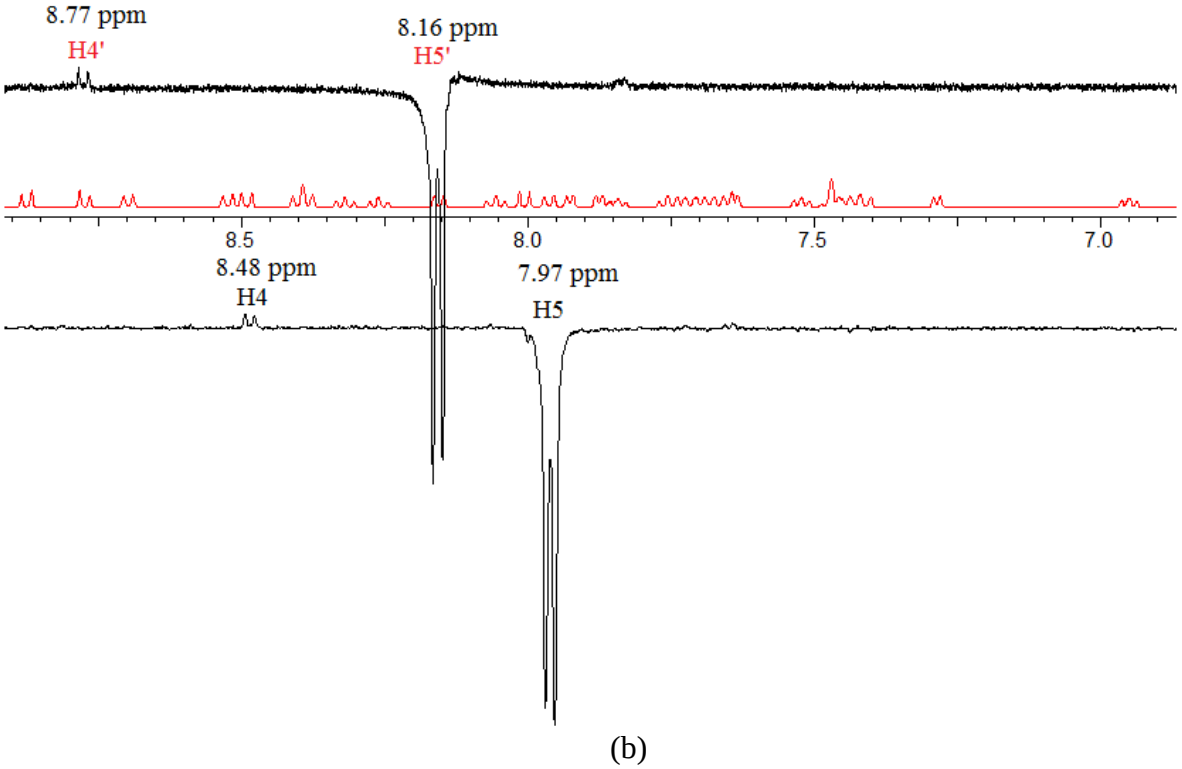

(b)

Figure 3.14. (a) gCOSY and (b) 1D ROESY spectra of **3.15**

Table 3.2. The ^{1}H NMR chemical shifts[a] and *CIS* values[b] of **3.4** and **3.15**

	H3	**H4**	**H5**	**H6**	**H7**	**H8**
3.4	8.09	8.57	8.30	7.92	7.75	8.10
3.15[c](black)[d]	8.16	8.48	7.97	7.66	7.73	7.42
CIS	*+0.07*	*–0.09*	*–0.33*	*–0.26*	*–0.02*	*–0.68*
3.15[e](red)	8.87	8.77	8.16	7.84	7.46	7.47
CIS	*+0.78*	*+0.20*	*–0.14*	*–0.08*	*–0.29*	*–0.63*

[a]In CD_3CN.
[b]*CIS* = $\delta_{complex} - \delta_{ligand.}$
[c]Coordinated ring of **3.4**.
[d]For colours, see Figure 3.12.
[e]Non–coordinated ring of **3.4**.

*Crystal Structure of **3.15***

Vapour diffusion of *n*–hexane into a solution of the complex in acetone gave **3.15** as red needles suitable for X–ray analysis. The complex solved in the monoclinic space group $P2_1/c$. The asymmetric unit contains one full cation with two hexafluorophosphate anions and one acetone molecule, as shown in Figure 3.15. The X–ray structure confirms the mononuclear nature of the complex with one $Ru(bpy)_2$ fragment coordinated to **3.4** using the N_{azo} (N7) and $N_{quinoline}$ (N5) atom. The coordinated quinoline ring is in the same plane as the azo with the torsion angle being 3.3(4)° (N5–C21–N6–N7), however, the non–coordinated ring is twisted with an angle of –37.7(4)° (N6–N7–C30–C31) to avoid non–bonding interactions with the ancillary ligands.

The Ru–N bond lengths are comparable with the previous complexes and once again the Ru–N_{azo} [Ru1–N7 1.957(2) Å] bond distance is the shortest of all. In the molecular packing, each molecule of **3.15** displays weak π – π interactions with an adjacent molecule through the benzene ring of the non–coordinated quinoline ring. Numerous other weaker interactions such as F···HC and acetone O···HC also exist, which stabilise the crystal packing.

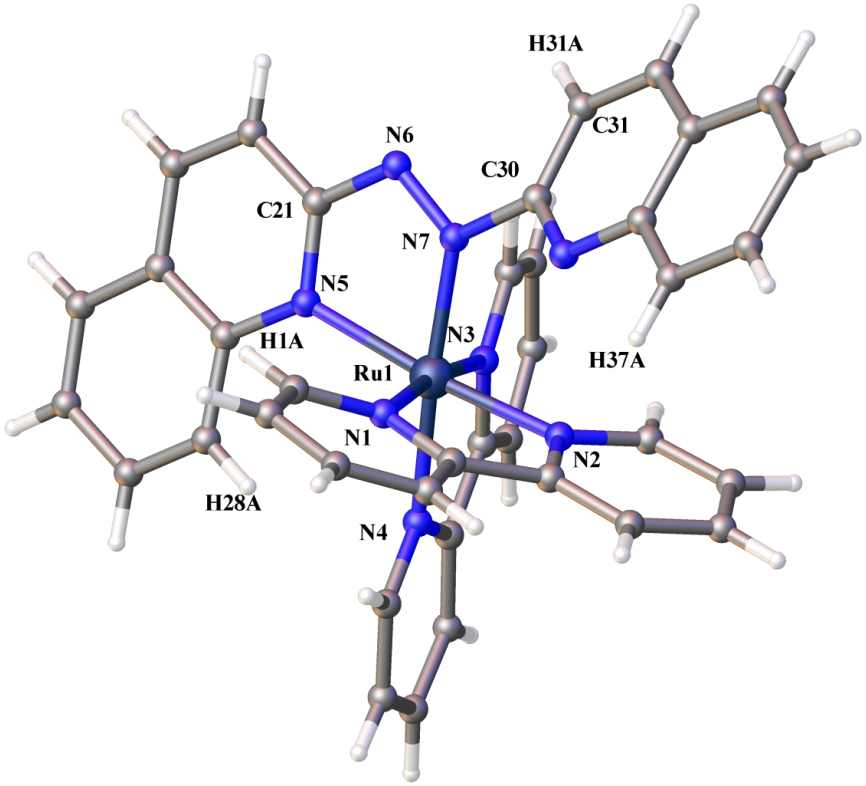

Figure 3.15. The X–ray structure of **3.15** with atom labelling. Counterions and the solvate molecule are omitted for clarity. Selected bond distances (Å): Ru1–N1 2.062(3), Ru1–N2 2.050(3), Ru1–N3 2.077(3), Ru1–N4 2.100(3), Ru1–N5 2.095(3), Ru1–N7 1.957(3), N6–N7 1.307(3). Selected bond angles (°): N7–Ru1–N2 97.91(10), N7–Ru1–N1 91.29(10), N2–Ru1–N1 78.48(11), N7–Ru1–N3 95.91(10), N2–Ru1–N3 97.84(11), N1–Ru1–N3 172.33(10), N7–Ru1–N5 76.31(10), N2–Ru1–N5 174.19(10), N1–Ru1–N5 100.85(10), N3–Ru1–N5 83.49(10), N7–Ru1–N4 173.35(11), N2–Ru1–N4 82.16(10), N1–Ru1–N4 95.23(10), N3–Ru1–N4 77.52(11), N5–Ru1–N4 103.65(10).

*Crystal Structure of **3.16***

A single crystal of **3.16** suitable for X–ray structure analysis was obtained by diffusing diisopropyl ether into an acetonitrile solution of the complex. The complex crystallised in the centrosymmetric triclinic space group *P*–1 with one ruthenium metal, three bidentate ligands, two hexafluorophosphate anions and three acetonitrile molecules in the asymmetric unit.

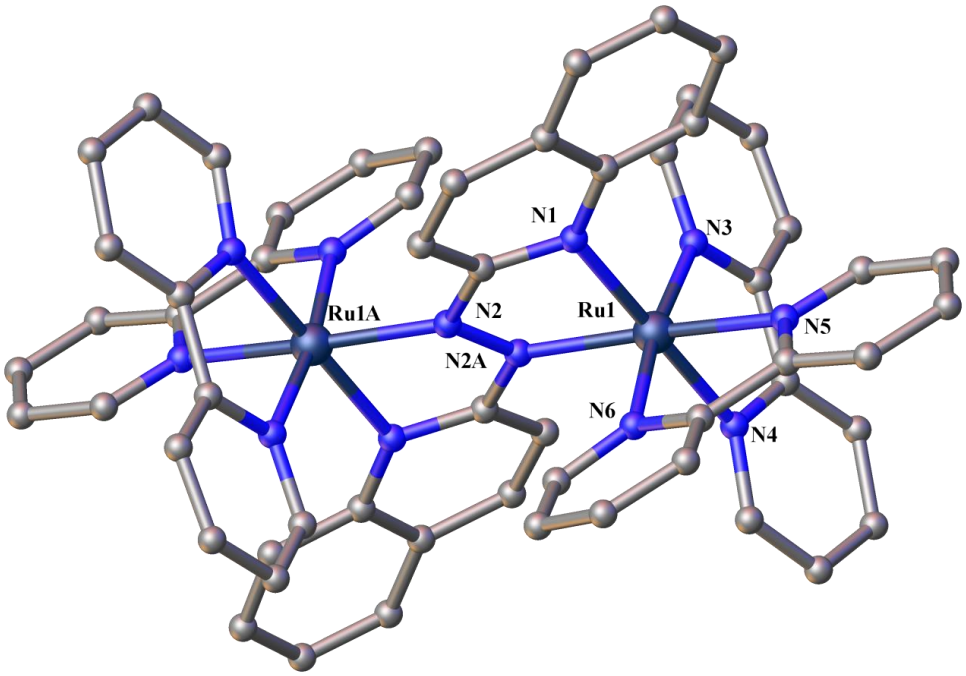

Figure 3.16. A perspective view of **3.16** with atom labelling. Hydrogen atoms, anions and solvate molecules are omitted for clarity. Selected bond distances (Å): Ru1–N1 2.069(3), Ru1–N2A 2.019(3), Ru1–N3 2.069(3), Ru1–N4 2.078(3), Ru1–N5 2.098(3), Ru1–N6 2.084(3), N2–N2A 1.346(6). Selected bond angles (°): N1–Ru1–N3 100.63(13), N1–Ru1–N4 179.26(13), N1–Ru1–N5 97.52(13), N1–Ru1–N6 83.44(13), N2A–Ru1–N1 76.55(13), N2A–Ru1–N3 94.95(13), N2A–Ru1–N4 103.08(13), N2A–Ru1–N5 169.26(13), N2A–Ru1–N6 92.20(13), N3–Ru1–N4 78.74(14), N3–Ru1–N5 94.94(13), N3–Ru1–N6 172.43(13), N4–Ru1–N5 82.94(13), N4–Ru1–N5 97.25(14), N6–Ru1–N5 78.12(13).

The molecular structure and selected bond parameters are shown in Figure 3.16. The crystallised complex is the *meso* (ΔΛ) isomer in which **3.4** acts as a non–planar bridge with the intramolecular Ru···Ru distance being 4.784(7) Å. Ligand **3.4** within the complex exhibits the usual s–*cis*/*E*/s–*cis* binding mode, chelating each ruthenium atom through azo and quinoline nitrogen donors. The torsion angle due to the twist is 10.122(2)°. The Ru–N distances are in the normal range with Ru–N_{azo} [Ru1–N2A 2.019(3) Å] being the shortest, arising from strong π back–bonding into the azo group from the Ru metal centre. The N_{azo}–N_{azo} [N2–N2A 1.346(6) Å] distance is in the normal range (1.26 – 1.37 Å] as observed in previous complexes containing non–reduced azo ligand. The crystal packing involves numerous weak interactions between the various components, such as C–H···π (*ca.* 3.15 Å), C–H···F (> 2.5 Å) and N··H–C (> 2.6 Å).

3.3.3. Ruthenium(II) Complexes of 3.5

In quinazoline subunits, shown in Figure 3.17a, the benzene ring fused to the d–bond of the pyrimidine ring distinguishes the nitrogen atoms into sterically 'more hindered' and 'less hindered'. This aspect of quinazoline was previously explored in our group using 2,2'–biquinazoline.[70] As shown in Figure 3.17b, the mononuclear complexes of 2,2'–biquinazoline with Pd(I), Cu(I), Cu(II) and Cd(II) were found to chelate using the less hindered N–atoms.

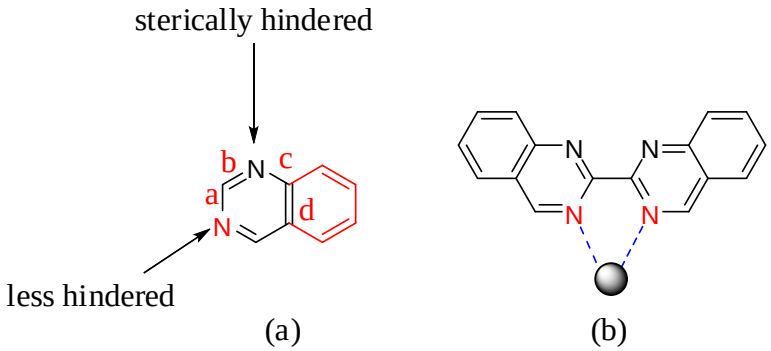

Figure 3.17. (a) Two types of nitrogen atoms in quinazoline and (b) preferred coordination in the complexes of 2,2'–biquinazoline

Ligand **3.5** can chelate and bridge metal centres using the azo N–atom and the more or less sterically hindered alternatives, as shown in Figure 3.18. To investigate the coordination chemistry of **3.5**, ruthenium(II) complexes were synthesised.

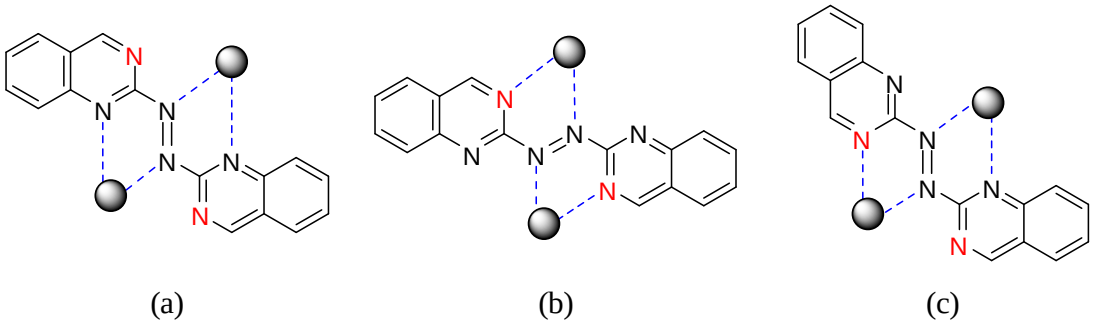

Figure 3.18. Possible coordination modes of **3.5**

Reaction of **3.5** with $[Ru(bpy)_2Cl_2]$ in aqueous ethanol, as shown in Scheme 3.13, gave a mixture of **3.17** and **3.18** in a 1:10 ratio. The complexes were separated by ion exchange chromatography on a Sephadex C–25 column using a 0.1 mol L^{-1} sodium chloride solution.

These complexes were characterised as the mononuclear species $[(bpy)_2Ru(\mathbf{3.5})](PF_6)_2$ by ESI–MS.

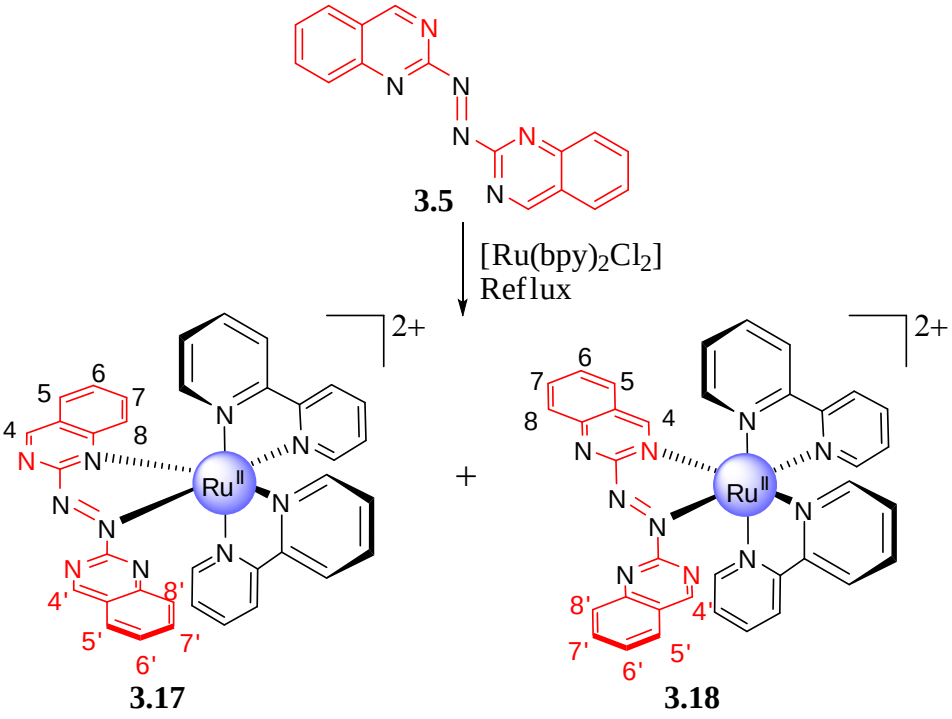

Scheme 3.13

The complex $[(bpy)_2Ru(\mathbf{3.5})]^{2+}$ was found to exist as a mixture of two isomers from the ^{1}H NMR spectrum as shown in Figure 3.19. Interestingly, the isomers exhibit different colours and were carefully separated by ion exchange chromatography into reddish orange **3.17** and dark red **3.18** fractions. In **3.17**, chelation to the ruthenium metal centre occurs *via* the sterically hindered N–atom. The complex **3.18** (dark red), involving chelation to the metal centre through the less hindered N–atom, was obtained as the major product.

Table 3.3 lists the ^{1}H NMR chemical shifts and *CIS* values for **3.5** ($CDCl_3$), **3.17** and **3.18** in CD_3CN. In **3.17**, the H8 proton (7.31 ppm) experiences maximum anisotropy due to the adjacent bpy rings. A similar, strongly shielded proton was observed for the coordinated quinoline ring in **3.15**, as the coordinated quinazoline ring in **3.17** behaves similarly to the quinoline ring in **3.15**. However, in **3.18** the H8 (8.13 ppm) and H8' (8.11 ppm) protons experience similar shielding effects. In **3.17**, the H4 proton (9.86 ppm) of the coordinated ring is strongly deshielded due to coordination induced changes in the conformation of the ligand. But in **3.18**, the H4 proton (9.02 ppm) experiences through–space anisotropy ring–current due to the adjacent terminal ligands. In **3.17** and **3.18**, the H4' protons (9.36 ppm and 9.37 ppm respectively) of the non–coordinated ring exhibit similar chemical shifts.

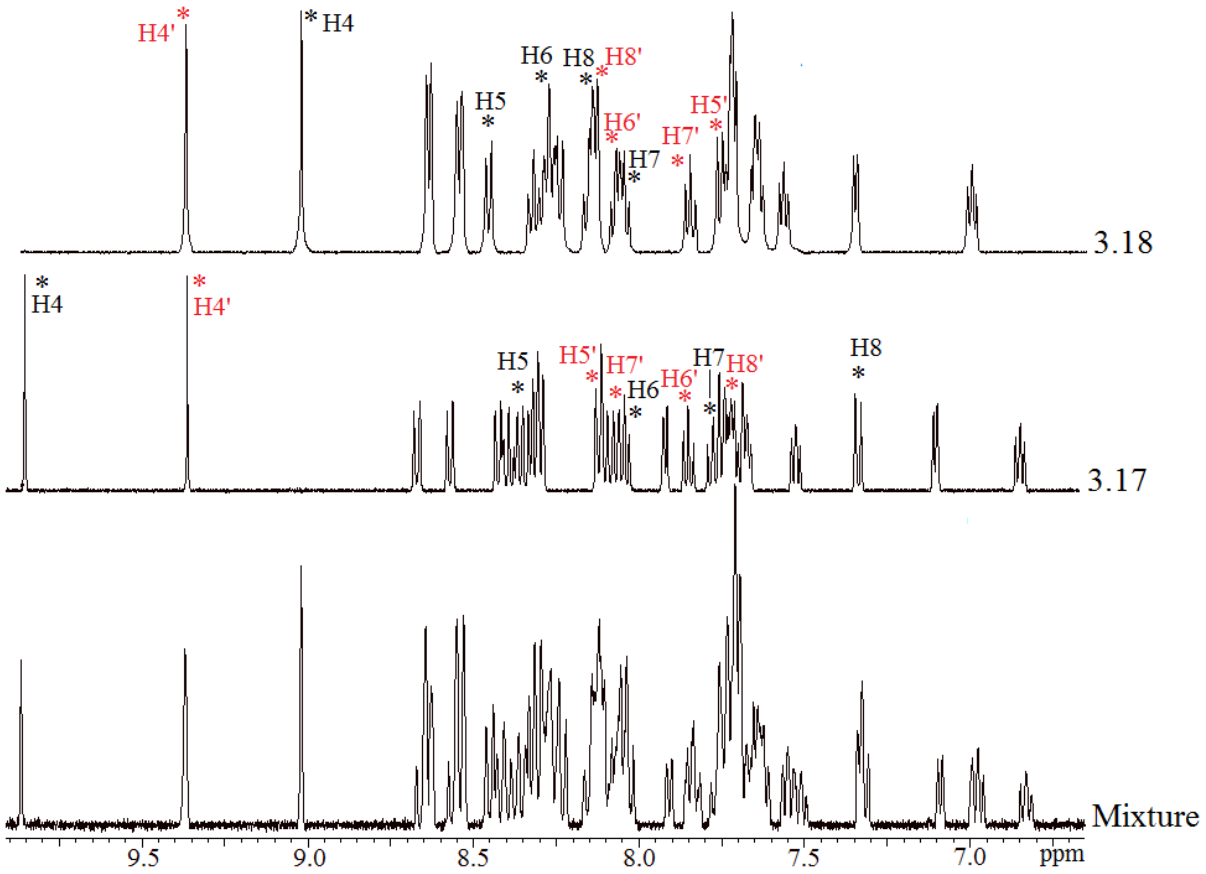

Figure 3.19. [1]H NMR of an approximately 1:1 mixture and the two purified isomers, **3.17** and **3.18** after separation.

Table 3.3. The [1]H NMR chemical shifts and approximate *CIS* values of **3.5**[a], **3.17**[b] and **3.18**[b].

	H4	**H5**	**H6**	**H7**	**H8**
3.5	9.65	8.11	8.05	7.81	8.31
3.17[c]	9.86	8.35	8.03	7.75	7.31
CIS	*+0.21*	*+0.24*	*–0.02*	*–0.06*	*–1.00*
3.17[d]	9.36	8.12	7.83	8.06	7.74
CIS	*–0.29*	*+0.01*	*–0.22*	*+0.25*	*–0.57*
3.18[c]	9.02	8.45	8.26	8.03	8.13
CIS	*–0.63*	*+0.34*	*+0.21*	*+0.22*	*–0.18*
3.18[d]	9.37	7.74	8.04	7.83	8.11
CIS	*–0.28*	*–0.37*	*–0.01*	*+0.02*	*–0.20*

[a]In chloroform–*d*.
[b]In acetonitrile–d_3.
[c]Coordinated ring of **3.5**.
[d]Non–coordinated ring of **3.5**.

*Crystal Structure of **3.17***

Crystals of **3.17** were obtained by vapour diffusion of petroleum ether into a solution of the complex in acetone. The complex crystallises in the monoclinic space group $P2_1/c$. The asymmetric unit contains one ruthenium metal, two bipyridine units, one ligand **3.5** with two hexafluorophosphate anions and one acetone solvate molecule, as shown in Figure 3.20. The X–ray crystal structure clearly verifies that the bridging ligand **3.5** within the complex of **3.17** is coordinated to the ruthenium atom using the azo nitrogen atom (N8) and the more hindered N–atom (N6).

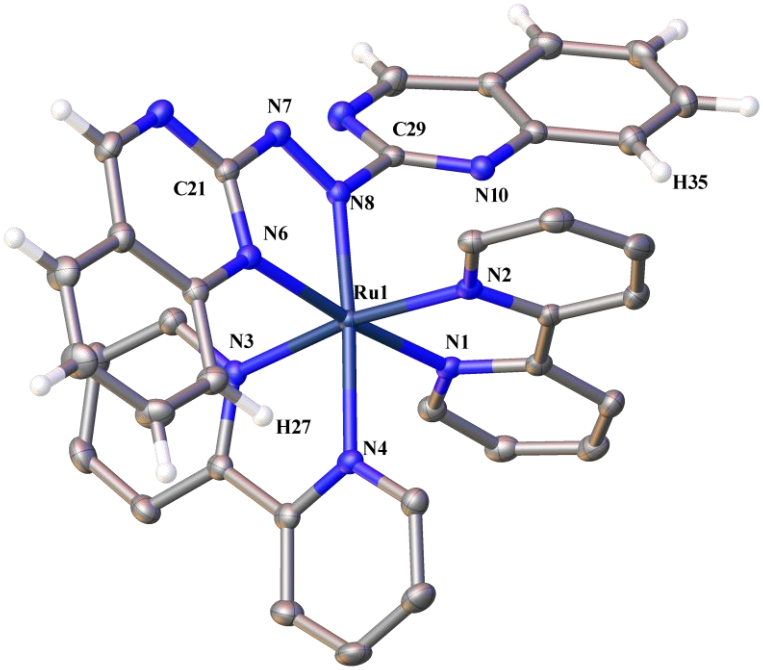

Figure 3.20. The X–ray structure of **3.17** with the bpy hydrogen atoms, counterions and solvate molecules omitted for clarity. Selected bond distances (Å): Ru1–N1 2.055(2), Ru1–N2 2.066(2), Ru1–N3 2.079(2), Ru1–N4 2.106(2), Ru1–N6 2.094(2), Ru1–N8 1.954(2), N7–N8 1.292(2). Selected bond angles (°): N1 Ru1–N2–78.48(6), N1–Ru1–N3 96.94(6), N1–Ru1–N4 80.87(6), N1–Ru1–N6 173.60(6), N2–Ru1–N3 171.18(6), N2–Ru1–N4 94.08(6), N2–Ru1–N6 100.65(6), N3–Ru1–N4 77.66(6), N3–Ru1–N6 84.73(6), N6–Ru1–N4 105.53(6), N8–Ru1–N1 97.99(6), N8–Ru1–N2 92.10(6), N8–Ru1–N3 96.03(6), N8–Ru1–N4 173.35(6).

Once again, the non–coordinated ring twists with a torsion angle of 48.8(2)°, while the coordinated ring is in the same plane as the azo group [N6–C21–N7–N8 2.4(2)°]. The ruthenium geometry is consistent with the Ru–N_{py} bond lengths ranging from 2.05–2.10 Å.

The stronger π back–bonding from the Ru centre to the azo group is evident from the shortening of the bond distance for Ru–N_{azo} [Ru1–N8 1.954(2) Å] compared to that of Ru–$N_{quinazoline}$ [Ru1–N6 2.094(2) Å]. The fused benzene ring of the non–coordinated ring in each molecule of **3.17** displays face to face π – π interactions with an adjacent molecule and edge to face interactions with a bpy ring.

As hypothesized from the ^{1}H NMR of **3.17** (Figure 3.19), the H8 proton (H27) lies directly over the pyridyl N–atom of an adjacent bpy ring, whereas the H8' proton (H35) is not affected much by the coordination. Unfortunately, attempts to grow crystals of **3.18** were unsuccessful.

The dinuclear complex was synthesised by reacting **3.5** with $[Ru(bpy)_2Cl_2]$ in aqueous ethanol at 90 °C for 3 days, as shown in Scheme 3.14. Interestingly, a mixture of diastereoisomers was obtained.

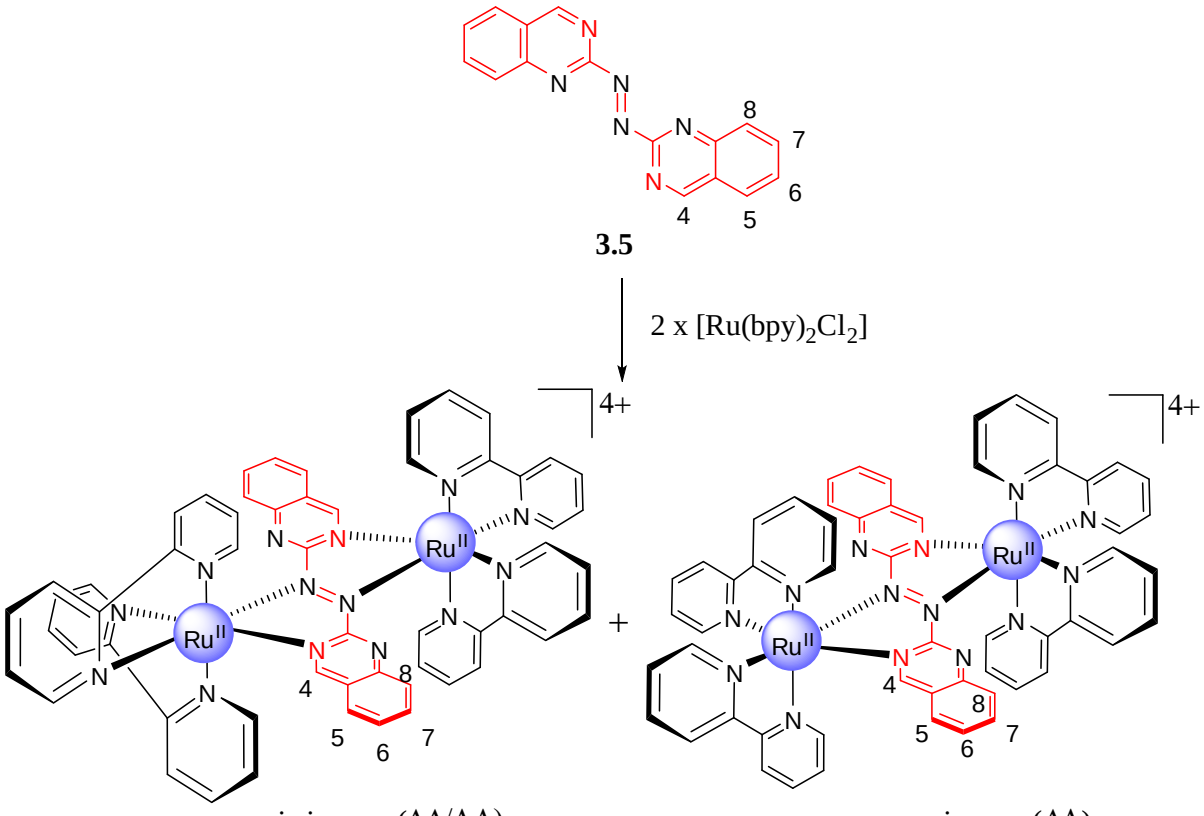

Scheme 3.14

The diaseteroisomer separation was achieved by cation–exchange chromatography on SP Sephadex C–25 support using 0.1 – 0.5 mol L^{-1} sodium tosylate solution as the eluent. The diastereoisomers differ in terms of the relative orientation of the terminal ligands and therefore interact differentially with the eluent anions.[65] In this case, the minor isomer **3.19** (*racemic*) eluted first followed by **3.20** (*meso*) as the major isomer. The structures of the two isomers were assigned by X–ray crystallography below. Usually, for such complexes, the *meso* isomer elutes first, however, in the case of 'stepped–parallel' bridging ligands, sometimes the reverse is possible.[84],[93]

Table 3.4. The ^{1}H NMR chemical shifts and approximate *CIS*[a] values of **3.5** and **3.20**.

	H4	**H5**	**H6**	**H7**	**H8**
3.5[b]	9.65	8.11	8.05	7.81	8.31
3.20[c]	8.88	8.00	7.93	8.01	6.93
CIS	*–0.77*	*–0.11*	*–0.12*	*+0.20*	*–1.38*

[a] $CIS = \delta_{complex} - \delta_{ligand}$.
[b] In $CDCl_3$.
[c] In CD_3CN.

Unfortunately, the ^{1}H NMR spectrum of **3.19** could not be obtained due to insufficient sample. The ^{1}H NMR spectrum of **3.20** displays 21 non–equivalent proton signals with five different ring environments. Using ^{1}H–^{1}H COSY NMR techniques in combination with 1D TOCSY, it was possible to completely assign the spectrum for **3.20**, as shown in Figure 3.21. The ^{1}H NMR chemical shifts and coordination–induced–shift values of **3.5** and **3.20** are given below in Table 3.4. The H4 (8.88 ppm) and H8 (6.93 ppm) protons of the bridging ligand **3.5** show large upfield shifts. Examination of the crystal structure shown below reveals that this is due to the ring–current of adjacent bpy ligands. In addition, the bpy–H6 proton (7.34 ppm) positioned directly over the pyridyl ring of the bridge shows the greatest difference in chemical shift.

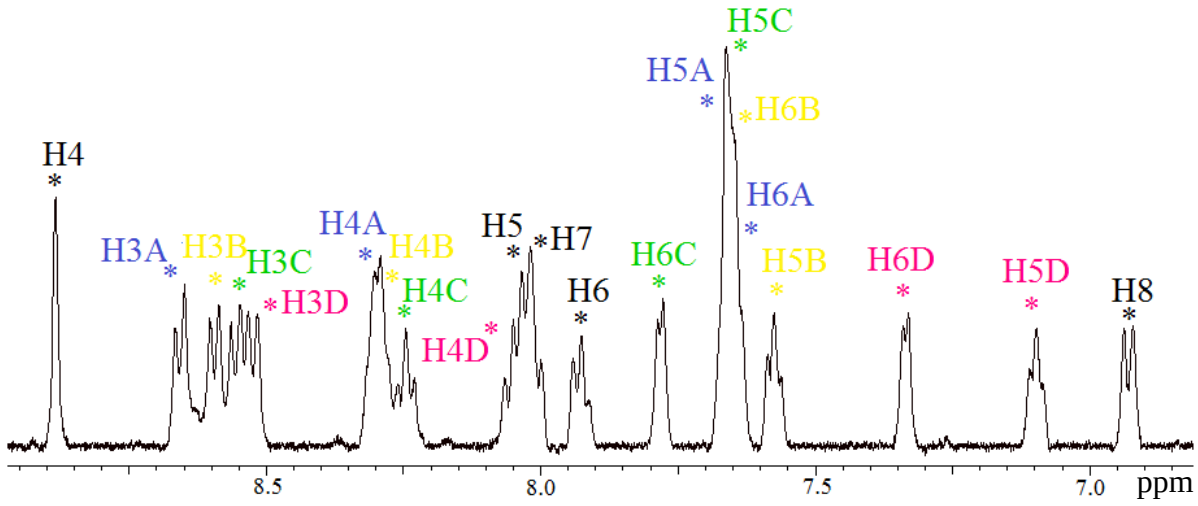

Figure 3.21. The ^{1}H NMR spectrum of **3.20.**

*Crystal Structures of **3.19** and **3.20***

Crystals of **3.19** and **3.20** were obtained by vapour diffusion of diisopropyl ether into an acetonitrile solution of the respective complex. Complex **3.19** crystallised in the monoclinic space group *P*2/*c*, and **3.20** in the monoclinic space group *C*2/*c*. The asymmetric unit of each complex contains half of the dinuclear cation at the crystallographic centre with one full and two half hexafluorophosphate anions and either two or four acetonitrile molecules.

The X–ray structures of **3.19** and **3.20** with atom labelling, shown in Figure 3.22, reveal that the ligand coordinates to the metal centre through the N_{azo} atom (N7) and the less hindered N–atom (N5). Contrary to the mononuclear complexes, no evidence was found for the dinuclear complexes involving the more hindered nitrogen atom. This suggests that **3.5** prefers to form dinuclear complexes using the less hindered nitrogen atoms. In both structures, the ruthenium atom possesses distorted octahedral geometry with comparable Ru–N bond lengths and N–Ru–N bond angles.

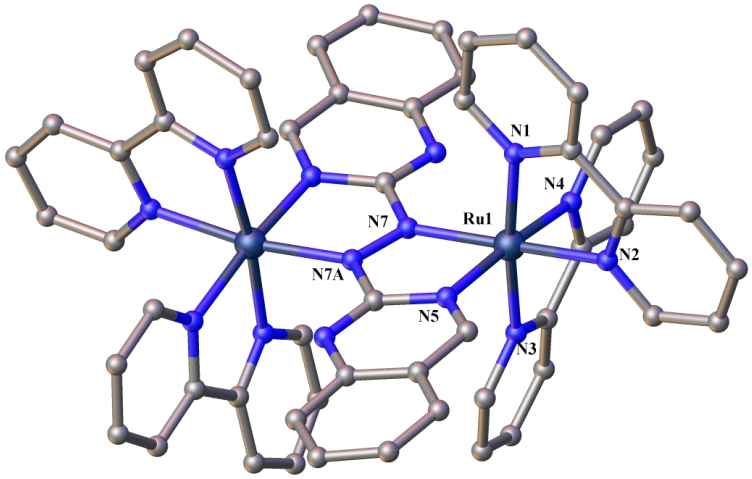

(a)

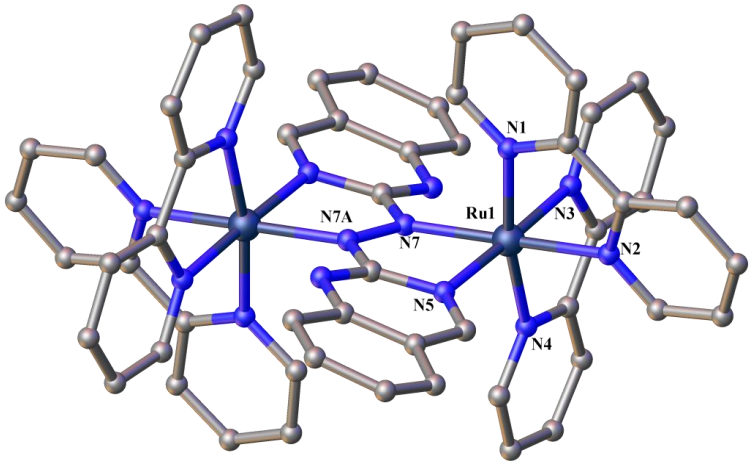

(b)

Figure 3.22. The perspective views of (a) **3.19** and (b) **3.20**. Hydrogen atoms, counterions and solvate molecules are omitted for clarity. Selected bond lengths (Å) and bond angles (°): (**3.19**) Ru1–N1 2.062(3), Ru1–N2 2.074(3), Ru1–N3 2.067(4), Ru1–N4 2.070(3), Ru1–N5 2.039 (3), Ru1–N7 2.015(3), N7–N7A 1.329(7), N2–Ru1–N1 78.02(14), N3–Ru1–N1 173.22(13), N3–Ru1–N2 98.01(13), N4–Ru1–N1 95.45(13), N4–Ru1–N2 86.03(14), N4–Ru1–N3 78.70(13), N5–Ru1–N1 91.28(13), N5–Ru1–N2 96.07(14), N5–Ru1–N3 94.62(13), N5–Ru1–N4 173.23(13), N7–Ru1–N1 96.51(13), N7–Ru1–N2 170.93(13), N7–Ru1–N3 88.11(13), N7–Ru1–N4 101.80(14), N7–Ru1–N5 76.68(14). (**3.20**) Ru1–N1 2.072(4), Ru1–N2 2.082(4), Ru1–N3 2.069(4), Ru1–N4 2.070(4), Ru1–N5 2.061(4), Ru1–N7 2.001(4), N7–N7A 1.336(7), N1–Ru1–N2 78.51(14), N3–Ru1–N1 93.32(14), N3–Ru1–N2 85.28(14), N3–Ru1–N4 79.28(15), N4–Ru1 N1 170.51(15), N4–Ru1–N2 94.83(14), N5–Ru1–N1 85.91(14), N5–Ru1–N2 95.89(14), N5–Ru1–N3 178.44(15), N5–Ru1–N4 101.62(15), N7–Ru1–N1 95.98(14), N7–Ru1–N2 171.36(14), N7–Ru1–N3 101.79(14), N7–Ru1–N4 91.39(15), N7–Ru1–N5 76.95(14).

Perspective views of **3.19** and **3.20** are shown in Figure 3.23, which show very different shapes of the two diastereoisomers. The terminal ligands 'above' and 'below' the plane of the bridging ligand are parallel in **3.19**, whereas in **3.20** they are orthogonal. This accounts for the difference in the association of the diastereoisomers with the eluent anion and the ease of separation by chromatography. Interestingly, in **3.19**, the bridging ligand **3.5** is substantially non–planar as a result of which the two cofacial bpy–pyridine rings are significantly bowed towards one another. The inter–metal separation is 4.826(6) Å for **3.19**. However, in **3.20** the bridging ligand **3.5** acts as a planar bridge with a distance of 4.797(7) Å between the ruthenium atoms.

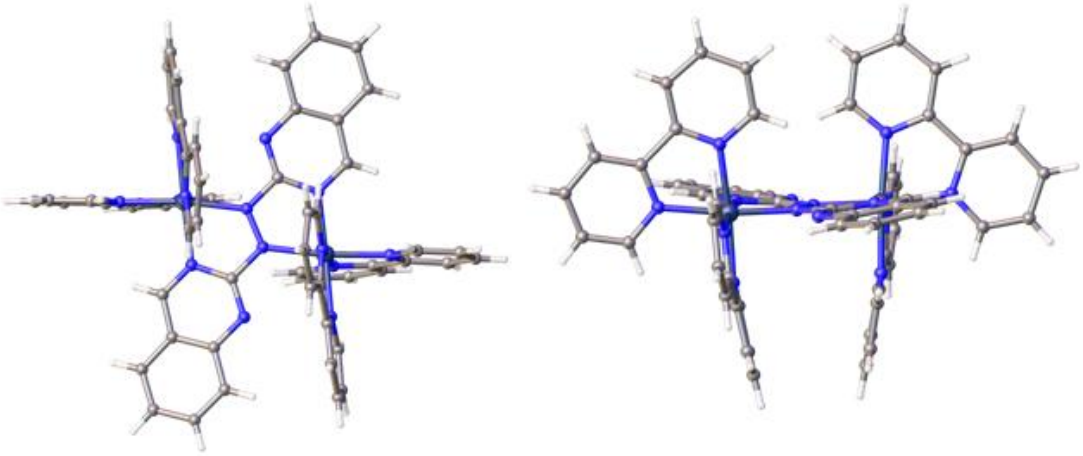

(a) **3.19** (*racemic*)

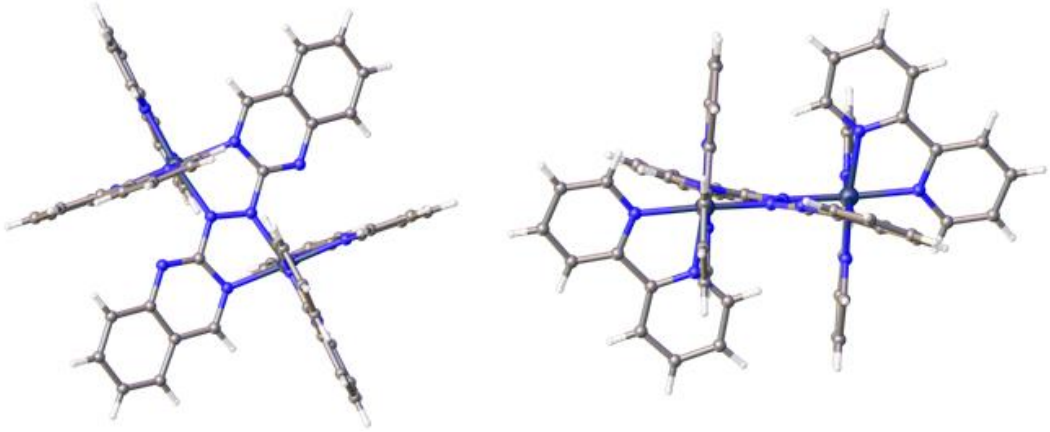

(b) **3.20** (*meso*)

Figure 3.23. Two perspective views of **3.19** and **3.20**, highlighting the different shapes of the two diastereoisomers.

3.3.4. Ruthenium(II) Complex of 3.6

Ligand **3.6** reacts with the ruthenium precursor to give complex **3.21** which was characterised as $[(bpy)_2Ru(\mathbf{3.6})](PF_6)_2$, as shown in Scheme 3.15. Despite being a doubly–chelating ligand all attempts to synthesise the dinuclear complex were unsuccessful.

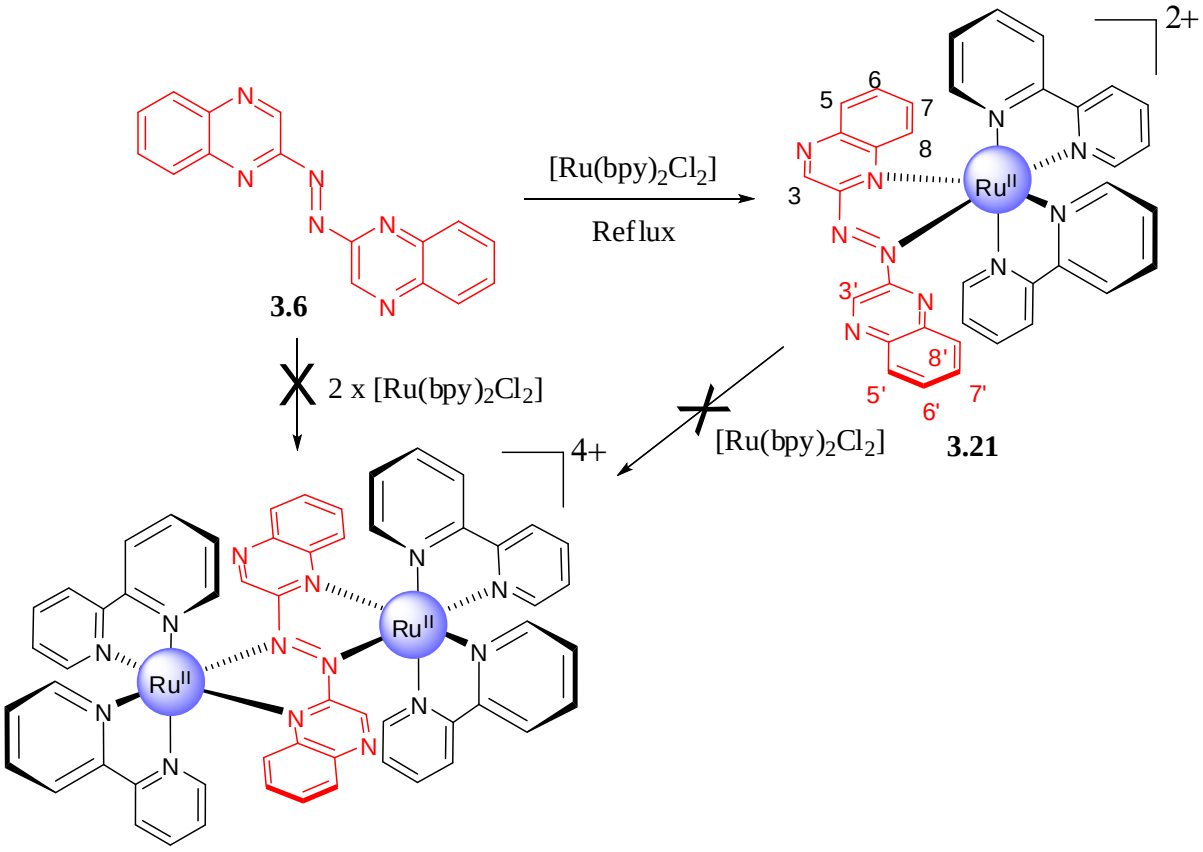

Scheme 3.15

The ^{1}H NMR chemical shifts and the *CIS* values of **3.6** and **3.21** are listed in Table 3.5. The proton labelling employed for the assignment of the ^{1}H NMR spectrum of **3.6** is shown in Scheme 3.15. The ^{1}H NMR chemical shifts were assigned by a combination of spin–spin coupling, ^{1}H COSY spectrum and X–ray crystal structure as shown in Figure 3.25.

Table 3.5. The ^{1}H NMR[a] and *CIS* values[b] of **3.6** and **3.21**.

	H3	**H5**	**H6**	**H7**	**H8**
3.6	9.49	8.34	8.29	8.03	8.01
3.21[c](black)[d]	10.15	8.31	8.09	7.78	7.41
CIS	*+0.66*	*–0.03*	*–0.20*	*–0.25*	*–0.60*
3.21[e](red)	9.75	8.14	7.91	7.55	7.36
CIS	*+0.26*	*–0.20*	*–0.38*	*–0.48*	*–0.65*

[a]In CD_3CN.
[b]$CIS = \delta_{complex} - \delta_{ligand.}$
[c]Coordinated ring of **3.4**.
[d]For colours, see Figure 3.24.
[e]Non–coordinated ring of **3.4**.

Due to the unsymmetrical nature of the coordinated ligand **3.6**, the two quinoxaline rings are non–equivalent and give rise to six different ring systems, two from the ligand **3.6** and four pyridine rings of the bipyridine ligands. The bridging ligand H3 and H3’ protons are directed away from the shielding influence of the adjacent bpy ligands and are assigned as the most downfield resonances at 10.15 ppm and 9.75 ppm, as shown in Figure 3.24. The former proton experiences a relatively greater downfield shift as a result of conformational changes induced due to the coordination to the metal centre. The H8 and H8’ protons of **3.6** are oriented over the plane of the adjacent bpy ligand and are assigned as the upfield resonances at 7.41 ppm and 7.36 ppm, respectively. The upfield resonances at 7.42 ppm and 7.30 ppm are assigned as bpy H6 protons from two different rings as these protons experience shielding effects from ligand **3.6**. The latter experiences a greater upfield shift since it is oriented over the nitrogen atom of the quinoxaline ring, whereas the former bpy H6 proton lies over the azo bridge.

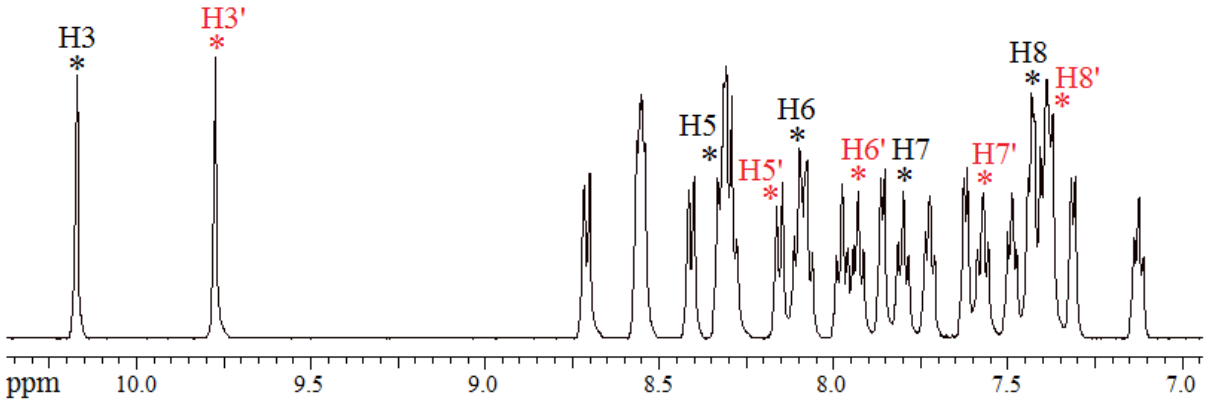

Figure 3.24. The ^{1}H NMR spectrum of **3.6**.

*Crystal Structure of **3.21***

Crystals of **3.21** were obtained by vapour diffusion of petroleum ether into an acetone solution of the complex. The complex crystallises in the monoclinic space group $P2_1/c$, with a full molecule of **3.21**, two hexafluorophosphate anions and two molecules of acetone in the asymmetric unit, as shown in Figure 3.25. The structure confirms the mononuclear nature of **3.21** and the ligand chelates to the ruthenium atom through the azo nitrogen (N8) and a quinoxaline nitrogen (N6). The non–coordinated quinoxaline ring is twisted with the torsion angle being 39.6(6)°.

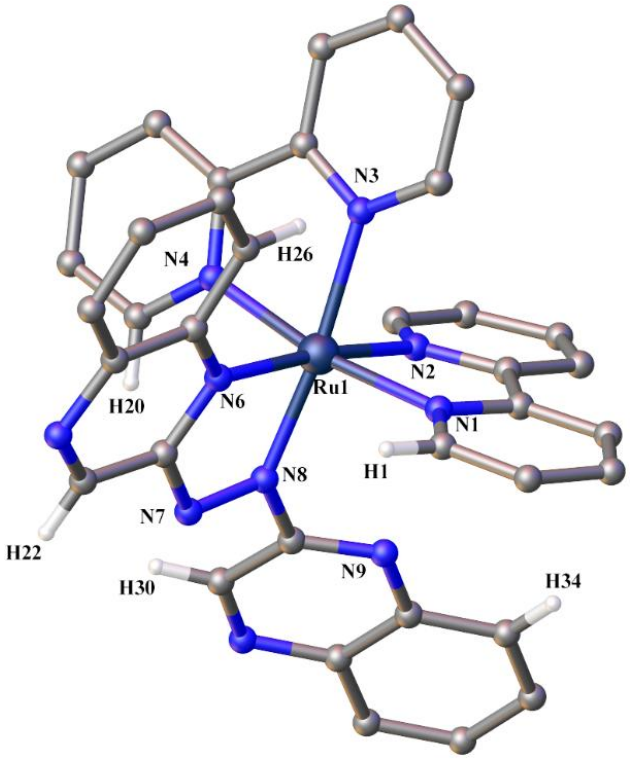

Figure 3.25. The asymmetric unit of **3.21** with the counterions, solvate molecules and the hydrogen atoms, except the ones discussed above omitted for clarity. Selected bond lengths (Å) and bond angles (°): Ru–N1 2.059(4), Ru1–N2 2.062(4), Ru1–N3 2.112(4), Ru1–N4 2.076(4), Ru1–N6 2.084(4), Ru1–N8 1.962(4), N7–N8 1.302(6), N1–Ru1–N2 78.84(16), N1–Ru1–N3 93.35(15), N1–Ru1–N4 169.89(15), N1–Ru1–N6 99.84(16), N2–Ru1–N3 83.54(15), N2–Ru1–N4 94.91(16), N2–Ru1–N6 173.31(15), N4–Ru1–N3 77.94(15), N4–Ru1–N6 87.27(15), N6–Ru1–N3 103.11(15), N8–Ru1–N1 94.30(16), N8–Ru1–N2 97.15(16), N8–Ru1–N3 172.30(16), N8–Ru1–N4 94.37(16), N8–Ru1–N6 76.35(16).

The bonding geometry of the ruthenium atom is slightly distorted with the *trans* N–Ru–N angles *ca.* 171.83(2)°. The bite angles of chelating ligand **3.6** and the terminal bpy ligands with the ruthenium atom are 73.35(16)°, 78.84(16)° and 77.94(15)°. All the Ru–N bond distances and N–Ru–N angles are consistent and comparable with the previously described complexes. The structure confirms the previously discussed ^{1}H NMR (Figure 3.24). As the structure shows, the H3 (H22) and H3' (H30) protons are highly deshielded as they point away from the shielding environment of the bpy rings. The H8 (H26) and H8' (H34) protons are positioned over the bpy rings and experience through–space ring–current anisotropy effects. The structure also shows that two bpy H6 (H1 and H20) protons lie over the plane of the bridge.

3.3.5. Ruthenium(II) Complexes of 3.7

Complexes **3.22** and **3.23** were prepared by reaction of ligand **3.7** with two equivalents of $[Ru(bpy)_2Cl_2]$ in refluxing ethanol/water, as shown in Scheme 3.16. The complexes were isolated as hexafluorophosphate salts.

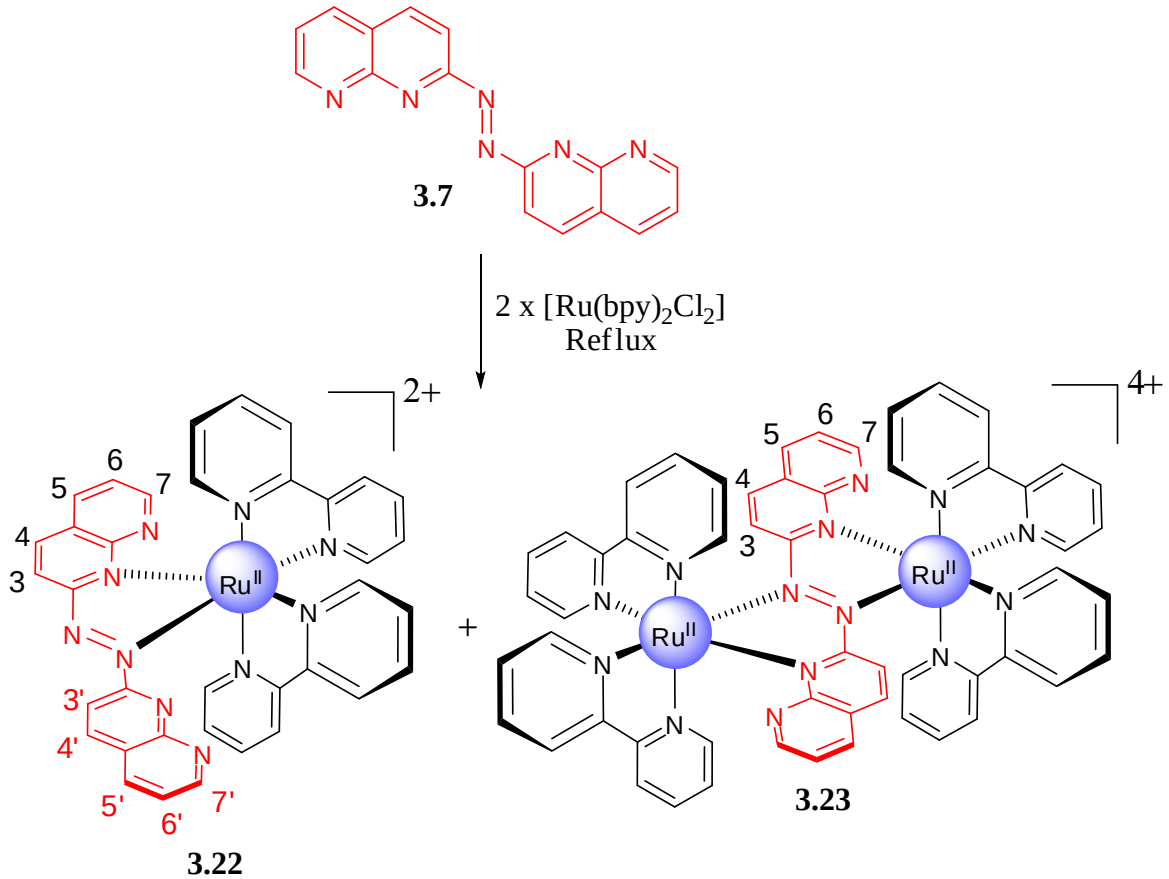

Scheme 3.16

The absence of symmetry in complex **3.22** gives rise to four different pyridyl rings of the bipyridine ligands and ten non–identical proton resonances corresponding to the ligand **3.7** resulting in 26 non–equivalent proton signals, as shown in Figure 3.26. The assignment of proton resonances are made in comparison with complex **3.15** (Section 3.3.2) in combination with spin–spin coupling and a gCOSY experiment. The H3 and H3' protons of ligand **3.7** point away from the shielding environment of the bpy rings, however, the H3' proton (8.93 ppm) is deshielded by the azo nitrogen, while the H3 proton (7.95 ppm) experiences an upfield shift due to conformational changes are therefore assigned as the resonances at 8.93 ppm and 7.95 ppm, respectively The proton resonances at 9.03 ppm and 8.29 ppm, respectively, are assigned as the H7 and H7' protons with the latter experiencing relatively greater through–space ring–current anisotropy since it lies in close proximity to the bpy rings compared to the former. One of the bpy–H5 and H6 protons are significantly deshielded due to the anisotropic interactions with the bridging ligand.

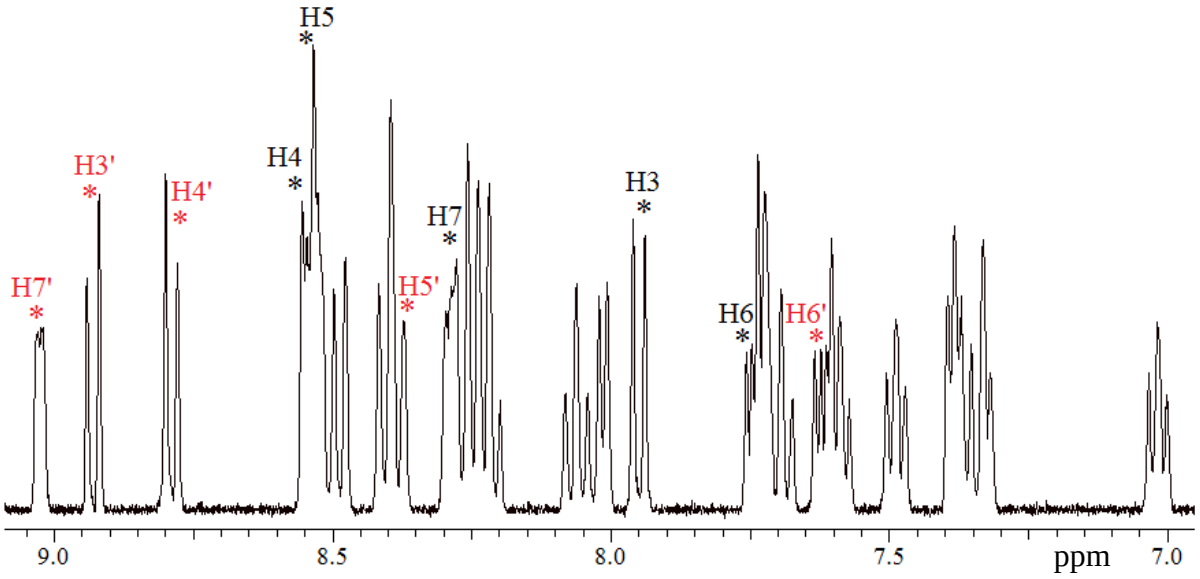

Figure 3.26. The ^{1}H NMR spectrum of complex **3.22** in acetonitrile–d_3.

*Crystal Structure of **3.22***

Vapour diffusion of petroleum ether into an acetone solution of the complex gave red–needles of **3.22** suitable for X–ray crystallography. Complex **3.22** crystallised in the monoclinic space group $P2_1/c$. The asymmetric unit contains one molecule of **3.22**, two hexafluorophosphate anions and one acetone molecule, as shown in Figure 3.27. As seen previously, the non–coordinated naphthyridine ring is twisted with a torsion angle of –

35.4(4)° [N7–N8–C29–C30] with respect to the azo nitrogen atom, to avoid a steric clash between the bpy rings as well as destabilising repulsion with the azo nitrogen atom (N7). The N7–N8 bond length of 1.293(4) is consistent with the N_{azo}–N_{azo} bond lengths in the mononuclear complexes of fused azines discussed above.

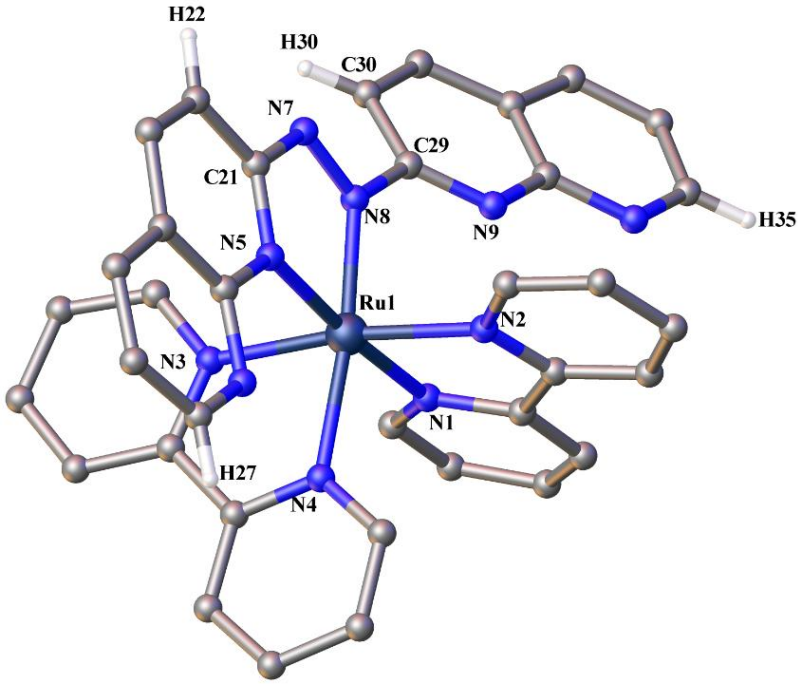

Figure 3.27. The X–ray crystal structure of **3.22**. Counterions, solvate molecules and hydrogen atoms, except the ones shown above are omitted for clarity. Selected bond distances (Å) and bond angles (°): Ru1–N1 2.051(3), Ru1–N2 2.066(3), Ru1–N3 2.088(3), Ru1–N4 2.108(3), Ru1–N5 2.075(3), Ru1–N8 1.968(3), N7–N8 1.293(4), N2–Ru1–N178.45(10), N3–Ru1–N1 98.11(10), N3–Ru1–N2 171.95(10), N4–Ru1–N1 83.78(10), N4–Ru1–N2 94.66(10), N4–Ru1–N3 77.67(10), N5–Ru1–N1 174.31(10), N5–Ru1–N2 100.55(10), N5–Ru1–N3 83.58(10), N5–Ru1–N4 101.90(10), N8–Ru1–N1 98.72(10), N8–Ru1–N2 92.12(10), N8–Ru1–N3 95.61(10), N8–Ru1–N4 173.13(10), N8–Ru1–N5 75.67(10).

The coordination sphere of the ruthenium atom involves coordination to two bpy ligands and one azo ligand **3.7** coordinating through the azo nitrogen and naphthyridine nitrogen atoms. The geometrical parameters for the ruthenium(II) atom are distorted octahedral with the *trans* N–Ru–N angles greater than 171°. As usual, the Ru–N_{azo} bond distance at 1.968(3) Å [Ru1–N8] is significantly shorter than the remaining average Ru–N bond distance of 2.078(3) Å. All the Ru–N bond distances and N–Ru–N bond angles are similar and comparable with the previous complexes.

3.3.6. Ruthenium(II) Complexes of 3.8

The reaction of **3.8** with two equivalents of $[Ru(bpy)_2Cl_2]$ in ethanol/water gave a red solution from which complex **3.24** was isolated as the hexafluorophosphate salt in reasonably good yield (Scheme 3.17). Attempts to synthesise the dinuclear complex were unsuccessful.

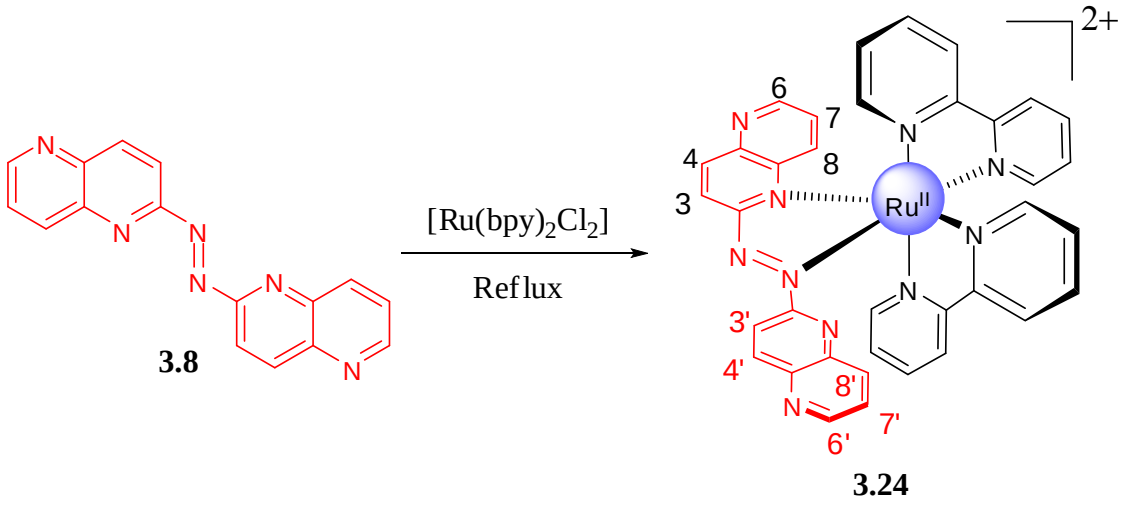

Scheme 3.17

The assignment of the ^1H NMR spectrum shown in Figure 3.28 was established by using ^1H–^1H COSY (Figure 3.29) and 1D ROESY spectra and by comparison with the previous complexes **3.15**, **3.17** and **3.18**. Four pyridine ring environments for the two bipyridine rings and two sets of three coupled protons and two sets of coupled doublets for the ligand **3.8** are observed. The bpy–H5 and H6 protons positioned over the plane of the ligand **3.8** experience maximum anisotropic interactions and are assigned as the upfield resonances at 6.98 ppm and 7.28 ppm, respectively. Unlike the previous fused azine complexes, two pyridyl–H6 protons (9.19 and 9.01 ppm) from two different bpy rings point away from the shielding influences of the adjacent rings and move downfield. Once again, the H8 and H8' protons are oriented over the plane of the adjacent bpy ligand and are assigned as the most upfield resonances at 7.70 ppm and 7.77 ppm, respectively.

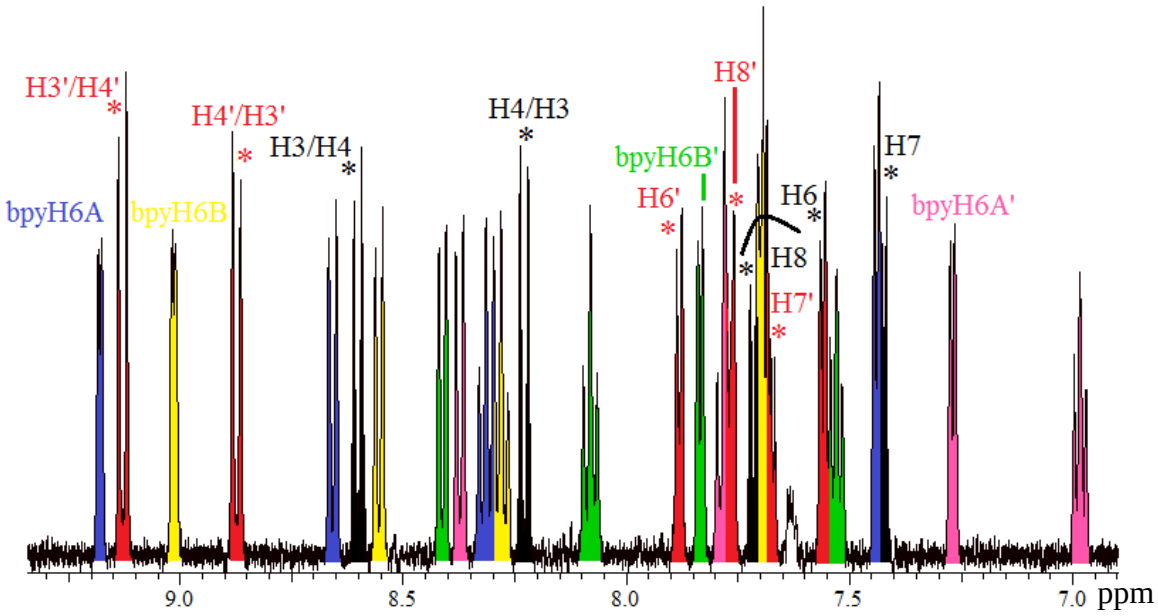

Figure 3.28. The ^{1}H NMR spectrum of **3.24** showing the different ring systems.

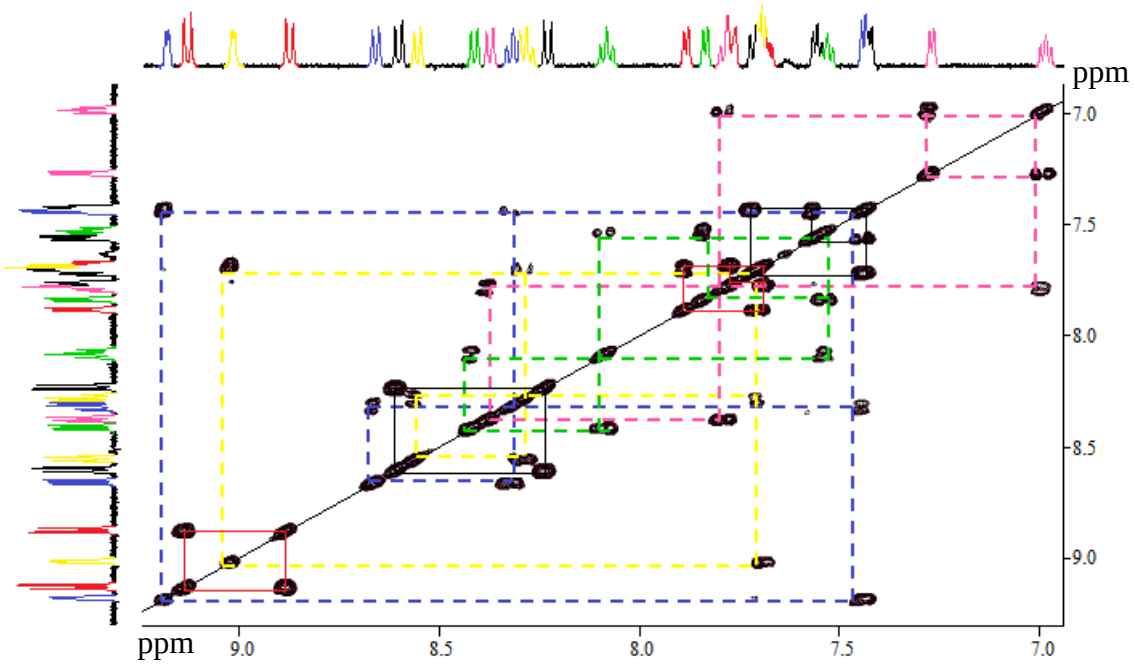

Figure 3.29. The gCOSY spectrum of complex **3.24.**

3.4. Electronic Absorption Spectroscopy

The electronic absorption spectra of the mononuclear complexes were recorded in acetonitrile and are shown in Figure 3.30. In Chapter 2, substitutions on the azopyridines did not have a profound effect on the Ru(dπ) → azo(π*) transitions in the subsequent complexes, however, the ligands discussed in this chapter show significant effects in the MLCT transitions. The complexes exhibit MLCT absorptions in the visible region arising from transitions to bpy and the azo ligand. The lowest energy absorptions are assigned as the Ru(dπ) → azo(π*) transitions due to the better π–accepting nature of the azo ligands. These complexes also display intense bands in the UV region arising from ligand–centered π → π* transitions. Table 3.6 lists the spectral data and extinction coefficients of the metal–to–ligand charge transfers.

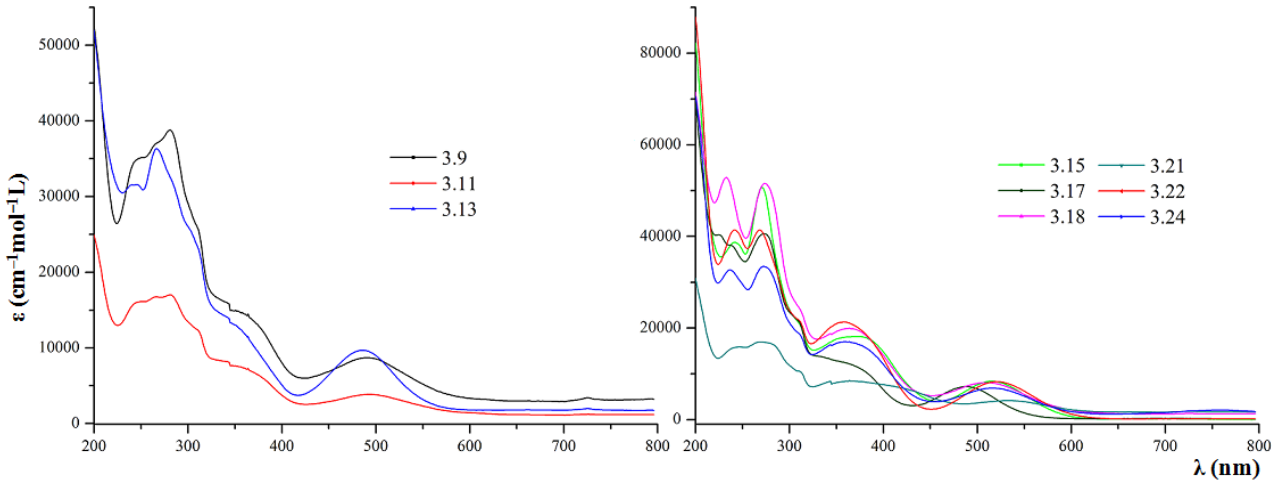

(a) (b)

Figure 3.30. The electronic absorption spectra of the mononuclear complexes.

When compared to the azobispyridine complex **2.7**, the pyrimidine–complexes **3.9**, **3.11** and **3.13** exhibit a slight blue–shift, whilst a red–shift in the lowest energy MLCT was observed in complexes containing fused aromatic azines **3.4** – **3.8** (Table 3.6). Although pyrimidines are known to be better π–acceptors than pyridines due to the relative energy of their π*–orbital,[271] the blue–shift indicates that the LUMO in these complexes is centered on the azo group rather than the pyrimidines. In the fused azine complexes, the non–coordinating nitrogen atoms as well as the extended conjugation influences the MLCT absorptions. Among the quinazoline isomers **3.17** and **3.18**, the former exhibits a blue–shift in the lowest energy MLCT probably, due to the steric strain involved in the metal–ligand

framework which disrupts the conjugation. Complex **3.21** displays a substantial red–shift at ~ 540 nm as pyrazines are better π–acceptors and interact more strongly on coordination.[271],[272] The MLCT absorptions arising from the transitions into the bpy ligands, however, do not show a noticeable change in these complexes.

Table 3.6. The absorption spectral data[a] of the mononuclear complexes.

Mononuclear Complexes	**MLCT/nm (ε/Lmol^{-1}cm^{-1})**		**LC/nm**
	Ru(dπ) → azo(π*)	Ru(dπ) → bpy(π*)	π → π*
2.7	508 (8250)	368 (11100)	279, 243
3.9	493 (8690)	368 (14500)	316, 285, 269, 248
3.11	497 (3840)	368 (7260)	314, 285, 269, 249
3.13	491 (9680)	368 (11500)	313, 271, 247
3.15	519 (8390)	379 (18200)	313, 275, 250
3.17	493 (7220)	361 (12600)	314, 277, 243, 229
3.18	513 (8060)	368 (20000)	316, 277, 236
3.21	540 (4150)	372 (8390)	316, 280, 246
3.22	524 (8290)	363 (21300)	313, 268, 245
3.24	520 (6890)	368 (17100)	277, 241

The UV/Visible spectra of the dinuclear complexes also measured in acetonitrile are shown in Figure 3.31 and the absorption data are summarised in Table 3.7. A colour change as well as red–shift in the MLCT is observed upon coordination to a second metal centre. All the complexes exhibit high energy absorption bands (λ below 320 nm) arising from intra–ligand transitions (π → π*). Unlike the azobispyridine complexes in Chapter 2, these complexes exhibit absorption bands arising from a MLCT transition Ru(dπ) → azo (π*) at higher energy (λ = 600 – 690 nm), except complex **3.20**, where the long wavelength maximum is greater than 800 nm. The MLCT band arising due to the transitions from Ru(dπ) to π* of bpy above 380 nm is similar to the azobispyridine complexes. In complexes **3.10** and **3.12**, a blue–shift in the MLCT absorption bands corresponding to Ru(dπ) → azo(π*) transition was observed. Complex **3.16** displays a red–shift at 685 nm compared to the pyrimidine–based ligands as a result of increased conjugation in the ligand backbone.

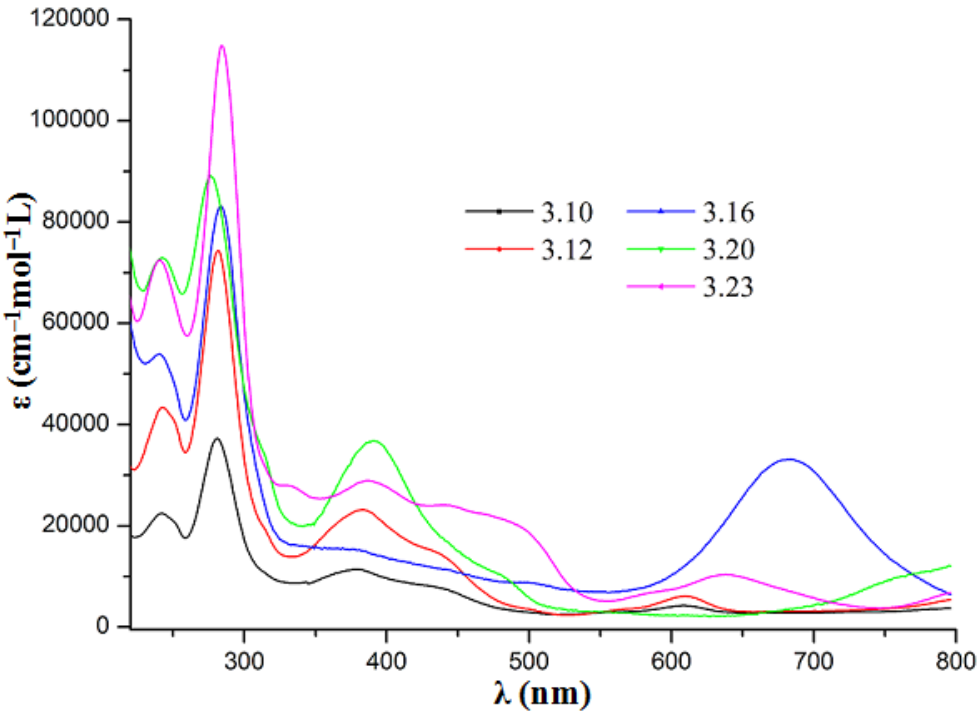

Figure 3.31. The UV/Visible absorption spectra of the dinuclear complexes in acetonitrile.

Table 3.7. UV/Visible absorption data[a] of the dinuclear complexes.

Dinuclear Complexes	**MLCT/nm (ε/Lmol^{-1}cm^{-1})** Ru(dπ) → azo(π*)	**λ/nm (ε/Lmol^{-1}cm^{-1})**
3.10	616(4173)	444(7583), 384(11376), 284(37169), 245(2241)
3.12	614(6103)	441(14506), 387(23175), 285(74312), 247(43335)
3.14	658(19156)	493(32684), 389(45451), 287(177575), 244(139027)
3.16	685(33149)	382(15333), 287(83093), 244(53931)
3.20	> 800	397(36719), 280(89123), 247(72861)
3.23	641 (10339)	498(19829), 392(28865), 289(114698), 244(72435)

[a] In acetonitrile.

3.5. Electrochemistry

The differential pulse voltammograms of some of the mononuclear complexes are shown in Figure 3.32. The redox potentials, summarised in Table 3.8, suggests that compared to the azobispyridine complex **2.7**, the complexes are more difficult to oxidise and easier to reduce. This could be as a result of replacing the pyridine rings with other N–containing rings, which facilitate effective π back–bonding in the subsequent complexes, and as a consequence results in an increased metal–centered oxidation potential.

The differential pulse voltammogram for all the complexes show reversible ruthenium–centered (Ru^{II}/Ru^{III}) oxidation. The oxidation potential in pyrimidine complexes **3.9**, **3.11** and **3.13** is positively shifted with respect to complex **2.7**. The electron–donating methyl groups in ligand **3.3** did not have an effect on the metal–centered oxidation in complex **3.13**. Replacement of the pyrimidines by fused N–heterocyclic rings in the azo ligands results in a cathodic shift of the metal–centred oxidation potentials for **3.15**, **3.18** and **3.22**. Complexes **3.21** and **3.24**, however, display oxidation potentials similar to the pyrimidine complexes.

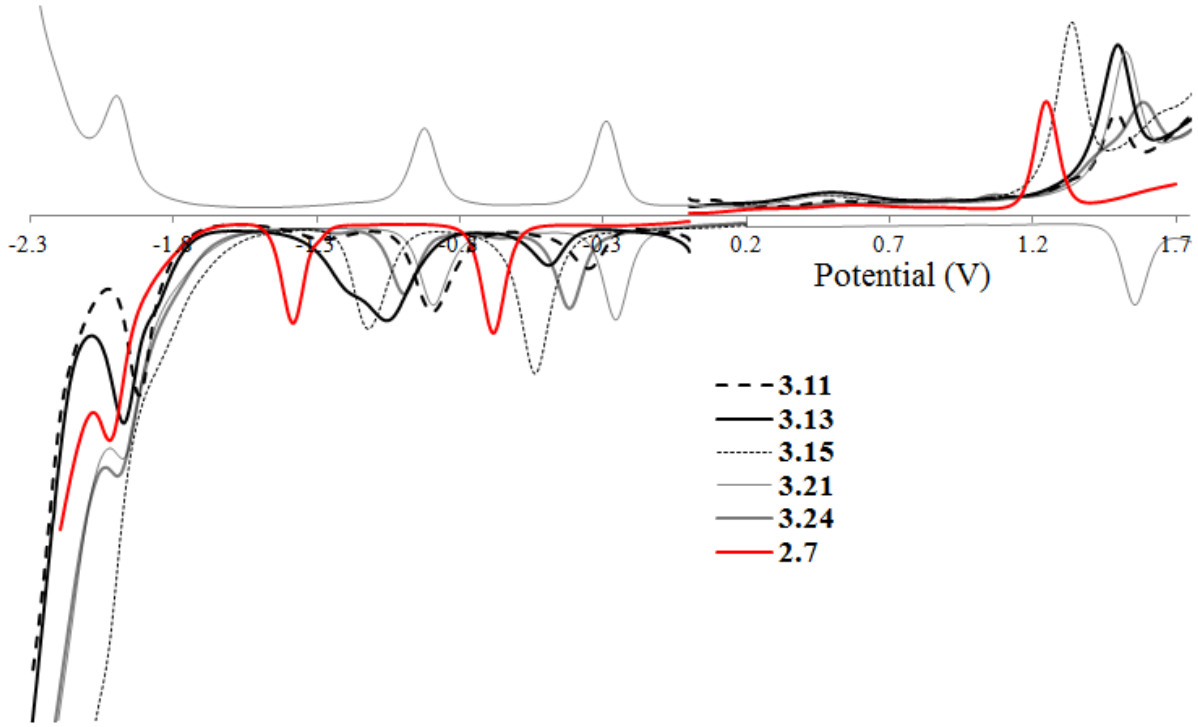

Figure 3.32. Differential pulse voltammograms of **2.7**, **3.11**, **3.13**, **3.15**, **3.21** and **3.24** in CH_3CN/0.1M $[(n\text{–}C_4H_9)_4]ClO_4$.

Table 3.8. Redox potentials[a,b] of the mononuclear complexes.

Mononuclear Complexes	$\Delta E_{ox/red}$[c] V	$E_{1/2ox1}$	$E_{1/2red1}$	$E_{1/2red2}$	$E_{1/2red3}$
2.7	1.95	+1.24	–0.71	–1.42	–2.03
3.9	1.88	+1.48	–0.40	–0.96	–1.96
3.11	1.84	+1.49	–0.35	–0.90	–1.92
3.13	2.04	+1.50	–0.54	–1.09	–2.00
3.15	1.88	+1.34	–0.54	–1.12	–2.05
3.17	1.96	+1.50	–0.46	–0.89	–
3.18	1.85	+1.31	–0.54	–1.04	–1.95
3.21	1.82	+1.53	–0.29	–0.92	–1.99
3.22	1.88	+1.38	–0.50	–1.00	–2.14
3.24	1.99	+1.58	–0.41	–0.99	–2.00

[a] In V *vs* $Ag/AgNO_3$ in CH_3CN/0.1M $[(n\text{–}C_4H_9)_4]ClO_4$.
[b] Calculated from differential pulse voltammetry.
[c] Difference between first oxidation and first reduction potentials.

All the complexes exhibit three successive reversible ligand–centered reduction waves at relatively positive values compared to complex **2.7**. Due to the greater π–accepting ability of the azo ligands compared to the bpy ligands, as seen in Chapter 2, the first two reductions are azo–centered and the third electron added to these complexes is localised on a bpy ligand. The pyrimidine–based complexes **3.9** and **3.11**, show similar redox behaviour, while the addition of an electron–rich methyl group raises the π*– orbital of the azo ligand **3.3** and shifts the reduction potential to a more negative potential making it harder to reduce. The fused aromatic rings raises the energy of the Ru(dπ) orbital, but also influences the LUMO of the azo ligand, making complexes **3.15**, **3.18** and **3.22** harder to reduce compared to the pyrimidine–based complexes. A reverse effect was observed in complexes **3.17**, **3.21** and **3.24** with **3.21** being easily reducible. Complex **3.17** exhibits an anodic shift for the oxidation, as well as the reduction when compared to the isomeric complex **3.18**, as shown in Figure 3.33.

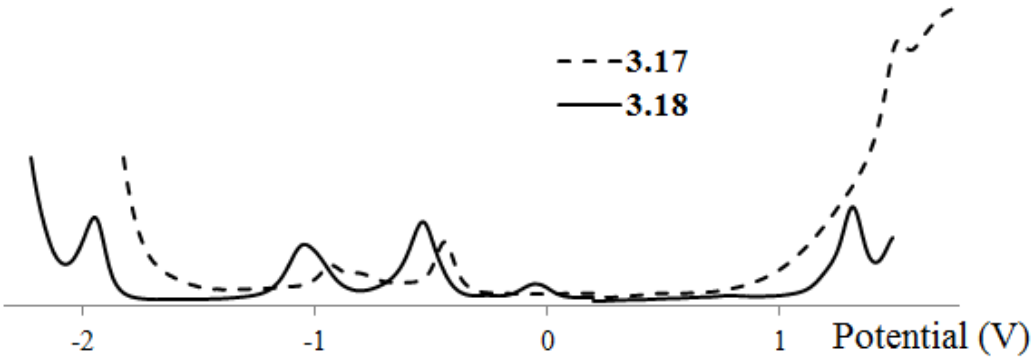

Figure 3.33. The differential pulse voltammograms of isomeric complexes **3.17** and **3.18** showing differences in their redox potentials.

The dinuclear complexes exhibit two reversible ruthenium–centred one–electron oxidation couples, as shown in Figure 3.34. The first oxidation redox couple is shifted cathodically when compared to the corresponding mononuclear complex, due to the stabilisation of the azo π–orbital upon bimetallic coordination. This also indicates an increase in the electron–withdrawing ability of the azo ligands in the dinuclear complexes. Unlike the mononuclear complexes discussed above, the first oxidation potential of these complexes is comparable with that of the azobispyridine complex **2.8**, although complexes **3.10** and **3.20** exhibit slight cathodic shifts. The second oxidation process in **3.14**, **3.16** and **3.23** also occurs at potentials comparable to that of **2.8**. In complexes **3.10** and **3.12**, the second oxidation process occurs at a more positive potential due to the presence of the additional nitrogen atom and electron–withdrawing halogen groups. Complex **3.23** displays a cathodic shift in the second ruthenium centred oxidation redox couple. Table 3.9 summarises the redox potentials of the dinuclear complexes.

The complexes display two successive one–electron and one two–electron redox couples corresponding to the reductions of the ligand. As explained previously, the first two electrons are attributed to a successive one–electron uptake by the azo–centered π–orbital. The subsequent two–electron redox couple corresponds to the reduction of the ancillary bpy ligands. Replacement of the pyridine ring by pyrimidines and fused N–aromatic rings in the azo ligand has a considerable effect on the ligand–centered redox couples in these complexes. Pyrimidine–containing complexes **3.10** and **3.12** show azo–based reductions at much lower potentials due to lowering of the π* level compared to the azobispyridine complex **2.8**. This also accounts for the stability of the radical azo anion in these complexes. The increased σ–donor ability of ligand **3.3** supports the cathodic shift in reduction potential of complex **3.14**.

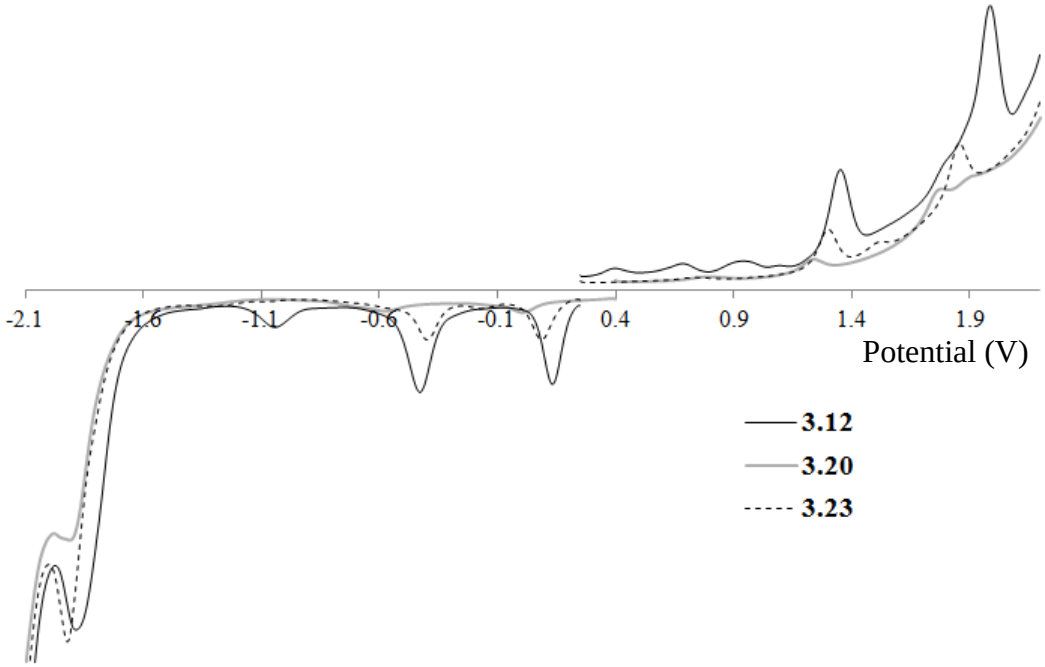

Figure 3.34. Differential pulse voltammograms of **3.12**, **3.20** and **3.23** *vs* $Ag/AgNO_3$ in CH_3CN/0.1M $[(n\text{–}C_4H_9)_4]ClO_4$.

Table 3.9. Redox potentials[a,b] of the dinuclear complexes.

Dinuclear Complexes	$\Delta E_{ox/red}$[c] V	$E_{1/2ox2}$	$E_{1/2ox1}$	$E_{1/2red1}$	$E_{1/2red2}$	$E_{1/2red3}$
2.8	1.42	+1.85	+1.36	–0.06	–0.071	–1.83($2e^-$)
3.10	1.23	+1.92	+1.28	+0.05	–0.50	–1.96($2e^-$)
3.12	1.22	+1.99	+1.35	+0.13	–0.43	–1.89($2e^-$)
3.14	1.31	+1.88	+1.31	+0.00	–0.54	–1.93($2e^-$)
3.16	1.37	+1.89	+1.36	–0.01	–0.57	–2.07($2e^-$)
3.20	1.28	+1.79	+1.24	–0.04	–0.62	–1.94($2e^-$)
3.23	1.22	+1.86	+1.30	+0.08	–0.39	–1.92($2e^-$)

[a] In V *vs*. $Ag/AgNO_3$ in CH_3CN/0.1M $[(n\text{–}C_4H_9)_4]ClO_4$.
[b] Calculated from DPV measurements.
[c] Difference between the first oxidation and first reduction potential.

As seen in Chapter 2, these complexes also exhibit two widely separated ruthenium–centered oxidation potentials. The separation between the oxidation potentials gives a measure of the extent of electronic coupling between the metal centres. Compared to azobispyridine complexes, these complexes exhibit a larger splitting between the two oxidation potential waves (ΔE_{ox} > 500mV), as summarised in Table 3.10.

Table 3.10. Electrochemical data of the dinuclear complexes.

Dinuclear Complexes	log K_c [a]	ΔE_{ox} [b] V	$E_{1/2ox2}$	$E_{1/2ox1}$
2.8	8.28	0.49	+1.85	+1.36
3.10	10.82	0.64	+1.92	+1.28
3.12	10.82	0.64	+1.99	+1.35
3.14	9.30	0.55	+1.88	+1.31
3.16	8.96	0.53	+1.89	+1.36
3.20	9.30	0.55	+1.79	+1.24
3.23	9.46	0.56	+1.86	+1.30

[a] Comproportionation constant, $K_c = \exp\{\Delta E_{ox}F/RT\}$, where $F/RT = 38.92\ V^{-1}$ at 298 K.
[b] Difference between the two successive oxidation potentials.

The comparison of the comproportionation constant suggests that incorporation of pyrimidine and fused N–aromatic rings facilitate the mixing of azo–centered π*–orbitals with the metal dπ–orbitals resulting in an increased coupling between the metal centres. The strongly π–accepting pyrimidine–based complexes **3.10** and **3.12** exhibit substantially higher electronic coupling, $K_c = 10^{10}$, while the σ–donating ability of ligand **3.3** in complex **3.12** reduces the coupling ($K_c = 10^9$) between the metal centres. In fused N–aromatic complex **3.16**, ligand **3.4** mediates communication comparable to that of azobispyridine complexes and ligands **3.5** and **3.7** results in an increased electronic interaction between the two ruthenium centres.

3.6. Summary

The synthesis and characterisation of mononuclear and dinuclear ruthenium(II) polypyridyl complexes **3.9** – **3.24** with bidentate azo ligands **3.1** –**3.8** containing pyrimidines and fused N–aromatic rings were described in this chapter. In this chapter also, the bromo–ligand **3.2** was reacted with $[Ru(bpy)_2(OTf)_2]$ to avoid the chloro–substitution of the bridging ligand in the dinuclear complex **3.12**. All attempts to synthesise the dinuclear complexes of **3.6** and **3.8** were unsuccessful.

The pyrimidine–based ligands facilitated the isolation and the X–ray crystallographic characterisation of two homodinuclear ruthenium complexes, $[(bpy)_2Ru(\mu$–**3.1**$)Ru(bpy)_2](PF_6)_3$, **3.10** and $[(bpy)_2Ru(\mu$–**3.2**$)Ru(bpy)_2](PF_6)_3$, **3.12** bridged by pyrimidine–

based azo anion radical species. Both **3.10** and **3.12** display long N_{azo}–N_{azo} bond lengths of *ca.* 1.36 Å corresponding to the reduced azo ligand.

The monoruthenium(II) complexes **3.17** and **3.18** containing ligand **3.5** were obtained as a 1:10 mixture, due to the nature of the nitrogen atom involved in the chelation and were isolated by cation–exchange chromatography. The diastereoisomeric forms **3.19** and **3.20** of dinuclear ruthenium(II) complex $[(bpy)_2Ru(\mu–\mathbf{3.5})Ru(bpy)_2]^{4+}$ were separated by cation–exchange chromatography and characterised by X–ray crystallography. The structures of **3.19** and **3.20** show coordination of the bridging ligand **3.5** to two $[Ru(bpy)_2]^{2+}$ fragments *via* azo N–atoms and the less hindered N–atoms on each side.

Varying the pyridine ring of the azo ligand to pyrimidines and fused N–aromatic rings has a considerable effect on the electronic properties of these complexes, which were probed by UV/Visible spectroscopy and electrochemical studies. Altering azo ligands influences the energy of both the Ru(dπ), as well as the π*–orbital of the azo ligands. Electrochemical studies reveal the complexes containing these ligands are easier to reduce than the azobispyridine complexes, but harder to oxidise. Comparison of the comproportionation constant in the dinuclear complexes suggests that incorporation of pyrimidine and fused N–aromatic rings facilitate the mixing of azo–centered π*–orbitals with the metal dπ–orbitals resulting in an increased coupling between the metal centres compared to the azobispyridine complexes.

Chapter 4

Tridentate ligands based on azobis(bidentates)

4. Tridentate ligands based on azobis(bidentates)

4.1. Introduction

Ruthenium(II) complexes based on bidentate ligands, such as bpy and phen have been of interest due to their photophysical and photochemical properties. However, their use in building polynuclear systems becomes complicated, since bpy–type ligands lead to stereoisomers with limited control over the geometry of the system.[72],[84],[99] This stereochemical problem may be avoided by the use of tridentate ligands of the type 2,2':6',2''–terpyridine (terpy).[79],[101] These ligands coordinate to an octahedral metal centre in a meridional manner creating a single isomer of the achiral $[Ru(terpy)_2]^{2+}$ complex cation, as shown in Figure 4.1. The achiral $[Ru(terpy)_2]^{2+}$ unit simplifies the synthesis as it gives unique products in polynuclear species if the bridging occurs through the 4'–position of the central pyridyl ring of the terpy ligand. However, $[Ru(terpy)_2]^{2+}$ does not luminesce at room temperature.[6],[115] Therefore, a number of efforts have been made to increase the lifetime of the $[Ru(terpy)_2]^{2+}$ chromophore, such as using electron–withdrawing groups at the 4'–position of the terpy ligand.[115–117],[273]

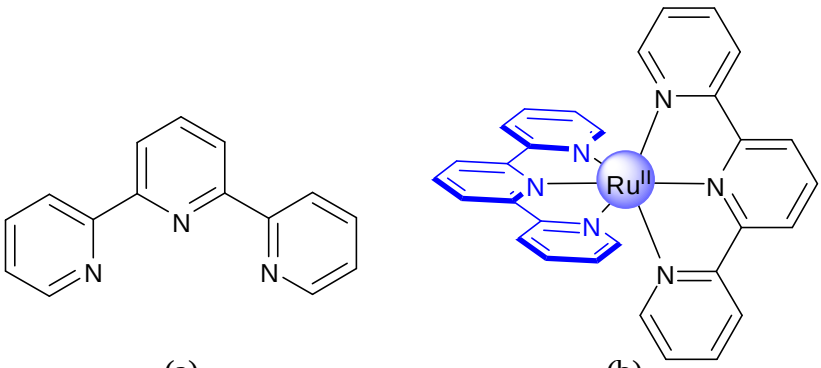

(a) (b)

Figure 4.1. (a) 2,2':6',2''–terpyridine (terpy) and (b) the unique (achiral) form of the $[Ru(terpy)_2]^{2+}$ complex.

In the context of this project, we have been interested in symmetrical terpy complexes of the type [(terpy)Ru^{II}–BL–Ru^{II}(terpy)], where BL is an azo–based ligand which coordinates in a bis–tridentate manner. The use of two symmetric tridentate ligand components coordinated to metal centres eliminates the possibility of stereoisomerism. In this sense, the bis–tridentate 2,3,5,6–tetrakis(2–pyridyl)pyrazine (tppz) (Figure 4.2) has been extensively used as a bridging ligand to prepare homo–nuclear and hetero–nuclear complexes with a

range of terminal ligands such as bpy and terpy.[102–104] Complexes of this ligand with octahedral transition metal ions such as Ru(II) and Os(II) have been studied for their redox, luminescence and mixed–valence properties by several workers.[105–111] In these complexes the metal centres are extremely close and exhibit a high degree of electronic coupling and mediate electron transfer through multiple redox states of the metal ions.

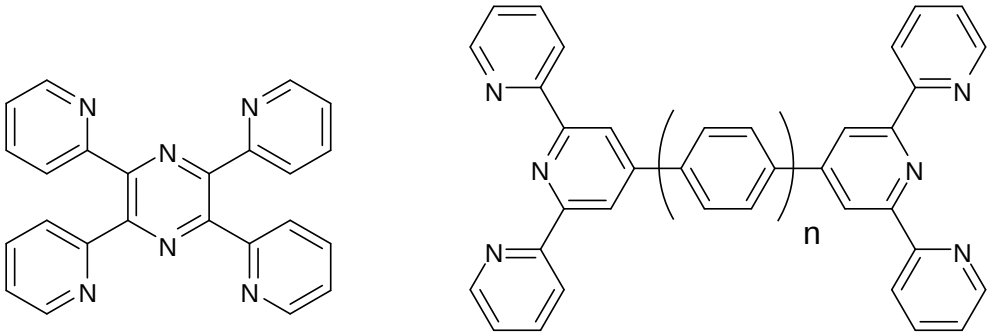

tppz

n = 0 (terpy-terpy)
n = 1 (terpy-Ph-terpy)
n = 2 (terpy-Ph_2-terpy)

Figure 4.2. Examples of bis–tridentate ligands.

A series of dinuclear complexes with bridging ligands containing two terpy units joined by 0–2 phenylene (Ph) units, terpy–terpy, terpy–Ph–terpy, terpy–Ph_2–terpy, were investigated for their photophysical properties (Figure 4.2).[112],[113] The inter–metal separation in these complexes ranges from 11–20 Å and they exhibit decreasing metal–metal interactions in the order of n = 0–2. Constable *et al.*[274],[275] have reported a number of homo and hetero–ditopic complexes with terpy and its functionalised derivatives, Figure 4.3a. Lehn and co–workers have established a classical bis–tridentate ligand series based on a central pyrimidine ring, shown in Figure 4.3b for the construction of 'rack–type' polynuclear complexes towards the development of inorganic molecular devices.[276],[277] Thummel *et al.*[278] have investigated a series of dinuclear Ru(II) complexes of tridentate ligands based on a diphen–disubstituted pyrazine, as shown in Figure 4.3c.

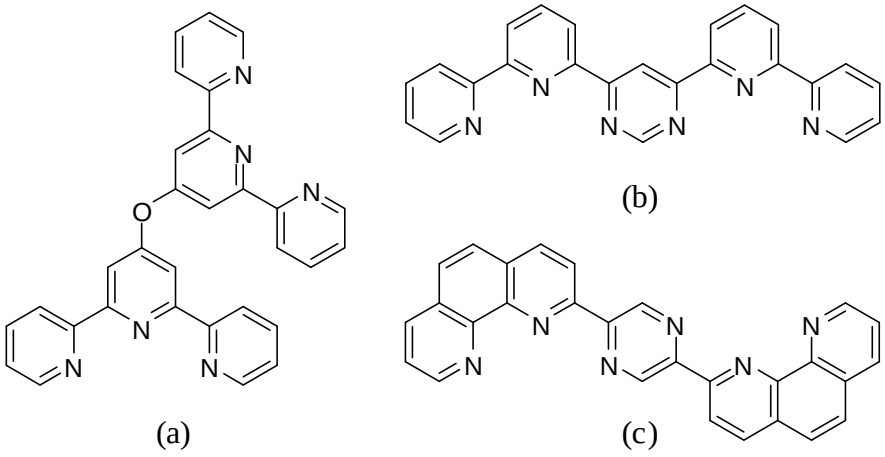

Figure 4.3. Examples of (a) functionalised terpy based ligands; (b) and (c) ligands used for 'rack–type' polynuclear complexes.

Azo groups have been used as linkers between bpy and terpy units, as shown in Figure 4.4.[279],[280] The ligands coordinate to the metal centre using the pyridyl N–atoms only and the azo functionality is not involved in the coordination. In the dinuclear Ru complex of azobpy, a short metal–metal separation (8.2 Å) and a very weak intermetallic interaction (K_c = 21) was detected.[279] However, electrochemical studies of dinuclear Ru complexes containing azoterpy ligand indicate no interaction between the metal centres.[280]

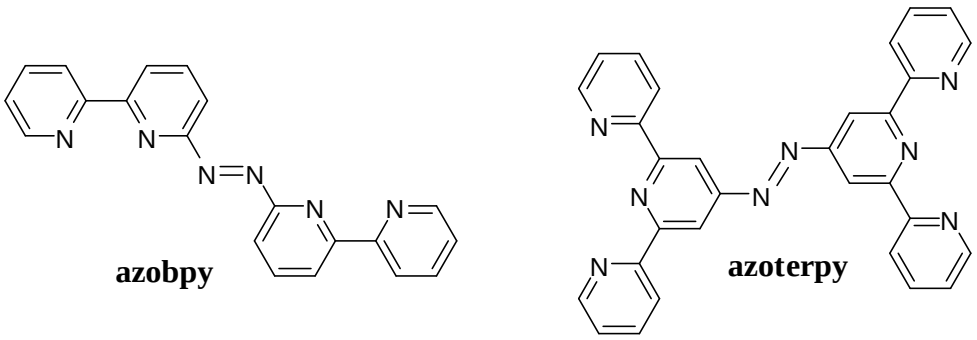

Figure 4.4. Tridentate ligands containing azo linkers.

The aim of this work was to prepare ligands which can coordinate in a bis–tridentate manner with the azo functionality being involved in coordination, as shown in Figure 4.5. The first ligand **4.1**, having an azo linker between two bpy subunits has been previously synthesised by Otsuki *et al.*[279] However, a different approach was used to synthesise **4.1** which is described in Section 4.2. A new ligand **4.2** was prepared in which two phen units are linked by the azo group.

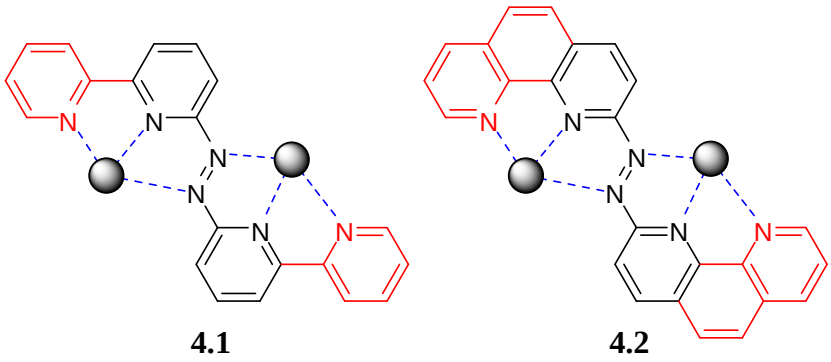

Figure 4.5. Tridentate ligands investigated in this chapter.

4.2. Syntheses of the ligands

Azobis[6–(2,2'–bipyridine)] **4.1** has previously been synthesised by reductive condensation of 6–nitro–2,2'–bipyridine using Zn powder in a mixture of aqueous NaOH solution and THF.[279] Instead, **4.1** was synthesised by oxidative coupling of 6–amino–2,2'–bipyridine using NaOCl, as shown in Scheme 4.1. The precursor amine was synthesised by a one–pot conversion of 2,2'–bipyridine mono N–oxide[281] using Ts_2O and *t*–$BuNH_2$, followed by *in situ* deprotection with TFA.[282]

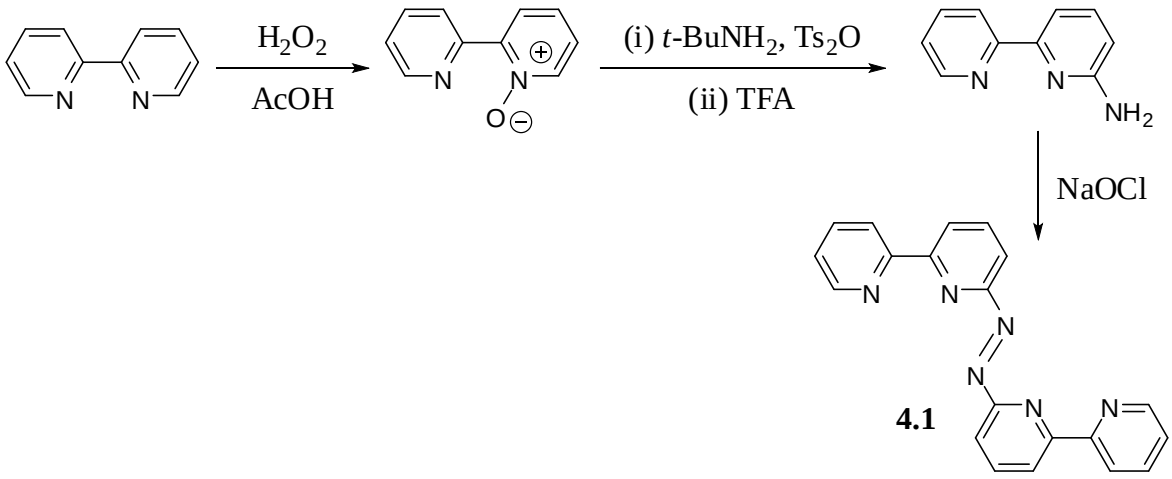

Scheme 4.1

The oxidative coupling of 2–amino–1,10–phenanthroline using NaOCl gave the new azobis(phenanthroline) ligand **4.2**, as shown in Scheme 4.2. The precursor amine was synthesised by using the method of Engel *et al.*,[283] which involves the heating of 2–chloro–1,10–phenanthroline[284] with acetamide in the presence of K_2CO_3.

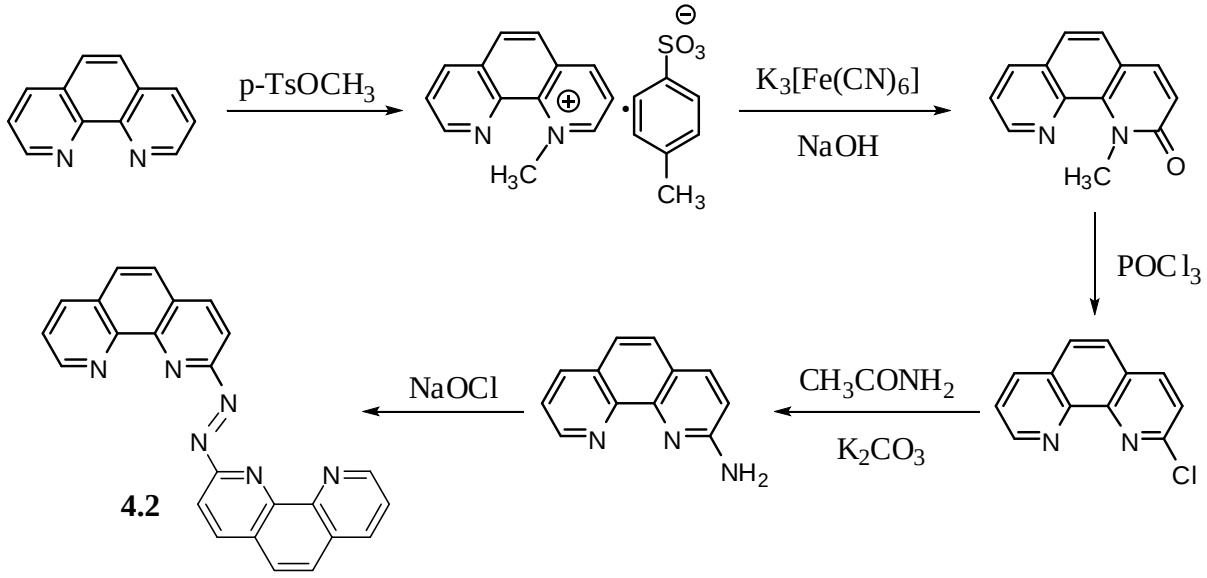

Scheme 4.2

4.3. Coordination chemistry of azobis(bidentate) ligands

The general procedure involves refluxing a suspension of azo ligand and [Ru(terpy)Cl_3] in ethylene glycol in a microwave oven for 10–12 minutes at intervals of 2 minutes. The complexes were precipitated as the hexafluorophosphate salts and purified by cation exchange column chromatography.

4.3.1. Complex of 4.1

The dinuclear complex of **4.1** with [Ru(bpy)Cl_2] (Figure 4.6) has been previously investigated by Otsuki *et al.*[279] for its electronic absorption and electrochemical properties. The metal–to–ligand charge–transfer band extends to 800 nm and the analysis of its redox properties indicates an intermetallic electronic interaction with a very weak comproportionation constant of 21.

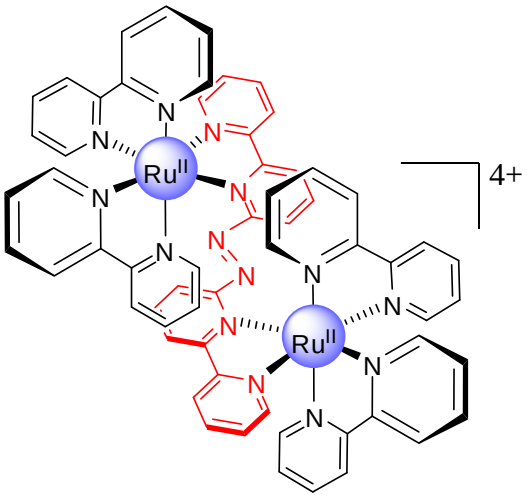

Figure 4.6. The dinuclear Ru(II) complex of **4.1** with Ru(bpy)$_2$ units reported in the literature.[279]

Here, we report a new dinuclear ruthenium complex, **4.3**, which was synthesised by refluxing a mixture of **4.1** with [Ru(terpy)Cl$_3$] in ethylene glycol in a microwave oven, as shown in Scheme 4.3. The complex was characterised as [{Ru(terpy)}$_2$(μ–**4.1**)](PF$_6$)$_4$ by ESI–MS and ^{1}H NMR spectroscopy.

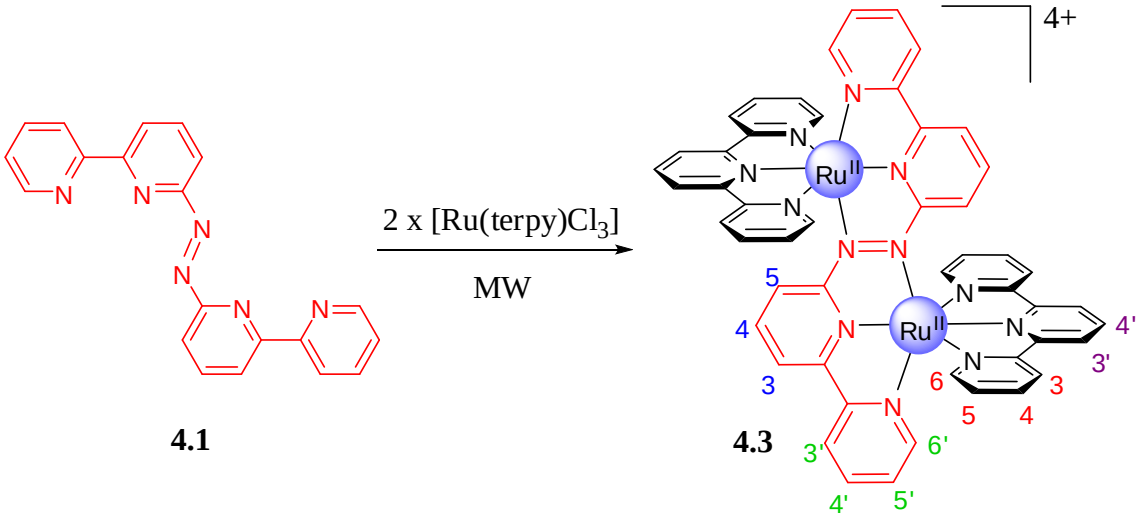

4.1 **4.3**

Scheme 4.3

The ^{1}H NMR and COSY spectra of **4.3** are shown in Figure 4.7. Table 4.1 lists the ^{1}H NMR chemical shifts and coordination–induced–shift values for **4.1** and **4.3**. The spectrum shows four different ring systems which were easily identified from the COSY spectrum and are color coded as shown below. The H3 proton (8.71 ppm) is slightly deshielded when compared to the H3' proton (8.46 ppm) due to changes in conformation upon chelation. The strong negative *CIS* value for the H6' proton (–1.88 ppm) indicates significant shielding due

to the anisotropic ring–current effects from the central terpy ring. A strongly shielded terpy–H6 proton is also observed due to through–space ring–anisotropy effects.

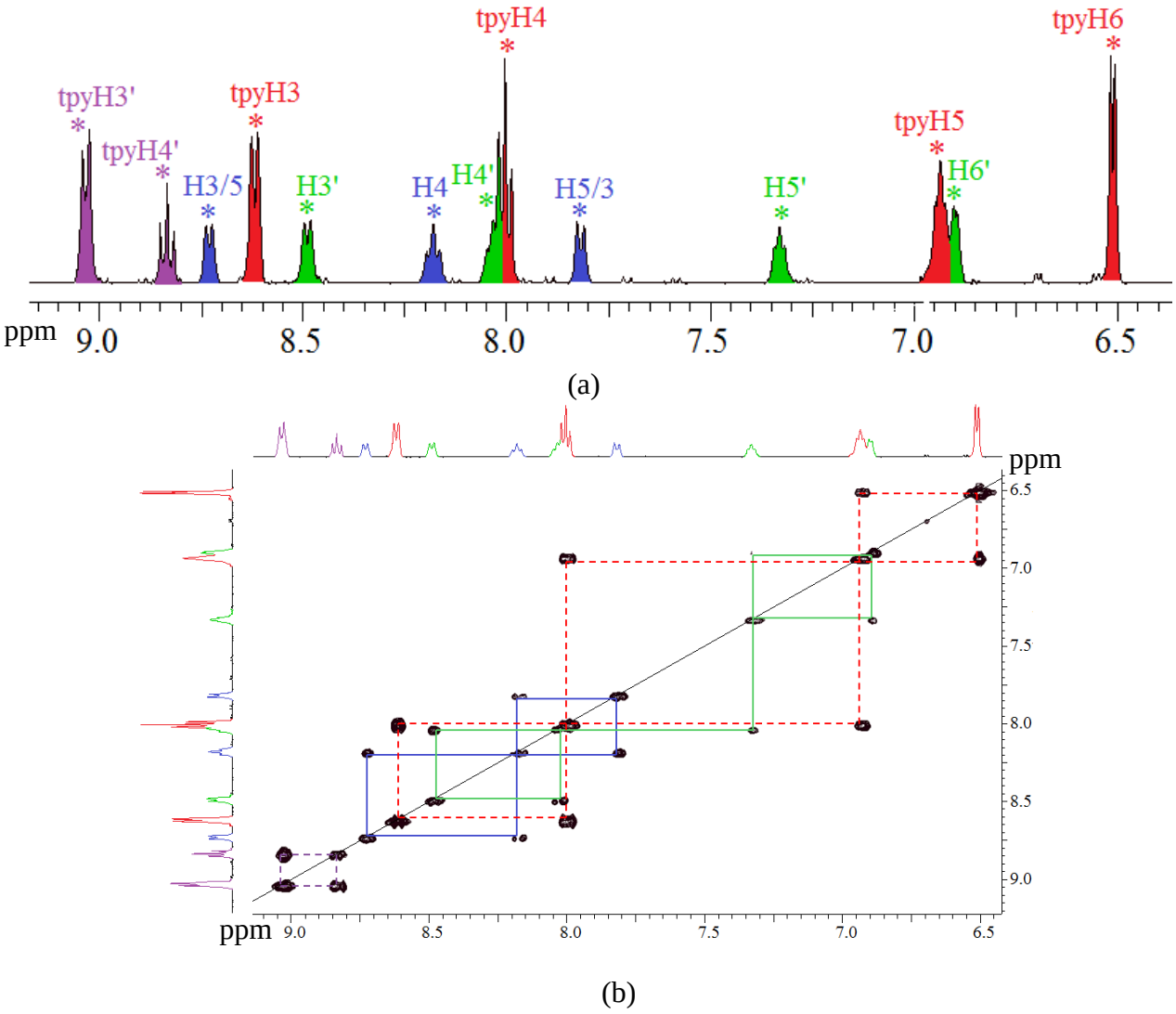

Figure 4.7. The (a) ^{1}H NMR and (b) gCOSY spectra of **4.3**.

Table 4.1. The ^{1}H NMR chemical shifts[a] and *CIS* values[b] (italics) for **4.1** and **4.3**.

	H3	**H4**	**H5**	**H3'**	**H4'**	**H5'**	**H6'**
4.1	8.68	8.21	8.00	8.59	7.91	7.49	8.76
4.3	8.71	8.15	7.79	8.46	8.03	7.30	6.88
CIS	*+0.03*	*–0.06*	*–0.21*	*–0.13*	*+0.12*	*–0.19*	*–1.88*

[a] In acetonitrile–d_3.
[b] $CIS = \delta_{complex} - \delta_{ligand}$.

*Crystal Structure of **4.3***

A single crystal, suitable for X–ray structure analysis, was grown by diffusing diisopropyl ether into an acetonitrile solution of the complex. The complex crystallises in the triclinic space group *P*–1, with half the dinuclear cation, two PF_6^- anions and an acetonitrile solvate molecule in the asymmetric unit. The crystal structure confirms the dinuclear nature of the complex.

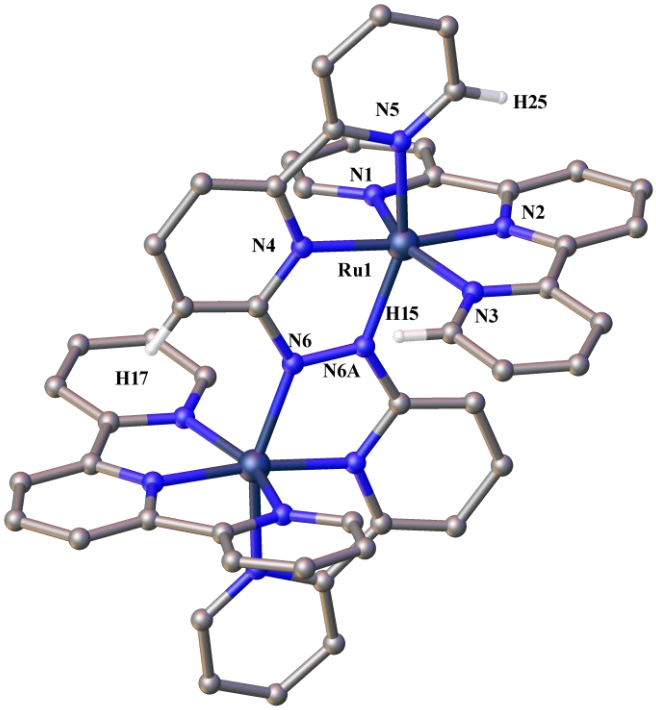

Figure 4.8. The X–ray crystal structure of **4.3**. Most of the hydrogen atoms, counterions and the solvate molecules are omitted for clarity. Selected bond distances (Å): Ru1–N1 2.072(3), Ru1–N2 2.002(3), Ru1–N3 2.082(3), Ru1–N4 1.955(3), Ru1–N5 2.083(3), Ru1–N6A 2.030(3), N6–N6A 1.349(5). Selected bond angles (°): N1–Ru1–N3 156.85(12), N1–Ru1–N5 93.06(11), N2–Ru1–N1 78.76(12), N2–Ru1–N3 78.36(12), N2–Ru1–N5 95.10(11), N2–Ru1–N6 108.87(11), N3–Ru1–N5 92.44(11), N4–Ru1–N1 97.28(12), N4–Ru1–N2 173.07(11), N4–Ru1–N3 105.84(12), N4–Ru1–N5 79.35(11), N4–Ru1–N6 76.78(11), N6–Ru1–N1 92.24(11), N6–Ru1–N3 91.81(11), N6–Ru1–N5 156.02(12).

Figure 4.8 shows the X–ray crystal structure of **4.3**, within which the azo ligand **4.1** acts as a hexadentate ligand coordinating to each ruthenium atom using an azo nitrogen atom and two N–atoms from a bipyridine unit. As seen in Chapter 2, the ligand adopts an "S–

conformation" in complex **4.3** and acts as a planar bridge between the two ruthenium atoms with a short inter–metal separation of 4.823(1) Å (Ru1···Ru1A), which is much shorter than that reported for $[\{Ru(bpy)_2\}_2(\mathbf{4.1})]^{4+}$ by Otsuki *et al.* (~ 8.2 Å). The ruthenium atom possesses distorted octahedral geometry with two meridional tridentate ligands (**4.1** and terpy) orthogonal to each other. Contrary to the dinuclear complexes described in Chapter 2, in this case the Ru–N_{py} bond distance [Ru1–N4 1.955(3) Å] is shorter when compared to the Ru–N_{azo} [Ru1–N6A 2.030(3) Å] due to geometric constraints. The Ru–N bond distance for the terpy is shorter for Ru–$N_{central}$ [Ru1–N2 2.002(3) Å] than the average Ru–N_{outer} [2.077(3) Å], as is normal for terpy complexes.[111],[285]

Examination of the crystal structure helps to explain the NMR chemical shifts. The H6 proton (H15) of the terpy experiences the greatest shielding and shifts upfield since it lies directly above the pyridyl ring of the bridge. The H6' proton (H25) of ligand **4.1** experiences a similar anisotropy effect from the adjacent terpy ring. The H5 proton (H17) also experiences some shielding since it lies in close proximity to an adjacent terpy ring

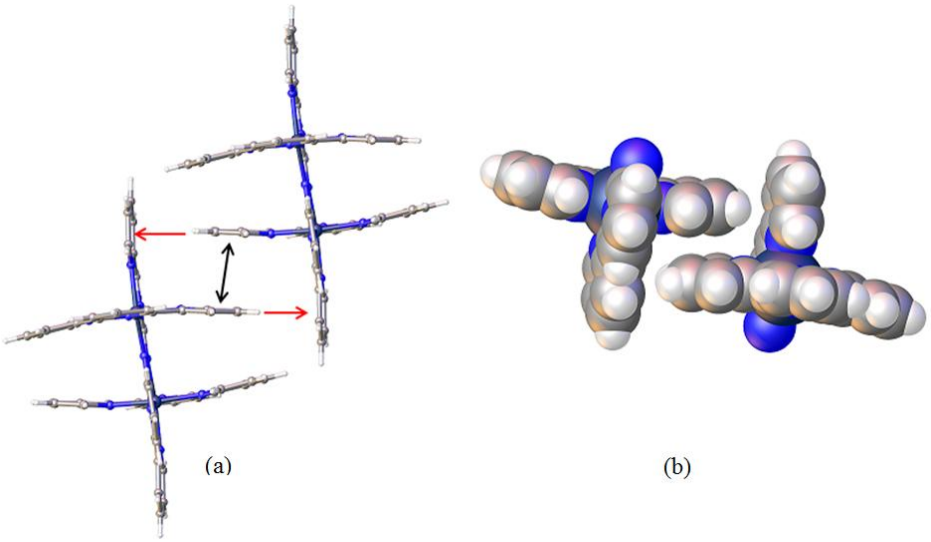

Figure 4.9. (a) The aryl embrace motif of **4.3** showing **OFF** (black) and **EF** (red) interactions. (b) Space–filling diagram showing these π–π interactions.

The crystal packing of **4.3** shows interesting aryl embraces where a pair of outer pyridyl rings are involved in offset face–to–face (**OFF**) interactions [ring···ring 3.709(2) Å] and each of these rings also addresses an edge–to–face (**EF**) interaction with the pyridyl ring of the bridging ligand [H···ring 2.770(1) Å], as shown in Figure 4.9. The features of intermolecular π–stacking interactions in metal complexes of terpy and related complexes have been described by Dance and coworkers,[286–288] Constable *et al.*[285],[289] and other authors.[290],[291]

These aryl embraces should propagate to generate a two–dimensional net, as shown in Figure 4.10. The molecular packing also exhibits numerous CH···F interactions, which contribute to the overall packing in the crystal structure.

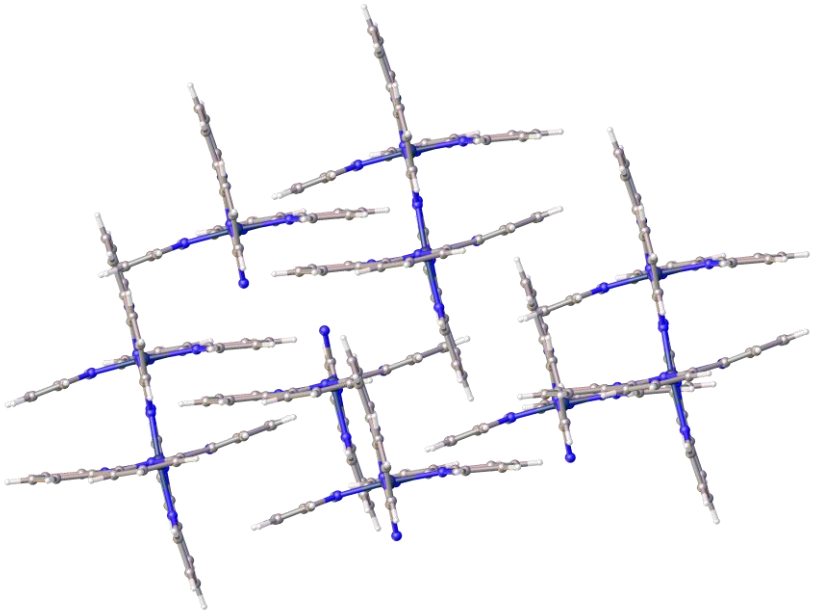

Figure 4.10. An arrangement of complexes showing **EF** and **OFF** interactions in the crystal structure.

4.3.2. Complexes of 4.2

The mononuclear complex **4.4** was synthesised by refluxing a mixture of ligand **4.2** and [Ru(terpy)Cl_3] in a 1:1 stoichiometric ratio. The complex was precipitated as the hexafluorophosphate salt and characterised as [(terpy)Ru(**4.2**)]$(PF_6)_2$. Microwave assisted reaction of **4.2** with a two–fold excess of [Ru(terpy)Cl_3] in ethylene glycol gave the expected dinuclear complex **4.5,** which was characterised as [{Ru(terpy)}$_2$(**4.2**)]$(PF_6)_4$, as shown in Scheme 4.4.

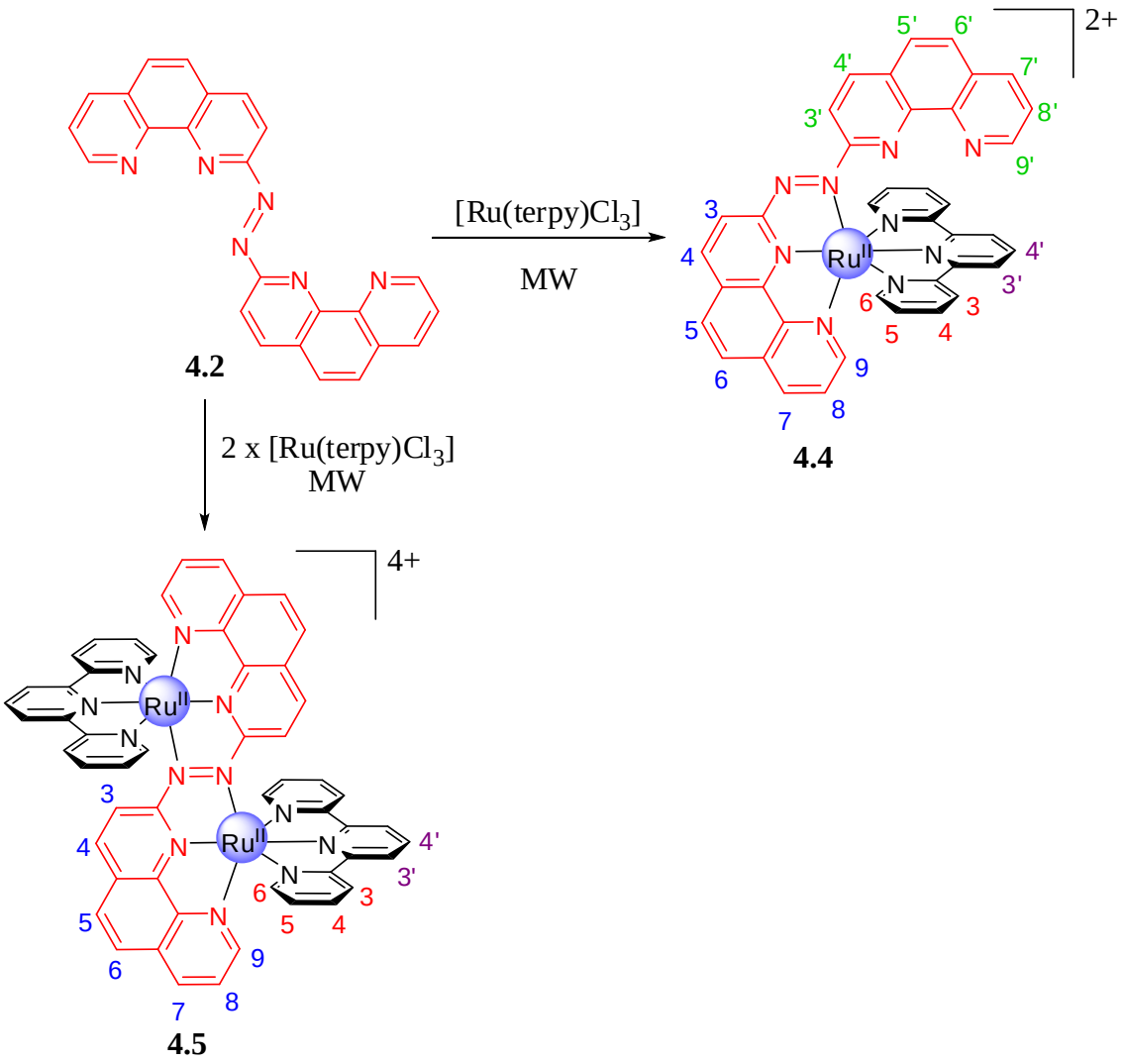

Scheme 4.4

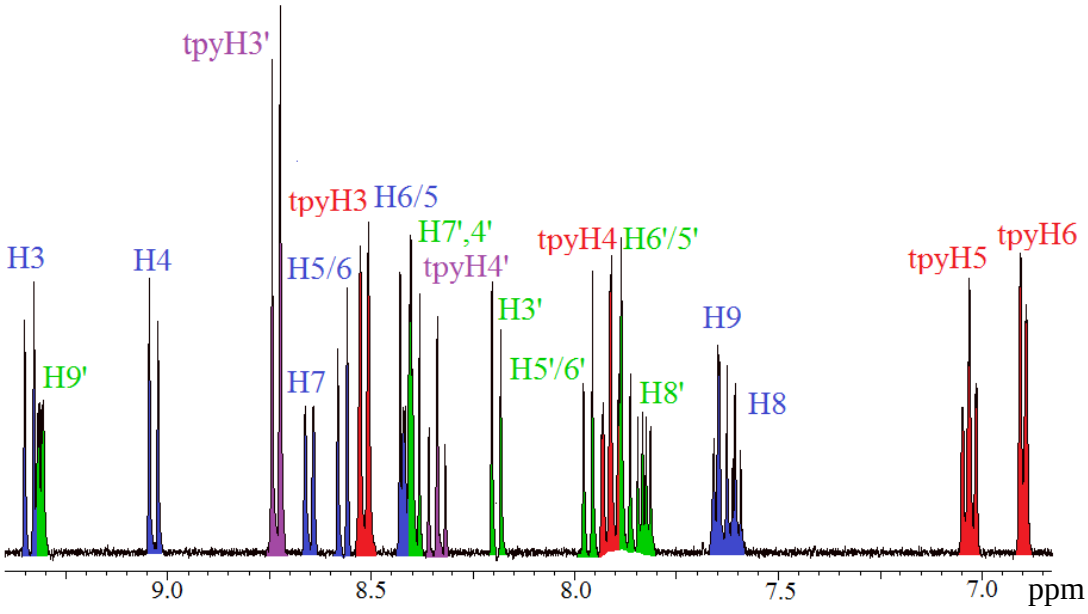

Figure 4.11. The ^{1}H NMR spectrum of **4.4**.

The ^{1}H NMR spectrum of complex **4.4**, in acetonitrile–d_3, is shown in Figure 4.11. Due to the unsymmetrical nature of the coordinated ligand **4.2**, the two phen rings are different and the spectrum shows 20 non–equivalent aromatic proton signals corresponding to eight different ring systems. Using a combination of spin–spin coupling, gCOSY and 1–D NOESY experiments, the ^{1}H NMR chemical shifts for complex **4.4** were fully assigned.

Table 4.2. The ^{1}H NMR chemical shifts and *CIS* values[a] (italics) for **4.2**[b] and **4.4**.[c]

	H3	**H4**	**H5**	**H6**	**H7**	**H8**	**H9**
4.2	8.57	8.50	7.94	7.94	8.34	7.72	9.32
4.4[d]	9.33	9.03	8.42	7.96	8.65	7.61	7.64
CIS	*+0.76*	*+0.53*	*+0.48*	*+0.02*	*+0.32*	*–0.11*	*–1.68*
4.4[e]	8.19	8.39	7.96	7.89	8.40	7.83	9.31
CIS	*–0.38*	*–0.11*	*+0.02*	*–0.05*	*0.06*	*+0.11*	*–0.01*

[a] $CIS = \delta_{complex} - \delta_{ligand.}$
[b] In chloroform–d.
[c] In acetonitrile–d_3.
[d] Coordinated phen ring of **4.2**.
[e] Free phen ring of **4.2**.

The H3 proton (9.33 ppm) of the coordinated phen is strongly deshielded, presumably due to a chelation induced conformational change, whereas the H9 proton (7.64 ppm) is strongly shielded since it experiences ring–current anisotropy due to the nearby central terpy ring. The X–ray crystal structure shown in Figure 4.12 further supports these observations. Table 4.2 lists the ^{1}H NMR chemical shifts and the approximate *CIS* values for **4.2** and **4.4** in $CDCl_3$ and CD_3CN respectively, as the free ligand **4.2** was insoluble in the same solvent as the complex.

*Crystal Structure of **4.4***

Crystals of **4.4** were obtained by diffusing petroleum ether into a solution of the complex in acetone. The complex crystallises in the monoclinic space group $P2_1/n$. The crystal structure confirms the mononuclear nature of the complex.

The asymmetric unit contains one full cation along with two hexafluorophosphate anions and an acetone solvate molecule, as shown in Figure 4.12. As seen in the mononuclear complexes discussed in previous chapters, in complex **4.4**, ligand **4.2** also adopts a s–*cis*/*E*/s–*trans* conformation with the ruthenium atom coordinated to an azo N–atom and both of the N–atoms of a phen ring. The coordinated phen ring is in the same plane as the azo group with

a torsion angle of 1.4(1)°, while the non–coordinated phen ring twists at an angle of 30.2(1)°. Similar conformations for the mononuclear complexes were observed in previous chapters. Once again the ruthenium geometry is normal with the Ru–$N_{central}$ bond distance [Ru–N8 2.011(2) Å] of terpy shorter than the average Ru–N_{outer} [2.081(2) Å]. Also, the Ru–N_{azo} bond length is shorter than the Ru–N_{phen} indicating the strong π*–acceptor ability of the azo moiety.

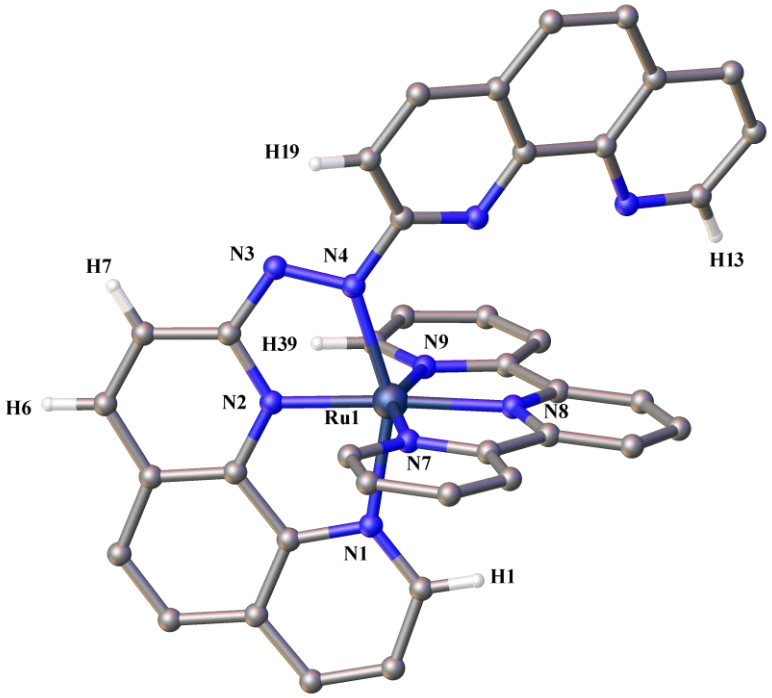

Figure 4.12. The asymmetric unit of **4.4**. Some of the hydrogen atoms, counterions and the solvate molecule are omitted for clarity. Selected bond distances (Å): Ru1–N1 2.131(2), Ru1–N2 1.950(2), Ru1–N4 2.036(2), Ru1–N7 2.084(2), Ru1–N8 2.011(2), Ru1–N9 2.078(2), N3–N4 1.313(3). Selected bond angles (°): N2–Ru1–N8 175.78(8), N2–Ru1–N4 74.96(8), N8–Ru1–N4 108.89(8), N2–Ru1–N9 100.06(8), N8–Ru1–N9 78.20(8), N4–Ru1–N9 93.23(7), N2–Ru1–N7 103.44(8), N8–Ru1–N7 78.15(8), N4–Ru1–N7 95.71(8), N9–Ru1–N7 156.31(8), N2–Ru1–N1 79.26(8), N8–Ru1–N1 96.94(8), N4–Ru1–N1 154.14(8), N9–Ru1–N1 93.11(7), N7–Ru1–N1 88.34(8).

Examination of the crystal structure reveals that in complex **4.4**, the terpy H6 proton (H39) is significantly shielded since it is positioned directly over the bridging ligand and experiences maximum ring–current anisotropy effects. Similar anisotropy from the adjacent terpy ring is experienced by the H9 proton (H1) of the coordinated phen ligand. The non–

coordinated phen ring is not affected much by the coordination, which is in agreement with the very small *CIS* values given in Table 4.2.

*Crystal Structure of **4.5***

Crystals of **4.5** were obtained by vapour diffusion of diisopropyl ether into a solution of the complex in acetonitrile. The complex crystallises in the triclinic space group *P*–1, with one ruthenium atom, half a bridging ligand **4.2**, one terpy unit, two counterions and one acetonitrile solvate molecule in the asymmetric unit, as shown in Figure 4.13.

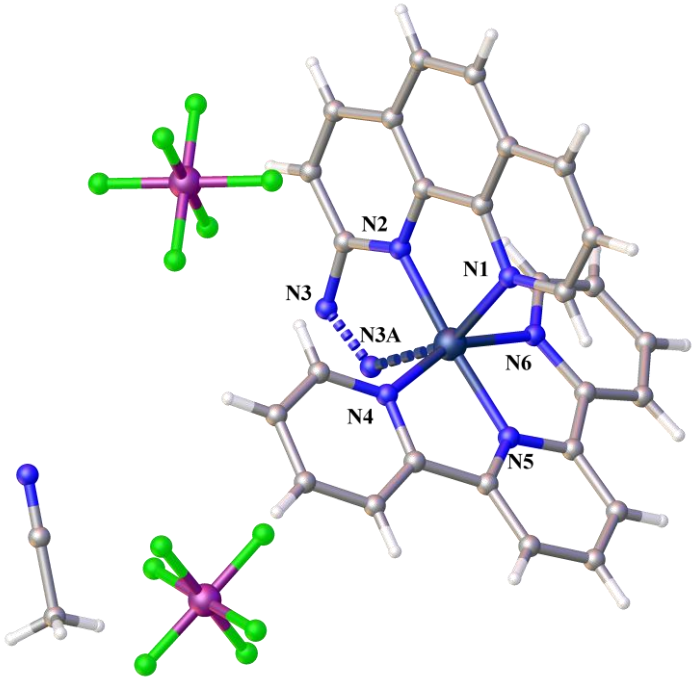

Figure 4.13. The full asymmetric unit of **4.5**. Selected bond distances (Å): Ru1–N1 2.113(3), Ru1–N2 1.947(3), Ru1–N3A 2.031(3), Ru1–N4 2.072(3), Ru1–N5 2.000(3), Ru1–N6 2.068(3), N3–N3A 1.374(5). Selected bond angles (°): N2–Ru1–N5 175.31(12), N2–Ru1–N3A 75.85(11), N5–Ru1–N3A 108.60(11), N2–Ru1–N6 99.85(12), N5–Ru1–N6 78.67(12), N3A–Ru1–N6 93.04(11), N2–Ru1–N4 103.32(11), N5–Ru1–N4 78.34(12), N3A–Ru1–N4 91.18(12), N6–Ru1–N4 156.78(11), N2–Ru1–N1 79.98(12), N5–Ru1–N1 95.58(12), N3A–Ru1–N1 155.81(11), N6–Ru1–N1 92.17(11), N4–Ru1–N1 93.27(12).

The structure of **4.5** exhibits a typical geometry for the ruthenium atom with the bridging ligand acting as a planar bridge between the two ruthenium atoms separated by 4.848(5) Å. In this case also, at the terminal terpy ligands the Ru–$N_{central}$ bond distance [Ru1–

N5 2.000(3) Å] is shorter when compared to the outer Ru–N bond distances due to geometric constraints. For the bridging ligand, the Ru–N_{azo} bond distance [Ru1–N3A 2.031(3) Å] is shorter than the outer Ru–N_{phen} bond distance [Ru–N1 2.113(3) Å] as a result of the stronger π–acceptor nature of the azo–centered bridge.

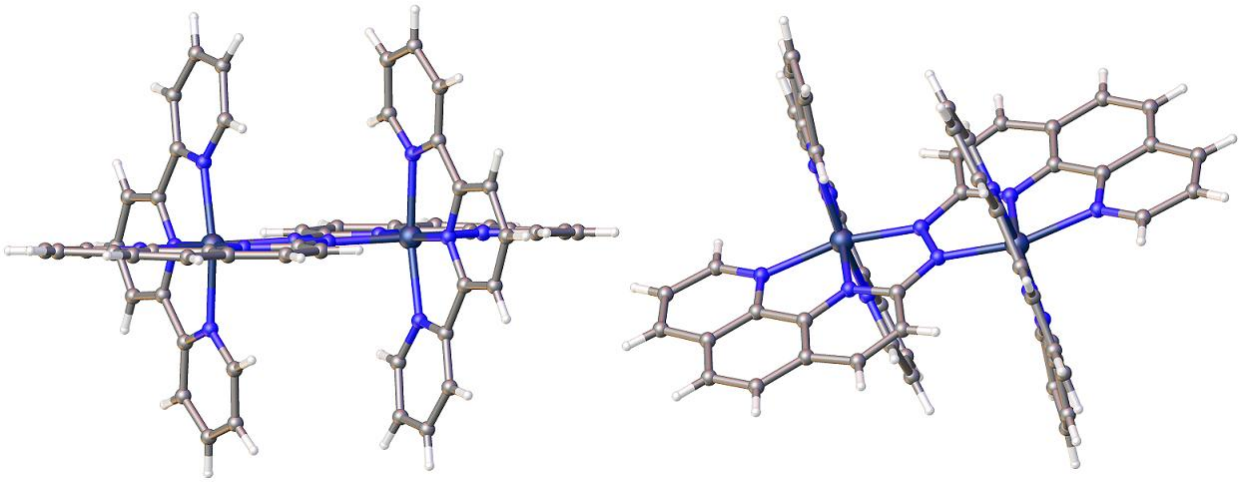

Figure 4.14. Two perspective views of the X–ray crystal structure of **4.5**, emphasising the planarity of the bridging ligand and the distortion in the terpy ligand.

The terpy ligand within the complex is surprisingly non–planar and adopts a bowed shape as shown in Figure 4.14, probably due to the mutual π–π interactions between the co–facial pyridine rings of the terpy ligands. Similar to **4.3**, the crystal packing of **4.5** also exhibits aryl embraces throughout the crystal structure, as shown in Figure 4.15. Offset face–to–face (**OFF**) interactions appear between the terpy pyridyl rings with a ring centroid separation of 3.536(3) Å. The ring also positions an edge towards the face of a phen ring of the bridging ligand (H···ring 2.684(5) Å). The crystal packing also exhibits extensive short F···H–C contacts between the hexafluorophosphate anions and the pyridyl ring protons in the range of 2.5 – 3.3 Å, which further stabilises the solid–state structure.

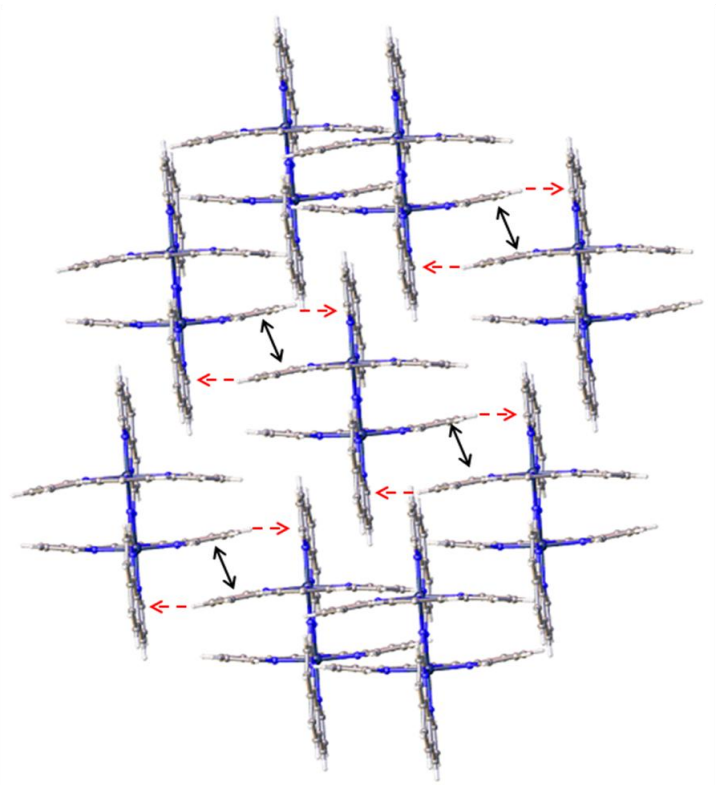

Figure 4.15. Crystal packing of **4.5** showing intermolecular interactions.

4.4. Electronic Absorption Spectroscopy and Electrochemistry

The UV/Visible spectral data and redox potentials for **4.3** – **4.5** are given in Table 4.3. The intense bands in the UV region correspond to the π → π* and n → π* transitions of the ligand. The mononuclear complex **4.4** exhibits absorption bands at 406 nm and a shoulder at 468 nm arising from Ru(dπ) → terpy(π*) and Ru(dπ) → **4.2**(π*) MLCT transitions, respectively. In dinuclear complexes **4.3** and **4.5**, the absorption bands arising from Ru(dπ) → BL(π*) transitions are shifted to a lower energy *ca.* 772 nm as a result of the low–lying π*–orbitals of the azo functionality, as well as further stabilisation of its π*–accepting nature upon coordination to a second metal centre. The band corresponding to the Ru(dπ) → terpy(π*) at *ca.* 409 nm is relatively unchanged in both **4.3** and **4.5**.

Table 4.3. The absorption maxima[a] and electrochemical[b,c] data for **4.3** – **4.5**.

Complexes	λ nm	E_{MLCT}[d] eV	$\Delta E_{ox/red}$[e] V	$E_{1/2ox}$ V	$E_{1/2red}$ V
[(terpy)Ru(**tppz**)]$^{2+}$[105]	476 310	1.58	2.45	+1.50	–0.95, –1.40, –1.60.
4.4	468[g] 406 329	2.65	1.79	+1.29	–0.50, –1.03, –1.94(2e¯).
[{Ru(terpy)}$_2$(**tppz**)]$^{4+}$[105] [f]	548 374 332 300	3.60	1.79	+1.71, +1.40	–0.39, –0.86, –1.43(2e¯), –1.86(2e¯).
4.3	771 475 409 330	1.60	1.36	> 2.0 +1.22	–0.04, –0.65, –1.83, –1.93.
4.5	773 472 406 329	1.60	1.27	> 2.0 +1.24	–0.03, –0.59, –1.77, –1.85.

[a] In acetonitrile (±2 nm).
[b] In V *vs* SCE in CH_3CN/0.1M $TBAPF_6$.
[c] Calculated from DPV measurement.
[d] Energy for the lowest MLCT absorption.
[e] Difference between first oxidation and first reduction potentials.
[g] shoulder.

The redox potentials indicate that these complexes are easier to oxidise and reduce than the tppz–bridged complexes. Complex **4.4** exhibits a one–electron metal centered oxidation (Ru^{II}/Ru^{III}) at +1.29 V. The oxidation potential is cathodically shifted when compared to [(terpy)Ru(tppz)]$^{2+}$. The complex displays two successive one–electron reductions, which are assigned to bridging ligand reduction processes, and a two–electron redox couple attributed to reduction of the terpy ligand. These are based on the fact that a similar potential difference (~500 mV) is observed between the first and the second reduction of the bridging ligand in both **4.3** and **4.5**. These assignments are consistent with those reported previously for Ru–terpy type complexes.[105]

The dinuclear complexes **4.3** and **4.5**, exhibit a one–electron redox process corresponding to the oxidation of the metal centre. Unfortunately, the second oxidation wave could not be observed before the oxidation of the electrolyte solution at about 2.0 V indicating a huge comproportionation constant of $K_c > 10^{13}$. The differential pulse voltammogram of complex **4.3** is shown in Figure 4.16. This increase in the communication between the metal centres is presumably due to the bis–chelating tridentate bridging ligand.

The difference in the metal–based oxidation potentials in complexes containing bischelating tridentate ligand tppz (ΔE_{ox} ~ 300mV) when compared to the bidentate bridging ligand 2,3–dpp (ΔE_{ox} ~ 200mV) has been seen previously,[6] which suggest that tridentate bridging ligands mediate stronger coupling between the metal centres.

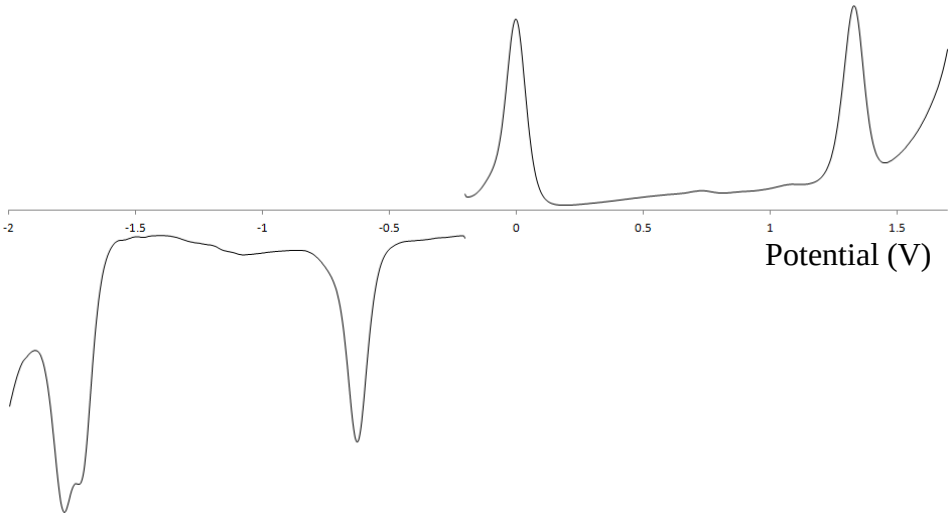

Figure 4.16. The differential pulse voltammogram for complex **4.3** *vs* $Ag/AgNO_3$.

The dinuclear complexes **4.3** and **4.5** exhibit two successive reversible one–electron reductions of the bridging ligand followed by subsequent reductions of the terminal terpy ligand. Replacement of bpy groups in **4.1** by phen in **4.2** did not have a profound effect on the redox properties of the bridging ligand in the subsequent complexes of **4.3** and **4.5**. However, when compared to the mononuclear complex **4.4**, the reduction of the bridging ligands is shifted anodically due to the stabilization of the π*–orbital on coordination to the second metal fragment.

4.5. Summary

This chapter has described the synthesis of azo–based ligands **4.1** and **4.2** which can coordinate in a bis–tridentate manner. The coordination chemistry of these ligands has been investigated by synthesising the mononuclear and dinuclear ruthenium(II) complexes.

The X–ray crystal structures of the dinuclear complexes **4.3** and **4.5** reveal that the azo ligands coordinate to the ruthenium atom using the azo nitrogen atom and two N–atoms from the bpy and phen group, respectively. The average inter–metal distance in the complexes is similar at *ca.* 4.835 Å. In the crystal packing, the terminal terpy ligands are involved in aryl embraces with the bridging ligand and the terpy ligand of another molecule, giving rise to

interesting two–dimensional supramolecular motifs. In the mononuclear complex **4.4**, the non–coordinated ring of the ligand **4.2** adopts a twisted confirmation.

The absorption spectrum exhibits overlapping MLCT bands due to Ru(dπ) → **4.2**(π*) and Ru(dπ) → terpy(π*) transitions in complex **4.4**. In the dinuclear complexes a large red shift in the Ru(dπ) → BL(π*) transition was observed due to the increased stabilisation of the azo–centered π*–orbital upon formation of the bimetallic system. Further insights into the electronic transitions are obtained from electrochemical studies which reveal a more positive reduction potential for the bridging ligand in the dinuclear complexes **4.3** and **4.5** when compared to **4.4**. Electrochemical studies also reveal that these ligands mediate very strong communication between the metal centres with comproportionation constants of $K_c > 10^{13}$.

Chapter 5

Bidentate ligands based on bis(pyridylimines)

5. Bidentate ligands based on bis(pyridylimines)

5.1. Introduction

This chapter describes a series of ligands that are Schiff bases derived from pyridine–2–carboxaldehyde. These molecules consist of two N=C–C=N moieties joined directly, or separated by spacers of different length, rigidity and conjugation.[292],[293] Transition metal complexes of pyridyl Schiff bases have found applications in catalysis[294] and crystal engineering,[295],[296] as these form coordination polymers[297] and 'grid–type' complexes.[298]

A large range of heterocyclic bridging ligands, with a variation at different points within the structure, can be represented by the generalised structure shown in Figure 5.1. The linker group X, can be varied by changing both the type[299–301] and/or the length of spacer.[292],[302–304] The former allows for the incorporation of different aromatic rings, while the latter allows for the changes in the flexibility of the ligand.[296],[302] Finally, the substituent R on the imine units can also be altered.[292],[303],[305] The ligands described in this chapter all have a structure in which the spacer group between the two imine halves is modified.

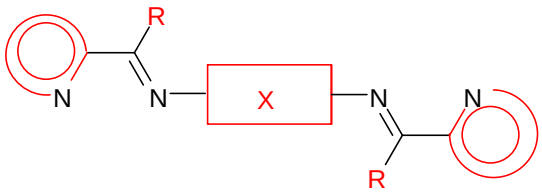

Figure 5.1. The generalised structure of the ligands.

In general, these ligands are similar to the azo ligands (discussed in previous chapters) as these possess low lying π*–orbitals, making them excellent π acceptors of metal d–orbital electron density. However, the N_2 linkages in azines with N–N single bonds are much more flexible when compared with the rigid moiety in azo compounds (N=N). Previous studies have shown that such ligands also present several possible mono– and binucleating coordination modes due to the flexibility of the ligand around the N–N single bond.[305],[306]

Recently, Cai *et al.*[307] reported long–range electron transfer processes for binuclear ruthenium complexes with two imine units linked directly or *via* spacers. According to their observations, the comproportionation constant K_c decreases with an increase in the number of phenyl rings or with the insertion of an oxygen atom between the two phenyl rings, while a

saturated CH_2 group increased the K_c values. Interestingly, the binuclear ruthenium complex containing a saturated $–OCH_2CH_2O–$ unit between the two phenyl groups gave a large K_c, which they attributed to the fact that the two metal sites could be close in space due to the increased flexibility of the bridging ligand.

It is clearly evident from previous studies that the extent of communication between metal centres decreases steadily as the π–overlap between the two halves of the bridging ligands decreases, which happens when the ligand is either lengthened, twisted or contains a saturated fragment. The research carried out by Chakraborty *et al.*[308] on a similar series of binuclear ruthenium complexes found only one quasi–reversible two–electron oxidation process, indicating simultaneous one electron oxidation of both the ruthenium centres [Ru(II)→Ru(III)]. This indicates that the metal–metal interaction decreases as the distance increases between the two imine units. On this basis we had reason to doubt the validity of the work reported by Cai *et al.*[307]

Thus, in order to investigate the results, a series of binuclear ruthenium complexes have been synthesised, in which the two pyridylimine ligands are linked at the imine nitrogen atom, either directly, or through a spacer of variable length, as shown in Figure 5.2.

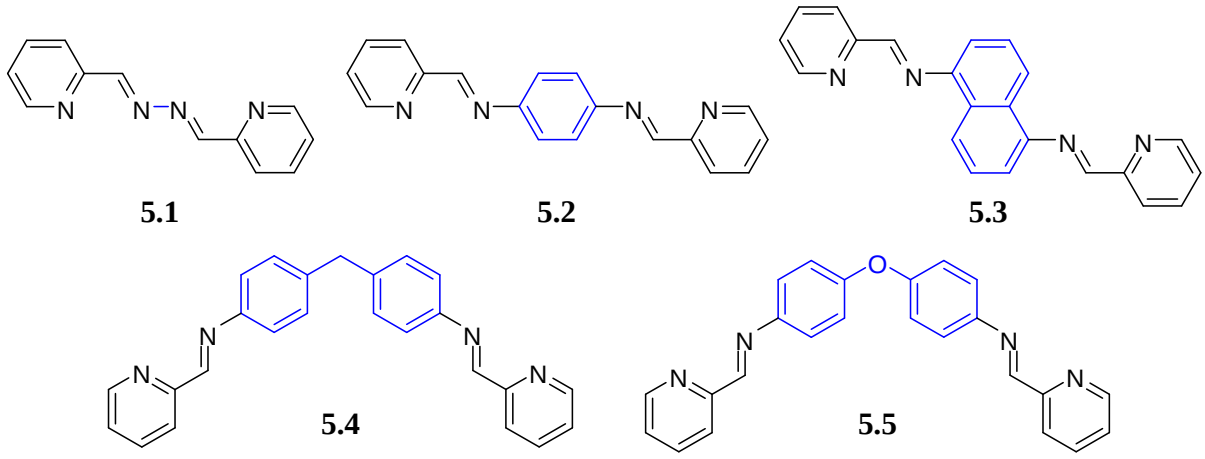

Figure 5.2. The doubly–bidentate pyridylimine–based bridging ligands.

5.2. Syntheses of the ligands

The bridging ligands, N,N'–bis(2–pyridylmethylene)azine **5.1**,[293] 1,4–bis(2–pyridylmethyleneamino)benzene **5.2**,[299] 1,5–bis(2–pyridylmethyleneamino)naphthalene **5.3**,[300] bis[4–(2–pyridylmethyleneamino)phenyl]methane **5.4**[299] and bis[4–(2–pyridylmethyleneamino)phenyl] ether **5.5**[301] were prepared by literature methods with some modifications to the purification techniques.

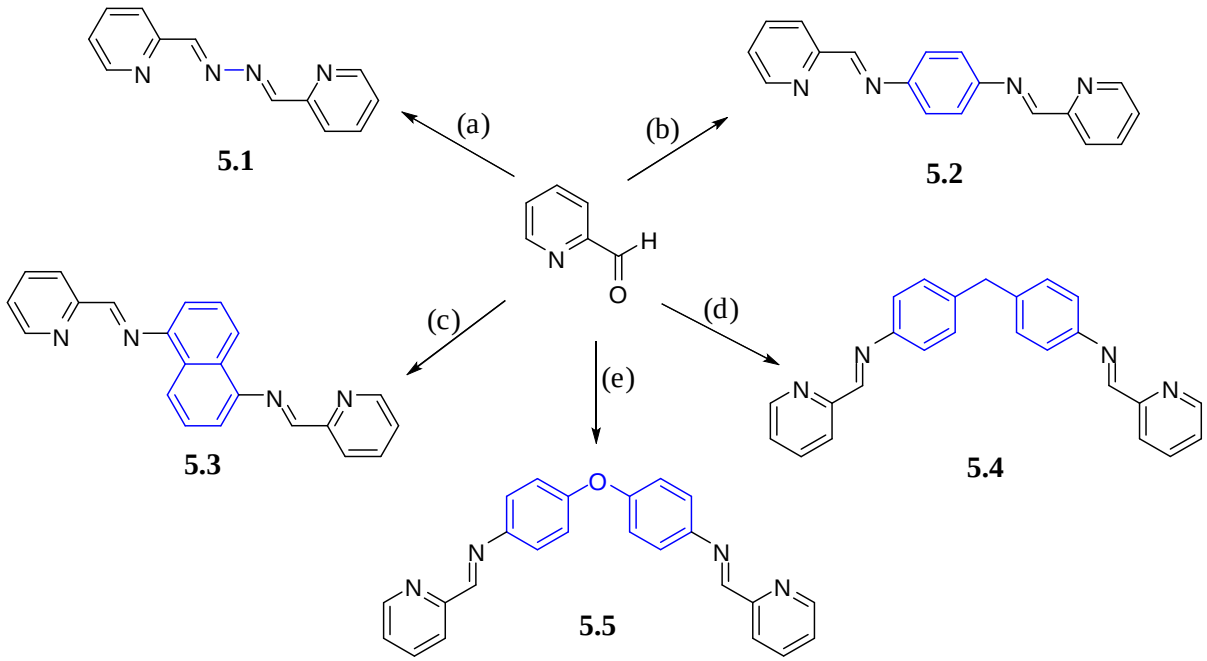

(a) NH_2NH_2, methanol, RT, 30 minutes, 56%; (b) 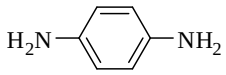 , ethanol, reflux, 4h, 69%;

(c) 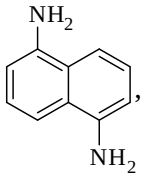 , ethanol, RT, 5h, 95%; (d) 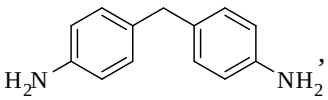 , methanol, reflux, 2h, 56%;

(e) 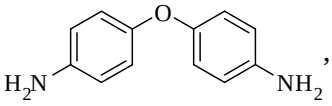 , methanol, reflux, 2h, 90%.

Scheme 5.1

The synthesis involved the condensation of pyridine–2–carbaldehyde with the corresponding diamine, as shown in Scheme 5.1, in a 2:1 stoichiometric ratio in ethanol or methanol to give the ligands **5.1** – **5.5** in moderate to high yields. All ligands were

characterised by NMR spectroscopy and mass spectrometry, and were found to be consistent with the previously reported literature data. The ^{1}H NMR spectra of the ligands show that both halves of the ligand are identical due to internal symmetry. The aromatic doublets corresponding to H6 and H3 of the pyridine ring were easily identified from the coupling constants and gCOSY experiments. The more downfield doublet was assigned to H6, since in a pyridine ring the 6–position is more electron deficient than the 3–position. The singlet corresponding to the azomethine proton (–HC=N–) ranges from δ~8.55 to 8.72 ppm. As an example, the ^{1}H NMR spectrum of **5.5** is shown in Figure 5.3.

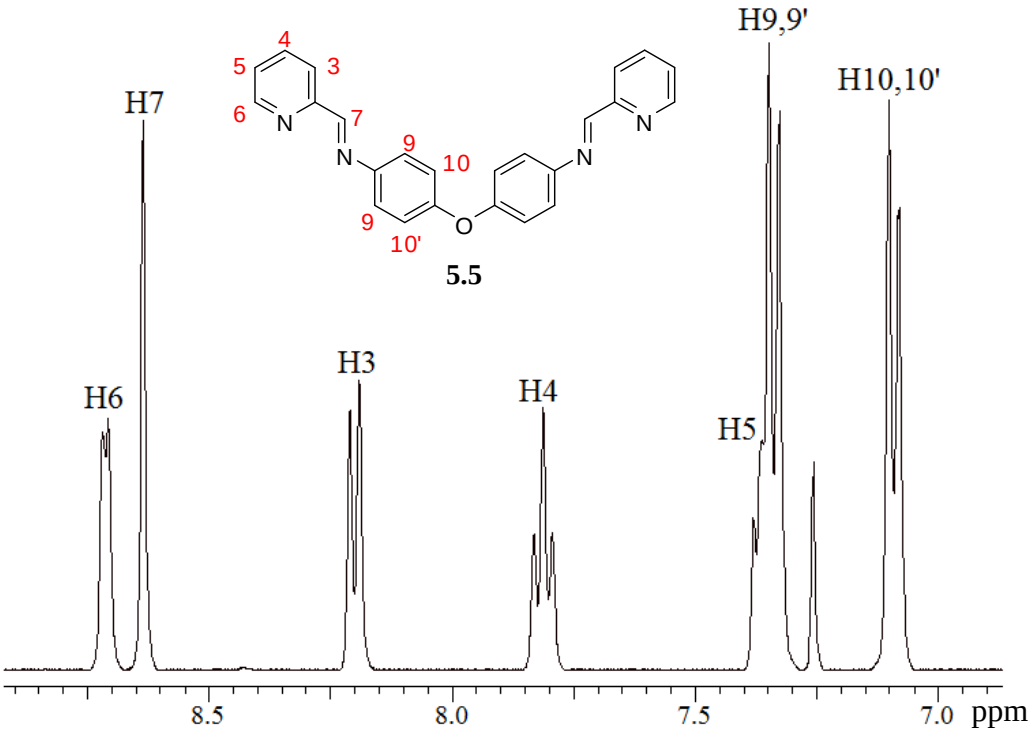

Figure 5.3. The ^{1}H NMR spectrum of ligand **5.5**.

5.3. Syntheses and Characterisations of the Complexes.

The bridging ligands **5.1** – **5.5** bind to the metal in a neutral and bidentate manner, forming bidentate chelate rings. The ruthenium complexes were synthesised by first heating a mixture of the ruthenium precursor, $[Ru(bpy)_2Cl_2]\cdot 2H_2O$ and silver perchlorate in ethanol for 1 hour. The reaction mixture was filtered through Celite®. The ligand was then added to the filtrate and the mixture was heated to reflux for 16 hours. The complexes were precipitated as perchlorate salts and purified by recrystallisation (Scheme 5.2).[308]

The reaction of the ruthenium starting complex $[Ru^{II}(bpy)_2(C_2H_5OH)_2]^{2+}$, with the ligands resulted in binuclear complexes, irrespective of the stoichiometric ratio used. All attempts to synthesise the corresponding mononuclear complexes were unsuccessful.

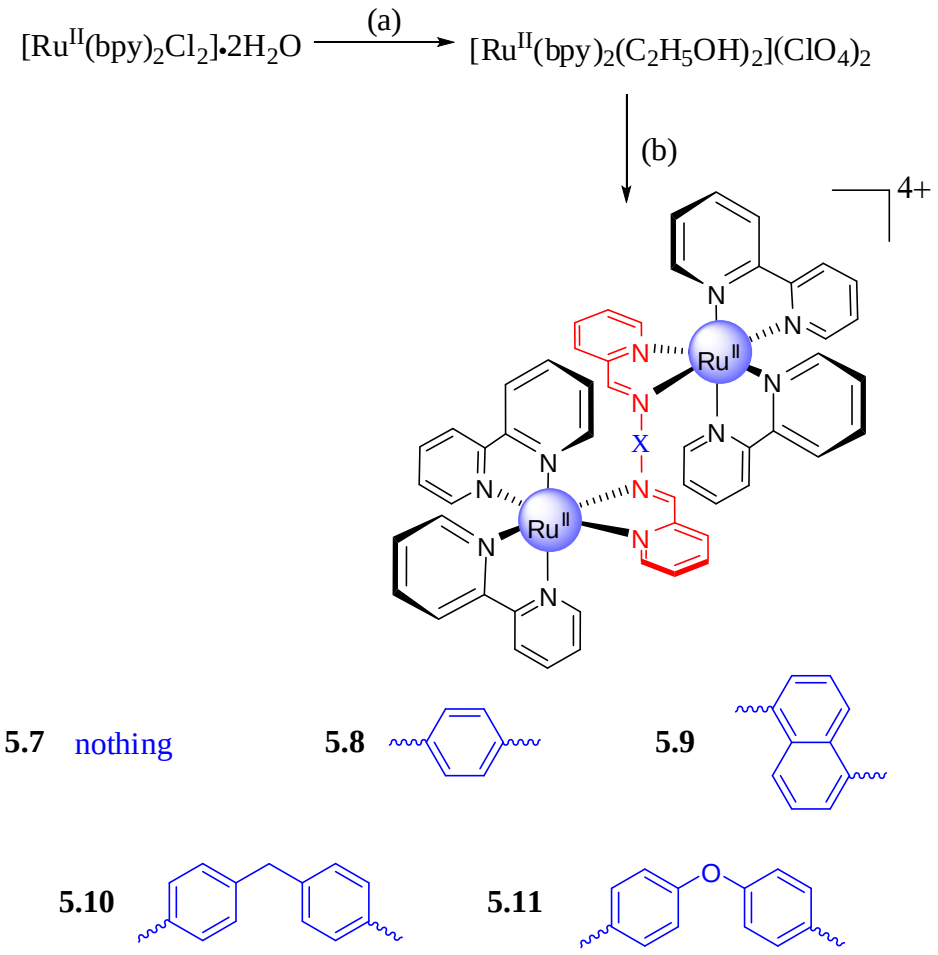

(a) $AgClO_4$, ethanol, reflux, 1h; (b) Ligand, reflux, 16h, 50-60%.

Scheme 5.2

5.3.1. Complexes of 5.1

During the synthesis of the binuclear complex **5.7** hydrolysis led to the *in situ* formation of the metal complex **5.6**, as shown in Scheme 5.3. The transition metal mediated hydrolysis of some Schiff bases have been reported previously.[309],[310] The hydrolysed mononuclear complex **5.6** was separated from the binuclear complex **5.7** on a SP Sephadex C–25 column *via* a gradient elution technique using a 0.1–0.5 M sodium chloride solution. The complex was then precipitated as a hexafluorophosphate salt.

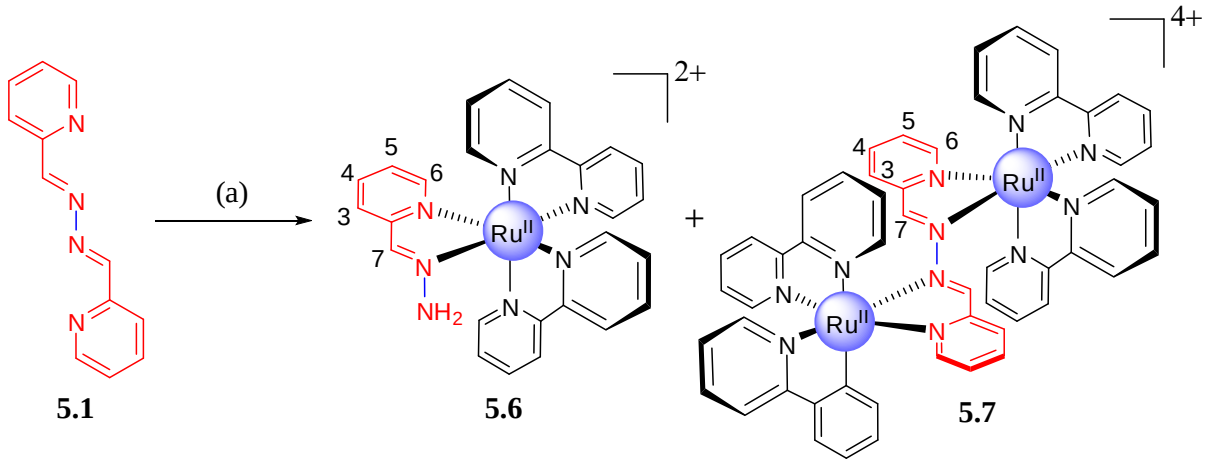

(a) [Ru(bpy)$_2$Cl$_2$], ethanol, reflux, 16h, 60%.

Scheme 5.3

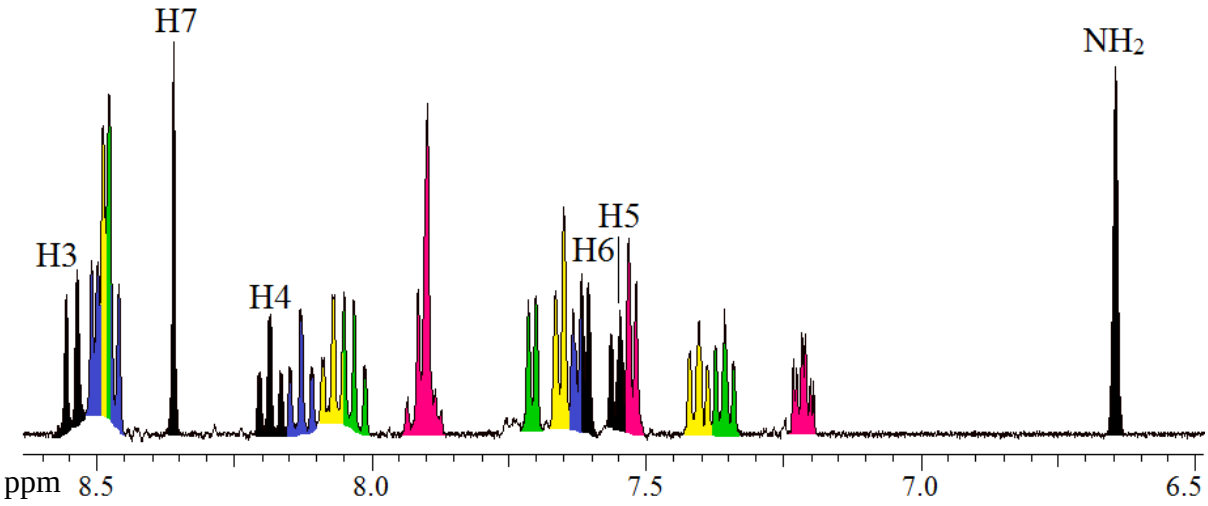

Figure 5.4. The ^{1}H NMR spectrum of complex **5.6**.

The ^{1}H NMR spectrum of the complex **5.6** is illustrated in Figure 5.4. The assignments were made on the basis of spin–spin coupling information, gCOSY and 1–D TOCSY experiments. The spectrum shows five different pyridyl ring environments, four for the bipyridines and one for the ligand pyridyl environment, which was identified by a gCOSY experiment in combination with HMBC, as shown in Figure 5.5. The imine carbon shows a correlation to the proton at δ~8.54 ppm indicating it as the H3 proton of the pyridine ring belonging to the ligand **5.1**. The presence of only five pyridyl ring environments and a broad singlet corresponding to NH_2 protons at 6.64 ppm indicates the hydrolysis of the non–coordinated imine to a free amine to give complex **5.6.** The proton signal corresponding to the azomethine (–HC=N) in complex **5.6** is at δ~8.36 ppm, which is more shielded relative to

the free ligand, δ~ 8.55 ppm. Unfortunately, attempts to grow crystals of **5.6** were unsuccessful.

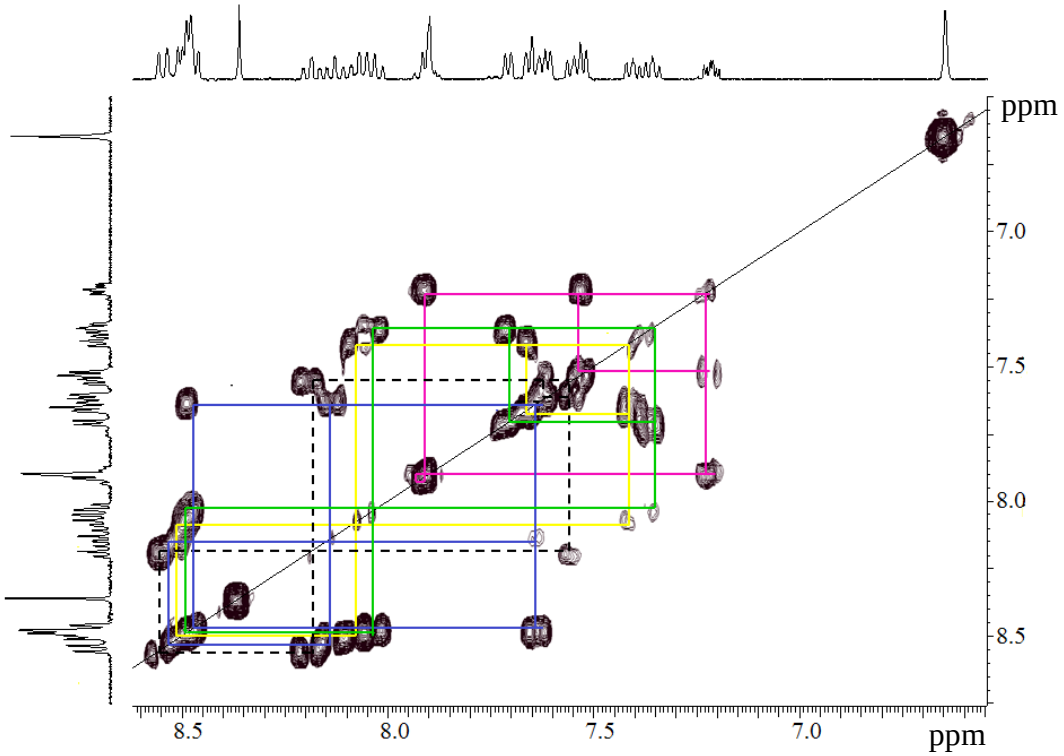

Figure 5.5. gCOSY spectrum of complex **5.6**.

In the binuclear complexes the presence of two–fold symmetry makes each half equivalent to the other. However, due to the asymmetric nature of the ligand, all five pyridine rings around each ruthenium centre are non–equivalent. The ^{1}H NMR spectrum for complex **5.7** in acetonitrile–d_3 is shown in Figure 5.6. The spectrum consists of 21 non–equivalent proton signals, 16 corresponding to the ancillary bipyridine ligands and five corresponding to the bridging ligand **5.1**.

The ^{1}H NMR spectrum shows five different pyridine ring environments, which are colour coded in Figure 5.6. The four rings corresponding to the ancillary bipyridines, and one for the ligand pyridine ring, were identified by previously discussed methods. The connectivity between the two pyridine rings of each bipyridine was identified by 1D ROESY experiments. The H3 proton (8.58 ppm) shows a correlation to the H3 proton (8.48 ppm) on the adjoining pyridyl ring of the same bipyridine. The azomethine singlet peak in complex **5.7** is strongly deshielded (δ 9.28 ppm) when compared to the free ligand (δ 8.55 ppm), due to the donation of electron density from the metal centre.

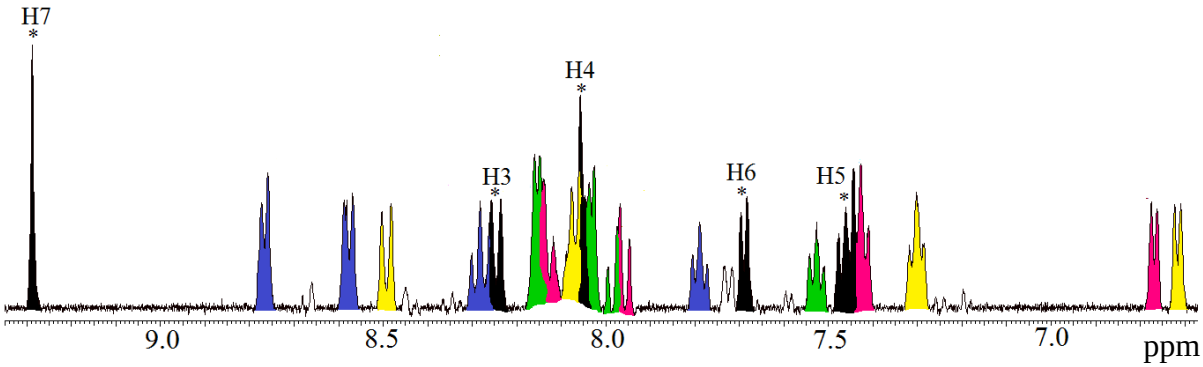

Figure 5.6. The ^{1}H NMR spectrum for the complex **5.7**.

In complex **5.7**, there are four environments for the H6 protons of the ancillary ligands. The H6 protons of pyridine rings from two different bipyridine ligands show the greatest change in chemical shift. This could be due to the fact that these protons are in close proximity to the ancillary ligands across the bridge. In the X–ray crystal structure (Figure 5.8), one of the protons lies directly over a pyridyl ligand of a bipyridine across the bridge, whereas the other one is in the plane of the ligand. The H6 proton of one of the pyridyl rings of bipyridine is strongly deshielded, due to the *trans*–effect of the metal. The fourth bpy–H6 proton is not in close proximity to the bridging ligand and hence experiences less ring–current anisotropy effects.

*Crystal Structure of **5.7***

Crystals of complex **5.7** were grown by vapour diffusion of diisopropyl ether into an acetonitrile solution of the complex. It crystallises in the triclinic space group *P*–1, with one ruthenium metal, half a ligand **5.1**, two bipyridine units, two hexafluorophosphate anions and one acetonitrile solvate molecule in the asymmetric unit, confirming the formation of the complex in a 2:1 metal to ligand ratio, as shown in Figure 5.7.

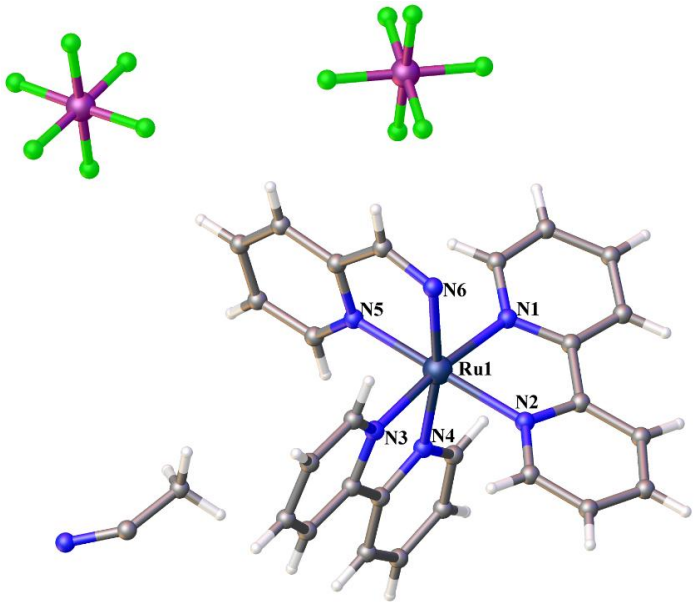

Figure 5.7. The asymmetric unit of complex **5.7.**

Due to the crystallographic centre of inversion at the centre of the ligand, the second half of the molecule is symmetry generated. The bridging ligand (**5.1**) binds to the ruthenium atom *via* the pyridine nitrogen (N5) and imine nitrogen (N6), as shown in Figure 5.8. The chelate angles are 78.65°(12) (N1–Ru1–N2), 79.15°(13) (N3–Ru1–N4) and 77.60°(11) (N5–Ru1–N6) with the *trans* N–Ru–N angles are greater that 170°, indicating a slight distortion in the octahedral geometry. The Ru–N_{py} bond distances (approximately 2.06 Å) are quite similar and correlate with previously reported literature values. The Ru–N_{imine} bond distance at 2.111(3) Å (Ru–N6) is slightly longer than the Ru–N_{py} bond distance of 2.066(3) Å (Ru1–N5). The distance between the two ruthenium metals is 5.297(5) Å, longer than the Ru···Ru distance in the azo containing complexes (*ca.* 4.9 Å), discussed in previous chapters.

The structure and conformation of the complex support the previously allocated ^{1}H NMR assignments. As the structure shows, the strongly shielded H3 proton (H23) of the pyridine ring from the bridging ligand lies directly over one of the bipyridine rings and is thus shielded due to through–space ring–current effects. The H6 proton (H11) of the pyridine ring from one bipyridine is strongly shielded, as it lies directly over the pyridyl ring of the bipyridine across the bridge. The significant deshielding of the H6 proton (H20) of a pyridyl ring is due to the *trans*–effect. The remaining two H6 protons, one of the pyridine ring of the bridging ligand and one of the ancillary ligand, are in relatively deshielded environments, since they are not directly over, or in the plane of the bridging ligand and hence experience less ring–current anisotropy.

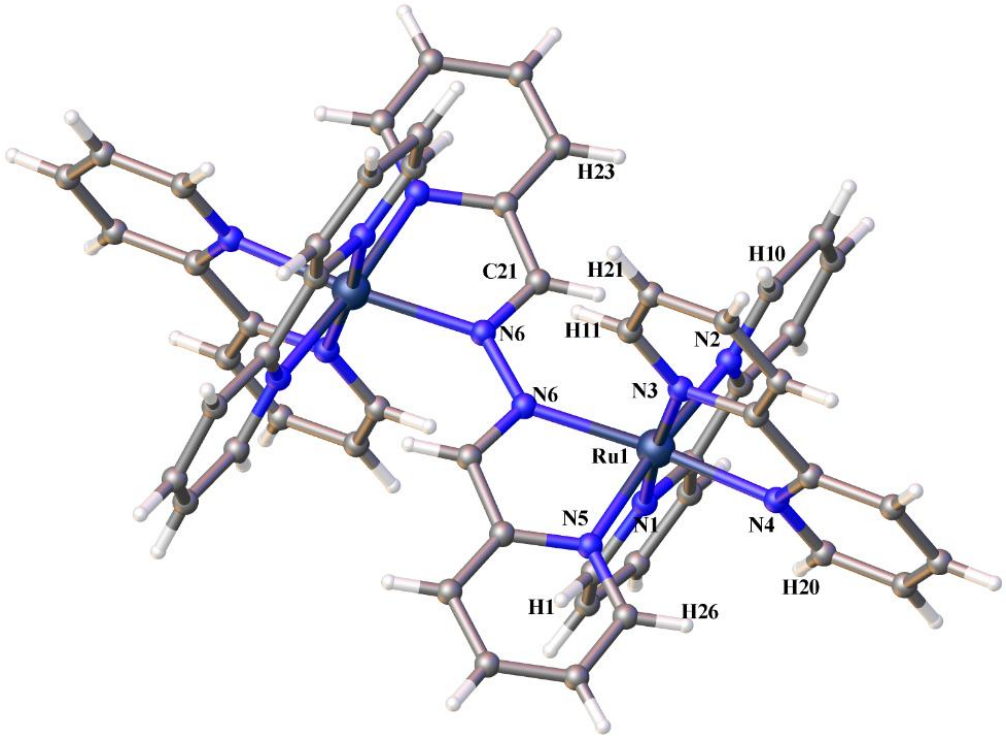

Figure 5.8. The X–ray crystal structure of complex **5.7**. The counterions and solvate molecules are omitted for clarity. Selected bond distances (Å) and bond angles (°): Ru1–N1 2.066(3), Ru1–N2 2.074(3), Ru1–N3 2.061(3), Ru1–N4 2.046(3), Ru1–N5 2.066(3), Ru1–N6 2.111(3), N6–N6 1.424(6), N1–Ru1–N2 78.65(12), N1–Ru1–N3 173.73(12), N1–Ru1–N4 96.97(12), N1–Ru1–N5 97.35(12), N1–Ru1–N6 89.43(11), N2–Ru1–N3 95.92(12), N2–Ru1–N4 83.28(12), N2–Ru1–N5 174.16(11), N2–Ru1–N6 106.43(11), N3–Ru1–N4 79.15(13), N3–Ru1–N5 87.83(12), N3–Ru1–N6 95.16(12), N4–Ru1–N6 169.32(11), N5–Ru1–N6 77.60(11).

5.3.2. Complexes of 5.2 – 5.5

Complexes **5.8** – **5.11** were all synthesised by the procedure described in Scheme 5.3. All the complexes were characterised by NMR spectroscopy and mass spectrometry. No evidence for any mononuclear complexes was seen. The ^{1}H NMR spectra of **5.8 – 5.11** are shown in Figure 5.9. Due to the presence of symmetry, both halves are equivalent, and accordingly each complex shows five different pyridyl rings irrespective of the spacer involved. The imine proton (H7) is the most deshielded of all with the H7 proton of **5.8** being more shielded (8.79 ppm) when compared to **5.7**, **5.9** – **5.11** ($\delta > 9.0$ ppm). The phenyl ring protons in **5.8** appear as a broad singlet at 6.13 ppm. No profound difference caused by the

phenyl methane spacer in **5.10** and the phenyl ether spacer in **5.11** were observed. The H6 protons of the bridging ligands **5.2** – **5.5** experience similar shielding due to the through–space ring–current anisotropy.

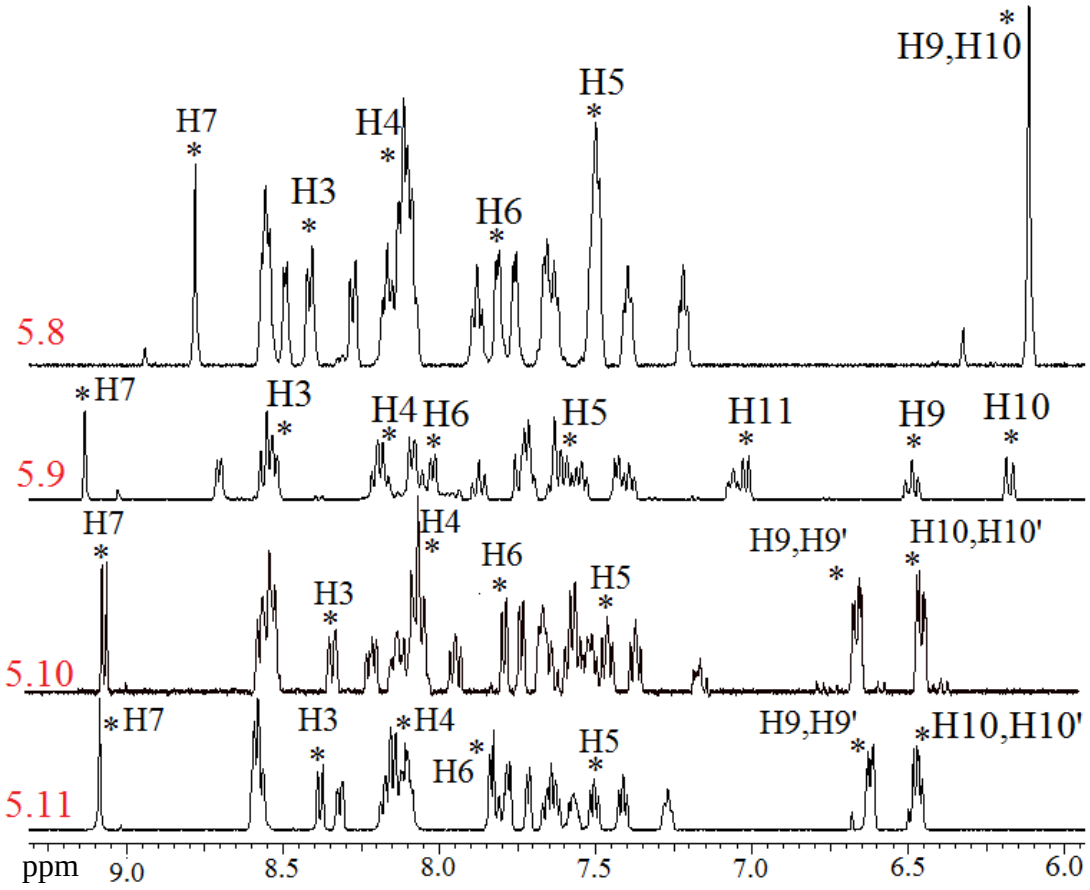

Figure 5.9. The ^{1}H NMR spectra of **5.8 – 5.11**.

*Crystal Structure of **5.8***

A single crystal suitable for X–ray analysis was obtained by diffusing diisopropyl ether into a solution of complex **5.8** in acetonitrile. The complex crystallises in the monoclinic space group $P2_1/c$, with half a molecule of **5.8**, two perchlorate anions and one acetonitrile solvate molecule in the asymmetric unit. The X–ray crystal structure of **5.8**, shown in Figure 5.10, contains each $Ru(bpy)_2$ fragment coordinated to the bridging ligand **5.2** through the imine nitrogen N6 and pyridyl nitrogen atom N5. The coordination sphere of ruthenium(II) is slightly distorted with the *trans* N–Ru–N angles greater than 172°. The Ru–N bond distances range between 2.05 – 2.07 Å and the terminal bipyridine chelate angles are 79.1(2)° and 78.88(2)°, which is similar to the complex **5.7**. The ligand **5.2** separates the two metal centres at a distance of 8.534(1) Å (Ru···Ru) significantly longer than complex **5.7** (5.296(1) Å). The

phenyl ring of the ligand **5.2** is twisted at *ca.* 52.30 Å and is between the cofacial bipyridine–pyridine rings within the complex, as shown in Figure 5.10. The oxygen atoms of the non–coordinating perchlorate anions are involved in weak hydrogen bonding with the ligand molecule, which stabilises the crystal packing.

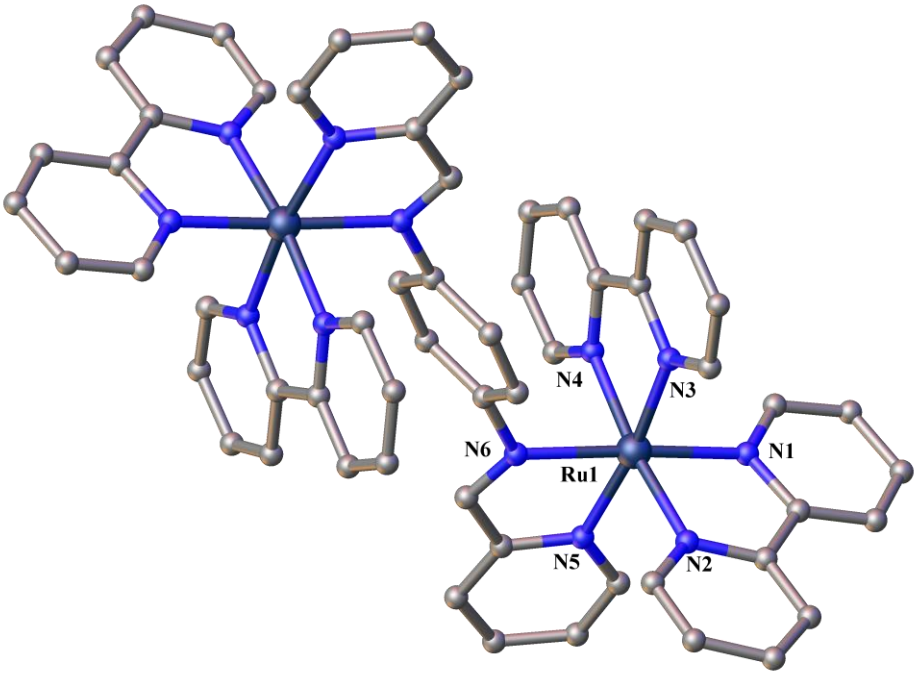

Figure 5.10. The X–ray crystal structure of **5.8** showing the twisted phenyl ring. Hydrogen atoms, counterions and solvate molecules are omitted for clarity. Selected bond distances (Å) and bond angles (°): Ru1–N1 2.055(3), Ru1–N2 2.062(2), Ru1–N3 2.047(3), Ru1–N4 2.066(3), Ru1–N5 2.059(3), Ru1–N6 2.069(2), N1–Ru1–N2 78.78(10), N3–Ru1–N1 90.09(12), N3–Ru1–N2 95.46(11), N4–Ru1–N1 96.83(11), N4–Ru1–N2 172.95(12), N4–Ru1–N3 78.93(14), N5–Ru1–N1 97.01(12), N5–Ru1–N2 89.46(10), N5–Ru1–N3 172.04(10), N5–Ru1–N4 96.59(13), N6–Ru1–N1 174.73(11), N6–Ru1–N2 102.03(9), N6–Ru1–N3 95.00(10), N6–Ru1–N4 82.85(10), N6–Ru1–N5 77.83(10).

5.4. Electronic Absorption Spectroscopy and Electrochemistry

The UV/Visible absorption spectra of all the complexes show strong ligand–centred absorptions below 300 nm and MLCT absorption bands at or above 400 nm, as shown in Figure 5.11. The mononuclear complex **5.6** exhibits a band at 438 nm with an associated shoulder at 411 nm. The visible absorption spectra for the binuclear complexes **5.7** – **5.11** are also shown in Figure 5.11. Complex **5.7** displays two distinct MLCT bands at 524 nm and 420 nm. Complexes **5.8 – 5.11** show similar transition patterns, with bands in the visible region arising from the MLCT transitions at *ca.* 483 nm, associated with shoulders at *ca.* 427 nm and 344 nm. Based on the intensity of these visible bands, the lowest energy band is assigned to the Ru(dπ) → BL(π*) transition, as this is the lowest energy gap, between the HOMO of the metal and LUMO of the ligand. The nature of the bridging ligands also influence the position of the bands. A distinct blue shift of ~40 nm was observed in complexes **5.8** and **5.9** compared to complex **5.7,** whereas a shift of only 5 nm was found between **5.10** and **5.11**.

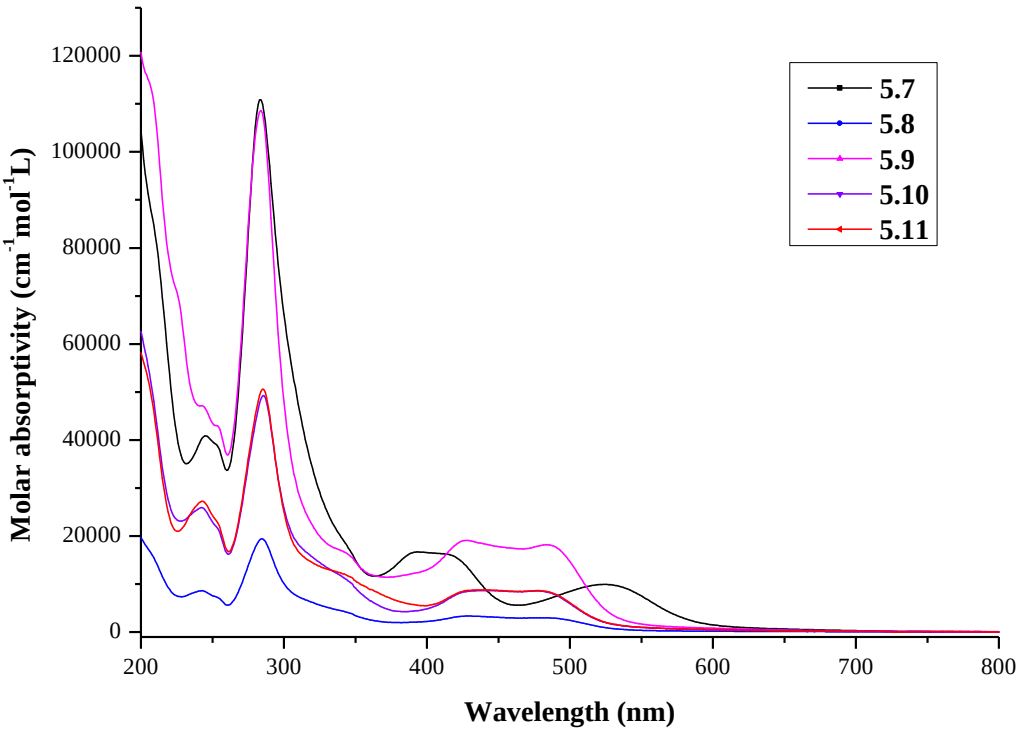

Figure 5.11. UV/Visible spectra for complexes **5.7** – **5.11** in acetonitrile at 298 K.

The redox properties of the complexes were studied by differential pulse voltammetry in an acetonitrile solution. Figure 5.12 shows the differential pulse voltammogram for **5.7** –

5.11. The ruthenium metal–based oxidation and the ligand–based reduction potentials are listed in Table 5.1. The redox potentials of the complexes **5.6** –**5.11** indicate that these complexes are easier to oxidise than $[Ru(bpy)_3]^{2+}$, except **5.7** which oxidises at a similar potential. The mononuclear complex **5.6** exhibits a one–electron redox couple for the ruthenium metal centre (Ru^{II}/Ru^{III}) and two well resolved, reversible reductions of the ligand. The binuclear complexes **5.8** – **5.11** all show one two–electron redox couple corresponding to the oxidation of the metal centres, except for **5.7**. Complex **5.7** exhibits two reversible one–electron redox couples corresponding to two successive oxidations of the metal centres separated by 100 mV (K_c = 49), indicating weak electron–coupling between the metal centres. However, the simultaneous two–electron oxidation of the metal centres in **5.8** – **5.11** suggest that the extent of communication between the metal centres decreases with increasing spacer length between the bis(pyridylimine) units.

Table 5.1. Absorption maxima[a] and reduction potentials[b,c] for complexes **5.6** – **5.11**.

Complex	λ, nm	$E_{1/2ox2}$	$E_{1/2ox1}$	$E_{1/2red1}$	$E_{1/2red2}$	$E_{1/2red3}$
$(Ru(bpy)_3^{2+})$[6]	452		+1.26	–1.33	–1.51	
5.6	438, 411		+0.98	–1.80	–2.04[d]	
5.7	524, 420, 393	+1.33	+1.23	–0.73	–1.22	–1.87[d]
5.8	483, 429, 344		+0.99[e]	–1.11[f]	–1.47[f]	–1.85[d]
5.9	483, 427, 344		+1.00[e]	1.16[f]	–1.37	–1.92[d]
5.10	478, 425, 343		+0.97[e]	–1.36	–1.85[d]	
5.11	478, 427, 343		+0.94[e]	–1.38	–1.86[d]	

[a] In acetonitrile (± 2 nm).
[b] In V *vs* $Ag/AgNO_3$ in CH_3CN/0.1 M $[(n–C_4H_9)_4]ClO_4$.
[c] Calculated from differential pulse voltammetry.
[d] Two–electron reduction.
[e] Two–electron oxidation.
[f] Irreversible process.

The binuclear complexes all show multiple ligand based reductions in the cathodic region. The first two reductions in **5.7** are assigned to reductions of the bridging ligand **5.1** in the low–lying π*–orbitals of the imine functionality. The introduction of both phenyl and naphthyl groups in **5.8** and **5.9**, respectively, shifts the reduction potential to more positive values due to the increased π–conjugation. In **5.10** and **5.11** the insertion of a $–CH_2–$ or a oxygen atom, respectively, between the phenyl group makes the reduction of the ligand more negative.

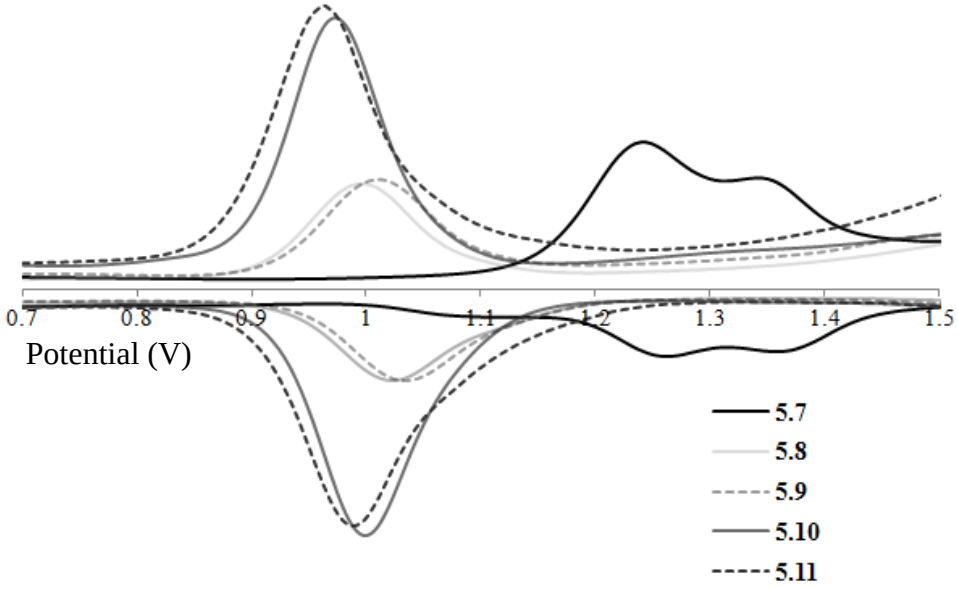

Figure 5.12. The oxidation waves of the differential pulse voltammograms for complexes **5.7** – **5.11**.

5.5. Summary

In summary, the bis(pyridylimine) ligands **5.1** – **5.5** were readily prepared by the condensation of pyridine–2–carboxaldehyde with the corresponding amine in reasonable yields. The binuclear ruthenium complexes **5.7** – **5.11** were synthesised by reaction of ligand with a ruthenium(II) precursor in a 1:2 ligand to metal ratio. A mononuclear complex **5.6** was also obtained as a result of the hydrolytic decomposition of ligand **5.1**.

The X–ray crystal structures of the binuclear complexes **5.7** and **5.8** show that varying the length of the spacer between the imine units results in an increase in the Ru···Ru separation. Electrochemical studies revealed that ligand **5.1** mediates a weak interaction between the metal centres. However, in the binuclear complexes **5.8** – **5.11**, a complete absence of communication between the metal centres was observed, presumably due to the increased distance and/or flexibility across the bridging ligand **5.2** – **5.5**. These results are in stark contrast to those reported by Cai *et al.*[307] and raise serious doubts as to the validity of their claim that all these ligands facilitate strong metal–metal interactions.

Chapter 6

Metallosupramlecular Chemistry

6. Metallosupramolecular Chemistry

6.1. Introduction

Supramolecular assemblies involving nitrogen heterocycles with different silver(I) salts have been extensively reported in the literature.[167],[190–195] The coordination sphere of silver(I) is very flexible and displays a variety of coordination numbers and geometries. Due to the weak nature of silver–ligand bonds, non–covalent interactions and crystal packing forces have a greater influence on the overall structure.[187–189] The self–assembly process with various counterions, ligand to metal molar ratio and the type of solvent, may lead to different molecular architectures.[189],[224–228]

In order to further explore the coordination chemistry of the azo ligands, a number of complexes were synthesised using different silver(I) salts in a 1L:2M ratio (where, L = ligand and M = metal) in an appropriate solvent. Slow evaporation of the resulting mixture gave crystals suitable for X–ray analysis. The complexes were also characterised by mass spectrometry, elemental analysis and IR spectroscopy.

6.2. Metallosupramolecular chemistry of azo–based ligands

*6.2.1. Complex of **2.1**, [Ag(**2.1**)](SO$_3$CF$_3$), **6.1***

Complex **6.1** was obtained from reaction of **2.1** with two equivalents of silver triflate. It crystallises in the monoclinic space group $P2_1/n$, with one silver atom, two half ligands of **2.1** and one non–coordinated triflate anion in the asymmetric unit, revealing a M_1L_1 type coordination complex, as shown in Figure 6.1. Each of the two independent ligands lies on a crystallographic centre of inversion.

The structure grows into a one–dimensional polymer, as shown in Figure 6.2, with four–coordinate silver atoms coordinated to two molecules of **2.1** through the N_{azo} and N_{py} atoms. The azo ligand **2.1** adopts an "S–frame" conformation and bridges two silver atoms at a distance of 5.487(2) Å. The Ag–N_{azo} bond distance [*ca.* 2.41 Å] is longer than the Ag–N_{py} bond distance [*ca.* 2.25 Å] due to the absence of π–backbonding and are consistent with these previously reported for [(CF_3SO_3)Ag(**2.1**)Ag(CF_3SO_3)].[162]

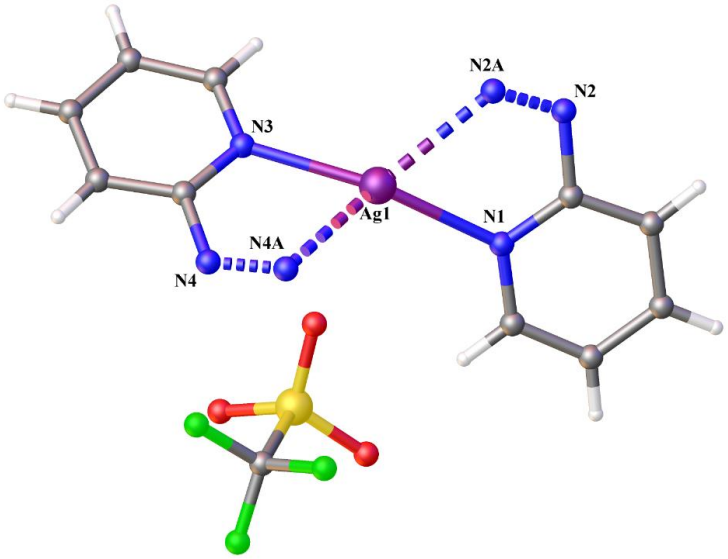

Figure 6.1. The asymmetric unit of **6.1** with atom labelling. Selected bond distances (Å): Ag1–N2 2.400(1), Ag1–N1 2.250(1), Ag1–N4 2.425(1), Ag1–N3 2.246(1), N2–N2A 1.253(3), N4–N4A 1.250(3). Selected bond angles (°): N1–Ag1–N2 68.96(5), N2–Ag1–N4 133.91(4), N1–Ag1–N4 116.94(5), N3–Ag1–N2 124.39(5), N3–Ag1–N1 157.46(5), N3–Ag1–N4 68.83(5).

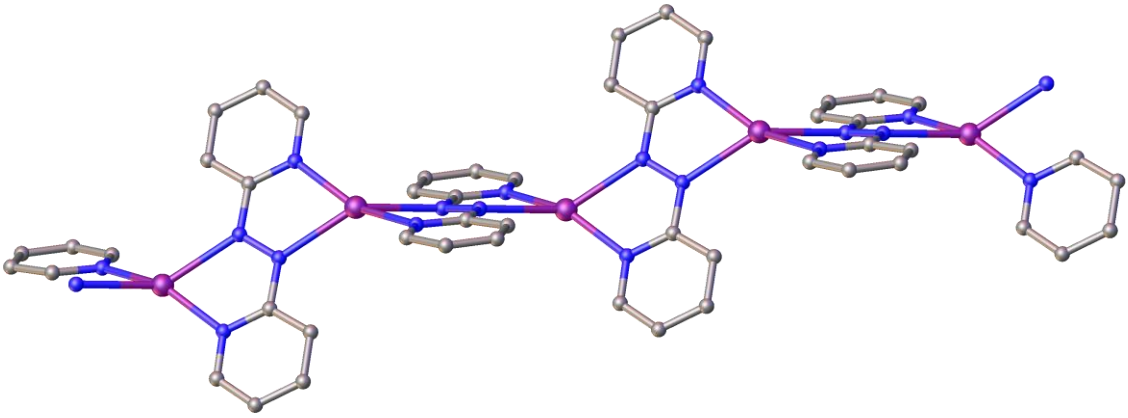

Figure 6.2. Part of the 1D polymeric structure of **6.1**. Hydrogen atoms and non–coordinating counterions are omitted for clarity.

6.2.2. Complex of 2.3, [Ag_2(2.3)](CO_2CF_3)$_2$, 6.2

Slow evaporation of **2.3** and silver(I) trifluoroacetate in a mixture of acetonitrile and methanol gave red crystals of **6.2**. The structure solved in the monoclinic space group $P2_1/n$, revealing a 1L:2Ag ratio or Ag_2L type coordination polymer. The asymmetric unit contains one full molecule of **2.3**, two silver atoms and two trifluoroacetate anions as shown in Figure

6.3. Once again, within the complex **6.2**, ligand **2.5** adopts the "S–frame" conformation and acts as a bridge separating the silver atoms at a distance of 5.783(3) Å [Ag1···Ag2A].

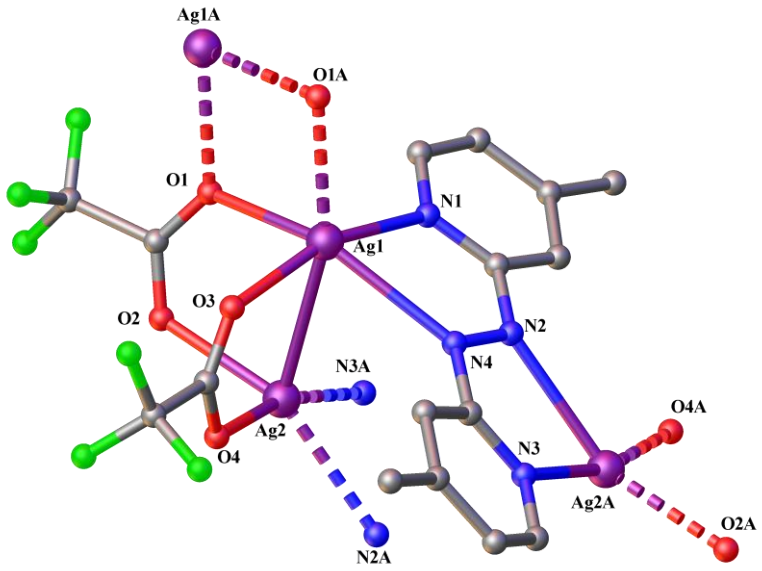

Figure 6.3. The asymmetric unit of complex **6.2**. All the hydrogen atoms are omitted for clarity. Selected bond distances (Å): Ag1–Ag2 2.925(2), Ag1–O1 2.497(2), Ag1–O1A 2.424(2), Ag1–O3 2.299(2), Ag1–N1 2.312(2), Ag1–N4 2.580(2), Ag2–O2 2.429(2), Ag2–O4 2.222(2), Ag2A–N2 2.625(2), Ag2A–N3 2.232(2), N2–N4 1.247(3). Selected bond angles (°): O1–Ag1–N4 127.34(6), O1–Ag1–Ag2 78.11(4), O1A–Ag1–N4 140.70(6), N1–Ag1–O1A 90.72(6), O2–Ag2–N2A 143.14(6), O3–Ag1–O1 94.28(6), O3–Ag1–N1 163.46(6), O3–Ag1–O1A 99.81(6), O4–Ag2–Ag1 85.33(5), O4–Ag2–N3 165.52(7), N1–Ag1–Ag2 88.54(5), N3A–Ag2–N2A 65.27(6), N1–Ag1–O1 96.38(6), O1–Ag1A–O1A 84.07(6), O1A–Ag1–Ag2 161.58(4), O2–Ag2–Ag1 85.09(4), N3A–Ag2–O2 97.15(7), O3–Ag1–Ag2 77.11(4), O3–Ag1–N4 101.41(6), O4–Ag2–O2 95.26(7), O4–Ag2–N2A 100.26(6), N1–Ag1–N4A 65.55(6), N4–Ag1–Ag2 70.79(4), N3A–Ag2–Ag1 103.12(5).

The asymmetric unit grows into a dimeric unit (Figure 6.4a) which extends into a one–dimensional coordination polymer with alternating Ag–O bonding, as shown in Figure 6.4b. The Ag–O bond distance within the dimeric unit [Ag1–O1 2.497(2) Å] is longer than the outer Ag–O bond distance [Ag1–O1A 2.424(2) Å].

The trifluoroacetate anions coordinate in a bidentate manner through O1, O2 and O3, O4 and bridge two silver atoms (Ag1–Ag2) at a relatively short distance of 2.925(3) Å. In addition, O1 adopts a bidentate coordination mode and bridges two silver atoms

(Ag1···Ag1A) at 3.655(4) Å. Two silver environments are present in the structure; one where the silver atom (Ag1) is six–coordinate with one silver atom (Ag2), two nitrogen atoms (N1 and N4) and two oxygen atoms of the trifluoroacetate anions (O3 and O1) and one oxygen atom from a crystallographically related anion (O1A). A second five–coordinate silver atom (Ag2) coordinates through one silver atom (Ag1), two nitrogen atoms (N2 and N3) and two oxygen atoms of the trifluoroacetate anions (O2 and O4). As expected, the average Ag–N_{azo} bond length is longer than the average Ag–N_{py} bond length at 2.60 and 2.27 Å, respectively.

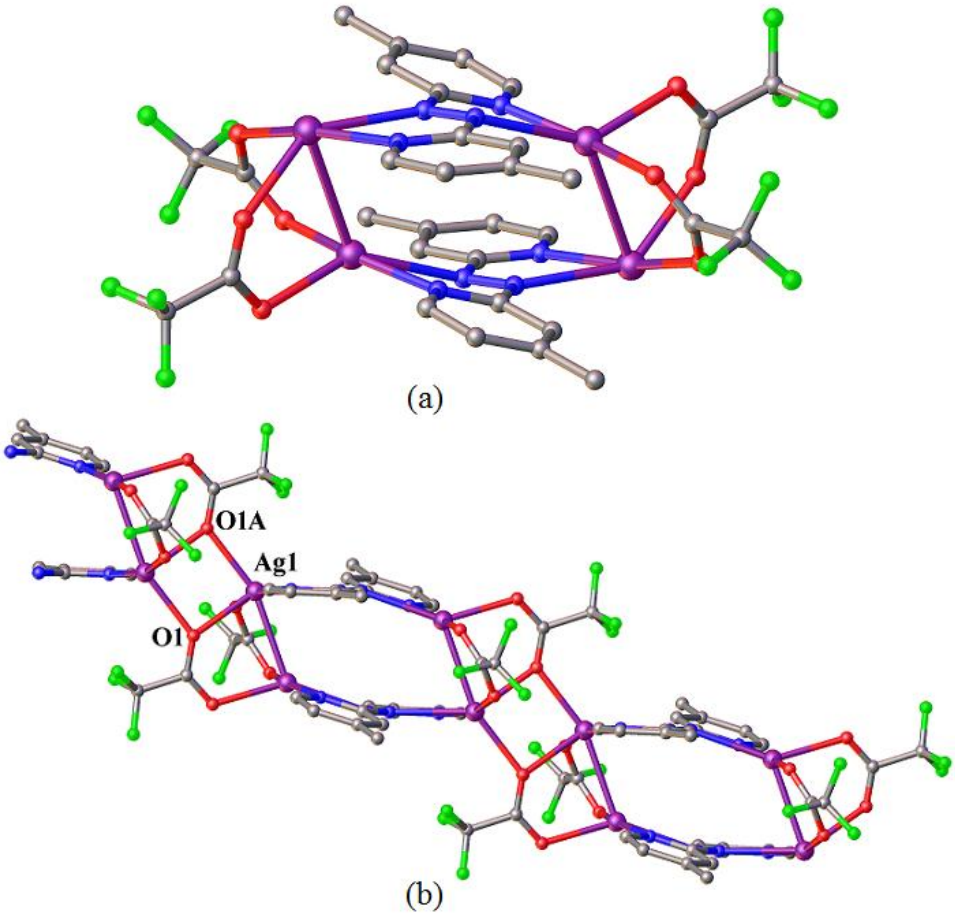

Figure 6.4. (a) Dimeric unit of **6.2**. (b) A perspective view of the extended 1D polymer of **6.2**.

6.2.3. Complex of 2.5

Reaction of silver(I) nitrate in acetonitrile with **2.5** in a mixture of methanol/dichloromethane resulted in a complex which was characterised by elemental analysis as $[Ag_2(\mathbf{2.5})](NO_3)_2{\cdot}CH_3OH{\cdot}H_2O$ (**6.3**). Slow evaporation of the reaction mixture

gave red crystals of **6.3**, which were suitable for X–ray crystallography. The structural analysis revealed a one–dimensional coordination polymer in a 1:1 silver to ligand ratio.

*[Ag_2(**2.5**)](NO_3)$_2$, **6.3***

Complex **6.3** crystallised in the tetragonal space group $P4_2/n$, with two half molecules of **2.5**, one silver atom, and one nitrate anion in the asymmetric unit, as shown in Figure 6.5. The silver atom has a distorted trigonal–bipyramidal geometry, involving coordination through the two pyridine nitrogen atoms of two different ligand molecules, two azo nitrogen atoms of the crystallographically related ligand molecules, and one oxygen atom of the nitrate anion.

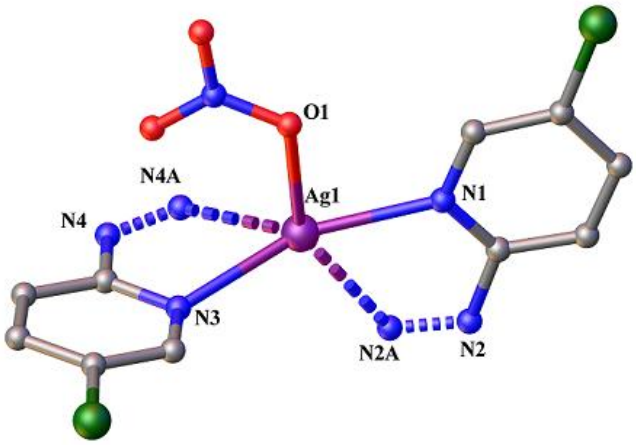

Figure 6.5. The full asymmetric unit of complex **6.3**. All the hydrogen atoms are omitted for clarity. Selected bond distances (Å) and bond angles (°): Ag1–N1 2.269(1), Ag1–N2A 2.589(1), Ag1–N3 2.326(1), Ag1–N4A 2.414(1), Ag1–O1 2.557(1), N2–N2A 1.249(2), N1–Ag1–N3 155.92(4), N1–Ag1–N4A 134.87(4), N3–Ag1–N4A 68.02(4), N1–Ag1–O1 86.13(4), N3–Ag1–O1 93.56(4), N4A–Ag1–O1 107.50(4), N1–Ag1–N2A 66.05(3), N3–Ag1–N2A 109.07(4), N4A–Ag1–N2 97.28(3), O1–Ag1–N2A 151.43(3).

Ligand **2.5** acts as a bidentate ligand, bridging the two silver atoms at a distance of 5.819(3) Å. All the silver–nitrogen and silver–oxygen bond lengths are consistent with structurally related molecules. In complex **6.3**, the Ag–N_{azo} bond length is longer than the Ag–N_{py} bond lengths. The overall structure is a one–dimensional coordination polymer with the nitrate ion alternating on opposite sides at each silver atom of the coordination polymer, as shown in Figure 6.6.

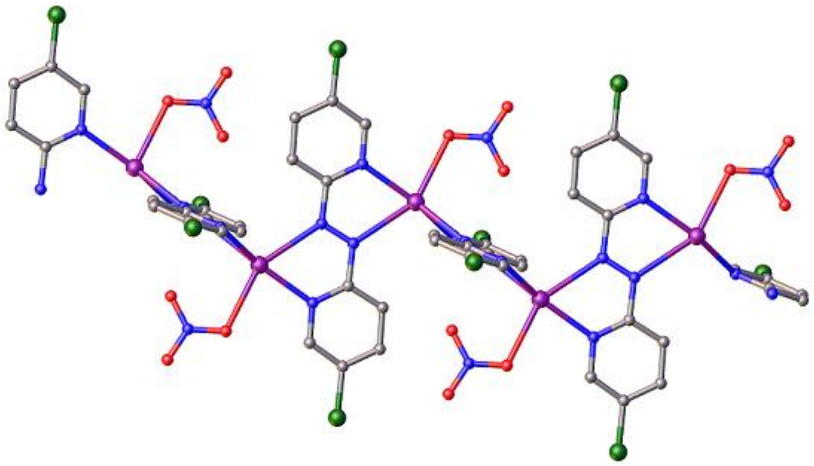

Figure 6.6. A perspective view of the 1D polymeric structure of **6.3** with hydrogen atoms omitted for clarity.

6.2.4. Complexes of 3.1

Ligand **3.1** gave a one–dimensional coordination polymer **6.4** and **6.5** with silver(I) perchlorate and silver(I) nitrate, respectively. Despite using a 1L:2M stoichiometric ratio of the reactants, the ratio was 1:1 as shown in Scheme 6.1. The compositions were confirmed by elemental analysis and the structures were unambiguously characterised by X–ray analysis.

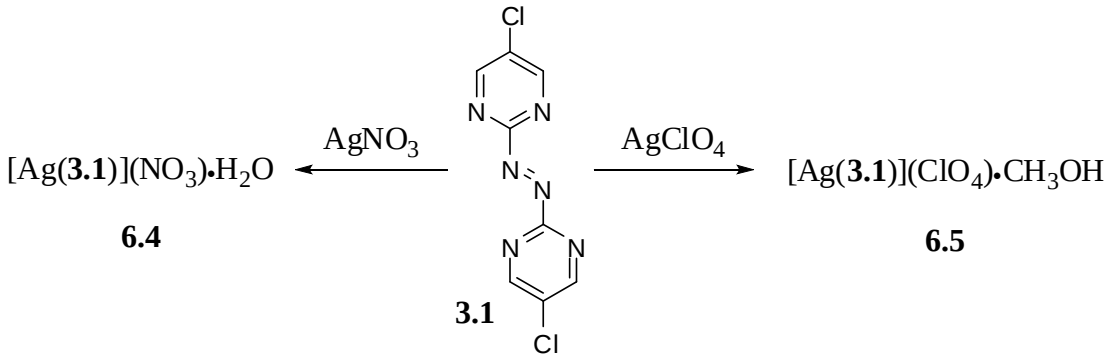

Scheme 6.1

*[Ag(**3.1**)](ClO$_4$), **6.4** and [Ag(**3.1**)](NO$_3$), **6.5***

Complex **6.4** crystallised in the triclinic space group *P*–1, with two half molecules of **3.1**, one silver atom and two half perchlorate anions, as shown in Figure 6.7a. The perchlorate ions are non–coordinating, disordered and lie on crystallographic centres of inversion.

Complex **6.5** crystallised in the triclinic space group *P*–1. The asymmetric unit contains one full, and two half molecules of **3.1** with two silver atoms and two non–coordinating nitrate anions as shown in Figure 6.7b.

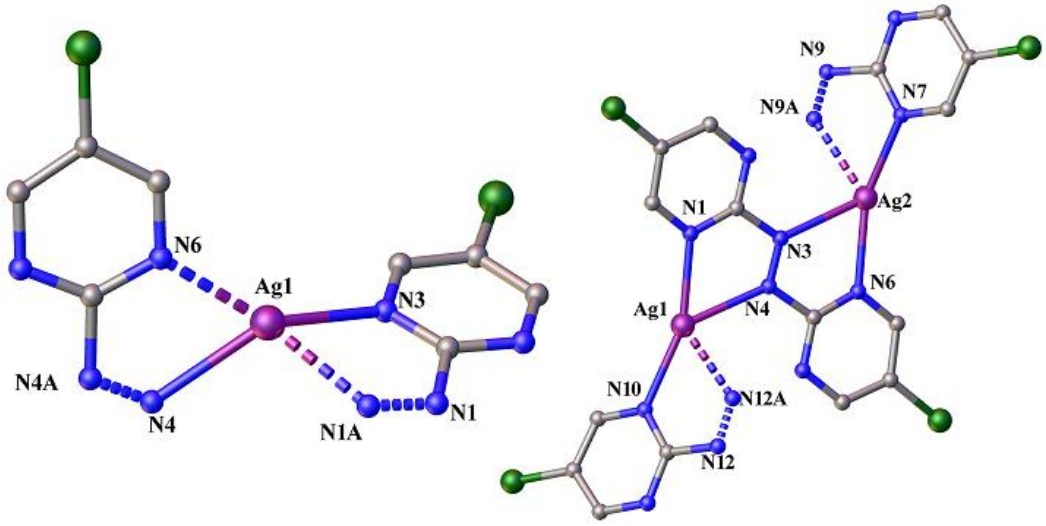

(a) (b)

Figure 6.7. The asymmetric unit of (a) **6.4** and (b) **6.5**. All the hydrogen atoms and counterions are omitted for clarity. Selected bond distances (Å) and bond angles (°): (**6.4**) Ag1–N1A 2.354(3), Ag1–N3 2.311(3), Ag1–N4 2.353(3), Ag1–N6 2.309(3), N1–N1A 1.234(5), N4–N4A 1.247(5), N3–Ag1–N1A 68.19(9), N3–Ag1–N4 138.47(9), N4–Ag1–N1A 105.32(9), N6–Ag1–N1A 133.18(9), N6–Ag1–N3 146.74(9), N6–Ag1–N4 68.11(9). (**6.5**) Ag1–N1 2.272(3), Ag1–N4 2.469(3), Ag1 N10 2.302(3), Ag1 N12A 2.423(3), Ag2–N3 2.496(3), Ag2 N6 2.312(3), Ag2 N7 2.329(3), Ag2 N9A 2.435(3), N3–N4 1.240(5), N4–Ag1–N1 66.83(11), N10–Ag1–N12A 67.41(12), N6–Ag2–N3 66.16(11), N7–Ag2–N9A 66.61(11), N10–Ag1–N1 160.83(12), N6–Ag2–N7 158.76(12), N10–Ag1–N4 128.80(11), N7–Ag2–N3 122.12(11), N12A–Ag1–N1 128.15(12), N12A–Ag1–N4 91.00(10), N3–Ag2–N9A 90.41(10), N6–Ag2–N9A 134.62(12).

In both **6.4** and **6.5**, the silver atom is four–coordinate with two azo nitrogen atoms and two pyridine nitrogen atoms from two molecules of the ligand. In **6.4**, the largest bond angle around Ag1 is between the pyridine nitrogen atoms of the two ligand molecules (N3–Ag1–N6) with a bond angle of 146.74(9)° and the second largest bond angle is between the azo nitrogen N4 and pyridine nitrogen atom N3 of 138.47(9)°. In **6.5**, the largest bond angle around Ag1 is also between the pyridine nitrogen atom N1 and N10 from two different ligand molecules with a bond angle of 160.83(12)° and the second largest bond angle of 128.80(11)° is between the pyridine nitrogen N10 and an azo nitrogen atom N4. Around Ag2, the largest

bond angle is between the pyridine nitrogen atom N6 and N7 from two different ligand molecules with a bond angle of 158.76(12)° and the second largest bond angle of 134.62(12)° is between the pyridine nitrogen N6 and an azo nitrogen atom N9A.The calculated τ_4 value[311] of 0.53 (Ag1) in **6.4** and 0.49 (Ag1) and 0.47 (Ag2) in **6.5**, reveal a seesaw geometry for the silver atoms.

In spite of the different arrangement of the symmetry elements in the structure, complexes **6.4** and **6.5** both propagate into one–dimensional coordination polymers, as shown in Figure 6.8, similar to **6.1** (Figure 6.2). Ligand **3.1** bridges two silver atoms at distances of 5.444(2) and 5.653(2) Å in **6.4** and **6.5**, respectively. The Ag–N bond lengths are consistent, and range from 2.3–2.5 Å, with the Ag–N_{azo} bond again longer than the Ag–N_{py} bond.

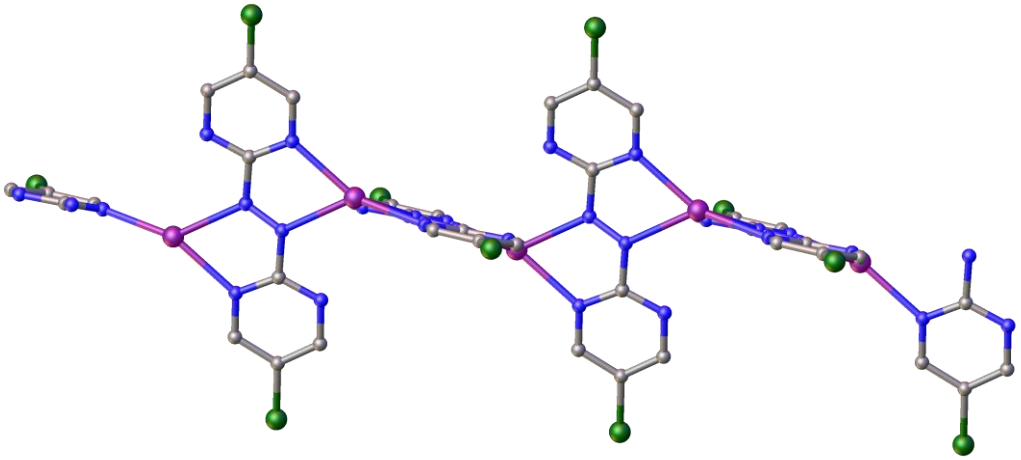

(a)

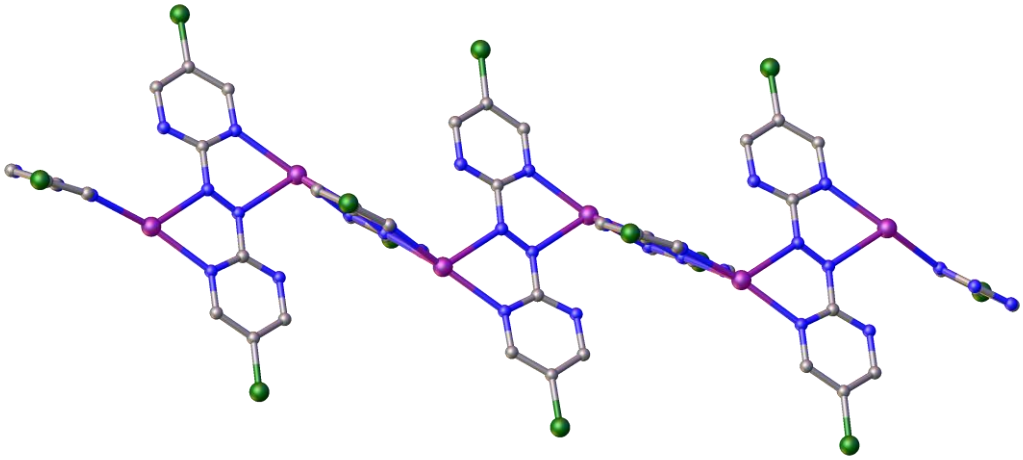

(b)

Figure 6.8. Perspective views of the 1D coordination polymers of **6.4** (a) and **6.5** (b). Hydrogen atoms and non–coordinating counterions are omitted for clarity.

6.2.5. Complex of 3.2, $[Ag_2(3.2)_2](SO_3CF_3)_2$, 6.6

Reaction of silver(I) triflate in acetonitrile with **3.2** in dichloromethane gave the complex **6.6** as red crystals suitable for X–ray crystallography. The complex crystallises in the triclinic space group *P*–1, revealing a M_2L_2 type coordination complex. The asymmetric unit contains one full, and one half molecule of **3.2**, one and a half silver atoms and one and a half non–coordinating triflate anions, as shown in Figure 6.9.

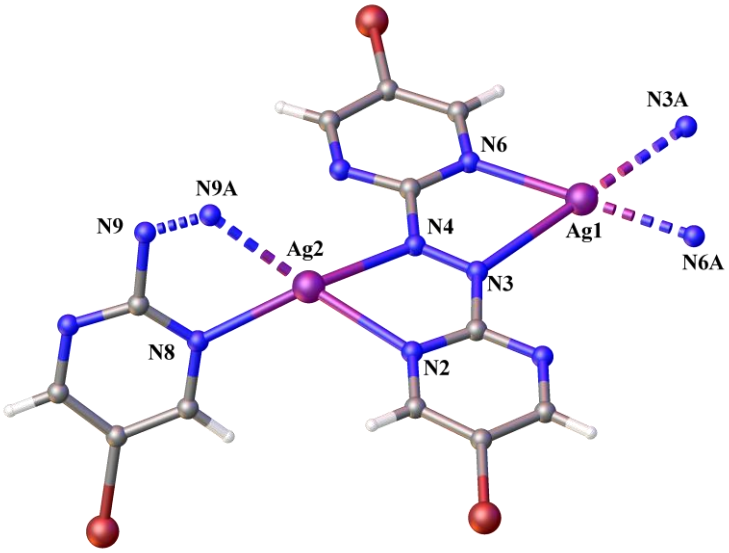

Figure 6.9. The asymmetric unit of **6.6** with the triflate counterions being omitted for clarity. Selected bond lengths (Å): Ag1–N3 2.629(4), Ag1–N6 2.215(4), Ag2–N2 2.338(4), Ag2–N4 2.282(4), Ag2–N8 2.314(4), Ag2–N9A 2.309(4), N3–N4 1.240(6), N9–N9A 1.265(8). Selected bond angles (°): N3–Ag1–N3A 180.0, N6–Ag1–N3 113.25(15), N6A–Ag1–N3A 66.75(15), N6–Ag1–N6 180.0, N4–Ag2–N2 67.63(15), N8–Ag2–N2 124.17(15), N4–Ag2–N8 140.39(15), N9A–Ag2–N2 144.52(15), N4–Ag2–N9A 126.26(15), N9A–Ag2–N8 68.89(15).

The two crystallographically independent silver atoms Ag1 and Ag2 are both four–coordinate through coordination to two azo–N and two pyridine–N atoms. Interestingly, the silver atoms have very different coordination geometries, as shown in Figure 6.10a. The Ag1 atom lies on an inversion centre, coordinating to two symmetry–related molecules of **3.2**, each binding through azo–N and pyridine–N atoms (Figure 6.10b). It adopts a crystallographically imposed square planar geometry with *trans* N–Ag1–N angles, N3–Ag1–N3A and N6–Ag1–N6A, of 180°, and the sum of the six–interbond angles Σ = 720°, which fits perfectly with Constable *et al.*'s[312] model for planarity. In addition, the crystallographic

symmetry about Ag1 gives rise to two longer Ag–N_{azo} bonds and two shorter Ag–N_{py} bonds which also supports the argument.[186] The coordination geometry of the second silver atom (Ag2), however is distorted tetrahedral (τ_4 = 0.53), and is coordinated to two different molecules of **3.2** (Figure 6.10).

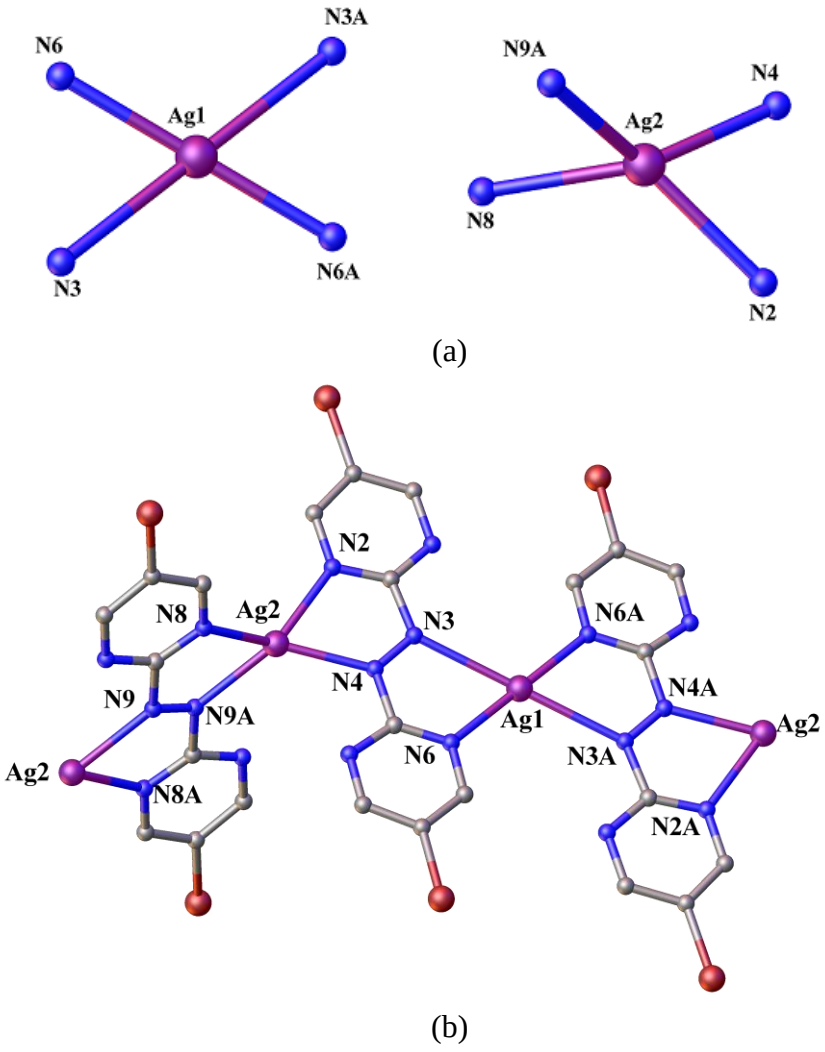

Figure 6.10. (a) The coordination sphere of the two silver atoms, Ag1(left) and Ag2 (right) in complex **6.6**. (b) A small section of the polymeric structure of **6.6**.

The asymmetric unit grows into a one–dimensional coordination polymer with one square planar Ag1 lying between two identical tetrahedral silver atoms (Ag2 and Ag2A), as shown in Figure 6.11. Ligand **3.2** separates Ag1 and Ag2 by 5.573(5) Å and Ag2···Ag2A by 5.374(9) Å due to the longer Ag1–N_{azo} bond distance [Ag1–N3 2.628(4) Å].

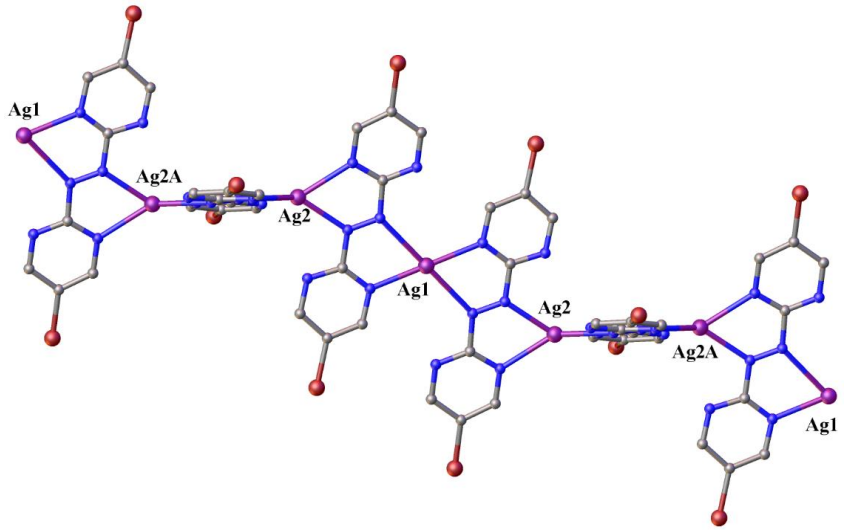

Figure 6.11. A perspective view of **6.6** emphasising the arrangement of components within the 1D coordination polymer. Hydrogen atoms and the counterions have been omitted for clarity.

6.2.6. Complexes of 3.3

Ligand **3.3** is similar to **3.1,** differing only in the introduction of electron–donating methyl groups. It forms similar M_2L_2 one–dimensional coordination polymers, **6.7** and **6.8**, on reaction with $AgNO_3$ and $AgClO_4$, respectively, in ligand to metal ratios of 1:2 (Scheme 6.2).

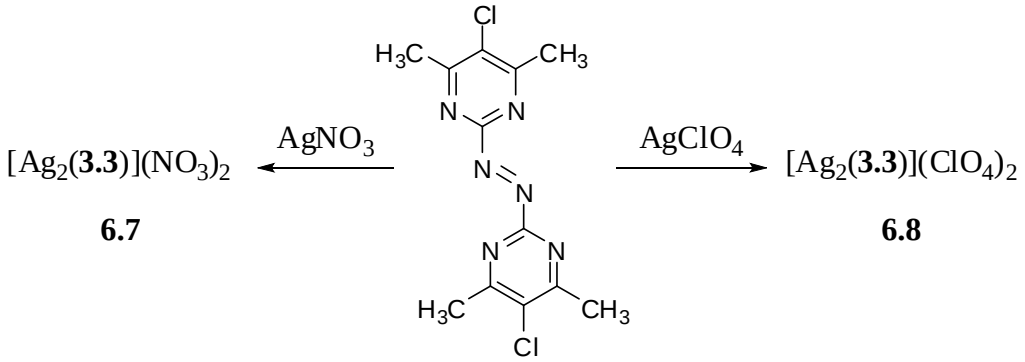

Scheme 6.2

*[Ag$_2$(**3.3**)](NO$_3$)$_2$, **6.7** and [Ag$_2$(**3.3**)](ClO$_4$)$_2$, **6.8***

Complex **6.7** crystallised in the triclinic space group *P*–1, with one silver atom, two half molecules of **3.3** and a coordinated nitrate anion in the asymmetric unit, as shown in Figure 6.12a. Similarly, complex **6.8** crystallised in the triclinic space group *P*–1, with the

asymmetric unit containing two half molecules of **3.3**, one silver atom and a coordinated perchlorate counterion, as shown in Figure 6.12b. The asymmetric units of **6.7** and **6.8** are similar to the previously described complex **6.3**.

In both **6.7** and **6.8**, the silver atom is five–coordinate through the coordination of two azo nitrogens and two pyridine nitrogen atoms from adjacent molecules of **3.3** and an oxygen atom of the coordinated anion. All the silver–carbon, silver–nitrogen and silver–oxygen bond lengths are in the expected ranges (2.3 – 2.6 Å); however, unlike **6.3**, the Ag–N_{azo} bond lengths are shorter than the Ag–N_{py} bond lengths in **6.7** and **6.8**, presumably due to the steric influence of the methyl groups.

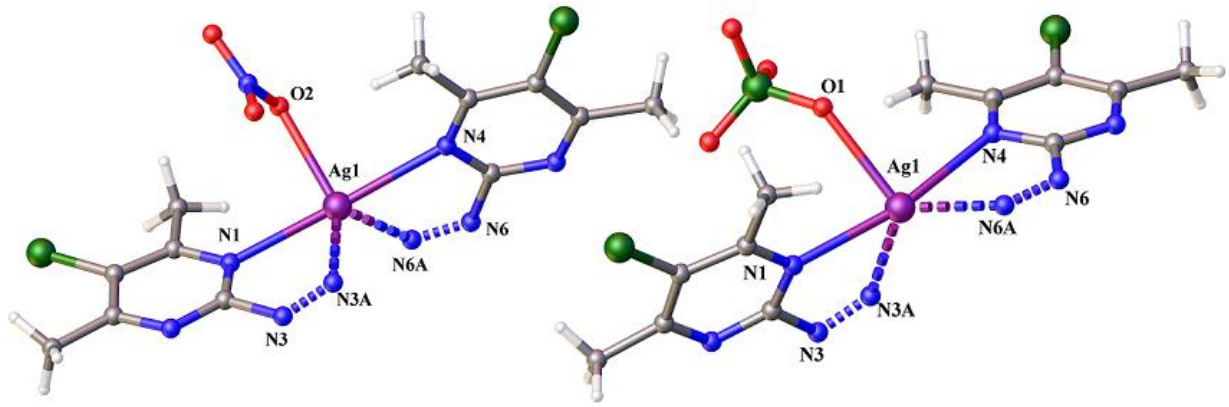

(a) (b)

Figure 6.12. The asymmetric unit of (a) **6.7** and (b) **6.8**. Selected bond lengths (Å) and bond distances (°): **6.7**: Ag1–N1 2.459(1), Ag1–N3A 2.410(1), Ag1–N4 2.519(1), Ag1–N6A 2.390(1), Ag1–O2 2.373(1), N3–N3A 1.254(3), N6–N6A 1.245(3), N3A–Ag1–N1 65.51(5), N6A–Ag1–N4 64.39(5), N3A–Ag1–N4 111.05(4), N6A–Ag1–N1 120.55(5), N1–Ag1–N4 174.59(4), N6A–Ag1–N3A 113.62(5), O2–Ag1–N1 88.86(5), O2–Ag1–N4 90.88(5), O2–Ag1–N3A 132.38(5), O2–Ag1–N6A 113.97(5). **6.8**: Ag1–N1 2.435(1), Ag1–N3A 2.355(1), Ag1–N4 2.568(1), Ag1–N6A 2.316(1), Ag1–O1 2.465(1), N6–N6A 1.248(2), N3–N3A 1.252(2), N3A–Ag1–N1 66.79(4), N6A–Ag1–N4 64.89(4), N3A–Ag1–N4 108.30(4), N6A–Ag1–N1 130.12(4), N1–Ag1–N4 164.88(4), N6A–Ag1–N3A 122.49(4), N1–Ag1–O1 81.07(4), O1–Ag1–N4 88.72(4), N3A–Ag1–O1 114.78(5), N6A–Ag1–O1 121.72(4).

Similar to **6.3**, the overall structures of **6.7** and **6.8** are one–dimensional coordination polymers, as shown in Figure 6.13, with the coordinating counterion alternating its position above and below each silver atom. In both complexes, ligand **3.3** acts as a chelating and bridging ligand with a Ag···Ag separation of 5.610(3) Å in **6.7** and 5.474(2) Å in **6.8**. The

crystal packing shows weak hydrogen bonding interactions between the oxygen atoms of the counterions and the methyl hydrogen atoms of the ligand molecule in both **6.7** and **6.8**. The chlorine atoms of ligand **3.3** also make short contacts with the methyl hydrogen atoms of an adjacent polymer, which further stabilises the structure.

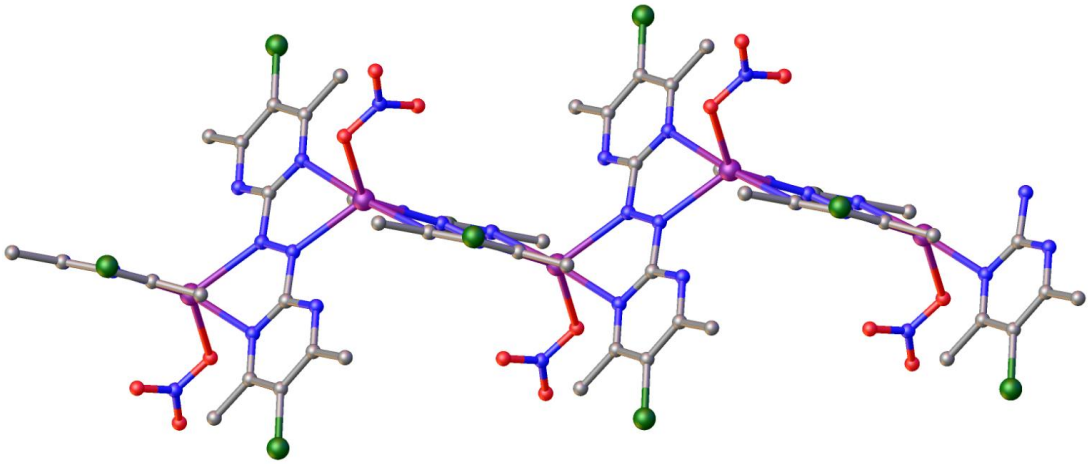

(a)

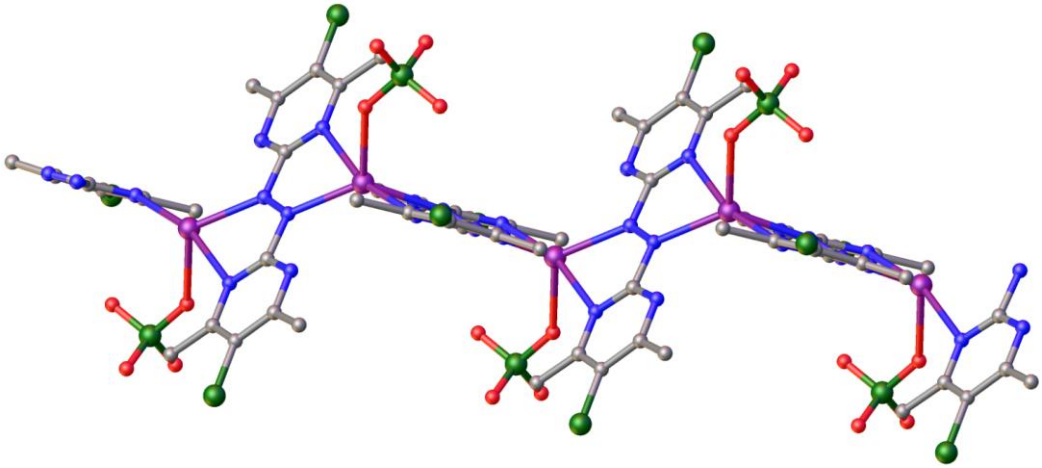

(b)

Figure 6.13. Perspective views of the 1D polymeric structure of (a) **6.7** and (b) **6.8**. All of the hydrogen atoms have been omitted for clarity.

6.2.7. Complexes of 3.4

Ligand **3.4** could potentially act as a chelating ligand as well as the previously seen bridging mode, as previously seen in Chapter 3. To further investigate its modes of coordination, **3.4** was reacted with different silver(I) salts in a 2:1 metal to ligand ratio, as shown in Scheme 6.3.

Reaction of silver(I) trifluoroacetate with ligand **3.4** gave complex **6.9**, which was characterised as [Ag(**3.4**)](CO_2CF_3) by elemental analysis. Despite using a 2:1 metal to

ligand ratio, a 1:1 complex was obtained. X–ray analysis unambiguously confirms the composition of **6.9**, revealing a M_1L_1 type one–dimensional coordination polymer, with the ligand bridging in a monodentate fashion. A similar 1D polymeric chain was obtained by reaction of **3.4** with silver(I) perchlorate. In complex **6.10**, ligand **3.4** coordinates to the silver atom using the same coordination mode as seen in **6.9**. In contrast, a discrete M_2L_2 binuclear complex **6.11** with silver(I) triflate was obtained, with a composition of $[Ag_2(\mathbf{3.4})_2](SO_3CF_3)_2{\cdot}H_2O$ as shown by elemental analysis.

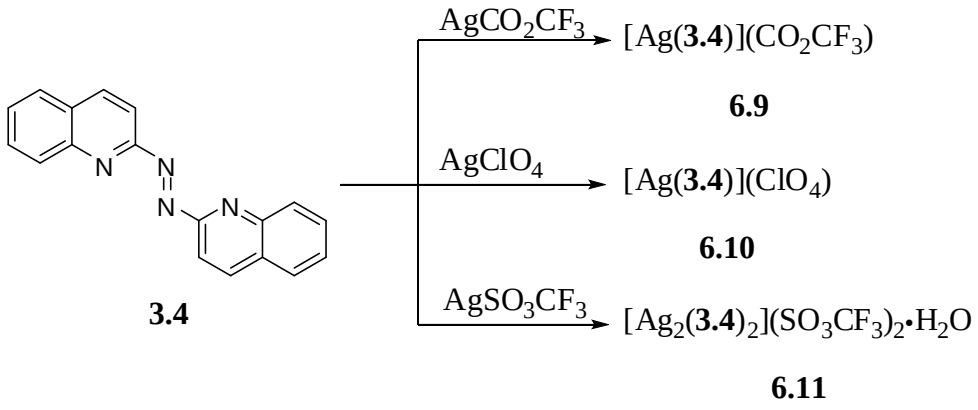

Scheme 6.3

[Ag(3.4)](CO$_2$CF$_3$), 6.9

Complex **6.9** crystallised in the monoclinic space group *C*2/*c*. The asymmetric unit contains one half molecule of **3.4**, half a silver atom and half a coordinated trifluoroacetate anion, revealing a 1L:1M ratio or M_1L_1 type coordination complex, as shown in Figure 6.14.

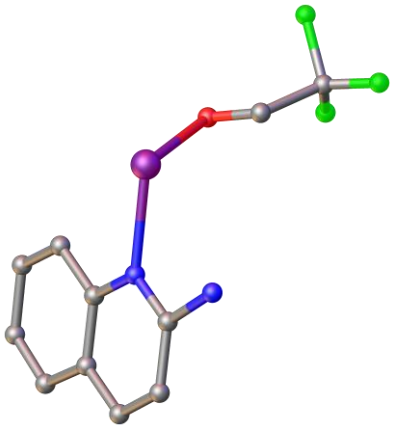

Figure 6.14. The asymmetric unit of **6.9** revealing the formation of the complex in a 1M:1L ratio. All the hydrogen atoms are omitted for clarity.

The overall structure propagates into a one–dimensional polymeric chain with the chelating bidentate trifluoroacetate anions positioned above and below the plane of the polymer at each silver atom, as shown in Figure 6.15. The silver atom lies on a two–fold rotation axis and is four–coordinate through coordination to two quinoline nitrogen atoms of crystallographically related molecules of **3.2**, and a bidentate trifluoroacetate anion. Interestingly, the azo nitrogen atoms are not involved in the coordination, unlike the previous complexes where the ligand adopts s–*cis*/*E*/s–*cis* conformation and bridges silver atoms to form a five–membered chelate ring. In complex **6.9**, ligand **3.4** lies on a centre of inversion and displays s–*trans*/*E*/s–*trans* conformation bridging two silver atoms in monodentate fashion at a relatively long Ag···Ag distance of 7.300(2) Å, as shown in Figure 6.15. A structurally similar binuclear gold complex $[(Ph_3P)Au(\mathbf{2.1})Au(PPh_3)](CF_3SO_3)_2$ was reported by Bardaji *et al.*[162], where **2.1** acts as a monodentate bridging ligand.

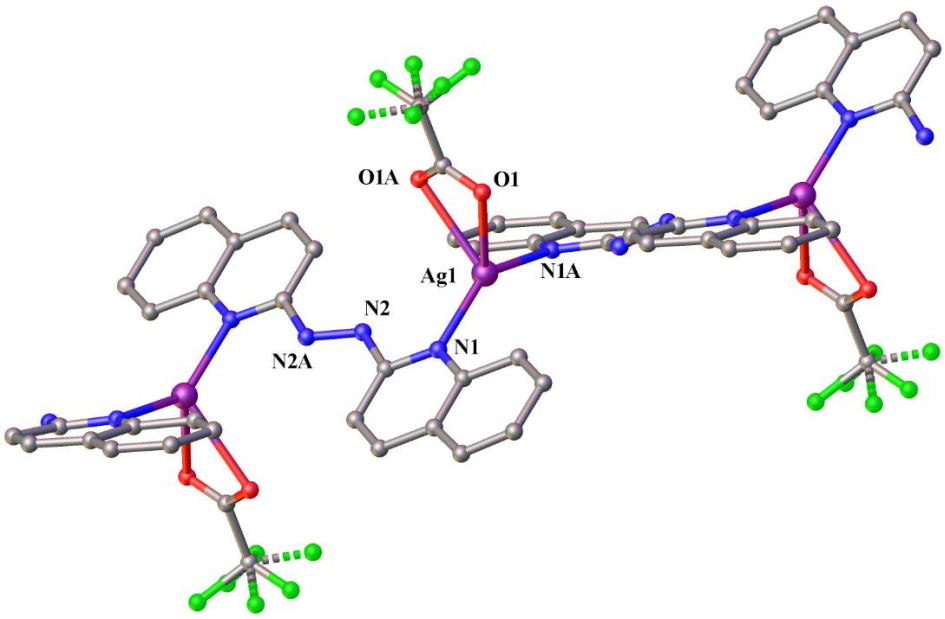

Figure 6.15. A part of the 1D polymeric structure of complex **6.9** illustrating the coordination of ligand **3.4** in a monodentate manner. Hydrogen atoms have been omitted for clarity. Selected bond lengths (Å) and bond angles (°): Ag1–N1 2.230(1), Ag1–O1 2.554(1), N2–N2A 1.258(2), N1–Ag1–N1A 143.72(7), N1–Ag1–O1 102.10(4), N1–Ag1–O1A 110.46(4), O1–Ag1–O1A 52.22(5).

The silver–nitrogen [Ag1–N1 2.230(1) Å] and the N_{azo}–N_{azo} bond lengths [N2–N2A 1.258(2) Å] are similar to the previous complexes. The largest bond angle around Ag1 is measured between the coordinated quinoline nitrogen atoms with a N1–Ag1–N1A angle of 143.72(7)°. The second largest bond angle of 110.46(4)° [N1–Ag1–O1A] is observed

between the coordinated quinoline nitrogen and the oxygen atom of the counterion. The calculated τ_4 value of 0.55 for Ag1 indicates a seesaw geometry.

*[Ag(**3.4**)](ClO$_4$), **6.10***

Complex **6.10** also crystallises in the monoclinic space group *C*2/*c*, with two full molecules of **3.4**, one full and two half silver atoms and two non–coordinating perchlorate anions as shown in Figure 6.16. The *trans* N–Ag–N angles greater than 172° denotes a linear geometry for the silver atoms, two of which lie on a two–fold rotation axis. Once again, ligand **3.4** coordinates in a monodentate fashion adopting a s–*trans/E*/s–*trans* confirmation. The monodentate coordination mode of the ligand bridges the two silver atoms with a separation of 7.103(1) Å, which is similar to **6.9**, but significantly longer than complexes where the ligand coordinates in a chelating manner.

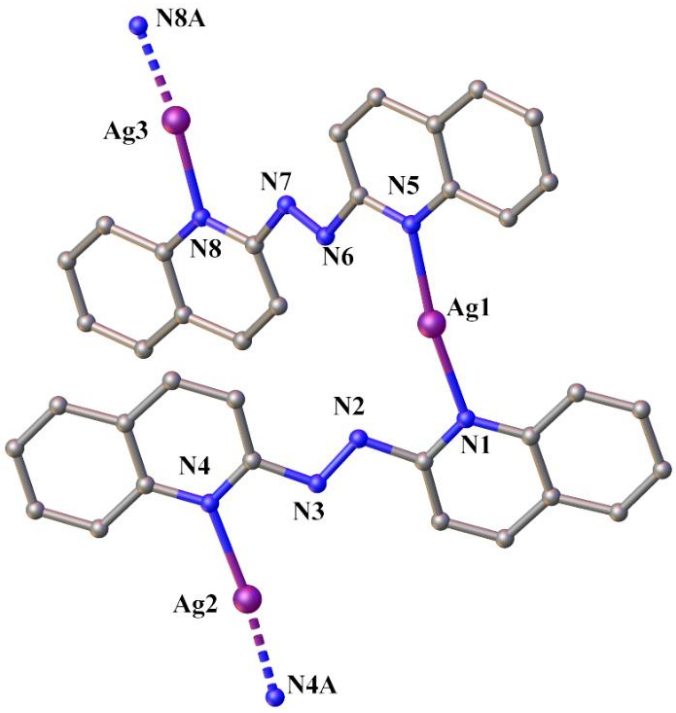

Figure 6.16. The asymmetric unit of **6.10** with atom labelling. All hydrogen atoms and counterions have been omitted for clarity. Selected bond distances (Å) and bond angles (°):Ag1–N1 2.192(1), Ag1–N5 2.194(1), Ag2–N4 2.209(1), Ag3–N8 2.167(1), N2–N3 1.257(2), N6–N7 1.263(2), N1–Ag1–N5 172.25(6), N4–Ag2–N4A 174.01(8), N8–Ag3–N8A 172.51(8).

Despite having similar linear coordination geometries, the coordination environments of the three silver atoms are all different. The overall structure grows into a one–dimensional

coordination polymer, as shown in Figure 6.17, with Ag1 coordinated to two different molecules of **3.4** through N1 and N5, whereas Ag2 is coordinated to identical ligands through N4 and N4A, and Ag3 through N8 and N8A.

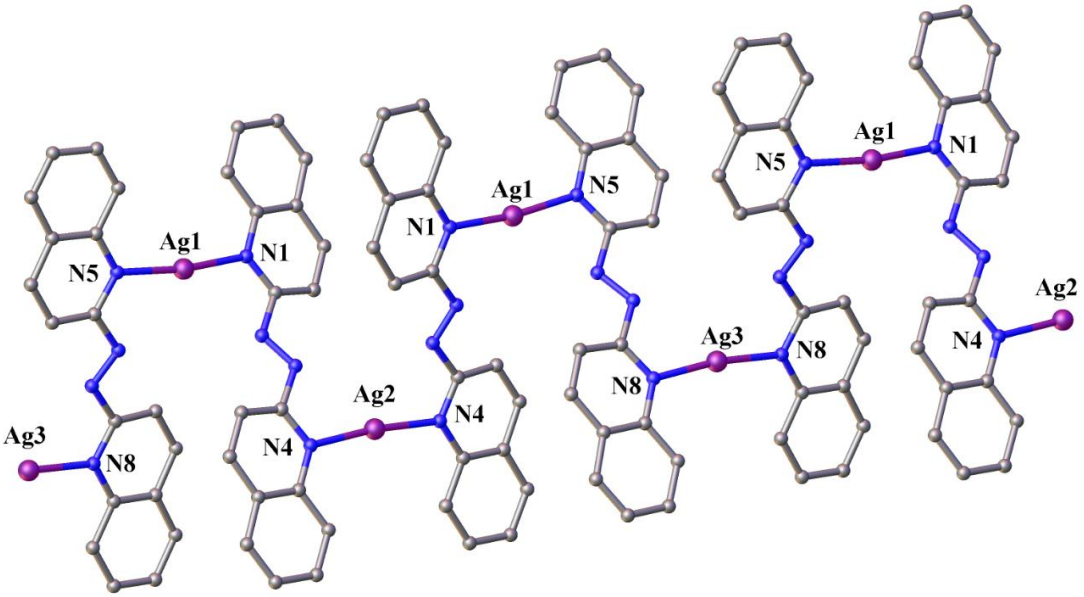

Figure 6.17. A perspective view of the 1D coordination polymer of complex **6.10**. Hydrogen atoms and counterions have been omitted for clarity.

*[Ag_2(**3.4**)$_2$](SO_3CF_3)$_2$·H_2O, **6.11***

An acetonitrile solution of silver(I) triflate was added to a hot solution of **3.4** in methanol/dichloromethane. Slow evaporation of the reaction mixture over a period of time resulted in red crystals of complex **6.11**, which were characterised as [Ag_2(**3.4**)$_2$](SO_3CF_3)$_2$·H_2O by elemental analysis. The X–ray crystal structure reveals a M_2L_2 discrete binuclear complex as shown in Figure 6.18. Complex **6.11** crystallised in the monoclinic space group *Cc*, with two silver atoms, two full molecules of ligand **3.4**, one water molecule, and two non–coordinating triflate anions in the asymmetric unit.

In complex **6.11**, two crystallographically independent silver atoms Ag1 and Ag2 are present. The four–coordinate silver atom Ag1 coordinates to two quinoline ring nitrogens (N1 and N8), one azo nitrogen (N6) and also forms a Ag1···Ag2 bond at a distance of 2.899(4) Å. On the other hand, Ag2 is five–coordinate through coordination to an oxygen atom (O1) of the water molecule along with three nitrogen atoms (N2, N4 and N5) and the Ag1···Ag2

bond. All of the Ag–N bond distances are consistent with the previous complexes, and range between 2.0 – 2.4 Å.

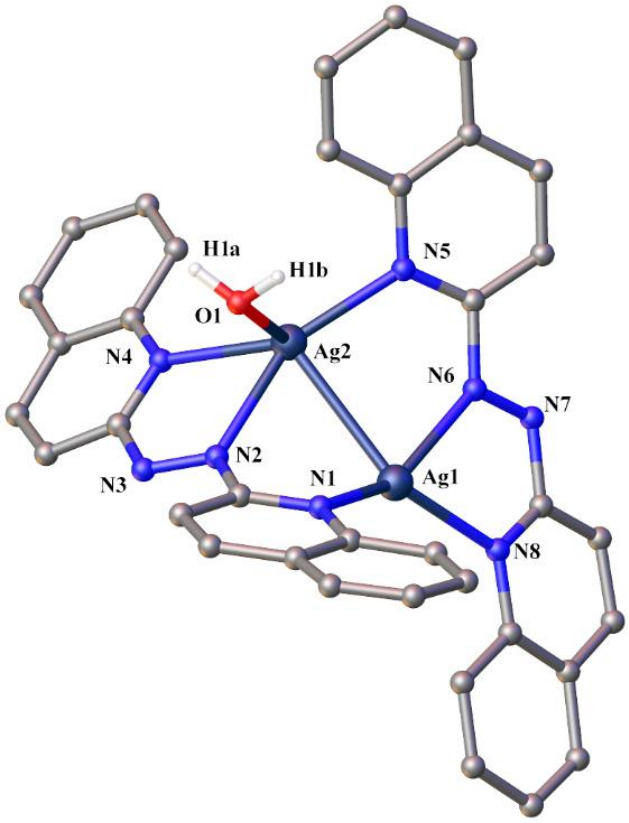

Figure 6.18. The X–ray crystal structure of **6.11** showing the formation of a binuclear M_2L_2 complex. The aromatic hydrogen atoms and the triflate anions have been omitted for clarity. Selected bond distance (Å): Ag1–N1 2.190(3), Ag2–N2 2.389(3), Ag2–N4 2.315(3), Ag2–N5 2.223(3), Ag1–N6 2.373(3), Ag1–N8 2.270(3), Ag2–O1 2.574(3), Ag1–Ag2 2.899(4), N2–N3 1.251(5), N6–N7 1.252(4). Selected bond angles (°): N1–Ag1–N8 135.21(11), N1–Ag1–N6 149.40(11), N1–Ag1–Ag2 87.17(8), N8–Ag1–N6 69.31(11), N8–Ag1–Ag2 137.08(8), N6–Ag1–Ag2 74.22(8), N5–Ag2–N4 139.02(11), N5–Ag2–N2 151.58(11), N4–Ag2–N2 68.09(11), N5–Ag2–O1 105.25(10), N4–Ag2–O1 98.04(10), N2–Ag2–O1 71.39(10), N5–Ag2–Ag1 86.99(8), N4–Ag2–Ag1 120.09(7), N2–Ag2–Ag1 67.14(8).

In **6.9** and **6.10**, coordination of ligand **3.4** to the silver atom involved only the quinoline ring nitrogen in a monodentate manner with the azo nitrogen atoms not involved. But in **6.11**, ligand **3.4** acts as a tridentate ligand coordinating to one silver atom by chelating azo nitrogens (N2 or N6) and quinoline nitrogen atoms (N4 and N8) and a second silver atom through the quinoline nitrogen atoms (N1 and N5) in a monodentate fashion. The chelating

bite angles for the two molecules are N8–Ag1–N6 69.31(11)° and N4–Ag2–N2 68.09(11)°. Contrary to **6.9** and **6.10**, the quinoline nitrogens of both the molecules of **3.4** involved in the bidentate coordination are in the same plane as the coordinated azo–nitrogen, however, the monodentate quinoline ring adopts a twisted conformation with a torsion angle greater than 19°. A similar coordination mode has previously been reported for Os and Pt complexes containing ligand **2.1**.[164],[230]

The oxygen atoms of the non–coordinating trifluoroacetate anions are involved in hydrogen bonding with the water molecule. The discrete binuclear complex is also further stabilised by a number of short contacts between the trifluoroacetate anions and the ligand molecules.

6.3. Summary

To conclude, in this section the metallosupramolecular chemistry of azo ligands **2.1**, **2.3**, **2.5**, and **3.1** – **3.4** with silver(I) metal ions and a range of counterions has been investigated. The self–assembly of silver(I) ions led to the formation of mostly coordination polymers as well as one discrete structure. The choice of anions profoundly influences the type of metallosupramolecular structure formed.

Most of the complexes were isolated as one–dimensional coordination polymers with 1:1 silver to ligand ratios with non–coordinating anions. The coordination of nitrate and perchlorate anions to the silver metal resulted in a similar one–dimensional coordination polymer with **2.5** and **3.3**. Ligand **2.3** gave a coordination polymer with a different topology due to the coordinating trifluoroacetate anions.

The ligands predominantly coordinate in a bidentate chelating manner adopting the usual "S–frame" conformation and bridging two silver atoms at a distance of approximately 5.5 Å, except for ligand **3.4**. Despite being a ditopic chelating ligand, as seen in Chapter 3, ligand **3.4** coordinates as a monodentate bridging ligand in complexes **6.9** and **6.10** coordinating through the quinoline nitrogen atom. In both complexes, ligand **3.4** exhibits a s–*trans*/*E*/s–*trans* conformation. It also acts as a tridentate ligand, which leads to the formation of dinuclear discrete complex **6.11** with a Ag···Ag interaction of 2.899(3) Å. The coordination modes exhibited by the ligands are shown in Figure 6.19.

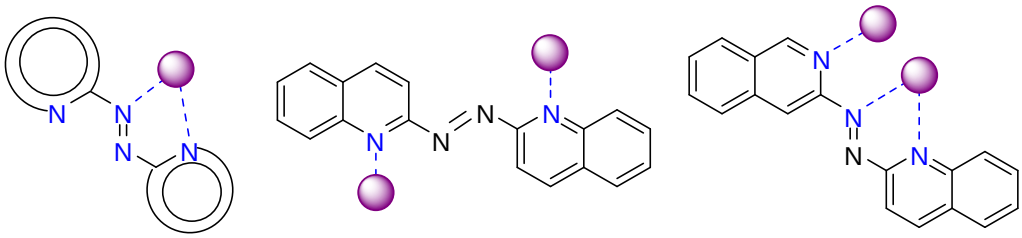

s–*cis*/*E*/s–*cis* s–*trans*/*E*/s–*trans*

(a) (b)

Figure 6.19. General representation of the coordination modes employed by most ligands (a) and by ligand **3.4** (b).

Chapter 7

Conclusions and Future Perspectives

7. Conclusions and Future Perspectives

7.1. Conclusions

The ability of nitrogen–containing heterocyclic ligands to function as bridges and control the electronic interactions between metal centres is of importance because of their wide applications, ranging from molecular devices to biological applications. This thesis has described the synthesis of sixteen symmetrical azo and five bis–pyridylimine ligands capable of coordinating as bis–chelating bridging ligands. The coordination and metallosupramolecular chemistry of these ligands with both ruthenium(II) and silver(I) has been investigated.

The azo ligands discussed in this thesis are divided into three categories; (i) azobispyridine–based ligands with varying substituents on the pyridine rings; (ii) ligands in which the pyridine ring is replaced by different heterocyclic rings, (iii) hexadentate ligands with bis–tridentate coordination through an azo nitrogen and two ring nitrogen atoms. Ligands based on bis(pyridylimines) with varying spacers between the imine subunits were also synthesised to investigate the effect of decreased degree of conjugation and increased distance on the inter–metal coupling.

In Chapter 2, the synthesis and characterisation of symmetrical azobispyridine ligands with different substituents on the pyridine ring was described. The mononuclear and dinuclear complexes of $[Ru(bpy)_2]^{2+}$ with bidentate azo ligands was investigated. Despite being potentially ditopic ligands, **2.2** and **2.4** afforded only mononuclear complexes, probably due to the steric interference of the methyl group at the 3– and 6–positions. Also, an unexpected substitution reaction of the bromo–ligand **2.6** in the diruthenium(II) complex was observed. This substitution was able to be avoided by using $[Ru(bpy)_2(OTf)_2]$ to give the corresponding complex $[(bpy)_2Ru(\mu–\mathbf{2.6})Ru(bpy)_2]^{4+}$, **2.16**.

Structural characterisation, using X–ray crystallography, showed that the ruthenium atom could bind to the azobispyridine ligand using the azo–N atom and the pyridine–N atom, to form a stable five–membered chelate ring. In mononuclear complexes, the non–coordinated pyridine ring of the azo ligand is twisted with respect to the azo–N atom and directed towards the adjacent bipyridine rings. In the dinuclear complexes, selective formation of only one diastereoisomer, the *meso* form, was observed. The X–ray crystal structures indicate that the

azo ligand acts as a planar bridge between the two ruthenium atoms separated by a short metal–metal separation of *ca.* 4.9 Å. The X–ray crystal structures of complexes $[(bpy)_2Ru(\mathbf{2.5})](PF_6)_2$, **2.13** and $[(bpy)_2Ru(\mu–\mathbf{2.5})Ru(bpy)_2](PF_6)_4$, **2.14** are shown in Figure 7.1

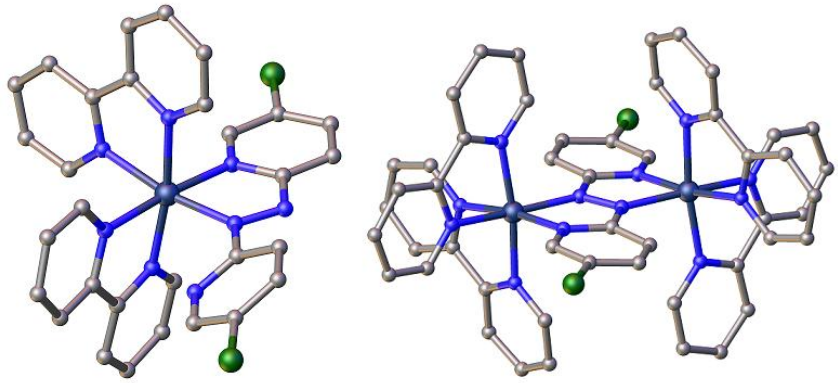

Figure 7.1. Perspective views of the X–ray crystal structures of $[(bpy)_2Ru(\mathbf{2.5})](PF_6)_2$, **2.13** (left) and $[(bpy)_2Ru(\mu–\mathbf{2.5})Ru(bpy)_2](PF_6)_4$, **2.14** (right). Hydrogen atoms, counterions and solvate molecules are omitted for clarity.

The dinuclear complexes exhibit MLCT absorption bands corresponding to Ru(dπ) → azo(π*) transitions at *ca.* 760 nm indicating a low–lying π*–orbital in the bridging ligand. The electronic properties were further established by electrochemical measurements, which revealed that the ligands are electron–deficient and act as good π–acceptors of metal d–orbital electron density. The existence of two widely separated one–electron metal–centred oxidation processes, as shown in Figure 7.2, suggest strong communication between the metal centres with comproportionation constants $K_c = 10^8$.

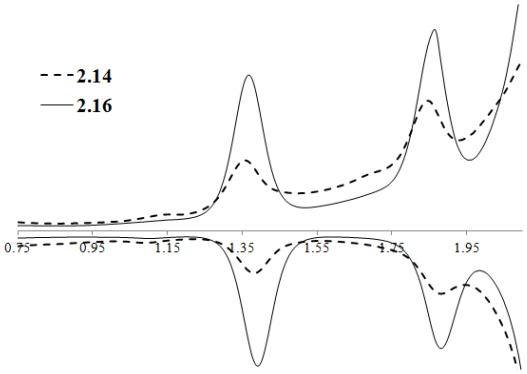

Figure 7.2. Differential pulse voltammograms for complexes $[(bpy)_2Ru(\mu–\mathbf{2.5})Ru(bpy)_2](PF_6)_4$, **2.14** and $[(bpy)_2Ru(\mu–\mathbf{2.6})Ru(bpy)_2](PF_6)_4$, **2.16.**

Chapter 3 described the investigation of azo ligands where the pyridine ring of the azobispyridine ligand was replaced by other heterocyclic rings, such as pyrimidine and benzo fused N–heterocyclic rings. Incorporation of these groups was found to have a considerable effect on the electronic properties of these complexes. This chapter documents the X–ray crystallographic characterisation of two homodinuclear ruthenium complexes, $[(bpy)_2Ru(\mu$–**3.1**$)Ru(bpy)_2](PF_6)_3$, **3.10** and $[(bpy)_2Ru(\mu$–**3.2**$)Ru(bpy)_2](PF_6)_3$, **3.12** bridged by pyrimidine–based azo anion radical species. Both **3.10** and **3.12** display long N_{azo}–N_{azo} bond lengths of *ca.* 1.36 Å corresponding to the reduced azo ligand.[249] The presence of three hexafluorophosphate anions, as shown in Figure 7.3, also confirms the radical nature of the complexes.

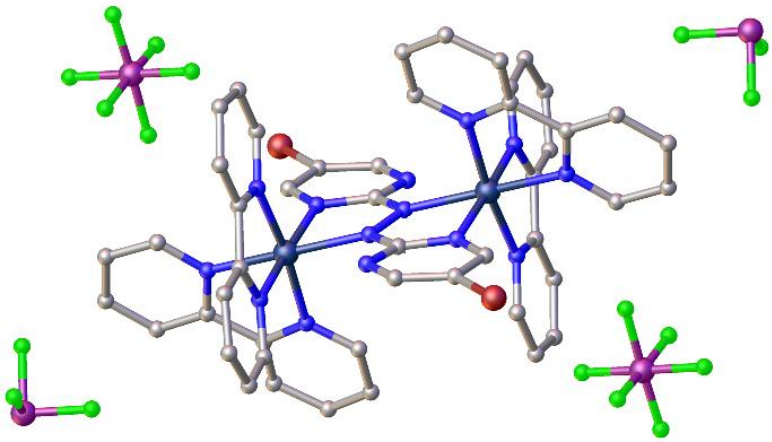

Figure 7.3. A perspective view of the X–ray structure of $[(bpy)_2Ru(\mu$–**3.2**$)Ru(bpy)_2](PF_6)_3$, **3.12**. Hydrogen atoms are omitted for clarity.

The mononuclear ruthenium(II) complex $[(bpy)_2Ru($**3.5**$)]^{2+}$ of the quinazoline azo ligand **3.5** was found to exist as a mixture of two isomers, **3.17** and **3.18**, in a 1:10 ratio, due to the nature of the N–atom involved in the chelation. The X–ray crystal structure of **3.17** shows coordination to the ruthenium atom through the azo nitrogen and the sterically more hindered N–atom. Absorption spectra and electrochemical studies reveal differences in the electronic properties of **3.17** and **3.18**. The diastereoisomeric forms, **3.19** and **3.20**, of the dinuclear ruthenium(II) complex $[(bpy)_2Ru(\mu$–**3.5**$)Ru(bpy)_2]^{4+}$ were separated by cation–exchange chromatography and characterised by X–ray crystallography. The structures of **3.19** and **3.20** show coordination of the bridging ligand **3.5** to two $[Ru(bpy)_2]^{2+}$ fragments *via* azo N–atoms and the less hindered N–atoms on each side. The ancillary bpy ligands adopt different shapes in the two isomers, as shown in Figure 7.4.

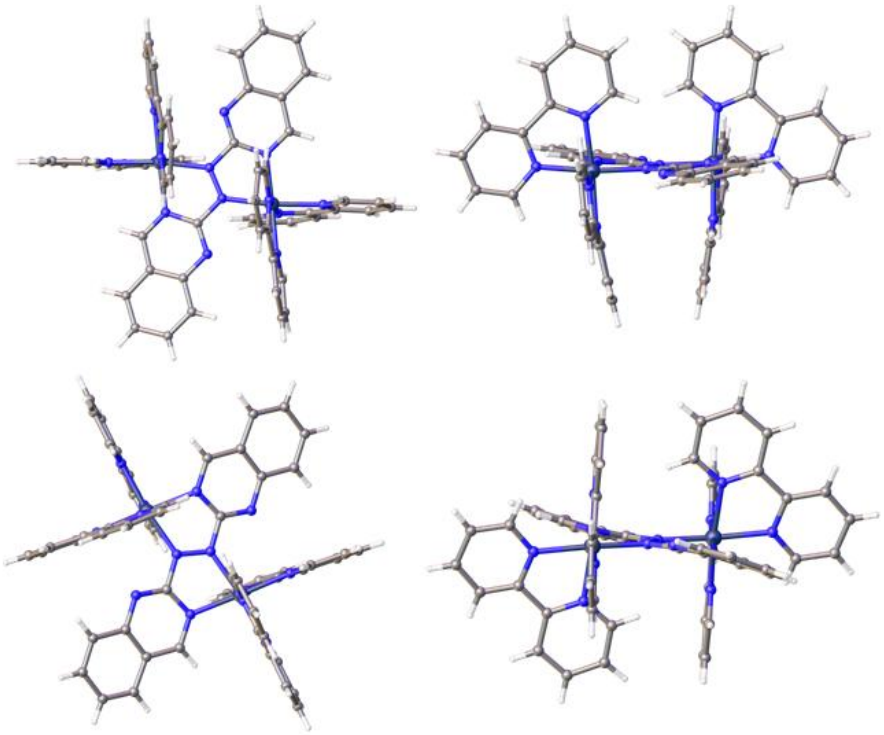

Figure 7.4. Two perspective views of the X–ray crystal structures of *rac* **3.19** (top) and *meso* **3.20** (bottom) isomers, emphasising the coordination modes of the bridging ligand **3.5** and the different orientations of the terminal bpy rings in the two forms.

Chapter 4 investigated the mononuclear and dinuclear $[Ru(terpy)]^{2+}$ complexes of the hexadentate ligands **4.1** and **4.2**, with potential coordination in a bis–chelating tridentate manner. The complexes were characterised by ^{1}H NMR and X–ray crystallography. The crystal packing in the homodiruthenium(II) complexes $[(terpy)Ru(\mu–\mathbf{4.1})Ru(terpy)]^{4+}$, **4.3**, and $[(terpy)Ru(\mu–\mathbf{4.2})Ru(terpy)]^{4+}$, **4.5**, exhibit interesting aryl embraces, where a pair of outer pyridyl rings of the terpy ligands are involved in offset face–to–face (**OFF**) interactions and each of these rings also addresses an edge–to–face (**EF**) interaction with the bridging ligands. These aryl embraces propagate in two–dimensions, as shown in Figure 7.5, giving rise to interesting two–dimensional supramolecular motifs.

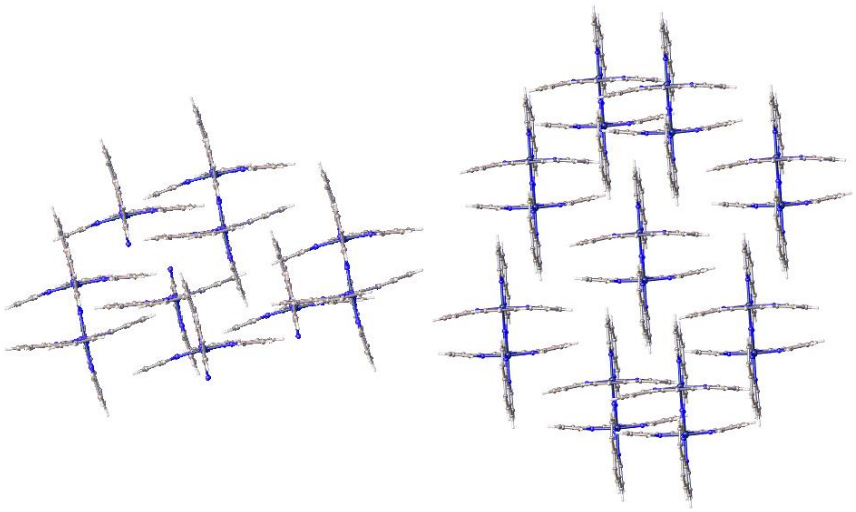

(a) (b)

Figure 7.5. Crystal packing of complexes in **4.3** (a) and **4.5** (b) showing **EF** and **OFF** interactions.

These green complexes exhibit a large red shift in the Ru(dπ) → azo(π*) transitions at *ca.* 772 nm due to the increased stabilisation of the azo–centered π*–orbital upon formation of the bimetallic system. Further insights into the electronic transitions were obtained from electrochemical studies, which revealed these ligands to mediate very strong communication between the metal centres with comproportionation constants of $K_c > 10^{13}$.

Chapter 5 described dinuclear ruthenium(II) complexes of five bis(pyridylimine) ligands. A mononuclear complex $[(bpy)_2Ru(\mathbf{5.1}–NH_2)](PF_6)_2$, **5.6**, was also obtained as a result of the hydrolytic decomposition of ligand **5.1**. All the diruthenium(II) complexes were characterised by NMR spectroscopy. Complexes $[(bpy)_2Ru(\mu–\mathbf{5.1})Ru(bpy)_2](PF_6)_4$, **5.7**, and $[(bpy)_2Ru(\mu–\mathbf{5.2})Ru(bpy)_2](PF_6)_3$, **5.8**, were characterised by X–ray crystallography. The electronic properties of the complexes were studied by differential pulse voltammetry, which revealed that ligand **5.1** mediates a weak interaction between the metal centres. However, a complete absence of communication between the metal centres was observed in the binuclear complexes **5.8** – **5.11**, presumably due to the increased distance and/or flexibility across the bridging ligands **5.2** – **5.5**. The oxidation waves of the differential pulse voltammograms for complexes **5.7** – **5.11** are shown in Figure 7.6. These results raise serious doubts about the validity of Cai *et al.*'s[307] claim that all these ligands facilitate strong metal–metal interactions.

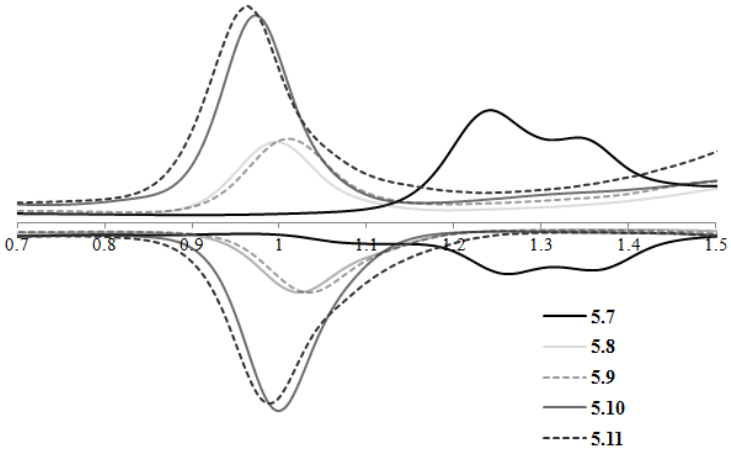

Figure 7.6. The differential pulse voltammograms of the diruthenium(II) complexes containing bis(pyridylimine) ligands with different spacers between the imine subunits.

In Chapter 6 the metallosupramolecular chemistry of the azo ligands with a range of silver(I) salts was discussed. Reaction with silver(I) ions generally led to the formation of coordination polymers in a 1:1 metal to ligand ratio. However, the choice of anion profoundly influenced the type of metallosupramolecular structure formed.

The ligands predominantly coordinate in a bidentate chelating manner adopting the an "S–frame" conformation mode and bridging two silver atoms at a distance of approximately 5.5 Å, except for ligand **3.4**, as shown in Figure 7.7. Despite being a ditopic chelating ligand, as seen in Chapter 3, ligand **3.4** coordinates as a monodentate bridging ligand in complexes [Ag(**3.4**)](CO_2CF_3), **6.9**, and [Ag(**3.4**)](ClO_4), **6.10**, by coordinating through the quinoline N–atom only. In both complexes, ligand **3.4** exhibits a s–*trans*/*E*/s–*trans* conformation. It also acts as a tridentate ligand, which leads to the formation of a dinuclear discrete complex [Ag_2(**3.4**)$_2$](SO_3CF_3)$_2$·H_2O, **6.11**, with an Ag···Ag interaction of 2.899(3) Å.

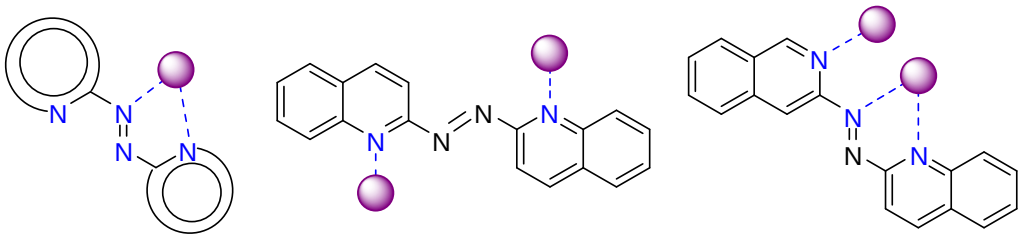

s–*cis*/*E*/s–*cis* s–*trans*/*E*/s–*trans*

(a) (b)

Figure 7.7. The coordination modes employed by most ligands (a) and by ligand **3.4** (b).

7.2. Future Perspectives

The dinuclear complexes of bis–chelating azobis(2–pyridine) **2.1**, have been the subject of interest for many years. The low–lying azo–centered π*–orbital, small inter–metal separation, strong metal–metal interactions and stable radical intermediates make it a suitable ligand to study metal–ligand charge transfer and mixed–valence state coupling between metal centres. The pyrimidine–substituted azo ligand **3.1** has also been studied in this context. However, the coordination chemistry of polydentate azo ligands is still in its early stages.

In this thesis, the variation within the dinuclear ruthenium(II) complexes was limited to modifications on the bridging ligand. Future work towards the investigation of ligand–mediated coupling between the metal centres could incorporate the use of different peripheral ligands, such as 4,4'–dimethyl–2,2'–bipyridine and 1,10–phenanthroline. In addition, homometallic $[(TL)_2M(\mu\text{–}BL)M(TL')_2]^{n+}$ and heterometallic complexes $[(TL)_2M(\mu\text{–}BL)M'(TL')_2]^{n+}$ (TL ≠ TL' and M ≠ M'), could be investigated, which would give an opportunity to study the effect of different metals and ancillary ligands towards the inter–metal communication. The bis–chelating hexadentate azo ligands **4.1** and **4.2** show an intriguing increased communication between the metal centers. An interesting development would be to study related ligands that might allow further insights into the origin of these effects.

The metallosupramolecular chemistry of the azo ligands presented in this thesis was predominantly studied with silver(I); further investigations could include other transition metals such as Cu(I) and Zn(II). Despite the numerous possible coordination modes, the five–membered chelate ring was the most favoured coordination mode. Extension of the work described here could potentially include investigation of other structural variations on these ligands.

Futhermore, the free azo functional group can also undergo photo–induced reversible *cis–trans* isomerisation under radiation, which makes these ligands excellent candidates for photoresponsive molecular devices. Therefore, complexes [Ag(**3.4**)](CO_2CF_3), **6.9**, and [Ag(**3.4**)](ClO_4), **6.10**, coordinating only through the quinoline nitrogen atom would be interesting to investigate further in this context.

Chapter 8

Experimental Procedures

8. Experimental Procedures

8.1. General Information

Unless otherwise stated, reagents were obtained from commercial sources and used as received. Water was purified by reverse osmosis *in–house*. HPLC–grade solvents were used for reactions and in case of moisture–sensitive reactions, solvents were dried by literature procedures and freshly distilled as required. Melting points were recorded on an Electrothermal melting point apparatus. Elemental analysis was done by the Campbell Microanalytical Laboratory, University of Otago.

Nuclear Magnetic Resonance

^{1}H and ^{13}C NMR spectra were recorded on Varian Unity 300, Agilent 400–MR and Varian 500 INOVA instruments operating for ^{1}H NMR at 300, 400 and 500 MHz, respectively and at 75, 100 and 125 MHz, respectively, for ^{13}C NMR. All the ^{1}H NMR spectra recorded in deutrated solvents were referenced to the solvent peak and/or TMS: $CDCl_3$, 7.26 ppm; CD_3CN, 2.0 ppm; CD_3OD, 3.3 ppm; DMSO, 2.6 ppm. ^{13}C NMR were all referenced to their solvent peaks: chloroform, 77.0 ppm; acetonitrile, 36.8 ppm; methanol, 49.3 ppm; DMSO, 39.6 ppm. When required, gCOSY, 1–D NOESY, 1–D TOCSY, 1–D ROESY, HSQC and HMBC experiments were performed using standard pulse sequences. The assignments for the compounds are denoted with primes to indicate the different rings of the multidentate ligands and with letters to distinguish the bpy and terpy rings.

Mass Spectrometry

Mass spectra were recorded by Dr. Marie Squire and Dr. Meike Holzenkaempfer on either a DIONEX Ultimate 3000 or Bruker MaXis 4G spectrometer, operated in high resolution positive ion electrospray mode. Samples were prepared by dissolving in an appropriate solvent at the required concentration.

Infrared Spectroscopy

Infrared spectra were recorded on a Perkin–Elmer Spectrum One FTIR instrument operating in diffuse reflectance mode with samples prepared as KBr pellets (KBr) or on a

Bruker FTIR spectrometer with Alpha's Platinum ATR single reflection diamond where the neat samples were recorded.

UV/Visible Spectroscopy

UV/Visible spectra were recorded on a Varian CARY Probe 50 UV/Visible spectrometer in acetonitrile (range 200 – 800 nm) at room temperature. Samples were measured in quartz cuvettes of 1cm path length and approximately 3 mL volume.

Electrochemical Studies

Electrochemical measurements were performed using a Eco Chemie Autolab PGSTAT302. Measurements were recorded in acetonitrile with 0.1 M $TBAPF_6$ or $TBAClO_4$ as supporting electrolyte. The working electrode was platinum (Pt), a platinum wire auxillary electrode and $Ag/AgNO_3$ (0.1 mol dm^{-3} $[[(n\text{–}C_4H_9)_4]PF_6/[(n\text{–}C_4H_9)_4]ClO_4$ in acetonitrile) reference electrode. The working electrode was polished using a microcloth and 1μm alumina powder slurry; then sonicated in water and washed thoroughly with water and dried in 60 °C oven. Ferrocene was added as an internal standard on completion of each experiment. Cyclic voltammetry was performed with a sweep rate of 100 mVs^{-1}. Differential pulse voltammetry was recorded with a sweep rate of 4 mVs^{-1} and a pulse amplitude, width and period of 50 mV, 60 ms and 1s, respectively. All experiments were measured in nitrogen sparged solutions at room temperature.

8.2. Synthesis of Precursors and Ligands

The following compounds were prepared by literature procedures: azobis(2–pyridine), **2.1**,[93] azobis(4–methyl–2–pyridine), **2.3**,[93] 2–amino–5–chloropyridine,[313] 2–amino–5–bromopyridine,[246] 2–amino–5–bromopyrimidine,[246] 2–amino–5–chloro–4,6–dimethyl pyrimidine,[259] quinoline N–oxide,[265] 2–chloroquinoline,[264] 2–aminoquinoline,[263] 2–aminoquinazoline,[266] 2–chloroquinoxaline,[268] 2–aminoquinoxaline,[269] 2–amino–5–nitropyridine,[314] 2,2'–bipyridine mono N–oxide,[281] 6–amino–2,2'–bipyridine,[282] 1–methyl–1,10–phenanthrolinium tosylate,[284] methyl–1,10–phenanthrolin–2(1H)–one,[284] 2–chloro–1,10–phenanthroline,[283] 2–amino–1,10–phenanthroline,[283] bis(2–pyridylmethylene)azine, **5.1**,[304] bis(2–pyridylmethyleneamino)benzene, **5.2**,[299] bis[4–(2–pyridylmethyleneamino)phenyl]ether, **5.3**,[315] bis[4–(2–pyridylmethyleneamino)phenyl] methane, **5.4**,[299] bis[4–(2–pyridylmethyleneamino)phenyl]ether, **5.5**,[301] bis(2,2'–

bipyridine)ruthenium(II) chloride, $[Ru(bpy)_2Cl_2]$,[316] bis(2,2'–bipyridine)ruthenium(II) carbonate, $[Ru(bpy)_2(CO_3)]$,[317] bis(2,2'–bipyridine)ruthenium(II) bis(trifluoromethanesulfonate), $[Ru(bpy)_2(OTf)_2]$[318] and (2,2':6',2"–terpyridine)ruthenium(III) trichloride, $[Ru(terpy)Cl_3]$.[285]

8.2.1. Bidentate ligands based on azobis(pyridines)

Azobis(3–methyl–2–pyridine), ***2.2***

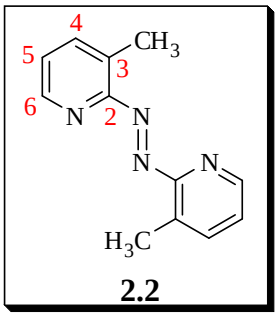

2.2

A solution of 2–amino–3–methylpyridine (2.00 g, 18.5 mmol) in acetonitrile:water (3:1) (20 mL) was added to an acetone/dry ice cooled solution of sodium hypochlorite (60.0 mL, 13.5% w/v). The reaction mixture was stirred at the same temperature for 30 minutes. After TLC analysis, the resulting orange solution was extracted rapidly with dichloromethane (2 x 20 mL). The organic layers were combined, washed with water (10 mL), dried over anhydrous magnesium sulfate and evaporated under reduced pressure. The residue was then purified using silica gel column chromatography (4% methanol:dichloromethane) to give a dark brown solid, which was recrystallised from petroleum ether to give **2.2** as a bright orange needles. Yield: 0.80 g (20%). M.p: 101°C.

^{1}H NMR (400 MHz, CD_3CN): δ 8.47 (d, *J* = 3.9 Hz, 1H, H6), 7.86 (d, *J* = 6.7 Hz, 1H, H4), 7.44–7.41 (m, 1H, H5), 2.60 (s, 3H, CH_3). **^{13}C NMR** (100 MHz, $CDCl_3$): δ 160.9 (C2), 146.9 (C6), 140.2 (C4), 132.3 (C3), 125.4 (C5), 17.13 (CH_3). **ESI MS**: Found MH^+ 213.1136, $C_{12}H_{13}N_4$ requires MH^+ 213.1135. **IR**: ν_{max} 2070, 2050, 2026, 1569, 1411, 1219, 1116, 803, 777, 743, 731, 592, 581 cm^{-1}.

Azobis(6–methyl–2–pyridine), ***2.4***

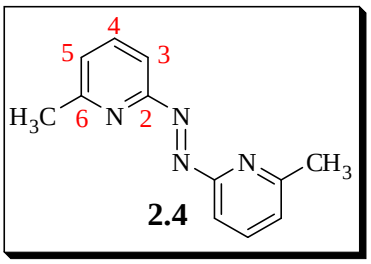

2.4

A rapidly stirred solution of sodium hypochlorite (50.0 mL, 13.5% w/v) was chilled in an acetone/dry ice bath until solids began to precipitate. A solution of 2–amino–6–methylpyridine (1.00 g, 9.24 mmol) in acetonitrile:water (3:1) (10 mL) was added to the above mixture. Stirring and cooling were continued for 15 minutes, after which the resulting orange solution was extracted rapidly with diethyl ether (2 x 20 mL). The organic layers were combined, washed

with water (10 mL), dried over anhydrous magnesium sulfate and evaporated under reduced pressure. The residue was then purified using silica gel column chromatography (2% methanol:dichloromethane) to give a dark brown solid, which was recrystallised from petroleum ether to give **2.4** as a brown solid. Yield: 0.50 g (26%). M.p: 105–110 °C.

^{1}H NMR (400 MHz, DMSO): δ 7.95 (t, *J* = 7.6 Hz, 1H, H4), 7.56 (d, *J* = 7.9 Hz, 1H, H3), 7.48 (d, *J* = 7.5 Hz, 1H, H5), 2.60 (s, 3H, CH_3). **^{13}C NMR** (400 MHz, DMSO): δ 162.5 (C2), 158.8 (C6), 139.6 (C4), 126.2 (C5), 111.2 (C3), 24.3 (CH_3). **ESI MS**: Found MNa^+ 235.0956, $C_{12}H_{12}N_4Na$ requires MNa^+ 235.0954. **IR** (KBr): ν_{max} 2924, 2851, 1910, 1820, 1588, 1560, 1448, 1375, 1261, 1146, 1083, 991, 807, 744 cm^{-1}.

Azobis(5–chloro–2–pyridine), ***2.5***

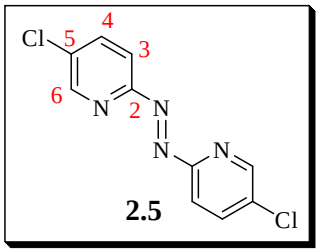

2.5

2–Amino–5–chloropyridine (0.30 g, 2.3 mmol) in methanol:acetonitrile:water (1:1:1) (6 mL) was added to an acetone/dry ice cooled solution of sodium hypochlorite (15.0 mL, 12.5% w/v). Stirring and cooling were continued for 10 minutes, after which the resulting orange solution was extracted with dichloromethane (2 x 30 mL). The organic layers were combined, washed with water (10 mL), dried over anhydrous magnesium sulfate and the solvent was evaporated under reduced pressure. The residue was then washed with diethyl ether (2 x 5 mL) to give **2.5** as a brown solid. Yield: 0.15 g (25%). M.p: 250 °C (lit[319] 248 °C).

^{1}H NMR (400 MHz, $CDCl_3$): δ 8.73 (d, *J* = 1.7 Hz, 1H, H6), 7.96–7.89 (m, 2H, H3, H4). **^{13}C NMR** (125 MHz, $CDCl_3$): δ 161.6 (C2), 148.7 (C6), 138.3 (C4), 134.9 (C5), 115.9 (C3). **ESI–MS**: Found MH^+ 253.0048, $C_{10}H_7Cl_2N_4$ requires MH^+ 253.0042. **IR**: ν_{max} 3035, 1558, 1452, 1375, 1106, 1006, 920, 847, 677, 641, 547, 427 cm^{-1}.

Azobis(5–bromo–2–pyridine), ***2.6***

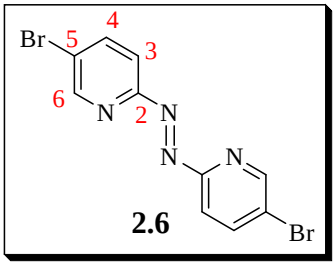

2.6

To an acetone/dry ice cooled solution of sodium hypochlorite (150 mL, 12.5% w/v), a solution of 2–amino–5–bromopyridine (3.00 g, 17.4 mmol) in methanol:water (3:1) (260 mL) was added and stirred for 30 minutes. After TLC analysis, the reaction mixture was extracted with dichloromethane (2 x 30 mL). The organic layers were combined, washed with water (20

mL), dried over anhydrous magnesium sulfate and the solvent was evaporated under reduced pressure. The residue was then purified by silica gel column chromatography (3% methanol:dichloromethane) to give **2.6** as a brown solid. Yield: 2.0 g (34%). M.p: 250 °C (lit[320] 260 °C).

^{1}H NMR (400 MHz, $CDCl_3$): δ 8.84 (d, *J* = 2.3 Hz, 1H, H6), 8.04 (dd, *J* = 8.6 Hz, 2.3 Hz, 1H, H4), 7.88 (d, *J* = 8.6 Hz, 1H, H3). **^{13}C NMR** (100 MHz, $CDCl_3$): δ 161.0 (C2), 150.9 (C6), 141.2 (C4), 123.9 (C5), 116.2 (C3). **ESI–MS**: Found MH^+ 340.9027, $C_{10}H_7Br_2N_4$ requires MH^+ 340.9032. **IR** (KBr): ν_{max} 1976, 1840, 1556, 1453, 1373, 1291, 1092, 1003, 923, 850, 836, 652, 632, 548 cm^{-1}.

8.2.2. Bidentate ligands based on azobis(N–heterocycles)

Azobis(5–chloro–2–pyrimidine), ***3.1***

A solution of 2–aminopyrimidine (1.00 g, 10.5 mmol) in water (10 mL) was added to an ice–cooled solution of sodium hypochlorite (50.0 mL, 13.5% w/v) and the resulting solution was stirred at 0 °C for 30 minutes. After TLC analysis, the aqueous layer was extracted with dichloromethane (3 x 50 mL). The organic layer was washed with water (2 x 10 mL), separated, dried over anhydrous magnesium sulfate and evaporated under reduced pressure to give the crude product as dark orange solid, which was recrystallised from petroleum ether to give **3.1** as orange needles. Yield: 0.79 g (31%). M.p: 198–200 °C.

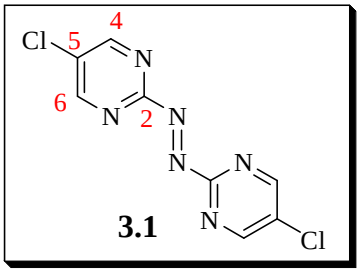

3.1

^{1}H NMR (400 MHz, $CDCl_3$): δ 8.95 (bs, 2H, H4, H6). **^{13}C NMR** (100 MHz, $CDCl_3$): 164.4 (C2), 157.4 (2C, C4, C6), 132.6 (C5). **ESI MS**: Found $[MH]^+$ 254.9946, $C_8H_5Cl_2N_6$ requires MH^+ 254.9947. **IR** (KBr): ν_{max} 3037, 1545, 1396, 1262, 1131, 1019, 812, 654, 554 cm^{-1}.

Azobis(5–bromo–2–pyrimidine), ***3.2***

Sodium hypochlorite (50.0 mL, 12.5% w/v) was chilled in an acetone/dry ice bath until solids began to precipitate. 2–Amino–5–bromopyrimidine (1.00 g, 5.75 mmol) in methanol:water (3:1) (10 mL) was added to the above mixture and stirred for 4 hours with cooling. After TLC analysis, the reaction mixture was extracted with dichloromethane (2 x 10

mL). The organic layers were combined, washed with water (10 mL), dried over anhydrous magnesium sulfate and the solvent was evaporated under reduced pressure. The residue was then purified by silica gel column chromatography (3% methanol:dichloromethane) to give **3.2** as an orange solid. Yield: 0.2 g (10%). M.p: 198 °C).

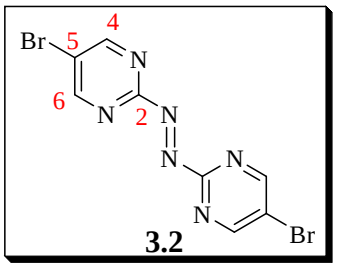

3.2

^{1}H NMR (500 MHz, $CDCl_3$): δ 9.06 (s, 2H, H4, H6). **^{13}C NMR** (100 MHz, $CDCl_3$): δ 164.8 (C2), 159.7 (2C, C4, C6), 121.7 (C5). **ESI–MS**: Found MH^+ 342.8933, $C_8H_5Br_2N_6$ requires MH^+ 342.8937. **IR**: ν_{max} 3035, 1540, 1393, 1371, 1269, 1258, 1113, 1008, 937, 809, 801, 641, 633, 551, 542 cm^{-1}. **Analysis**: Calc. For $C_8H_4Br_2N_6$: C, 27.93; H, 1.17; N, 24.43. Found: C, 28.44; H, 1.31; N, 24.75.

Azobis(5–chloro–4,6–dimethyl–2–pyrimidine), ***3.3***

A solution of sodium hypochlorite (25.0 mL, 13.5% w/v) was chilled in acetone/dry ice bath till solids began to precipitate. A solution of 2–amino–5–chloro–4,6–dimethylpyrimidine (0.50 g, 4.1 mmol) in acetonitrile/water (1:1) (5 mL) was added to the above mixture. The reaction mixture was stirred at the same temperature for 15 minutes. After TLC analysis, the aqueous layer was extracted with dichloromethane (2 x 10 mL). The organic layer was washed with water (2 x 5 mL), separated, dried over anhydrous magnesium sulfate and evaporated under reduced pressure. The crude residue was recrystallised from diethyl ether to give **3.3** as light brown solid. Yield: 0.25 g (20%). M.p: 184 °C.

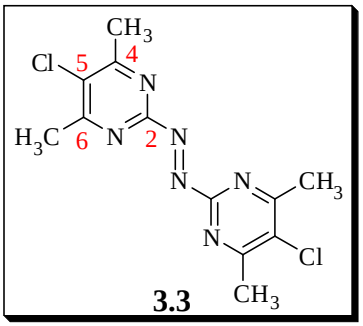

3.3

^{1}H NMR (500 MHz, DMSO): δ 2.66 (s, 6H, 4–CH_3, 6–CH_3). **^{13}C NMR** (100 MHz, $CDCl_3$): δ 166.2 (2C, C4, C6), 163.1 (C2), 130.9 (C5), 22.6 ($2CH_3$). **ESI–MS**: Found MH^+ 311.0581, $C_{12}H_{13}Cl_2N_6$ requires MH^+ 311.0573. **IR** (KBr): ν_{max} 1559, 1517, 1424, 1385, 1325, 1065, 1029, 955, 801, 543 cm^{-1}. **Analysis**: Calc. For $C_{12}H_{12}Cl_2N_6$: C, 46.32; H, 3.89; N, 27.01. Found: C, 46.99; H, 3.97; N, 27.22.

Azobis(2–quinoline), ***3.4***

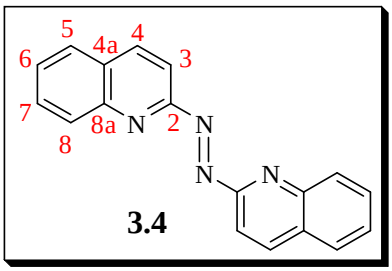

To an acetone/dry ice cooled solution of sodium hypochlorite (15.0 mL, 13.5% w/v) a solution of 2–aminoquinoline (0.30 g, 2.10 mmol) in acetonitrile:water (3:1) (5 mL) was added. Stirring and cooling were continued for 30 minutes, after which the resulting orange solution was extracted rapidly with dichloromethane (2 x 15 mL). The organic layers were combined, washed with water (2 x 10 mL), dried over anhydrous magnesium sulfate, and the solvent was removed under reduced pressure.The residue was then purified using silica gel column chromatography (5% methanol:dichloromethane) to give **3.4** as an orange solid. Yield: 0.25 g (42%). M.p: 233 °C (lit[261]. 232–233 °C).

^{1}H NMR (500 MHz, DMSO) δ 8.67 (d, *J* = 8.6 Hz, 1H, H4), 8.23 (d, *J* = 8.3 Hz, 1H, H5), 8.15 (d, *J* = 8.1 Hz, 1H, H8), 8.03 (d, *J* = 8.8 Hz, 1H, H3), 7.91 (t, *J* = 7.0 Hz, 1H, H6), 7.76 (t, *J* = 7.1 Hz, 1H, H7). **^{13}C NMR** (100 MHz, $CDCl_3$): δ 161.7 (C2), 147.6 (C8a), 138.9 (C4),130.5 (C7, C8), 129.5 (C4a), 128.5 (C6), 127.6 (C5), 110.6 (C3). **ESI–MS**: Found MH^+ 285.1130, $C_{18}H_{13}N_4$ requires MH^+ 285.1135. **IR**: ν_{max} 3043, 1592, 1565, 1498, 1425, 1226, 874, 840, 750, 626, 475 cm^{-1}.

Azobis(2–quinazoline), ***3.5***

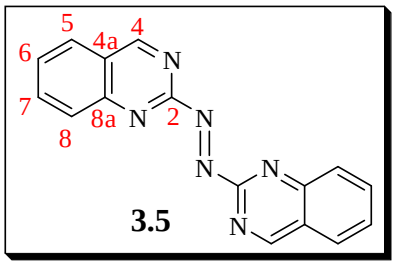

2–Aminoquinazoline (0.10 g, 0.70 mmol) in acetonitrile:water (3:1) (5 mL) was added to a an acetone/dry ice bath cooled solution of sodium hypochlorite (5.00 mL, 13.5% w/v). Stirring and cooling were continued for 30 minutes, after which the resulting orange solution was extracted rapidly with diethyl ether (2 x 10 mL). The organic layers were combined, dried over anhydrous magnesium sulfate, and the solvent was removed under reduced pressure. The residue was then purified using silica gel column chromatography (3% methanol:dichloromethane) to give **3.5** as a brown solid. Yield: 0.08 g (39%). M.p: 180 °C.

^{1}H NMR (500 MHz, DMSO): δ 9.98 (s, 1H, H4), 8.43 (d, *J* = 8.0 Hz, 1H, H8), 8.31–8.24 (m, 2H, H5,7), 8.01–7.98 (m, 1H, H6). **^{13}C NMR**: (100 MHz, DMSO): δ 164.1 (2C, C4, C2), 150.5 (C8a), 136.3 (C7), 130.0 (C6), 129.0 (C5), 128.7 (C8), 124.8 (C4a). **ESI MS**:

Found MH^+ 287.1037, $C_{16}H_{11}N_6$ requires MH^+ 287.1040. **IR** (KBr): ν_{max} 3023, 1931, 1683, 1559, 1491, 1376, 1236, 1207, 993, 813, 768, 725 cm^{-1}.

Azobis(2–quinoxaline), ***3.6***

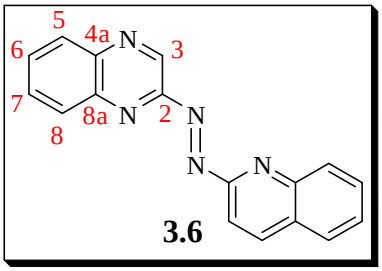

Sodium hypochlorite (12.5 mL, 13.5% w/v) was chilled in an acetone/dry ice slush bath until solids began to precipitate. A solution of 2–aminoquinoxaline (0.25 g, 1.72 mmol) in methanol:water (3:1) (5 mL) was added to this and the reaction mixture was stirred at the same temperature for 10 minutes. The resulting orange solution was extracted with dichloromethane (2 x 10 mL). The organic layers were combined, washed with water (2 x 10 mL), dried over anhydrous magnesium sulfate, and the solvent was removed under reduced pressure. The residue was then washed with diethyl ether (2 x 10 mL), filtered and dried to give **3.6** as orange needles. Yield: 0.16 g (33%). M.p:142–148 °C (lit 143.5–145 °C).

^{1}H NMR (400 MHz, $CDCl_3$): δ 9.62 (bs, 1H, H3), 8.39–8.35 (m, 1H, H5), 8.29–8.26 (m, 1H, H8), 7.97–7.92 (m, 2H, H6, H7). **^{13}C NMR** (100 MHz, $CDCl_3$): δ 154.8 (C2), 144.0 (C4a), 141.4 (C8a), 137.0 (C3), 132.3 (C7), 131.4 (C6), 130.7 (C5), 129.4 (C8). **ESI–MS**: Found MH^+ 287.1044, $C_{16}H_{11}N_6$ requires MH^+ 287.1040. **IR**: ν_{max} 1607, 1557, 1487, 1460, 1361, 1202, 1127, 984, 967, 911, 769, 695, 616, 555, 414 cm^{-1}.

Azobis[2–(1,8–napthyridine)], ***3.7***

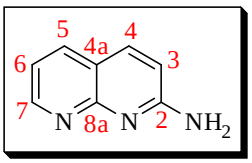

Step 1 – 2–Amino–1,8–napthyridine: 2,6–diaminopyridine (2.00 g, 18.0 mmol), sodium *m*–nitrobenzenesulfonate (8.25 g, 36.7 mmol), glycerol (8.44 g, 91.7 mmol), concentrated sulphuric acid (7.2 mL) and water (12 mL) were heated, with stirring at 135 °C for 48 hours. Upon cooling, the reaction mixture was poured into crushed ice and the pH was adjusted to 13 by the addition of sodium hydroxide pellets. The reaction mixture was filtered through Celite® and the filtrate was extracted with hot chloroform (3 x 20 mL). The combined organic layer was washed with water (2 x 10 mL), brine (15 mL), dried over anhydrous magnesium sulfate and evaporated under reduced pressure. The crude product was then purified using silica gel column chromatography (5:1 methanol:dichloromethane) to give 8–amino–1,7–napthyridine as a brown solid. Yield: 0.50 g (19%). M.p: 150 °C (lit[321] 142–144 °C)

^{1}H NMR (400 Hz, CD_3OD): δ 8.65 (d, *J* = 4.3 Hz, 1H, H7), 8.07 (d, *J* = 7.8 Hz, 1H, H5), 7.93 (d, *J* = 9.0 Hz, 1H, H4), 7.22 (dd, *J* = 7.5 Hz, 4.0 Hz, 1H, H6), 6.88 (d, *J* = 9.0 Hz, 1H, H3), 6.90 (bs, 2H, NH_2). **IR**: ν_{max} 3056, 1674, 1594, 1451, 1370, 1328, 900, 841, 523, 503, 463, 441 cm^{-1}.

Step 2: 2–amino–1,8–napthyridine (0.10 g, 0.69 mmol) in methanol (10 mL) as added to a acetone/dry ice chilled solution of sodium hypochlorite (5.00 mL, 13.5% w/v) Stirring and cooling were continued for 15 minutes, after which the resulting orange solution was extracted rapidly with dichloromethane (2 x 10 mL). The organic layers were combined and dried over anhydrous magnesium sulfate, and the solvent was removed under reduced pressure. The residue was then recrystallised from diethyl ether/methanol (10:1) to give **3.7** as an orange solid. Yield: 0.10 g (50%). M.p: 295 °C.

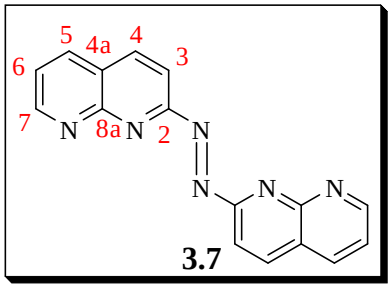

3.7

^{1}H NMR (400 MHz, $CDCl_3$–CD_3OD): δ 9.19 (bs, 1H, H7), 8.48 (d, *J* = 8.6 Hz, 1H, H4), 8.36 (d, *J* = 8.2 Hz, 1H, H5), 8.22 (d, *J* = 8.6 Hz, 1H, H3), 7.63 (dd, *J* = 7.8 Hz, 4.3 Hz, 1H, H6). **^{13}C NMR** (100 MHz, $CDCl_3$–CD_3OD): 163.4 (C2), 154.9 (C8a), 154.6 (C7), 140.6 (C4), 137.5 (C5), 124.7 (C4a), 123.8 (C6), 112.2 (C3). **ESI MS**: Found MH^+ 287.1039, $C_{16}H_{11}N6$ requires MH^+ 287.1040. **IR**: ν_{max} 3043, 1597, 1545, 1483, 1451, 1425, 1111, 852, 815, 779, 725 cm^{-1}.

Azobis[2–(1,5–napthyridine)], ***3.8***

Step 1 – 2,5–Diaminopyridine: 10% Palladium on carbon (0.01 g, cat.) was added to a solution of 2–amino–5–nitropyridine (0.50 g, 3.6 mmol) in methanol (10 mL). The suspension was stirred under hydrogen pressure of 10 psi for 3 hours. After the completion of reaction (monitored by TLC), the reaction mixture was filtered through Celite®. The filtrate was evaporated under reduced pressure to give 2,5–diaminopyridine as a black solid, which was used without further purification. Yield: 2.8 g (76%). M.p: 120 °C.

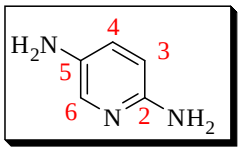

^{1}H NMR (500 Hz, DMSO) δ 7.36 (d, *J* = 4.2 Hz, 1H, H6), 6.76 (dd, *J* = 8.7 Hz, 3.0 Hz, 1H, H4), 6.25 (d, *J* = 8.5 Hz, 1H, H3), 4.91 (bs, 2H, NH_2) and 4.24 (bs, 2H, NH_2). **ESI–MS**: Found MH^+ 110.0714, $C_5H_8N_3$ requires MH^+ 110.0713. **IR**: ν_{max} 2871, 1667, 1557, 1505, 1477, 1431, 1215, 1138, 1125, 891, 828, 764, 755 cm^{-1}.

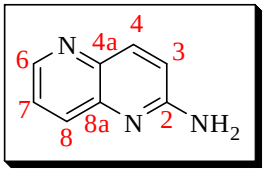

Step 2 – 2–Amino–1,5–napthyridine: 2,5–diaminopyridine (0.48 g, 4.4 mmol), sodium *m*–nitrobenzenesulfonate (1.98 g, 8.80 mmol), glycerol (1.6 mL, 22 mmol), concentrated sulphuric acid (2 mL), water (3 mL) were heated, with stirring at 135 °C for 48 hours. Upon cooling, the reaction mixture was poured into crushed ice and the pH was adjusted to 13 by the addition of sodium hydroxide pellets. The reaction mixture was filtered through Celite® and the filtrate was extracted with hot chloroform (3 x 20 mL). The combined organic layer was washed with water (2 x 10 mL), brine (15 mL), dried over anhydrous magnesium sulfate and evaporated under reduced pressure. The crude product was then purified using silica gel column chromatography (5:1 methanol:dichloromethane) to give 2–amino–1,5–napthyridine[270] as a brown solid. Yield: 0.5 g (19%). M.p: 162 °C (lit[322] 203.5–205 °C).

^{1}H NMR (400 Hz, DMSO): δ 9.12 (d, *J* = 4.3 Hz, 1H, H6), 8.55 (d, *J* = 9.0 Hz, 1H, H4), 8.41 (d, *J* = 8.6 Hz, 1H, H8), 8.01 (q, *J* = 4.3 Hz, 1H, H7), 7.55 (d, *J* = 9.0 Hz, 1H, H3), 6.01 (bs, 2H, NH_2). **ESI–MS**: Found MH^+ 146.0710, $C_8H_8N_3$ requires MH^+ 146.0713. **IR**: ν_{max} 3311, 3120, 1733, 1661, 1502, 1418, 1327, 1289, 1112, 839, 807, 619, 540, 499 cm^{-1}.

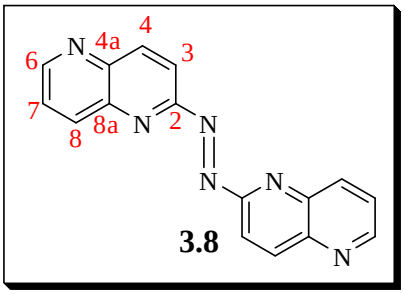

Step 3: A rapidly stirred solution of sodium hypochlorite (12.5 mL, 13.5% w/v) was chilled in an acetone/dry ice slush bath until solids began to precipitate. To this was added (all at once), a solution of 2–amino–1,5–napthyridine (0.25 g, 1.7 mmol) in acetonitrile:water (3:1) (5 mL). Stirring and cooling were continued for 15 minutes, after which the resulting orange solution was extracted rapidly with dichloromethane (2 x 10 mL). The organic layers were combined and dried over anhydrous magnesium sullfate, and the solvent was removed under reduced pressure. The residue was then purified using silica gel column chromatography (3% methanol:dichloromethane) to give **3.8** as an orange solid. Yield: 0.16 g (33%). M.p: 271 °C.

^{1}H NMR (400 Hz, $CDCl_3$): δ 9.11 (d, *J* = 4.3 Hz, 1H, H6), 8.72–8.64 (m, 2H, H8, H4), 8.42 (dd, *J* = 9.0 Hz, 1.2 Hz, 1H, H3), 7.79–7.77 (m, 1H, H7). **^{13}C NMR**: (100 MHz, $CDCl_3$): δ 161.5 (C2), 152.8 (C6), 144.7 (C4a), 143.3 (C8a), 140.4 (C4), 138.3 (C8), 125.4 (C7), 114.5 (C43). **ESI MS**: Found MH^+ 287.1043, $C_{16}H_{11}N_6$ requires MH^+ 287.1040. **IR**: ν_{max} 3024, 1586, 1482, 1316, 1227, 1191, 1103, 856, 819, 786, 626, 563 cm^{-1}.

8.2.3. Tridentate ligands based on azobis(bidentates)

*Azobis[6–(2,2'–bipyridine)], **4.1***

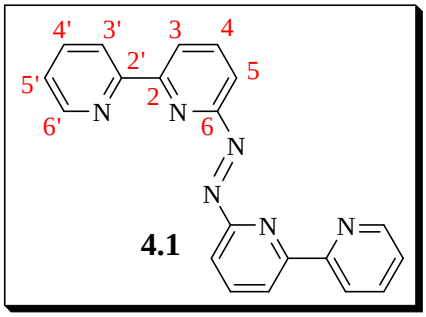

6–Amino–2,2'–bipyridine (0.10 g, 0.58 mmol) dissolved in methanol:water (3:1) (5 mL) was added to a solution of sodium hypochlorite (5.00 mL, 13.5% w/v) chilled in an acetone/dry ice bath. Stirring and cooling were continued for 15 minutes, after which the resulting orange solution was extracted rapidly with diethyl ether (2 x 10 mL). The organic layers were combined, dried over anhydrous magnesium sulfate and the solvent was removed under reduced pressure. The residue was then purified using silica gel column chromatography (3% methanol:dichloromethane) to give **4.1** as an orange solid. Yield: 0.070 g (27%). M.p: 212 °C.

^{1}H NMR (400 MHz, $CDCl_3$): δ 8.73 (d, *J* = 4.3 Hz, 1H, H6'), 8.67 (d, *J* = 7.8 Hz, 1H, H3'), 8.63 (d, *J* = 7.8 Hz, 1H, H3), 8.07 (t, *J* = 7.9 Hz, 1H, H4), 7.95 (d, *J* = 7.5 Hz, 1H, H5), 7.87 (td, *J* = 7.6 Hz, 1.6 Hz, 1H, H4'), 7.36 (dd, *J* = 6.6 Hz, 4.8 Hz, 1H, H5'). **^{13}C NMR**: (400 MHz, $CDCl_3$): δ 162.8 (C6), 156.4 (C2), 155.2 (C2'), 149.2 (C6'), 139.2 (C4), 137.0 (C4'), 124.2 (C5'), 123.4 (C3), 121.8 (C3'), 113.3 (C5). **ESI MS**: Found MH^+ 339.1358, $C_{20}H_{15}N_6$ requires MH^+ 339.1353. **IR** (KBr): ν_{max} 3059, 1919, 1582, 1557, 1478, 1430, 1271, 1151, 1077, 992, 831, 781, 744, 667, 640, 624 cm^{-1}.

*Azobis[2–(1,10–phenanthroline)], **4.2***

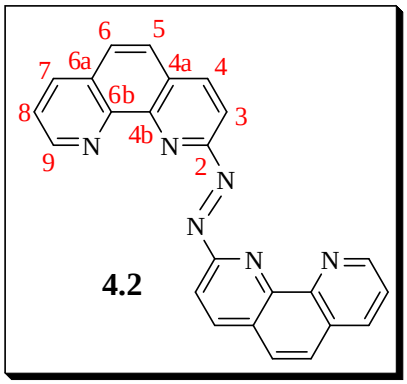

A solution of sodium hypochlorite (70.0 mL, 13.5% w/v) was chilled in an acetone/dry ice slush bath until solids began to precipitate. 2–Amino–1,10–phenanthroline (1.4 g, 7.2 mmol) dissolved in methanol:water (3:1) (70 mL) was added to the reaction mixture. The reaction was stirred for 30 minutes. The resulting solution was extracted with dichloromethane (2 x 20 mL). The combined organic layers were separated, dried over anhydrous magnesium sulfate and the solvent was evaporated under reduced pressure. The crude residue was then purified by silica gel column chromatography (3% methanol:dichloromethane) to give **4.2** as an orange solid. Yield: 1.2 g (43%). M.p: > 260 °C.

^{1}H NMR (400 MHz, $CDCl_3$) δ 9.32 (bs, 1H, H9), 8.57 (d, *J* = 8.7 Hz, 1H, H3), 8.50 (d, *J* = 8.6 Hz, 1H, H4), 8.34 (d, *J* = 8.2 Hz, 1H, H7), 7.94 (bs, 2H, H5, H6), 7.72 (dd, *J* = 7.8 Hz, 4.5 Hz, 1H, H8). **^{13}C NMR** (125 MHz, $CDCl_3$–one drop of CD_3OD was added to increase the solubility): δ 161.4 (C2), 147.9 (C9), 141.1 (C7), 139.6 (C4), 131.0 (C4a), 129.7 (C6a), 128.0 (C6), 127.8 (C5), 124.6 (C8), 115.4 (C3). **ESI MS**: Found MH^+ 387.1353, $C_{24}H_{15}N_6$ requires MH^+ 387.1353. **IR** (KBr): ν_{max} 3050, 1969, 1557, 1491, 1398, 1324, 861, 834, 795, 786, 749, 674, 629 cm^{-1}.

8.3. Ruthenium Complexes with azobis(pyridines)

8.3.1. Complexes of 2.1

*$[(bpy)_2Ru(\mathbf{2.1})](PF_6)_2$, **2.7** and $[(bpy)_2Ru(\mu$–**2.1**$)Ru(bpy)_2](PF_6)_4$, **2.8***

Ligand **2.1** (0.050 g, 0.27 mmol) and bis(2,2'–bipyridine)ruthenium(II) dichloride (0.39 g, 0.81 mmol) were refluxed in 50% aqueous methanol (15 mL) for 3 days. After cooling, the solvent was removed *in vacuo* and the residue was redissolved in water and filtered through Celite®. The aqueous solution was loaded on a SP Sephadex C–25 cation exchanger. Separation of the mononuclear and dinuclear products from the crude mixture was achieved *via* a gradient elution procedure using aqueous 0.1–0.5 mol L^{-1} sodium chloride as the eluent. Three bands were eluted: Band 1 (dark red, 0.1 mol L^{-1} NaCl), Band 2: (purple, 0.2 mol L^{-1}) and Band 3: (green, 0.3 mol L^{-1}). The fractions were precipitated by addition of a saturated solution of ammonium hexafluorophosphate to each band. The resultant products were extracted into dichloromethane and the solvent was removed under reduced pressure. The solid residues were recrystallised from acetone/diethyl ether. The composition of Bands 1, 2 and 3 were established by electrospray mass spectrometry and ^{1}H NMR. Analysis of Band 1 revealed the presence of the mononuclear ruthenium species, Band 2 as the ruthenium(II) precursor and Band 3 as the dinuclear ruthenium species. Yields: Band 1 = (**2.7**) 0.090 g (37%). Band 3 = (**2.8**) 0.090 g (20%).

(2.7): **M.p**: 185 °C. **^{1}H NMR** (400 MHz, CD_3CN): δ 8.88 (d, 1H, H3'), 8.62 (d, 1H, bpyH3A), 8.55 (d, 1H, bpyH3'A), 8.44 (d, 1H, bpyH3B), 8.29–8.14 (m, 5H, bpyH3'B, H4', bpyH4A, bpyH4'A, bpyH4B), 8.06 (d, 1H, bpyH6'A), 7.99 (t, 1H, bpyH4'B), 7.92–7.88 (m, 3H, H6, H6', H4), 7.70 (t, 1H, H5'), 7.62–7.55 (m, 4H, bpyH6A, H3, bpyH5A, bpyH6'B), 7.52–7.47 (m, 2H, bpyH5'A, bpyH5B), 7.38 (t, 1H, H5), 7.30–7.26 (m, 2H, bpyH6B,

bpyH5'B). **^{13}C NMR** (100 MHz, CD_3CN): δ 166.2 (C2), 163.8 (C2'), 157.2 (bpyC2'B), 156.0 (bpyC2'A), 155.8 (bpyC2B), 154.7 (bpyC2A), 153.2 (bpyC6'A), 152.3 (bpyC6'B), 151.8 (bpyC6B), 150.2 (bpyC6A), 149.9 (C6'), 148.2 (C6), 139.9_5 (bpyC4A), 139.8_8 (C4'), 139.7_9 (bpyC4B), 139.6 (bpyC4'A), 139.4 (C4), 138.6 (bpyC4'B), 128.8 (C3'), 128.7 (C5'), 128.3_0 (bpyC5A), 128.2_7 (bpyC5'A), 128.0 (bpyC5B), 126.7 (C5), 126.2 (bpyC5'B), 124.7 (2C, bpyC3A, bpyC3'A), 124.2 (bpyC3B), 123.3 (bpyC3'B), 115.7 (C3). **ESI–MS**: Calc. for ($[(bpy)_2Ru(\mathbf{2.1})\cdot(PF_6)]^{1+}$): 743.0812, Found: 743.0808; Calc. for ($[(bpy)_2Ru(\mathbf{2.1})]^{2+}$): 299.0582, Found: 299.0583 **IR** (KBr): ν_{max} 3419, 2924, 2854, 2013, 1715, 1637, 1606, 1469, 1448, 1431, 1328, 1244, 841, 765, 557 cm^{-1}. **UV** (CH_3CN): λ_{max} 508, 279, 243 nm.

(2.8): **M.p**: 248 °C. **^{1}H NMR** (500 MHz, CD_3CN): δ 8.62 (d, 1H, bpyH3A), 8.60–8.56 (m, 3H, bpyH3B, bpyH3'A, bpyH3'B), 8.29–8.23 (m, 3H, bpyH4A, bpyH4'B, bpyH4B), 8.16 (t, 1H, bpyH4'A), 8.05 (d, 1H, H3), 7.89 (d, 1H, H6), 7.83 (d, 1H, bpyH6B), 7.77 (t, 1H, H4), 7.71 (t, 1H, bpyH5'B), 7.66 (t, 1H, H5), 7.62 (t, 1H, bpyH5B), 7.56 (t, 1H, bpyH5A), 7.49 (d, 1H, bpyH6A), 7.25–7.20 (m, 3H, bpyH5'A, bpyH6'B, bpyH6'A). **^{13}C NMR** (100MHz, CD_3CN) δ 166.18, 163.77, 151.9 (bpyC6'A), 151.8 (bpyC6'B), 151.3 (C6), 150.9 (bpyC6B), 140.6 (bpyH4A), 140.5 (bpyH4'B), 140.4 (bpyH4B), 140.2 (H4), 139.7 (bpyC4'A), 129.1 (C5), 129.0 (bpyC5B), 128.8 (bpyC5A), 128.7 (bpyC5'B), 127.6 (bpyC5'A), 126.3 (C3), 125.5 (2C, bpyC3'A, bpyC3'B), 125.2 (bpyC3B), 125.2 (bpyC3A). **ESI–MS**: Calc. for ($[\{Ru(bpy)_2\}_2(\mu\text{–}\mathbf{2.1})\cdot(PF_6)_2]^{2+}$): 651.0431, Found: 651.0436; Calc. for ($[\{Ru(bpy)_2\}_2(\mu\text{–}\mathbf{2.1})\cdot(PF_6)]^{3+}$) 385.7071, Found: 385.7069; Calc. for ($[\{Ru(bpy)_2\}_2(\mu\text{–}\mathbf{2.1})]^{4+}$): 253.0392, Found: 253.0390. **IR** (KBr): ν_{max} 2939, 2857, 1597, 1468, 1446, 1314, 1256, 1240, 839, 765, 554 cm^{-1}. **UV** (CH_3CN) λ_{max} 508, 280, 244 nm.

8.3.2. Complex of 2.2

*$[(bpy)_2Ru(\mathbf{2.2})](PF_6)_2$, **2.9***

A solution of **2.2** (0.014 g, 0.064 mmol) and bis(2,2'–bipyridine)ruthenium(II) triflate (0.050 g, 0.064 mmol) in ethylene glycol (5 mL) was heated at reflux in a modified microwave oven at 600 W for 6 minutes, at intervals of 2 minutes.. Upon cooling, the resultant red solution was diluted with water (~ 15 mL) and precipitated by addition of saturated solution of ammonium hexafluorophosphate. The resultant product was filtered and recrystallised from acetone/hexane to give **2.9** as red powder. Yield: 0.060 g (94%). M.p: 166 °C.

^{1}H NMR (500 MHz, CD_3CN): δ 8.64–8.62 (m, 2H, bpyH6A, bpyH3A), 8.56 (d, 1H, bpyH3'A), 8.34 (d, 1H, bpyH3B), 8.23–8.16 (m, 3H, bpyH4A, bpyH4B, bpyH4'A), 8.07–8.05 (m, 2H, bpyH3'B, H4'), 8.01 (d, 1H, H6), 7.85 (t, 1H, bpyH4'B), 7.70–7.68 (m, 2H, H6', bpyH6'B), 7.63–7.51 (m, 6H, H5', bpyH6B, H4, bpyH5A, bpyH5B, bpyH5'A), 7.48 (d, 1H, bpyH6'A), 7.25 (t, 1H, bpyH5'B), 7.16 (dd, 1H, H5), 2.90 (s, 3H, 3'–CH_3), 1.43 (s, 1H, 3–CH_3). **^{13}C NMR** (125 MHz, CD_3CN): δ 164.3 (C2'), 161.1 (C2), 156.8 (bpyC2'B), 155.7 (bpyC2'B), 155.2 (bpyC2B), 154.7 (bpyC2A), 154.3 (bpyC6A), 152.9 (bpyC6'A), 152.8 (bpyC6'B), 150.2 (bpyC6B), 147.0 (C6'), 146.1 (C6), 141.5 (C4), 141.1 (C4'), 140.2 (bpyC4B), 140.0 (2C, C3, C3'), 139.7 (bpyC4A), 139.2 (bpyC4'A), 138.5 (bpyC4'B), 129.3_0 (C5'), 128.2_9 (bpyC5'A), 128.0 (bpyC5B), 127.9 (bpyC5A), 126.7 (bpyC5'B), 124.6_0 (bpyC3A), 124.5_8 (C5), 124.4_0 (bpyC2'A), 124.3_8 (bpyC3B), 123.1 (bpyC3'B), 17.8 (3'–CH_3), 15.3 (3–CH_3). **ESI–MS**: Calc. for ($[(bpy)_2Ru(\mathbf{2.2})\cdot(PF_6)]^{1+}$): 771.1125, Found: 771.1126; Calc. for ($[(bpy)_2Ru(\mathbf{2.2})]^{2+}$): 313.0739, Found: 313.0742. **IR**: ν_{max} 1605, 1468, 1448, 1207, 1124, 1086, 1025, 998, 825, 756, 648, 623, 555 cm^{-1}. **UV** (CH_3CN): λ_{max} 503, 382, 280, 245 nm. **Analysis**: Calc. for $[(bpy)_2Ru(\mathbf{2.2})](PF_6)_2\cdot 3H_2O$: C, 39.64; H, 3.53; N, 11.56. Found: C, 39.28; H, 2.85; N, 10.96.

8.3.3. Complexes of 2.3

*$[(bpy)_2Ru(\mathbf{2.3})](PF_6)_2$, **2.10***

Bis(2,2'–bipyridine)ruthenium(II) dichloride (0.10 g, 0.23 mmol) and **2.3** (0.050 g, 0.23 mmol) were refluxed in 50% aqueous methanol (5 mL) for 16 h. After cooling, the solvent was removed *in vacuo* and purified by silica gel column chromatography using 7:1 acetonitrile:saturated potassium nitrate. The red solution was precipitated by addition of a saturated solution of ammonium hexafluorophosphate. The resultant product was extracted into dichloromethane and the solvent was removed *in vacuo*. The solid residues were recrystallised from acetone/hexane to give **2.10** as red needles. Yield: 0.14 g (66%). M.p: 158 °C.

^{1}H NMR (400 MHz, CD_3CN): δ 8.71 (s, 1H, H3'), 8.60 (d, 1H, bpyH3A), 8.53 (d, 1H, bpyH3B), 8.42 (d, 1H, bpyH3C), 8.27 (d, bpyH3D), 8.23–8.12 (m, 3H, bpyH4A, bpyH4C, bpyH4B), 8.01 (d, 1H, bpyH6B), 7.95 (td, 1H, bpyH4D), 7.77 (d, 1H, H6), 7.71 (d, 1H, H6'), 7.60 (d, 1h, bpyH6A), 7.57–7.47 (m, 5H, bpyH5A, H5, bpyH6D, bpyH5B, bpyH5C), 7.33 (s, 1H, H3), 7.30 (d, 1H, bpyH6C), 7.26 (t, 1H, bpyH5D), 7.18 (d, 1H, H5), 2.67 (s, 3H, 4'–

CH_3), 2.31 (s, 1H, 4–CH_3). **^{13}C NMR** (100 MHz, CD_3CN): δ 165.9 (C2'), 163.9 (C2), 157.3 (bpyC2C), 156.1 (bpyC2D), 155.9 (bpyC2B), 154.7 (bpyC2A), 153.1 (bpyC6B), 152.1 (bpyC6C), 151.9 (bpyC6D), 151.6 (2C, C4, C4'), 150.2 (bpyC6A), 148.8 (C6'), 147.8 (C6), 139.9 (bpyC4A), 139.7 (bpyC4C), 139.3 (bpyC4B), 138.4 (bpyC4D), 129.5 (C5'), 129.2 (C3'), 128.2 (2C, bpyC5A, bpyC5B), 128.0 (bpyC5C), 126.8 (C5), 126.6_5 (bpyC5D), 124.6_0 (2C, bpyC3A, bpyC3B), 124.1 (bpyC3C), 123.2 (bpyC3D), 116.0 (C3), 20.2 (4'–CH_3), 20.0 (4–CH_3). **ESI–MS**: Calc. for ($[(bpy)_2Ru(\mathbf{2.3})\cdot(PF_6)]^{1+}$): 771.1125, Found 771.1124; Calc. for ($[(bpy)_2Ru(\mathbf{2.3})]^{2+}$): 313.0739, Found: 313.0739. **IR** (KBr): ν_{max} 3093, 2928, 1706, 1602, 1470, 1450, 1345, 1251, 1155, 842, 759, 558 cm^{-1}. **UV** (CH_3CN): λ_{max} 508, 280, 244 nm.

*$[(bpy)_2Ru(\mu$–**2.3**$)Ru(bpy)_2](PF_6)_4$, **2.11***

The mononuclear complex **2.10** (0.080 g, 0.090 mmol), bis(2,2'–bipyridine)ruthenium(II) dichloride (0.060 g, 0.13 mmol) and silver nitrate (0.020 g, 0.13 mmol) were refluxed in methanol:water (3:1) (10 mL) for 6 days. After cooling, the solvent was removed *in vacuo* and the residue was redissolved in water and filtered through Celite®. The aqueous solution was loaded on a SP Sephadex C–25 cation exchanger. Separation of the dinuclear product from the crude mixture was achieved *via* a gradient elution procedure using aqueous 0.1–0.5 mol L^{-1} sodium chloride as the eluent. Three bands were eluted: Band 1 (dark red, 0.1 mol L^{-1} NaCl), Band 2: (purple, 0.2 mol L^{-1}) and Band 3: (green, 0.3 mol L^{-1}). The fractions were precipitated by addition of saturated solution of ammonium hexafluorophosphate to each band. The resultant products were extracted into dichloromethane and the solvent was removed under reduced pressure. The solid residues were recrystallised from acetone/diethyl ether. The composition of Bands 1, 2 and 3 were established by electrospray mass spectrometry and ^{1}H NMR. Analysis of Band 1 revealed the presence of unreacted mononuclear ruthenium species, Band 2 as unreacted $[Ru(bpy)_2Cl_2]$ precursor and Band 3 as the dinuclear ruthenium species. Yield: 0.070 g (51%). M.p: > 300 °C.

^{1}H NMR (400 MHz, CD_3CN): δ 8.63 (d, 1H, bpyH3A), 8.60–8.53 (m, 3H, bpyH3B, bpyH3C, bpyH3D), 8.28–8.23 (m, 3H, bpyH4A, bpyH4B, bpyH4C), 8.14 (t, 1H, bpyH4C), 7.87 (d, 1H, bpyH6A), 7.71 (s, 1H, H3), 7.71 (t, 1H, bpyH5B), 7.67–7.63 (m, 2H, H6, bpyH5A), 7.54 (t, 1H, bpyH5D), 7.50–7.47 (m, 2H, bpyH6D, H5), 7.24–7.18 (m, 3H, bpyH5C, bpyh6C, bpyH6B), 2.10 (s, 3H, 4–CH_3). **ESI–MS**: Calc. for ($[\{Ru(bpy)_2\}_2(\mu$–**2.3**$)]^{2+}$): 519.5906, Found: 519.5933; Calc. for ($[\{Ru(bpy)_2\}_2(\mu$–**2.3**$)]^{3+}$): 346.3969, Found:

346.3970. calc. for ([{Ru(bpy)$_2$}$_2$(μ–**2.3**)]$^{4+}$): 260.0471; Found: 260.0471.**IR** (KBr): ν_{max} 3665, 2924, 1638, 1618, 1468, 1316, 1259, 1163, 1033, 956, 843, 766, 558 cm^{-1}. **UV** (CH_3CN): λ_{max} 757, 392, 280, 247 nm. **Analysis**: Calc. for [(bpy)$_2$Ru(μ–**2.3**)Ru(bpy)$_2$](PF$_6$)$_4$: C, 38.58; H, 2.74; N, 10.38. Found: C, 38.65; H, 3.00; N, 10.10.

8.3.4. Complex of 2.4

*[(bpy)$_2$Ru(**2.4**)](PF$_6$)$_2$, **2.12***

A suspension of **2.4** (0.020 g, 0.090 mmol) and bis(2,2'–bipyridine)ruthenium(II) dichloride (0.090 g, 0.19 mmol) in 50% aqueous methanol (10 mL) were refluxed for 16 h. After cooling, the solvent was removed *in vacuo* and the residue was redissolved in water and filtered through Celite®. The aqueous solution was precipitated by addition of a saturated solution of ammonium hexafluorophosphate. The resultant product was extracted into dichloromethane (2 x 15 mL) and the solvent was removed under reduced pressure. The solid residues were recrystallised from acetone/hexane to give **2.12** as a red powder. Yield: 0.071 g (83%). M.p: 142 °C.

^{1}H NMR (400 MHz, CD_3CN): δ 8.68 (d, 1H, H3'), 8.55–8.49 (m, 3H, bpyH3A, bpyH3B, bpyH3C), 8.28–8.24 (m, 2H, bpyH3C, bpyH4C), 8.20–8.11 (m, 3H, H4', bpyH4B, bpyH4A), 8.02 (d, 1H, bpyH6B), 7.87 (t, 1H, bpyH4D), 7.71 (t, 1H, H4), 7.67–7.65 (m, 3H, H5', bpyH6C, bpyH6A), 7.58–7.55 (m, 2H, bpyH5B, bpyH5C), 7.50 (t, 1H , bpyH5A), 7.23–7.20 (m, 2H, H3, bpyH6D), 7.13 (d, 1H, H5), 7.11 (t, 1H, bpyH5D). **^{13}C NMR** (100 MHz, CD_3CN): δ 166.0 (C2), 163.5 (C2'), 163.2 (C6'), 158.0 (C6), 157.5 (bpyC2C), 156.4 (bpyC2B), 155.8 (bpyC2D), 154.2 (bpyC2A), 153.8 (bpyC6C), 151.8 (bpyC6B), 151.3 (bpyC6D), 150.0 (bpyC6A), 140.2 (bpyC4C), 140.0 (bpyC4A), 139.7 (C4, C4'), 139.2 (bpyC4B), 138.6 (bpyC4D), 129.1 (C5), 128.4 (bpyC5A), 128.1$_2$ (bpyC5B), 128.1$_0$ (bpyC5C), 126.9 (C3'), 126.7 (bpyC5D), 125.1 (bpyC3C), 124.9 (C5), 124.7 (bpyC3B), 124.4 (bpyC3A), 123.6 (bpyC3D), 112.2 (C3), 24.4 (6'–CH_3), 22.6 (6–CH_3). **ESI–MS**: Calc. for ([(bpy)$_2$Ru(**2.4**)·(PF$_6$)]$^{1+}$): 771.1125, Found: 771.1144; Calc. for ([(bpy)$_2$Ru(**2.4**)]$^{2+}$): 313.0739, Found: 313.0749. **IR**: ν_{max} 1605, 1468, 1446, 1343, 1315, 831, 798, 763, 729, 555 cm^{-1}. **UV** (CH_3CN): λ_{max} 498, 287, 244 nm. **Analysis**: Calc. for [(bpy)$_2$Ru(**2.4**)](PF$_6$)$_2$·H$_2$O: C, 41.17; H, 3.24; N, 12.00. Found: C, 41.19; H, 3.14; N, 11.39.

8.3.5. Complexes of 2.5

*[(bpy)$_2$Ru(**2.5**)](PF$_6$)$_2$, **2.13***

Ligand **2.5** (0.020 g, 0.080 mmol) and bis(2,2'–bipyridine)ruthenium(II) dichloride (0.040 g, 0.080 mmol) were refluxed in 50% aqueous methanol (10 mL) for 16 h. Upon cooling, the solvent was removed *in vacuo* and the residue was redissolved in water and filtered through Celite®. The red solution was precipitated by addition of saturated solution of potassium hexafluorophosphate (10 mL) and extracted into dichloromethane (2 x 10 mL) and the solvent was removed under reduced pressure. The solid residues were recrystallised from acetonitrile/diethyl ether to give **2.13** as a red powder. Yield: 0.050 g (64%). M.p: 212 °C.

^{1}H NMR (400 MHz, CD_3CN): δ 8.84 (d, 1H, H3'), 8.60 (d, 1H, bpyH3A), 8.55 (d, 1H, bpyH3'A), 8.44 (d, 1H, bpyH3B), 8.33–8.27 (m, 2H, bpyH3'B, H4'), 8.25–8.15 (m, 3H, bpyH4A, bpyH4B, bpyH4'A), 8.05 (t, 1H, bpyH4'B), 7.96–7.92 (m, 2H, H4, H6'), 7.89–7.86 (m, 2H, H6, bpyH6'A), 7.78 (d, 1H, H3), 7.58–7.57 (m, 2H, bpyH6A, bpyH5A), 7.51–7.45 (m, 3H, bpyH5'A, bpyH5B, bpyH6'B), 7.35 (d, 1H, bpyH6B), 7.30 (t, 1H, bpyH5'B). **^{13}C NMR** (100 MHz, CD_3CN): δ 164.7 (C2'), 162.1 (C2), 157.1 (bpyC2B), 155.9_0 (bpyC2'A), 155.8_7 (bpyC2'B), 154.6 (bpyC2A), 153.1 (C6), 152.7 (bpyC6B), 151.6 (bpyC6'B), 150.3 (bpyC6A), 148.7 (C6'), 146.7 (bpyC6'A), 140.1 (bpyC4A), 140.0 (bpyC4'B), 139.8 (C4'), 139.6 (bpyC4'A), 139.3 (C4), 138.8 (bpyC4'B), 135.9 (C5), 134.6 (C5'), 129.4 (C3'), 128.4 (bpyC5A), 128.3 (bpyC5B), 127.9 (bpyC3'A), 127.0 (bpyC5'B), 124.9 (bpyC3'A), 124.8 (bpyC3A), 124.3 (bpyC3B), 123.6 (bpyC3'B). **ESI–MS**: Calc. for ([(bpy)$_2$Ru(**2.5**)·(PF$_6$)]$^{1+}$): 811.0026, Found: 811.0035; Calc. for ([(bpy)$_2$Ru(**2.5**)]$^{2+}$): 333.0189, Found: 333.0190. **IR** (KBr): ν_{max} 3669, 1709, 1637, 1608, 1543, 1469, 1458, 1450, 1314, 1295, 1243, 1116, 841, 766, 558 cm^{-1}. **UV** (CH_3CN): λ_{max} 517, 277, 242 nm. **Analysis**: Calc. for [(bpy)$_2$Ru(**2.5**)](PF$_6$)$_2$·5H$_2$O: C, 34.43; H, 3.08; N, 10.71. Found: C, 34.09; H, 2.22; N, 10.70.

*[(bpy)$_2$Ru(μ–**2.5**)Ru(bpy)$_2$](PF$_6$)$_4$, **2.14***

Ligand **2.5** (0.10 g, 0.39 mmol) and bis(2,2'–bipyridine)ruthenium(II) dichloride (0.38 g, 0.792 mmol) were refluxed in 50% aqueous methanol (15 mL) for 5 days. After cooling, the solvent was removed *in vacuo* and the residue purified by silica gel column chromatography using acetonitrile:saturated potassium nitrate (7:1) as eluent. The fractions were precipitated by addition of saturated solution of ammonium hexafluorophosphate to

each band. The resultant products were extracted into dichloromethane (3 x 10 mL) and the solvent was removed under reduced pressure. The solid residues were recrystallised from acetone/diethyl ether to give **2.14** as a green crystalline powder. Yield: 0.13 g (20%). M.p: 270 °C.

^{1}H NMR (400 MHz, CD_3CN): δ 8.62 (d, 1H, bpyH3A), 8.59–8.54 (m, 3H, bpyH3'A, bpyH3B, bpyH3'B), 8.32–8.23 (m, 3H, bpyH4'B, bpyH4A, bpyH4'A), 8.18 (t, 1H, bpyH4B), 7.90 (d, 1H, H3), 7.79–7.71 (m, 4H, H6, H4, bpyH6'A, bpyH5'B), 7.61 (t, 1H, bpyH5'A), 7.55 (t, 1H, bpyH5A), 7.48 (d, 1H, bpyH6A), 7.29 (d, 1H, bpyH6'B), 7.24 (t, 1H, bpyH5B), 7.09 (d, 1H, bpyH6B). **^{13}C NMR** (100 MHz, CD_3CN): δ 165.0 (C2), 156.9 (bpyC2'B), 155.9 (bpyC2B), 155.8 (bpyC2'A), 154.8 (bpyC2A), 152.3 (bpyC6B), 152.2 (bpyC6'B), 151.0 (bpyC6'A), 150.9 (bpyC6A), 149.7 (C6), 140.9 (bpyC6'B), 140.7 (bpyC4A), 140.7 (bpyC4'A), 140.2 (2C, bpyC4B, C4), 137.1 (C5), 129.2 (bpyC5'A), 128.9 (bpyC5A), 128.7 (bpyC5'B), 127.9 (bpyC5B), 126.6 (C3), 125.8 (bpyC3'B), 125.6 (bpyC3B), 125.6 (2C, bpyC3A, bpyC3'A). **ESI–MS**: Calc. for ($[\{Ru(bpy)_2\}_2(\mu$–**2.5**$)\cdot(PF_6)_2]^{2+}$): 685.0045, Found: 685.0041; Calc. for ($[\{Ru(bpy)_2\}_2(\mu$–**2.5**$)\cdot(PF_6)]^{3+}$): 408.3481, Found: 408.3477; Calc. for ($[\{Ru(bpy)_2\}_2(\mu$–**2.5**$)]^{4+}$): 270.0199, Found: 270.0195. **IR** (KBr): ν_{max} 3411, 2253, 1638, 1608, 1470, 1450, 1317, 1245, 1127, 843, 769, 558 cm^{-1}. **UV** (CH_3CN): λ_{max} 758, 391, 281, 246 nm.

8.3.6. Complexes of 2.6

*$[(bpy)_2Ru($**2.6**$)](PF_6)_2$,* ***2.15***

Ligand **2.6** (0.050 g, 0.15 mmol) and bis(2,2'–bipyridine)ruthenium(II) dichloride (0.070 g, 0.15 mmol) were refluxed in 50% aqueous methanol (10 mL) for 16 h. After cooling, the solvent was removed *in vacuo* and the residue was redissolved in water and filtered through Celite®. The red solution was precipitated by addition of saturated solution of potassium hexafluorophosphate (10 mL). The resultant product was extracted into dichloromethane and the solvent was removed under reduced pressure. The solid residues were recrystallised from acetonitrile/diethyl ether to give **2.15** as a red powder. Yield: 0.090 g (61%). M.p: 205 °C.

^{1}H NMR (400 MHz, CD_3CN): δ 8.76 (d, 1H, H3'), 8.60 (d, 1H, bpyH3A), 8.54 (d, 1H, bpyH3'A), 8.45–8.42 (m, 2H, bpyH3B, H4'), 8.31 (d, 1H, bpyH3'B), 8.24–8.14 (m, 3H, bpyH4A, bpyH4B, bpyH4'A), 8.10 (dd, 1H, H4), 8.03–7.96 (m, 3H, bpyH4'B, H6', H6),

7.86 (d, 1H, bpyH6'A), 7.72 (d, 1H, H3), 7.58–7.56 (m, 2H, bpyH6A, bpyH5A), 7.51–7.47 (m, 2H, bpyH5'A, bpyH5B), 7.44 (d, 1H, bpyH6'B), 7.34 (d, 1H, bpyH6B), 7.29 (t, 1H, bpyH5'B).**^{13}C NMR** (100 MHz, CD_3CN): δ 165.0 (C2'), 162.5 (C2), 157.1 (bpyC6B), 155.9 (2C, bpyC2'A, bpyC2B), 154.6 (bpyC2'B), 153.1 (bpyC6'A), 152.8 (bpyC6B), 151.6 (bpyC6'B), 150.6 (C6'), 150.3 (bpyC6A), 148.9 (C6), 146.7 (bpyC6'A), 142.8 (C4'), 142.2 (C4), 140.1 (bpyC4B), 140.0 (bpyC4'A), 139.6 (bpyC4A), 138.8 (bpyC4'B), 129.5 (C3'), 128.4 (bpyC5A), 128.3 (bpyC5B), 127.9 (bpyC5'A), 127.0 (bpyC5'B), 124.9 (bpyC3A), 124.8 (bpyC3'A), 124.3 (2C, bpyC3B, C5'), 123.6 (bpyC3'B), 123.5 (C5), 117.5 (C3). **ESI–MS**: Calc. for ($[(bpy)_2Ru(\mathbf{2.6})]^{2+}$): 377.9678, Found: 377.9675. **IR** (KBr): ν_{max} 3665, 3098, 1709, 1637, 1606, 1537, 1470, 1450, 1368, 1315, 1296, 1242, 1100, 841, 765, 558 cm^{-1}. **UV** (CH_3CN): λ_{max} 523, 368, 277, 241 nm. **Analysis**: Calc. for $[(bpy)_2Ru(\mathbf{2.6})](PF_6)_2 \cdot H_2O$: C, 33.88; H, 2.27; N, 10.54. Found: C, 34.05; H, 2.48; N, 9.94.

*$[(bpy)_2Ru(\mu$–**2.6**$)Ru(bpy)_2](PF_6)_4$, **2.16***

Bis(2,2'–bipyridine)ruthenium(II) triflate (0.08 g, 0.107 mmol) and ligand **2.6** (0.018 g, 0.054 mmol) were refluxed in ethylene glycol (10 mL) for 3 days. After cooling, the solvent was removed *in vacuo* and the residue was redissolved in the minimum amount of acetonitrile:saturated KNO_3 (7:1). The resulting solution was loaded on a silica gel column and eluted with 7:1 acetonitrile:saturated KNO_3 mixture. The fractions were precipitated by addition of a saturated solution of ammonium hexafluorophosphate. The resultant products were extracted into dichloromethane (3 x 10 mL) and the solvent was removed under reduced pressure. The crude solid was recrystallised from acetone/diethyl ether to give **2.16** as a green solid. Yield: 0.02 g (21%). M.p: 278 °C.

^{1}H NMR (400 MHz, CD_3CN): δ 8.63 (d, 1H, bpyH3A), 8.59–8.54 (m, 3H, bpyH3'A, bpyH3B, bpyH3'B), 8.31–8.22 (m, 3H, bpyH4'B, bpyH4A, bpyH4'A), 8.17 (t, 1H, bpyH4B), 7.92 (d, 1H, H3), 7.87 (s, 1H, H6), .81 (d, 1H, H4), 7.75–7.72 (m, 2H, bpyH6'A, bpyH5'B), 7.61 (t, 1H, bpyH5'A), 7.55 (t, 1H, bpyH5A), 7.48 (d, 1H, bpyH6A), 7.29 (d, 1H, bpyH6'B), 7.24 (t, 1H, bpyH5B), 7.08 (d, 1H, bpyH6B). **ESI–MS**: Calc. for ($[\{Ru(bpy)_2\}_2(\mu$–**2.6**$)]^{3+}$): 389.9927, Found: 389.9918. **IR**: ν_{max} 1605, 1467, 1449, 1426, 1242, 1107, 829, 760, 729, 710, 555, 421 cm^{-1}. **UV** (CH_3CN): λ_{max} 764, 431, 373, 276, 243 nm. **Analysis**: Calc. for $[(bpy)_2Ru(\mu$–**2.6**$)Ru(bpy)_2](PF_6)_4 \cdot CH_3CN$: C, 34.90; H, 2.31; N, 10.17. Found: C, 35.11; H, 2.42; N, 10.49.

8.4. Ruthenium Complexes with azobis(N–heterocycles)

8.4.1. Complexes of 3.1

*$[(bpy)_2Ru(\mathbf{3.1})](PF_6)_2$, **3.9***

Ligand **3.1** (0.050 g, 0.20 mmol) and bis(2,2'–bipyridine)ruthenium(II) dichloride (0.09 g, 0.20 mmol) were refluxed in 50% aqueous ethanol (10 mL) for 24 h. After cooling, the solvent was removed *in vacuo* and the residue was redissolved in water and filtered through Celite®. The aqueous solution was loaded on a SP Sephadex C–25 cation exchanger and eluted using aqueous 0.1–0.5 mol L^{-1} sodium chloride as the eluent. The red fraction obtained with 0.2 mol L^{-1} sodium chloride was precipitated by addition of a saturated solution of ammonium hexafluorophosphate. The solid precipitate was filtered and recrystallised from acetone/diethyl ether to give **3.9** as red needles. Yield: 0.14 g (78%). M.p: 210 °C.

^{1}H NMR (400 MHz, CD_3CN): δ 9.23 (d, 1H, H4/6), 8.61–8.51 (m, 2H, bpyH3A, H4', H6', bpyH3B, bpyH3C), 8.35–8.29 (m, 3H, bpyH3D, H6/4, bpyH4C), 8.26–8.19 (m, 2H, bpyH4A, bpyH4B), 8.10 (d, 1H, bpyH6B), 8.01 (t, 1H, bpyH4D), 7.62–7.51 (m, 5H, bpyH5A, bpyH5B, bpyH5C, bpyH6A, bpyH6C), 7.23–7.21 (m, 2H, bpyH5D, bpyH6D). **^{13}C NMR** (100 MHz, CD_3CN): δ 159.7 (C4/6), 157.5 (C6/4), 157.3 (2C, C4, C6), 153.3 (bpyC6C), 152.9 (bpyC6B), 151.1 (bpyC6D), 149.9 (bpyC6A), 140.9 (bpyC4C), 140.4 (bpyC4A), 140.0 (bpyC4B), 139.3 (bpyC4C), 128.8 (bpyC5A), 128.3 (bpyC5B), 128.2 (bpyC5C), 127.2 (bpyC5D), 124.8_5 (bpyC3A), 124.7_6 (bpyC3B), 124.5 (bpyC3C), 124.0 (bpyC3D). **ESI–MS**: Calc. for $([(bpy)_2Ru(\mathbf{3.1})\cdot(PF_6)]^{1+}$): 812.9930. Found: 812.9925; Calculated for $([(bpy)_2Ru(\mathbf{3.1})]^{2+}$): 334.0142. Found: 334.0141. **IR** (KBr): ν_{max} 3657, 1637, 1608, 1522, 1471, 1402, 1303, 1136, 841, 765, 558 cm^{-1}. **UV/Vis** (CH_3CN) λ_{max} 493, 368, 285, 269, 248 nm. **Analysis**: Calc. for $[(bpy)_2Ru(\mathbf{3.1})](PF_6)_2\cdot H_2O$: C, 34.44; H, 2.27; N, 14.34. Found: C, 34.47; H, 2.27; N, 13.62.

*$[(bpy)_2Ru(\mu–\mathbf{3.1})Ru(bpy)_2](PF_6)_3$, **3.10***

Complex **3.9** (0.08 g, 0.08 mmol) and bis(2,2'–bipyridine)ruthenium(II) dichloride (0.060 g, 0.12 mmol) were refluxed in ethanol:water (3:1) (10 mL) for 24 h. After cooling, the solvent was removed *in vacuo* and the residue was redissolved in water and filtered through Celite®. The aqueous solution was loaded on a SP Sephadex C–25 cation exchanger. Separation of the dinuclear product from the crude mixture was achieved *via* a gradient

elution procedure using aqueous 0.1–0.5 mol L^{-1} sodium chloride as the eluent. The green fraction was precipitated by addition of a saturated solution of ammonium hexafluorophosphate. The resultant product was extracted into dichloromethane (2 x 10 mL) and the solvent was removed under reduced pressure. The solid residues were recrystallised from acetone/diethyl ether to give **3.10** as a green powder which was paramagnetic. Yield: 0.070 g (51%). M.p: >300 °C.

^{1}H NMR (500 MHz, CD_3CN): δ 8.63 (d, 1H, bpyH3A), 8.53–8.52 (m, 2H, bpyH3B, bpyH3C), 8.46 (d, 1H, bpyH3D), 8.30–8.20 (m, 4H, bpyH4C, bpyH4A, H4, H6), 8.17–8.11 (m, 2H, bpyH4D, bpyH4B), 7.71 (t, 1H, bpyH5C), 7.61–7.54 (m, 3H, bpyH6C, bpyH5A, bpyH6A), 7.45 (t, 1H, bpyH5D), 7.41 (d, 1H, bpyH6D), 7.14 (t, 1H, bpyH5B), 6.88 (d, 1H, bpyH6B). **ESI–MS**: Calc. for ($[\{Ru(bpy)_2\}_2(\mu–\mathbf{3.1})\cdot(PF_6)]^{3+}$): 613.5176, Found: 613.5178; Calc. for ($[\{Ru(bpy)_2\}_2(\mu–\mathbf{3.1})]^{3+}$): 360.6902, Found: 360.6803. **IR** (KBr): ν_{max} 3665, 3087, 1605, 1467, 1448, 1392, 1341, 1244, 1133, 842, 764, 558 cm^{-1}. **UV** (CH_3CN): λ_{max} 612, 446, 383, 285, 246 nm. **Analysis**: Calc. for $[(bpy)_2Ru(\mu–\mathbf{3.1})Ru(bpy)_2](PF_6)_3\cdot 4H_2O$: C, 36.28; H, 2.79; N, 12.34. Found: C, 35.51; H, 2.40; N, 12.64.

8.4.2. Complexes of 3.2

*$[(bpy)_2Ru(\mathbf{3.2})](PF_6)_2$, **3.11***

Ligand **3.2** (0.02 g, 0.06 mmol) and bis(2,2'–bipyridine)ruthenium(II) dichloride (0.03 g, 0.06 mmol) were refluxed in 50% aqueous methanol (10 mL) for 16 h. After cooling, the solvent was removed *in vacuo* and the residue was redissolved in water. The aqueous solution was precipitated by addition of saturated solution of ammonium hexafluorophosphate. The solid obtained was filtered and recrystallised from acetone/diethyl ether to give **3.11** as a red crystalline powder. Yield: 0.050 g (80%). M.p: 229 °C.

^{1}H NMR (400 MHz, CD_3CN) δ 9.31 (d, 1H, H4/H6), 8.87 (s, 2H, H4', H6'), 8.61 (d, 1H, bpyH3A), 8.57–8.52 (m, 2H, bpyH3'A, bpyH3B), 8.41 (s, 1H, H6/H4), 8.36–8.29 (m, 2H, bpyH3'B, bpyH4B), 8.27–8.19 (m, 2H, bpyH4A, bpyH4'A), 8.10 (d, 1H, bpyH6'A), 8.01 (m, 1H, bpyH4'B), 7.62–7.52 (m, 5H, bpyH5'A, bpyH5A, bpyH5B, bpyH6A, bpyH6B), 7.23–7.22 (m, 2H, bpyH5'B, bpyH6'B). **^{13}C NMR** (100 MHz, CD_3CN): δ 171.3 (C2), 164.5 (C2'), 162.0 (C4/C6), 159.8 (2C, C4', C6'), 159.6 (C6/C4), 156.9 (bpyC2B), 155.9 (bpyC2'B), 155.6 (bpyC2'A), 154.1 (bpyC2A), 153.4 (bpyC6B), 153.0 (bpyC6'A), 151.3 (bpyC6'B), 150.1 (bpyC6A), 141.0 (bpyC4B), 140.5 (bpyC4A), 140.2 (bpyC4'A), 19.4

(pyC4'B), 128.8 (bpyC5'A), 128.6 (bpyC5A), 128.2 (bpyC5B), 127.4 (bpyC5'B), 125.0$_4$ (bpyC3'A), 124.9$_7$ (bpyC3A), 124.6 (bpyC3B), 124.1 (bpyC3'B), 121.6 (C5'), 120.1 (C5). **ESI–MS**: Calc. for ($[(bpy)_2Ru(\mathbf{3.2})\cdot(PF_6)]^{1+}$) 902.8908, Found: 902.8916; Calc. for ($[(bpy)_2Ru(\mathbf{3.2})]^{2+}$): 378.9631, Found: 378.9654. **IR**: ν_{max} 1606, 1469, 1448, 1399, 1301, 1116, 826, 759, 728, 647, 611, 554 cm^{-1}. **UV/Vis** (CH_3CN) λ_{max} 499, 367, 314, 285, 269, 249 nm. **Analysis**: Calc. for $[(bpy)_2Ru(\mathbf{3.2})](PF_6)_2$: C, 32.11; H, 1.92; N, 13.37. Found: C, 32.71; H, 2.13; N, 13.05.

*$[(bpy)_2Ru(\mu$–**3.2**$)Ru(bpy)_2](PF_6)_3$, **3.12***

Bis(2,2'–bipyridine)ruthenium(II) triflate (0.06 g, 0.08 mmol) and **3.2** (0.01 g, 0.04 mmol) were refluxed in 50% aqueous methanol (5 mL) for 3 days. After cooling, the solvent was removed *in vacuo* and the residue was redissolved in the minimum amount of acetonitrile:saturated KNO_3 (7:1). The resulting solution was loaded on a silica gel column and eluted with 7:1 acetonitrile:saturated KNO_3 mixture. The fractions were precipitated by addition of a saturated solution of ammonium hexafluorophosphate. The resultant products were extracted into dichloromethane (4 x 10 mL) and the solvent was removed under reduced pressure. The crude solid was recrystallised from acetone/diethyl ether to give **3.12** as a green solid. Yield: 0.020 g (21%). M.p: 260 °C.

ESI–MS: Calc. for ($[\{Ru(bpy)_2\}_2(\mu$–**3.2**$)\cdot(PF_6)]^{2+}$): 658.4667, Found: 658.4686; Calc. for ($[\{Ru(bpy)_2\}_2(\mu$–**3.2**$)]^{2+}$): 585.9846, Found: 585.9801; Calc. for ($[\{Ru(bpy)_2\}_2(\mu$–**3.2**$)]^{3+}$): 390.6562, Found: 390.6172. **IR**: ν_{max} 1465, 1447, 1388, 1338, 1310, 1242, 1163, 1113, 828, 759, 729, 641, 555 cm^{-1}. **UV** (CH_3CN) λ_{max} 613, 444, 386, 285, 246 nm. **Analysis**: Calc. for $[(bpy)_2Ru(\mu$–**3.2**$)Ru(bpy)_2](PF_6)_3$: C, 35.90; H, 2.26; N, 12.21. Found: C, 36.67; H, 2.70; N, 11.53.

8.4.3. Complexes of 3.3

*$[(bpy)_2Ru($**3.3**$)](PF_6)_2$, **3.13** and $[(bpy)_2Ru(\mu$–**3.3**$)Ru(bpy)_2](PF_6)_4$, **3.14***

Ligand **3.3** (0.02 g, 0.06 mmol) and bis(2,2'–bipyridine)ruthenium(II) dichloride (0.06 g, 0.13 mmol) were refluxed in 50% aqueous methanol (10 mL) for 24 h. Upon cooling, the reaction mixture was filtered through Ceite® and the solvent was removed *in vacuo*. The residue was loaded on a silica gel column and eluted with acetonitrile:saturated KNO_3 (7:1). The fractions were precipitated by addition of a saturated solution of potassium

hexafluorophosphate, extracted into dichloromethane (3 x 10 mL) and the solvent was removed under reduced pressure. The solid residues were recrystallised from acetonitrile/diethyl ether to give **3.13** and **3.14** as a red and green solid, respectively. Yield: (**3.13**): 0.090 g (61%), (**3.14**): 0.02g (19%).

(**3.13**): **M.p**: 230°C. **^{1}H NMR** (400 MHz, CD_3CN): δ 8.62–8.53 (m, 3H, bpyH3A, bpyH3B, bpyH3C), 8.39–8.35 (m, 2H, bpyH4A, bpyH3D), 8.24 (d, 1H, bpyH6B), 8.22–8.17 (m, 2H, bpyH4B, bpyH4C), 7.95–7.91 (m, 1H, bpyH4D), 7.84 (d, 1H, bpyH6A), 7.72–7.64 (m, 3H, bpyH5B, bpyH6C, bpyH5A), 7.58–7.54 (m, 1H, bpyH5C), 7.09–7.05 (m, 1H, bpyH5D), 7.02(d, 1H, bpyH6D), 2.92 (s, 3H, 4–CH_3), 2.35 (s, 6H, 4'/6'–CH_3), 2.18 (s, 3H, 6–CH_3). **^{13}C NMR** (100MHz, CD_3CN): δ 169.1 (C4), 168.9 (C2), 168.5 (C6), 166.6 (2C, C4', C6'), 162.5 (C2'), 157.3 (bpyC2A), 156.5 (bpyC2D), 155.4 (bpyC2C), 154.5 (bpyC6A), 154.0 (bpyC2B), 151.7 (bpyC6B), 151.4 (bpyC6D), 149.8 (bpyC6C), 141.0 (bpyC4A), 140.5 (bpyC4C), 139.9 (bpyC4B), 139.4 (bpyC4D), 130.5 (C5'), 129.9 (C5), 128.9 (bpyC5B), 128.7 (bpyC5C), 128.4 (bpyC5A), 127.3 (bpyC5D), 125.2 (bpyC3C), 124.9 (bpyC3B), 124.6 (bpyC3A), 124.0 (bpyC3D), 22.6 (4–CH_3), 22.0 (6–CH_3), 21.6 (4'/6'–CH_3). **ESI–MS**: Calc. for ($[(bpy)_2Ru(\mathbf{3.3})\cdot(PF_6)]^{1+}$): 869.0557, Found: 869.0560; Calc. for ($[(bpy)_2Ru(\mathbf{3.3})]^{2+}$): 362.0455, Found: 362.0458. **IR** (KBr): ν_{max} 1638, 1609, 1473, 1449, 1428, 1357, 1311, 1275, 1091, 839, 774, 764, 558 cm^{-1}. **UV** (CH_3CN): λ_{max} 491, 361, 313, 271, 247 nm. **Analysis**: Calc. for $[(bpy)_2Ru(\mathbf{3.3})](PF_6)_2\cdot H_2O$: C, 37.22; H, 2.93; N, 13.57. Found: C, 37.20; H, 2.65; N, 13.12.

(**3.14**): **M.p**: >300 °C. **ESI–MS**: Calc. for ($[\{Ru(bpy)_2\}_2(\mu–\mathbf{3.3})\cdot(PF_6)_2]^{2+}$): 714.0311, Found: 714.0309; Calc. for ($[\{Ru(bpy)_2\}_2(\mu–\mathbf{3.3})\cdot(PF_6)]^{3+}$): 427.6991, Found: 427.6987; Calc. for ($[\{Ru(bpy)_2\}_2(\mu–\mathbf{3.3})]^{2+}$): 568.5630, Found: 568.5632; Calc. for ($[\{Ru(bpy)_2\}_2(\mathbf{3.3})]^{3+}$): 379.3777, Found: 379.3774. **IR** (KBr): ν_{max} 2917, 1605, 1558, 1468, 1449, 1424, 1317, 1237, 1180, 1031, 848, 766, 558 cm^{-1}. **UV** (CH_3CN) λ_{max} 658, 493, 389, 287, 244 nm.

8.4.4. Complexes of 3.4

*$[(bpy)_2Ru(\mathbf{3.4})](PF_6)_2$, **3.15***

Bis(2,2'–bipyridine)ruthenium(II) dichloride (0.12 g, 0.25 mmol) and **3.4** (0.070 g, 0.25 mmol) were refluxed in 50% aqueous methanol (15 mL) for 24 h. Upon cooling, the solvent was removed *in vacuo* and the residue was redissolved in water. The aqueous solution was

precipitated by addition of a saturated solution of potassium hexafluorophosphate. The resultant solid was filtered and recrystallised from acetone/diethyl ether to give **3.15** as a red powder. Yield: 0.15 g (62%). M.p: 230°C.

^{1}H NMR (500 MHz, CD_3CN): δ 8.87 (d, 1H, H3'), 8.77 (d, 1H, H4'), 8.69 (d, 1H , bpyH3A), 8.53 (d, 1H, bpyH3B), 8.48 (d, 1H, H4), 8.41–8.37 (m, 2H, bpyH3'A, bpyH3'B), 8.32 (t, 1H, bpyH4A), 8.26 (t, 1H, bpyH4B), 8.16 (d, 1H, H5'), 8.05 (t, 1H, bpyH3'B), 7.99 (d, 1H, H3), 7.97 (d, 1H, H5), 7.93 (d, 1H, bpyH3B), 7.88 (d, 1H, bpyH6'B), 7.84 (t, 1H, H6'), 7.82–7.63 (m, 5H, bpyH4'A, H7, bpyH5B, H6, bpyH6A), 7.52 (t, 1H, bpyH5'D), 7.48–7.40 (m, 4h, H8', H7', bpyH5A, H8), 7.29 (d, 1H, bpyH6'B), 6.96 (t, 1H, bpyH5'B). **^{13}C NMR** (125 MHz, CD_3CN): δ 166.4 (C2'), 162.8 (C2), 158.0 (bpyC2B), 156.6 (bpyC2A), 155.4 (bpyC2'A), 154.5 (bpyC2'B), 153.7 (bpyC6A), 151.6 (bpyC6'A), 151.4 (bpyC6'B), 149.5 (bpyC6B), 147.5 (C9'), 145.4 (C9), 141.0 (C4'), 140.6 (bpyC4A), 140.5 (bpyc4B), 140.4 (C4), 139.6 (bpyC4'B), 138.8 (bpyC4'A), 132.8 (C7'), 131.1 (C7), 130.1 (C5'), 129.9 (C6'), 129.6 (C10'), 128.8_0 (C6), 128.7_6 (bpyC5B), 128.5 (C8), 128.4 (bpyC5'B), 128.3 (C10), 128.1 (C5), 127.9 (bpyC5A), 126.9 (bpyC5'A), 124.8 (bpyC3B), 124.7 (bpyC3A), 124.6 (bpyC3'B), 124.0 (C8'), 123.9 (bpyC3'A), 123.7 (C3'), 114.2 (C3). **ESI–MS**: Calc. for ($[(bpy)_2Ru(\mathbf{3.4})\cdot(PF_6)]^{2+}$): 349.0740, Found: 349.0746. **IR** (KBr): ν_{max} 3099, 1970, 1710, 1605, 1502, 1448, 1332, 1152, 848, 761, 558 cm^{-1}. **UV/Vis** (CH_3CN) λ_{max} 519, 371, 313, 275, 250 nm. **Analysis**: Calc. for $[(bpy)_2Ru(\mathbf{3.4})](PF_6)_2\cdot CH_3COCH_3$: C, 47.09; H, 3.28; N, 10.72. Found: C, 46.61; H, 3.25; N, 10.31.

*$[(bpy)_2Ru(\mu$–**3.4**$)Ru(bpy)_2](PF_6)_4$, **3.16***

Complex **3.15** (0.03 g, 0.03 mmol) and bis(2,2'–bipyridine)ruthenium(II) dichloride (0.02 g, 0.04 mmol) were refluxed in degassed 50% aqueous methanol (10 mL) for 3 days. Upon cooling, the solvent was removed *in vacuo* and the residue purified by silica gel column chromatography using acetonitrile:saturated potassium nitrate (7:1) as eluent. The fractions were precipitated by addition of saturated solution of ammonium hexafluorophosphate to each band. The resultant products were extracted into dichloromethane (3 x 10 mL) and washed with copious amount of water. The organic layer was separated and evaporated under reduced pressure. The solid residues were recrystallised from acetone/diethyl ether to give **3.16** as a green solid. Yield: 0.030 g (54%). M.p: 230°C.

ESI–MS: Calc. for ([{Ru(bpy)$_2$}$_2$(μ–**3.4**)·(PF$_6$)$_2$]$^{2+}$): 701.0587, Found: 701.0600; Calc. for ([{Ru(bpy)$_2$}$_2$(μ–**3.4**)·(PF$_6$)]$^{3+}$): 419.0509, Found: 419.0514; Calc. for ([{Ru(bpy)$_2$}$_2$(μ–**3.4**)]$^{3+}$): 370.7295, Found: 370.7302. **IR** (KBr): ν_{max} 3099, 1970, 1710, 1605, 1502, 1448, 1332, 1152, 848, 761, 558 cm^{-1}. **UV/Vis** (CH$_3$CN) λ_{max} 685, 288, 244 nm.

8.4.5. Complexes of 3.5

*[(bpy)$_2$Ru(**3.5**)](PF$_6$)$_2$, **3.17/3.18***

Ligand **3.5** (0.02 g, 0.07 mmol) and bis(2,2'–bipyridine)ruthenium(II) dichloride (0.03 g, 0.07 mmol) were refluxed in 50% aqueous ethanol (10 mL) for 16 h. Upon cooling, the solvent was removed *in vacuo*; the residue was loaded on a silica gel column and eluted with acetonitrile: saturated KNO$_3$ (7:1) into Band 1 (reddish orange) and Band 2 (red). The fractions were precipitated by addition of saturated solution of ammonium hexafluorophosphate to each band. The resultant products were extracted into dichloromethane (2 x 10 mL), wahed with water (4 x 10 mL) and the solvent was removed under reduced pressure. The solid residues were recrystallised from acetone/diethyl ether. The composition of Bands 1 and 2 were established by ^{1}H NMR. Analysis of Band 1 revealed the presence of two isomers and Band 2 as the major isomer **3.18** as a dark red crystalline solid. The Band 1 product was dissolved in methanol and was converted to chloride salt using Amberlite IRA resin. The solution was filtered, concentrated *in vacuo* and the residue was redissolved in water. The aqueous solution was loaded on a SP Sephadex C–25 column and eluted using 0.1 mol L^{-1} sodium chloride. The fractions were precipitated using saturated solution of potassium hexafluorophosphate. The products were extracted with dichloromethane (2x 10 mL), dried over anhydrous magnesium sulfate and evaporated under reduced pressure. The solid residue was recrystallised from acetone and diethyl ether to give **3.17** as reddish orange needles. Yields: (**3.17**) 0.0070 g (10%); (**3.18**) 0.056 g (80%).

(**3.17**): M.p: 250 °C. **^{1}H NMR** (500 MHz, CD$_3$CN): δ 9.86 (s, 1H, H4), 9.36 (s, 1H, H4'), 8.66 (d, 1H, bpyH3A), 8.56 (d, 1H, bpyH3B), 8.42–8.27 (m, 6H, bpyH3C, bpyH4A, H5, bpyH6C, bpyH3D, bpyH4B), 8.12–8.01 (m, 4H, H5'bpyH4C, H7', H6), 7.91 (d, 1H, bpyH6B), 7.83 (t, 1H, H6'), 7.77–7.64 (m, 6H, H7, H8', bpyH5B, bpyH6A, bpyH4D, bpyH5C), 7.51 (t, 1H, bpyH5A), 7.31 (d, 1H, H8), 7.09 (d, 1H, bpyH6D), 6.82 (t, 1H, bpyH5D). **ESI–MS**: Calc. for ([(bpy)$_2$Ru(**3.5**)·(PF$_6$)]$^{1+}$): 845.1031, Found: 845.1039; Calc.

for ([(bpy)$_2$Ru(**3.5**)]$^{2+}$): 350.0692, Found: 350.0692. **IR**: ν_{max} 2921, 1606, 1570, 1469, 1447, 1408, 828, 758, 728, 555 cm^{-1}. **UV/Vis** (CH_3CN): λ_{max} 493, 369, 314 (sh), 278, 243, 230 nm.

(**3.18**): **M.p**: 220 °C. **^{1}H NMR** (500 MHz, CD_3CN): δ 9.37 (s, 1H, H4'), 9.02 (s, 1H, H4), 8.64–8.62 (m, 2H, bpyH3A, bpyH3B), 8.54–8.53 (m, 2H, bpyH3C, bpyH4A), 8.45 (d, 1H, H5), 8.32–8.22 (m, 4H, bpyH4C, bpyH4B, H6, bpyH3D), 8.16–8.11 (m, 3H, bpyH5A, H8, H8'), 8.07–8.02 (m, 2H, H6', H7), 7.83 (t, 1H, H7'), 7.75–7.69 (m, 4H, H5', bpyH5B, bpyH4D, bpyH6C), 7.44–7.53 (m, 2H, bpyH6B, bpyH6A), 7.55 (t, 1H, bpyH5C), 7.33 (d, 1H, bpyH6D), 6.97 (t, 1H, bpyH5D). **ESI–MS**: Calc. for ([(bpy)$_2$Ru(**3.5**)·(PF$_6$)]$^{1+}$): 845.1031, Found: 845.1038; Calc. for ([(bpy)$_2$Ru(**3.5**)]$^{2+}$): 350.0692, Found: 350.0694. **IR**: ν_{max} 2921, 2852, 1606, 1570, 1469, 1447, 1330, 828, 758, 728, 555 cm^{-1}. **UV/Vis** (CH_3CN): λ_{max} 513, 368, 317, 278, 236 nm. **Analysis**: Calc. for [(bpy)$_2$Ru(**3.5**)](PF$_6$)$_2$·CH_3COCH_3·H_2O: C, 43.95; H, 3.22; N, 13.14. Found: C, 43.49; H, 3.06; N, 12.51.

*[(bpy)$_2$Ru(μ–**3.5**)Ru(bpy)$_2$](PF$_6$)$_4$, **3.19/3.20***

Ligand **3.5** (0.010 g, 0.035 mmol) and bis(2,2'–bipyridine)ruthenium(II) dichloride (0.034 g, 0.070 mmol) were refluxed in ethanol:water (3:1) (10 mL) for 3 days. Upon cooling, the solvent was removed *in vacuo* and the residue was redissolved in water and filtered through Celite®. The aqueous solution was loaded on a SP Sephadex C–25 cation exchanger. Separation of the dinuclear product from the crude mixture was achieved *via* a gradient elution procedure using aqueous 0.2–0.5 mol L^{-1} sodium tosylate as the eluent. The fractions were precipitated by addition of saturated solution of ammonium hexafluorophosphate to each band. The resultant products were extracted into dichloromethane (3 x 10 mL) and the solvent was removed under reduced pressure. The solid residues were recrystallised from acetone/diethyl ether to give **3.19** and **3.20** as a olive green and green pwder, respectively. Yields: (**3.19**) 8.0 mg (13%); (**3.20**) 0.090 g (37%).

(**3.20**): **M.p**: 270 °C. **^{1}H NMR** (400 MHz, CD_3CN): δ 8.88 (s, 1H, H4), 8.67–8.52 (m, 4H, bpyH3A, bpyH3B, bpyH3C, bpyH3D), 8.30–8.25 (m, 3H, bpyH4A, bpyH4B, bpyH4C), 8.07–8.00 (m, 3H, bpyH4D, H5, H7), 7.93 (t, 1H, H6), 7.79 (d, 1H, bpyH6C), 7.67–7.63 (m, 4H, bpyH5A, bpyH5C, bpyH6B, bpyH6A), 7.57 (t, 1H, bpyH5B), 7.34 (d, 1H, bpyH6D), 7.10 (t, 1H, bpyH5D), 6.93 (d, 1H, H8). **ESI–MS**: Calc. for ([{Ru(bpy)$_2$}$_2$(μ–**3.5**)·(PF$_6$)$_2$]$^{2+}$): 702.0540, Found: 702.0548; Calc. for ([{Ru(bpy)$_2$}$_2$(μ–**3.5**)·(PF$_6$)]$^{3+}$): 419.7148, Found: 419.7151; Calc. for ([{Ru(bpy)$_2$}$_2$(μ–**3.5**)]$^{3+}$): 371.0604, Found: 371.0603. **IR**: ν_{max} 1607,

1487, 1469, 1372, 1243, 1218, 826, 761, 728, 689, 662, 628, 554, 421 cm^{-1}. **UV/Vis** (CH_3CN): λ_{max} 515, 368, 317 (sh), 278, 247 nm. **Analysis**: Calc. for [$(bpy)_2Ru(\mu$–**3.5**)$Ru(bpy)_2$]$(PF_6)_4 \cdot CH_3CN$: C, 40.17; H, 2.62; N, 12.12. Found: C, 40.06; H, 2.79; N, 12.60.

8.4.6. Complex of 3.6

*[$(bpy)_2$Ru(**3.6**)]$(PF_6)_2$, **3.21***

Ligand **3.6** (0.05 g, 0.17 mmol) and bis(2,2'–bipyridine)ruthenium(II) dichloride (0.08 g, 0.17 mmol) were refluxed in 50% aqueous methanol (10 mL) for 16 h. Upon cooling, the solvent was removed *in vacuo* and the residue was redissolved in water. The aqueous solution was precipitated by addition of saturated potassium hexafluorophosphate. The resultant solid was filtered and recrystallised from acetone/diethyl ether to give **3.21** as a red powder. Yield: 0.08 g (46%). M.p: > 220 °C (decomposes).

^{1}H NMR (500 MHz, CD_3CN): δ 10.15 (s, 1H, H3), 9.75 (s, 1H, H3'), 8.69 (d, 1H , bpyH3A), 8.55–8.52 (m, 2H, bpyH3B, bpyH3C), 8.39 (d, 1H, bpyH3D), 8.31–8.26 (m, 3H, H5, bpyH4B, bpyH4A), 8.14 (d, 1H, H5'), 8.09–8.04 (m, 2H, H6, bpyH4D), 7.96 (t, 1H, bpyH4C), 7.91 (t, 1H, H6'), 7.85 (d, 1H, bpyH6B), 7.78 (t, 1H, H7), 7.71 (t, 1H, bpyH5B), 7.61 (d, 1H, bpyH6D), 7.42–7.35 (m, 4H, bpyH6A, H8, bpyH5A, H8'), 7.30 (d, 1H, bpyH6C), 7.11 (t, 1H, bpyH5C). **^{13}C NMR** (125 MHz, CD_3CN): δ 161.7 (C2), 157.7 (2C, C2', bpyC2A), 156.2 (bpyC3C), 155.2 (2C, bpyC2D, bpyC2B), 153.7 (bpyC6A), 152.1 (bpyC6D), 151.7 (bpyC6C), 149.5 (bpyC6B), 147.5 (C3), 143.4 (C8a), 142.7 (C8'a), 141.2_0 (bpyC4B), 141.1_6 (bpyC4A), 140.2 (bpyC4d), 139.7 (bpyC4C), 139.3 (C3'), 133.6 (C6), 133.3 (C7'), 132.7 (C6'), 131.9 (C7), 131.4 (C5), 129.2 (C5), 129.1 (bpyC5B), 128.9 (C8'), 128.8 (bpyC5D), 128.0 (bpyC5A), 127.4 (bpyC5C), 125.0 (bpyC3B), 124.9_9 (bpyC3A), 124.9_5 (bpyC3D), 124.2 (bpyC3C), 123.9 (C8). **ESI–MS**: Calc. for ([$(bpy)_2$Ru(**3.6**)$\cdot(PF_6)$]$^{1+}$): 845.1031, Found: 845.1036; Calc. for ([$(bpy)_2$Ru(**3.6**)]$^{2+}$): 350.0692, Found: 350.0693. **IR** (KBr): ν_{max} 2922, 2852, 1708, 1604, 1590, 1467, 1448, 1305, 1284, 827, 807, 776, 758, 727, 54 cm^{-1}. **UV/Vis** (CH_3CN) λ_{max} 541, 373, 316, 268, 246 nm. **Analysis**: Calc. for [$(bpy)_2$Ru(**3.5**)]$(PF_6)_2 \cdot 2H_2O$: C, 42.16; H, 2.95; N, 13.66. Found: C, 41.60; H, 2.44; N, 13.21.

8.4.7. Complexes of 3.7

*$[(bpy)_2Ru(\mathbf{3.7})](PF_6)_2$, **3.22** and $[(bpy)_2Ru(\mu–\mathbf{3.7})Ru(bpy)_2](PF_6)_4$, **3.23***

Ligand **3.7** (0.02 g, 0.07 mmol) and bis(2,2'–bipyridine)ruthenium(II) carbonate (0.07 g, 0.14 mmol) were refluxed in 50% aqueous ethanol (10 mL) for 48 h. After cooling, the solvent was removed *in vacuo* and the residue was redissolved in the minimum amount of acetonitrile:saturated KNO_3 (7:1). The resulting solution was loaded on a silica gel column and eluted with 7:1 acetonitrile:saturated KNO_3 mixture. The fractions were precipitated by addition of a saturated solution of ammonium hexafluorophosphate. The resultant products were extracted into dichloromethane (3 x 10 mL) and the solvent was removed under reduced pressure. The crude solid was recrystallised from acetone/diethyl ether to give **3.22** and **3.23** as a red and green solid, respectively. Yields: (**3.22**): 0.020 g (21%); (**3.23**): 0.030 g (25%).

(**3.22**): **M.p**: 231 °C. **^{1}H NMR** (400 MHz, CD_3CN): δ 9.03 (d, 1H, H7'), 8.93 (d, 1H, H3'), 8.79 (d, 1H, H4'), 8.56–8.53 (m, 3H, H4, H5, bpyH3A), 8.49 (d, 1H, bpyH3B), 8.42–8.37 (m, 2H, bpyH3C, H5'), 8.30–8.20 (m, 4H, H7, bpyH3D, bpyH4A, bpyH4B), 8.06 (t, 1H, bpyH4C), 8.01 (d, 1H, bpyH6C), 7.95 (d, 1H, H3), 7.76–7.67 (m, 3H, H6, bpyH6B, bpyH4D), 7.63–7.57 (m, 2H, H6', bpyH5B), 7.49 (t, 1H, bpyH5C), 7.40–7.32 (m, 3H, bpyH6D, bpyH5A, bpyH6A), 7.02 (t, 1H, bpyH5D). **^{13}C NMR** (100 MHz, CD_3CN): δ 155.3 (C7'), 154.5 (C7), 153.3 (bpyC6A), 152.2 (bpyC6C), 151.3 (bpyC6D), 149.7 (bpyC6B), 142.0 (C4), 140.9 (C4'), 140.2 (bpyC4A), 139.7 (bpyc4B), 139.4 (bpyC4B), 138.3 (C5), 138.4 (bpyC4D), 137.4 (C5'), 127.6 (2C, bpyC5A, bpyC5C), 127.0 (bpyC5B), 126.8 (bpyC5D), 124.9 (C6), 124.2 (bpyC3A), 124.1 (2C, bpyC3C, bpyC3D), 123.8 (C3'), 123.7 (C6'), 123.4 (bpyC3B), 114.7 (C3). **ESI–MS**: Calc. for $([(bpy)_2Ru(\mathbf{3.7})\cdot(PF_6)]^{1+}$): 845.1031, Found: 845.1033; Calc. for $([(bpy)_2Ru(\mathbf{3.6})]^{2+}$): 350.0692, Found: 350.0693. **IR**: ν_{max} 2923, 1729, 1604, 1592, 1499, 1446, 1430, 1397, 1311, 825, 759, 532 cm^{-1}. **UV/Vis** (CH_3CN) λ_{max} 526, 363, 315 (sh), 268, 246 nm.

(**3.23**): **M.p**: 272 °C. **ESI–MS**: Calc. for $([\{Ru(bpy)_2\}_2(\mu–\mathbf{3.7})\cdot(PF_6)]^{2+}$): 629.5719, Found: 629.5731; Calc. for $([\{Ru(bpy)_2\}_2(\mu–\mathbf{3.7})]^{3+}$): 371.3930, Found: 371.3938. **IR**: ν_{max} 2923, 1729, 1604, 1592, 1499, 1446, 1430, 1397, 1311, 825, 759, 532 cm^{-1}. **UV/Vis** (CH_3CN) λ_{max} 645, 498, 391, 287, 244 nm. **Analysis**: Calc. for $[(bpy)_2Ru(\mu–\mathbf{3.7})Ru(bpy)_2](PF_6)_3$: C, 43.45; H, 2.73; N, 12.67. Found: C, 42.38; H, 2.95; N, 12.22.

8.4.8. Complexes of 3.8

*[(bpy)$_2$Ru(**3.8**)](PF$_6$)$_2$, **3.24***

Ligand **3.8** (0.03 g, 0.10 mmol) and bis(2,2'–bipyridine)ruthenium(II) chloride (0.10 g, 0.21 mmol) were refluxed in 50% aqueous methanol (10 mL) for 48 h. After cooling, the solvent was removed *in vacuo* and the residue was dissolved in the minimum amount of water. The aqueous solution was precipitated by addition of a saturated solution of ammonium hexafluorophosphate. The resultant solid was filtered, dried and recrystallised from acetone/diethyl ether to give **3.24** as a red solid. Yield: 0.090 g (37%). M.p: 305 °C.

^{1}H NMR (400 MHz, CD_3CN): δ 9.18 (d, 1H, bpyH6A), 9.12 (d, 1H, H3'/4'), 9.01 (d, 1H, bpyH6B), 8.87 (d, 1H, H4'/3'), 8.65 (d, 1H, bpyH3A), 8.60 (d, 1H, H3/4), 8.55 (d, 1H, bpyH3B), 8.41 (d, 1H, bpyH3'B), 8.37 (d, 1H, bpyH3'A), 8.33–8.26 (m, 2H, bpyH4A, bpyH4B), 8.22 (d, 1H, H4/3), 8.08 (t, 1H, bpyH4'B), 7.88 (d, 1H, H6'), 7.84 (d, 1H, bpyH6'B), 7.80–7.76 (m, 2H, bpyH4'A, H8'), 7.72–7.66 (m, 3H, bpyH5B, H8, H7'), 7.56–7.51 (m, 2H, H6, bpyH5'B), 7.45–7.41 (m, 2H, bpyH5A, H7), 7.28 (d, 1H, bpyH6'A), 6.98 (t, 1H, bpyH5'A). **ESI–MS**: Calc. for ([(bpy)$_2$Ru(**3.8**)·(PF$_6$)]$^{1+}$): 845.1031, Found: 845.1044; Calc. for ([(bpy)$_2$Ru(**3.8**)]$^{2+}$): 350.0692, Found: 350.0700. **IR**: ν_{max} 2922, 2852, 1504, 1467, 1447, 1315, 1262, 1243, 1110, 826, 760, 729, 554 cm^{-1}. **UV/Vis** (CH_3CN) λ_{max} 540, 383, 281, 239 nm.

8.5. Ruthenium Complexes with azobis(bidentates)

8.5.1 Complexes of 4.1

*[(terpy)Ru(μ–**4.1**)Ru(terpy)](PF$_6$)$_4$, **4.3***

A suspension of ligand **4.1** (0.050 g, 0.11 mmol) and (2,2':6',2"–terpyridine)ruthenium(III) trichloride (0.0038 g, 0.11 mmol) in ethylene glycol (5 mL) was heated at reflux in a modified microwave oven (Sharp Model R–2V55, 600 W, 2450 MHz) at high power for 10 minutes at intervals of 2 minutes. Upon cooling, the black solution was diluted with water (10 mL) and loaded on a SP Sephadex cation exchanger. Separation of the mononuclear product from the crude mixture was achieved *via* a gradient elution procedure using aqueous 0.1–0.5 mol L^{-1} sodium chloride as the eluent. The fractions were precipitated by addition of a saturated solution of ammonium hexafluorophosphate to each band. The

resultant product was extracted into dichloromethane and the solvent was removed under reduced pressure. The solid residues were recrystallised from acetone/hexane to give **4.3** as red needles. Yield: 0.020 g (14%). M.p: 220 °C.

^{1}H NMR (500 MHz, CD_3CN): δ 9.01 (d, 2H, terpyH3'), 8.81 (t, 1H, terpyH4'), 8.71 (d, 1H, H3), 8.59 (d, 2H, terpyH3, terpyH3''), 8.46 (d, 1H, H3'), 8.15 (t, 1H, H4), 8.02–7.96 (m, 3H, H4', terpyH4, terpyH4''), 7.79 (d, 1H, H5), 7.30 (t, 1H, H5'), 6.91 (t, 2H, terpyH5, terpyH5''), 6.88 (d, 1H, H6'), 6.49 (d, 2H, terpyH6, terpyH6''). **^{13}C NMR** (125 MHz, CD_3CN): δ 164.4 (C6), 157.6 (terpyC2), 157.1 (C2'), 156.4 (C2), 154.4 (terpyC2'), 153.2 (terpyC6), 150.5 (C6'), 140.7 (C4'), 140.5 (terpyC4'), 140.1 (terpyC4), 138.9 (C4), 129.2 (C5'), 128.5 (terpyC5), 125.9 (terpyC3), 125.7 (C3'), 125.6 (terpyC3'), 123.2 (C5), 122.7 (C3). **ESI–MS**: Calc. for ($[\{Ru(terpy)\}_2(\mu$–**4.1**$)\cdot(PF_6)_3]^{1+}$): 1443.0196, Found: 1443.0212; Calc. for ($[\{Ru(terpy)\}_2(\mu$–**4.1**$)\cdot(PF_6)]^{2+}$): 576.5457, Found: 576.5466; Calc. for ($[\{Ru(terpy)\}_2(\mu$–**4.1**$)]^{3+}$): 336.0424, Found: 336.0432. **UV/Vis** (CH_3CN): λ_{max} 772, 409, 330, 299, 264, 240 nm. **Analysis**: Calc. for $[\{Ru(terpy)\}_2(\mu$–**4.1**$)](PF_6)_4\cdot 2H_2O$: C, 37.84; H, 2.29; N, 10.59. Found: C, 37.83; H, 2.65; N, 11.06.

8.5.2. Complexes of 4.2

*[(terpy)Ru(**4.2**)](PF$_6$)$_2$, **4.4***

A suspension of ligand **4.2** (0.020 g, 0.052 mmol) and (2,2':6',2''–terpyridine)ruthenium(III) trichloride (0.020 g, 0.052 mmol) in ethylene glycol (5 mL) was heated at reflux in a modified microwave oven (Sharp Model R–2V55, 600 W, 2450 MHz) at high power for 10 minutes at an interval of 2 minutes. Upon cooling, the black solution was diluted with water (10 mL) and loaded on a SP Sephadex C–25 cation exchanger. Separation of the mononuclear product from the crude mixture was achieved *via* a gradient elution procedure using aqueous 0.1–0.5 mol L^{-1} sodium chloride as the eluent. The red fraction was precipitated by addition of a saturated solution of ammonium hexafluorophosphate. The resultant products were extracted into dichloromethane and the solvent was removed under reduced pressure. The solid residues were recrystallised from acetone/hexane to give **4.4** as red needles. Yield: 0.050 g (91%). M.p: > 300 °C.

^{1}H NMR (400 MHz, CD_3CN): δ 9.33 (d, 1H, H3), 9.31 (dd, 1H, H9'), 9.03 (d, 1H, H4), 8.73 (d, 2H, terpyH3'), 8.65 (dd, 1H, H7), 8.57 (d, 1H, H5/H6), 8.51 (d, 2H, terpyH3, terpyH3''), 8.43–8.38 (m, 3H, H6/H5, H7', H4'), 8.33 (t, 1H, terpyH4'), 8.19 (d, 1H, H3'),

7.96 (d, 1H, H5'/H6'), 7.93–7.86 (m, 3H, terpyH4, terpyH4'', H6'/H5'), 7.83 (dd, 1H, H8'), 7.65–7.59 (m, 2H, H9, H8), 7.02 (t, 2H, terpyH5, terpyH5''), 6.89 (d, 2H, terpyH6, terpyH6''). **^{13}C NMR** (100MHz, CD_3CN): δ 158.6 (terpyC2), 153.9 (terpyC2'), 153.5 (C9), 153.3 (terpyC6), 150.0 (C9'), 139.5 (terpyC4), 139.4 (C4'), 137.8 (terpyC4), 137.5 (C7), 136.5 (C7'), 134.6 (C4), 130.0 (C6/C5), 129.4 (C6'/C5'), 128.1 (C5/C6), 127.2 (terpyC5), 127.2 (C8), 126.0 (C5'/C6'), 124.8 (terpyC3), 124.5 (C3), 124.3 (terpyC3'), 123.8 (C8'), 116.2 (C3'). **ESI–MS**: Calc. for ([(terpy)Ru(**4.2**)]$^{2+}$): 360.5638, Found: 360.5640. **UV/Vis** (CH_3CN): λ_{max} 406, 329, 229 nm. **Analysis**: Calc. for [(terpy)Ru(**4.2**)]$(PF_6)_2 \cdot CH_3COCH_3 \cdot H_2O$: C, 46.42; H, 3.06; N, 11.60. Found: C, 46.77; H, 3.50; N, 11.59.

*[(terpy)Ru(μ–**4.2**)Ru(terpy)](PF$_6$)$_4$, **4.5***

A suspension of ligand **4.2** (0.050 g, 0.13 mmol) and (2,2':6',2''–terpyridine)ruthenium(III) trichloride (0.11 g, 0.26 mmol) in ethylene glycol (5 mL) was heated at reflux in a modified microwave oven (Sharp Model R–2V55, 600 W, 2450 MHz) at high power for 10 minutes at intervals of 2 minutes. Upon cooling, the black solution was diluted with water (10 mL) and loaded on a SP Sephadex cation exchanger. Separation of the dinuclear product from the crude mixture was achieved *via* a gradient elution procedure using aqueous 0.1–0.5 mol L^{-1} sodium chloride as the eluent. The fractions were precipitated by addition of a saturated solution of ammonium hexafluorophosphate to each band. The resultant products were extracted into dichloromethane and the solvent was removed under reduced pressure. The solid residues were recrystallised from acetone/hexane to give **4.5** as red needles. Yield: 0.18 g (87%). M.p: > 290 °C.

^{1}H NMR (400 MHz, CD_3CN): δ δ 9.01 (d, 2H, terpyH3'), 8.89 (t, 1H, terpyH4'), 8.67–8.61 (m, 3H, terpyH3, terpyH3'', H4), 8.36 (dd, 2H, H5, H6), 8.02–7.95 (m, 3H, terpyH4, terpyH4'', H3,), 7.59 (t, 1H, H8), 7.42 (d, 1H, H9), 6.83 (t, 2H, terpyH5, terpyH5''), 6.46 (d, 2H, terpyH6, terpyH6''). **ESI–MS**: Calc. for ([{Ru(terpy)}$_2$(μ–**4.2**)$\cdot$(PF$_6$)]$^{2+}$): 600.5454, Found: 600.5467; Calc. for ([{Ru(terpy)}$_2$(μ–**4.2**)]$^{3+}$): 352.0420, Found: 352.0428. **IR**: ν_{max} 1601, 1451, 1385, 1090, 827, 781, 764, 735, 644, 554 cm^{-1}. **UV/Vis** (CH_3CN): λ_{max} 773, 472, 406, 329 nm.

8.6. Ruthenium Complexes with bis(pyridylimines)

8.6.1. Complexes of 5.1

*$[(bpy)_2Ru(\mathbf{5.1–NH_2})](PF_6)_2$, **5.6** and $[(bpy)_2Ru(\mu–\mathbf{5.1})Ru(bpy)_2](PF_6)_4$, **5.7***

Ligand **5.1** (0.080 g, 0.38 mmol) and bis(2,2'–bipyridine)ruthenium(II) dichloride (0.18 g, 0.38 mmol) were refluxed in 50% aqueous methanol (15 mL) for 24 h. After cooling, the solvent was removed *in vacuo* and the residue was redissolved in water and filtered. The aqueous solution was loaded on a SP Sephadex C–25 cation exchanger. Separation of the mononuclear and dinuclear products from the crude mixture was achieved *via* a gradient elution procedure using aqueous 0.1–0.5 mol L^{-1} sodium chloride as the eluent. Three bands were eluted: Band 1 (reddish yellow, 0.1 mol L^{-1} NaCl), Band 2: (dark brown, 0.15 mol L^{-1}) and Band 3: (dark red, 0.2 mol L^{-1}). The fractions were precipitated by addition of saturated solution of ammonium hexafluorophosphate to each band. The resultant products were extracted into dichloromethane and the solvent was removed under reduced pressure. The solid residues were recrystallised from acetone/diethyl ether. The composition of Bands 1 and 3 were established by electrospray mass spectrometry and ^{1}H NMR. Analysis of Band 1 revealed the presence of a mononuclear ruthenium species and Band 3 as a dinuclear ruthenium species. Yields: Band 1 = (**5.6**) 0.090 g (28%). Band 3 = (**5.7**) 0.12 mg (19%).

(**5.6**): M.p: 160 °C. **^{1}H NMR** (400 MHz, CD_3CN): δ 8.54 (d, 1H, H3), 8.51–8.46 (m, 4H, bpyH3A, bpyH3B, bpyH3C, bpyH6A), 8.36 (s, 1H, H7), 8.18 (td, 1H, H4), 8.15 (td, 1H, bpyH4A), 8.09–8.01 (m, 2H, bpyH4B, bpyH4C), 7.91–7.89 (m, 2H, bpyH3D, bpyH4D), 7.71 (d, 1H, bpyH6C), 7.66 (d, 1H, bpyH6B), 7.63–7.60 (m, 2H, bpyH5A, H6), 7.56–7.51 (m, 2H, H5, bpyH6D), 7.40 (t, 1H, bpyH5B), 7.35 (t, 1H, bpyH5C), 7.21 (td, 1H, bpyH5D), 6.64 (bs, 2H, NH2). **^{13}C NMR** (100 MHz, CD_3CN): δ 157.4 (C2), 157.2 (bpyC2D), 157.1 (bpyC2C), 156.8 (bpyC2B), 156.7 (bpyC2A), 152.0 (bpyC6A), 151.9 (C6), 151.8 (bpyC6C), 151.4 (bpyC6B), 151.1 (bpyC6D), 143.3 (C7), 138.1 (2C, bpyC4C, C4), 138.0 (bpyC4A), 137.9 (bpyC4B), 137.3 (bpyC4D), 127.8 (C5), 127.8 (bpyC5A), 127.6 (bpyC5B), 127.3 (bpyC5C), 125.1 (bpyC3D), 125.0 (bpyC5D), 124.1_9 (bpyC3A), 124.1_8 (C3), 124.1 (bpyC3B), 123.9 (bpyC3C). **ESI–MS**: Calc. for $([(bpy)_2Ru(\mathbf{5.1–NH_2})\cdot(PF_6)]^{1+}$): 613.5176, Found: 613.5164; Calc. for $([(bpy)_2Ru(\mathbf{5.1–NH_2})]^{2+}$): 360.6902' Found: 360.6894. **IR**: ν_{max} 1767, 1690, 1466, 1444, 1350, 1246, 1158, 831, 760, 728, 555 cm^{-1}. **UV** (CH_3CN): λ_{max} 438, 411, 285, 243 nm.

(**5.7**): **M.p**: decomposes at 260 °C. **^{1}H NMR** (400 MHz, CD_3CN): δ 9.28 (s, 1H, H7), 8.76 (d, 1H, bpyH6A), 8.58 (d, 1H , bpyH3A), 8.49 (d, 1H, bpyH3'A), 8.28–8.23 (m, 2H, bpyH4A, H3), 8.16–8.11 (m, 2H, bpyH6B, bpyH4'B), 8.07–8.02 (m, 3H, bpyH4'A, H4, bpyH3B), 7.99–7.94 (m, 2H, bpyH4B, bpyH3'B), 7.78 (t, 1H, bpyH5A), 7.69 (d, 1H, H6), 7.52 (t, 1H, byH5B), 7.47–7.41 (m, 2H, H5, bpyH5'B), 7.30 (t, 1H, bpyH5'A), 6.77 (d, 1H, bpyH6'B), 6.71 (d, 1H, bpyH6'A). **^{13}C NMR** (100 MHz, CD_3CN): δ 165.4 (C7), 156.7 (bpyC2'A), 156.4 (2C, bpyC2A, bpyC2B), 155.6 (C2), 155.5 (bpyC2'B), 153.9 (bpyC6A), 153.1 (C6), 152.3 (bpyC6B), 151.6 (bpyC6'B), 150.4 (bpyC6'A), 139.5 (bpyC4B), 139.4 (bpyC4'B), 139.1 (bpyC4A), 139.0 (bpyC4'A), 138.4 (C4), 133.1 (C3), 130.2 (C5), 128.7 (bpyC5'B), 128.6 (bpyC5A), 128.2 (2C, bpyC5'A, bpyC5B), 125.3 (bpyC3'B), 125.0 (bpyC3A), 124.7 (2C, bpyC3'A, bpyC3B). **ESI–MS**: Calc. for ($[\{Ru(bpy)_2\}_2(\mu$–**5.1**$)\cdot(PF_6)_2]^{2+}$): 664.0513, Found: 664.0514; Calc. for ($[\{Ru(bpy)_2\}_2(\mu$–**5.1**$)]^{2+}$): 519.0871, Found: 519.0865; Calc. for ($[\{Ru(bpy)_2\}_2(\mu$–**5.1**$)]^{4+}$): 259.5435, Found: 259.5428. **IR**: ν_{max} 1720, 1603, 1447, 1422, 1119, 1087, 1068, 1025, 1000, 835, 823, 758, 555 cm^{-1}. **UV** (CH_3CN): λ_{max} 524, 393, 282, 245 nm.

8.6.2 Complex of 5.2

*$[(bpy)_2Ru(\mu$–**5.2**$)Ru(bpy)_2](ClO_4)_4$, **5.8***

A solution of bis(2,2'–bipyridine)ruthenium(II) dichloride (0.10 g, 0.21 mmol) and silver perchlorate (0.080 g, 0.42 mmol) in ethanol (10 mL) was refluxed for 1 h. The reaction mixture was cooled and the solution was filtered through Celite®. Ligand **5.2** (0.030 g, 0.11 mmol) was added to the above filtrate and the reaction mixture was heated at reflux for 16 hours. The reaction mixture was then cooled in refrigerator for 1 hour. The precipitate thus formed was filtered and washed with cold ethanol and benzene. The crude product was then recrystallised from acetonitrile and benzene mixture to give **5.8** as a brownish–orange solid. Yield: 0.065 g (25%). M.p: > 260 °C.

^{1}H NMR (500 MHz, CD_3CN): δ 8.77 (s, 1H, H7), 8.56–8.53 (m, 2H, bpyH3A, bpyH3B), 8.47 (d, 1H, bpyH6A), 8.41 (d, 1H, H3), 8.26 (d, 1H, bpyH3C), 8.16 (t, 1H, bpyH4A), 8.10–8.07 (m, 4H, H4, bpyH3D, bpyH4C, bpyH4B), 7.87 (t, 1H, bpyH4D), 7.81 (d, 1H, H6), 7.74 (d, 1H, bpyH6B), 7.65–7.61 (m, 2H, bpyH6C, bpyH5A), 7.53–7.49 (m, 3H, bpyH5C, H5, bpyH6D), 7.39 (t, 1H, bpyH5B), 7.21 (t, 1H, bpyH5D), 6.11 (bs, 2H, H9, H10). **^{13}C NMR** (125 MHz, CD_3CN): δ170.1 (C7), 157.7_1 (C2), 157.6_6 (bpyC2C), 157.6 (2C,

bpyC2A, bpyC2B), 157.2 (bpyC2D), 153.9 (bpyC6A), 153.1 (bpyC6C), 153.0 (C6), 152.8 (bpyC6B), 152.4 (bpyC6D), 148.6 (C8), 139.2 (bpyC4B), 139.1 (bpyC4A), 139.1 (bpyC4C), 138.7 (2C, bpyC4D, C4), 131.8 (C3), 129.9 (C5), 128.9 (bpyC5A), 128.8 (bpyC5C), 128.4 (bpyC5B), 128.2 (bpyC5D), 125.4 (bpyC3A), 125.3 (bpyC3B), 124.7 (bpyC3C), 124.6 (bpyC3D), 122.8 (2C, C9, C10). **ESI–MS**: Calc. for ($[\{Ru(bpy)_2\}_2(\mu–\mathbf{5.2})\cdot(ClO_4)_2]^{2+}$): 656.0513, Found: 656.0514; Calc. for ($[\{Ru(bpy)_2\}_2(\mu–\mathbf{5.2})\cdot(ClO_4)]^{3+}$): 404.3847, Found: 404.3845; Calc. for ($[\{Ru(bpy)_2\}_2(\mu–\mathbf{5.2})]^{4+}$): 278.5509, Found: 278.5511. **IR**: ν_{max} 1605, 1497, 1465, 1445, 1421, 1079, 837, 763, 730, 621, 543 cm^{-1}. **UV/Vis** (CH_3CN): λ_{max} 483, 429, 285, 243 nm.

8.6.3. Complex of 5.3

*$[(bpy)_2Ru(\mu–$**5.3**$)Ru(bpy)_2](ClO_4)_4$, **5.9***

A mixture of bis(2,2'–bipyridine)ruthenium(II) carbonate (0.14 g, 0.30 mmol) and silver perchlorate (0.12 g, 0.59 mmol) in ethanol (10 mL) were refluxed for 1 h. After cooling, the reaction mixture was filtered through Celite®. The ligand **5.3** (0.050 g, 0.18 mmol) was added to the filtrate and the reaction mixture was heated at reflux for 16 hours. Upon cooling, the precipitate thus formed was filtered and washed with cold ethanol and benzene. The crude product was recrystallised from a mixture of acetonitrile and benzene (1:1, v/v) to give **5.9** as a brown solid. Yields: 0.02 g (8%). M.p: decomposes at 260 °C.

^{1}H NMR (400 MHz, CD_3CN): δ 9.13 (d, 1H, H7), 8.70 (d, 1H, bpyH6A), 8.57–8.52 (m, 3H, bpyH3A, bpyH3B, H3), 8.22–8.16 (m, 2H, bpyH4A, H4), 8.10–8.06 (m, 2H, bpyH6C, bpyH4B), 8.02 (d, 1H, H6), 7.87 (1H, t, bpyH4C), 7.76–7.70 (m, 3H, bpyH3C, bpyH6B, bpyH5A), 7.65–7.54 (m, 4H, bpyH3D, bpyH4D, H5, bpyH5C), 7.43 (d, 1H, bpyH6D), 7.39 (t, 1H, bpyH5B), 7.06 (t, 1H, bpyH5D), 7.02 (d, 1H, H11), 6.48 (t, 1H, H10), 6.17 (d, 1H, H9). **^{13}C NMR** (100 MHz, CD_3CN): δ 172.5 (C7), 156.8 (bpyC2C), 156.7 (C2), 156.6_3 (bpyC2A), 156.6_0 (bpyC2B), 155.8 (bpyC2D), 153.0 (bpyC6C), 152.3 (bpyC6A), 152.2 (C6), 151.7 (bpyC6D), 151.4 (bpyC6B), 143.2 (C8), 138.4 (bpyC4C), 138.2_2 (bpyC4B), 132.1_6 (C4), 137.8 (bpyC4A), 137.3 (bpyC4D), 131.4 (C3), 129.4 (C5), 128.0 (bpyC5C), 127.9 (bpyC5A), 127.4 (bpyC5B), 126.9 (bpyC5D), 125.5 (C10), 124.5 (bpyC3B), 124.3 (bpyC3A), 123.4 (bpyC3C), 122.7 (bpyC3D), 119.2 (C9), 118.9 (C11). **ESI–MS**: Calc. for ($[\{Ru(bpy)_2\}_2(\mu–\mathbf{5.3})\cdot(ClO_4)]^{3+}$): 421.0567, Found: 421.0564; Calc. for ($[\{Ru(bpy)_2\}_2(\mu–\mathbf{5.3})]^{4+}$): 291.0548, Found: 291.0548. **IR**: ν_{max} 1722, 1603, 1466, 1446,

1317, 1301, 1272, 1084, 1001, 962, 893, 768, 622 cm^{-1}. **UV/Vis** (CH_3CN): λ_{max} 483, 427, 284, 242 nm. **Analysis**: Calc. for $[(bpy)_2Ru(\mu–$**5.3**$)Ru(bpy)_2](ClO_4)_4 \cdot 4CH_3COCH_3$: C, 49.56; H, 4.05; N, 9.37. Found: C, 49.83; H, 4.34; N, 8.70.

8.6.4. Complex of 5.4

*$[(bpy)_2Ru(\mu–$**5.4**$)Ru(bpy)_2](ClO_4)_4$, **5.10***

A mixture of bis(2,2'–bipyridine)ruthenium(II) dichloride (0.10 g, 0.21 mmol) and silver perchlorate (0.080 g, 0.42 mmol) in ethanol (10 mL) were refluxed for 1 h. After cooling, the reaction mixture was filtered through Celite®. The ligand **5.4** (0.030 g, 0.10 mmol) was added to the filtrate and the reaction mixture was heated at reflux for 16 hours. Upon cooling, the precipitate thus formed was filtered and washed with cold ethanol and benzene. The crude product was recrystallised from a mixture of acetonitrile and benzene (1:1, v/v) to give **5.10** as a brownish–orange solid. Yields: 0.030 g (14%). M.p: decomposes at 260 °C.

^{1}H NMR (500 MHz, CD_3CN): δ 9.07 (d, 1H, H7), 8.58–8.53 (m, 3H, bpyH6A, bpyH3A, bpyH3B), 8.34 (d, 1H, H3), 8.22 (d, 1H, bpyH3C), 8.16–8.06 (m, 4H, bpyH4A, bpyH4D, bpyH4B, bpyH4C), 7.95 (d, 1H, bpyH3D), 7.80 (d, 1H, bpyH6B), 7.75 (d, 1H, bpyH6C), 7.69–7.66 (m, 2H, bpyH6C, bpyH4D), 7.60–7.51 (m, 3H, bpyH5A, bpyH6D, bpyH5C), 7.47 (t, 1H, bpyH5B), 7.38 (t, 1H, H5), 7.18 (t, 1H, bpyH5D), 6.68 (dd, 2H, H9, H9'), 6.48 (dd, 2H, H10, H10'), 3.62 (s, 1H, H12). **^{13}C NMR** (100 MHz, CD_3CN): δ 168.4 (C7), 157.1 (C2), 156.9 (bpyC2A), 156.7 (bpyC2B), 156.7 (bpyC2C), 156.4 (bpyC2D), 153.1 (bpyC6A), 152.1 (bpyC6C), 152.0 (bpyC6B), 151.9 (C6), 151.7 (bpyC6D), 156.9 (C8), 141.3 (C11), 138.2 (bpyC4A), 138.1_4 (bpyC4C), 130.0_9 (bpyC4B), 137.7 (C4), 137.4 (bpyc4D), 130.4 (C3), 129.1 (C9), 128.8 (bpyC5B), 128.0 (bpyC5C), 127.9 (bpyC5A), 127.5 (C5), 127.0 (bpyC5D), 124.5 (bpyC3A), 124.4 (bpyC3B), 123.5 (bpyC3C), 123.2 (bpyC3D), 121.3 (C10). **ESI–MS**: Calc. for $([\{Ru(bpy)_2\}_2(\mu–$**5.4**$)\cdot(ClO_4)_2]^{2+}$): 701.0751, Found: 701.0755; Calc for $([\{Ru(bpy)_2\}_2(\mu–$**5.4**$)\cdot(ClO_4)]^{3+}$): 434.4005, Found: 434.4010; Calc. for $([\{Ru(bpy)_2\}_2(\mu–$**5.4**$)]^{4+}$): 301.0627, Found: 301.0635. **IR**: ν_{max} 2915, 2847, 1603, 1543, 1464, 1446, 1804, 1067, 1026, 1001, 961, 768, 757, 620 cm^{-1}. **UV/Vis** (CH_3CN): λ_{max} 478, 425, 343, 285, 243 nm.

8.6.5. Complex of 5.5

*$[(bpy)_2Ru(\mu$–**5.5**$)Ru(bpy)_2](ClO_4)_4$,* ***5.11***

A mixture of bis(2,2'–bipyridine)ruthenium(II) dichloride (0.10 g, 0.21 mmol) and silver perchlorate (0.090 g, 0.42 mmol) in ethanol (10 mL) were refluxed for 1 h. After cooling, the reaction mixture was filtered through Celite®. Ligand **5.5** (0.040 g, 0.11 mmol) was added to the filtrate and the reaction mixture was heated at reflux for 16 hours. Upon cooling, the precipitate thus formed was filtered and washed with cold ethanol and benzene. The crude product was recrystallised from a mixture of acetonitrile and benzene (1:1, v/v) to give **5.11** as a brownish–orange solid. Yield: 0.022 mg (13%). M.p: decomposes at 260 °C.

^{1}H NMR (500 MHz, CD_3CN): δ 9.04 (s, 1H, H7), 8.59–8.54 (m, 3H, bpyH3A, bpyH6A, bpyH3b), 8.35 (d, 1H, H3), 8.28 (d, 1H, bpyH3C), 8.16–7.81 (m, 5H, bpyH4A, bpyH3D, bpyH4C, H4, bpyH4B), 7.81–7.78 (m, 2H, H6, bpyH4D), 7.75 (d, 1H, bpyH6B), 7.69 (d, 1H, bpyH6C), 7.64–7.58 (m, 2H, bpyH6D, bpyH5A), 7.54 (t, 1H, bpyH5C), 7.48 (t, 1H, H5), 7.39 (t, 1H, bpyH5B), 7.24 (t, 1H, bpyH5D), 6.59 (m, 2H, H9, H9'), 6.45 (m, 2H, H10, H10'). **^{13}C NMR** (125 MHz, CD_3CN): δ 168.6 (C7), 157.0 (C2), 156.8 (bpyC2C), 156.7_3 (bpyC2A), 156.6_8. (bpyC2B), 156.5 (bpyC2D), 156.2 (C11), 153.1 (bpyC6A), 152.2 (bpyC6C), 152.1 (C6), 151.9 (bpyC6B), 151.8 (bpyC6D), 144.6 (C8), 138.3 (bpyC4C), 138.2 (bpyC4B), 138.1 (bpyC4A), 137.8 (C4), 137.5 (bpyC4D), 130.5 (C3), 128.8 (C5), 128.1 (bpyC5C), 127.9 (bpyC5A), 127.5 (bpyC5B), 127.2 (bpyC5D), 124.5 (bpyC3A), 124.4 (bpyC3B), 123.6 (bpyC3C), 123.4 (bpyC3D), 123.2 (2C, C9, C9'), 118.9 (2C, C10, C10'). **ESI–MS**: Calc. for $([\{Ru(bpy)_2\}_2(\mu$–**5.5**$)\cdot(ClO_4)_2]^{2+}$): 702.0646, Found: 702.0646; Calc. for $([\{Ru(bpy)_2\}_2(\mu$–**5.5**$)\cdot(ClO_4)]^{3+}$): 435.0602, Found: 435.0600; Calc. for $([\{Ru(bpy)_2\}_2(\mu$–**5.5**$)]^{4+}$): 301.5575, Found: 301.5576. **IR**: ν_{max} 1604, 1492, 1463, 1445, 1423, 1243, 1200, 1165, 1082, 838, 763, 730, 622, 543 cm^{-1}. **UV/Vis** (CH_3CN): λ_{max} 439, 285, 243 nm.

8.7. Metallosupramolecular Chemistry

8.7.1. Complex of 2.1

*[Ag(**2.1**)](SO$_3$CF$_3$), **6.1***

To a solution of **2.1** (0.010 g, 0.054 mmol) in methanol (1 mL), was added a solution of silver(I) triflate (0.030 g, 0.11 mmol) in acetonitrile (1 mL). Slow evaporation of the methanol/acetonitrile solution over time resulted in red coloured crystals, which were collected, washed with dichloromethane and dried *in vacuo*. Yield: 0.014 g (59%). M.p: 245 °C.

ESI–MS: Calc. for ([Ag(**2.1**)$_2$]$^+$): 475.0549, Found: 475.0546; Calc. for ([Ag(**2.1**)]$^+$): 290.9794, Found: 290.9793. **IR**: ν_{max} 1598, 1467, 1443, 1238, 1206, 1169, 1154, 1021, 1011, 798, 624, 575, 514, cm^{-1}. **Analysis**: Calc. for [Ag(**2.1**)](SO$_3$CF$_3$): C, 29.95; H, 1.83; N, 12.92. Found: C, 29.70; H, 1.78; N, 12.41.

8.7.2. Complex of 2.3

*[Ag$_2$(**2.3**)](CO$_2$CF$_3$)$_2$, **6.2***

An acetonitrile solution (1 mL) of silver(I) trifluoroacetate (0.02 g, 0.09 mmol) was added to a solution of **2.3** (0.010 g, 0.047 mmol) in methanol (2 mL). Slow evaporation of the solution resulted in red coloured crystals, which were collected, washed with dichloromethane and dried. Yield: 0.012 g (59%). M.p: 242 °C.

ESI–MS: Calc. for ([Ag(**2.3**)$_2$]$^+$): 531.1169, Found: 531.1175; Calc. for ([Ag(**2.3**)]$^+$): 319.0107, Found: 319.0107. **IR**: ν_{max} 1663, 1610, 1423, 1197, 1176, 1137, 1123, 837, 790, 722, 457 cm^{-1}. **Analysis**: Calc. for [Ag$_2$(**2.3**)](CO$_2$F$_3$)$_2$: C, 29.38; H, 1.85; N, 8.57. Found: C, 29.18; H, 1.91; N, 8.56.

8.7.3. Complex of 2.5

*[Ag$_2$(**2.5**)](NO$_3$)$_2$, **6.3***

Silver(I) nitrate (0.013 g, 0.079 mmol) in acetonitrile (1 mL) was added to a mixture of **2.5** (0.010 g, 0.040 mmol) in methanol/dichloromethane (2 mL). Dark red crystals were obtained when the solution was left to evaporate slowly. Yield: 8.0 mg (48%). M.p: 217 °C.

ESI–MS: Calc. for ([Ag(**2.5**)$_2$]$^+$): 610.8984, Found: 610.8991; Calc. for ([Ag(**2.5**)]$^+$): 358.9015, Found: 358.9015. **IR**: ν_{max} 1554, 1313, 1285, 1201, 1107, 1016, 860, 849, 836, 824, 649, 541 cm^{-1}. **Analysis**: Calc. for [Ag$_2$(**2.5**)](NO$_3$)$_2$·CH$_3$OH·H$_2$O: C, 22.11; H, 1.70; N, 15.04. Found: C, 22.69; H, 1.38; N, 14.54.

8.7.4. Complexes of 3.1

*[Ag(**3.1**)](ClO$_4$), **6.4***

A solution of silver(I) perchlorate (0.016 g, 0.078 mmol) in acetonitrile (1 mL) was added to a solution of **3.1** (0.010 g, 0.039 mmol) in dichloromethane and methanol (1:1). Slow evaporation of the solution gave bright red crystals suitable for X–ray crystallography. Yield: 0.015 g (88%). M.p: 262 °C.

ESI–MS: Calc. for ([Ag(**3.1**)$_2$]$^+$): 614.8794, Found: 614.8797; Calc. for ([Ag(**3.1**)]$^+$): 360.8920, Found: 360.8919. **IR**: ν_{max} 1560, 1541, 1401, 1134, 1070, 931, 800, 665, 619, 575, 541, 421 cm^{-1}. **Analysis**: Calc. for [Ag(**3.1**)](ClO$_4$)·CH$_3$OH: C, 21.86; H, 1.63; N, 17.00. Found: C, 21.54; H, 1.96; N, 18.36.

*[Ag(**3.1**)](NO$_3$), **6.5***

Silver(I) nitrate (0.013 g, 0.078 mmol) in acetonitrile (1 mL) was added to a solution of **3.1** (0.010 g, 0.039 mmol) in dichloromethane and methanol (1:1). The solution on slow evaporation gave red crystals. Yield: 0.026 g (80%). M.p: 149 °C.

ESI–MS: Calc. for ([Ag(**3.1**)$_2$]$^+$): 614.8794, Found: 614.8797; Calc. for ([Ag(**3.1**)]$^+$): 360.8920, Found: 360.8919. **IR**: ν_{max} 1558, 1544, 1402, 1316, 1283, 1264, 1130, 937, 926, 824, 801, 662, 570, 545, 419 cm^{-1}. **Analysis**: Calc. for [Ag(**3.1**)](NO$_3$)·H$_2$O: C, 21.69; H, 1.37; N, 22.13. Found: C, 22.41; H, 1.14; N, 22.11.

8.7.5. Complex of 3.2

*$[Ag_2(\mathbf{3.2})](SO_3CF_3)_2$, **6.6***

A solution of silver(I) triflate (0.014 g, 0.058 mmol) in acetonitrile (1 mL) was added to a solution of **3.2** (0.010 g, 0.029 mmol) in dichloromethane (2 mL). Slow evaporation of the solution gave red coloured crystals suitable for X–ray crystallography. Yield: 0.026 g (76%). M.p: 308 °C.

ESI–MS: Calc. for ($[Ag(\mathbf{3.2})_2]^+$): 794.6740, Found: 794.6740; Calc. for ($[Ag(\mathbf{3.1})\cdot(CH_3CN)]^+$): 489.8175, Found: 489.8160; Calc. for ($[Ag(\mathbf{3.1})]^+$): 448.7910, Found: 448.7906. **IR**: ν_{max} 1621, 1408, 1241, 1193, 1117, 1046, 1023, 932, 798, 762, 699, 630, 574, 541, 515 cm^{-1}. **Analysis**: Calc. for $[Ag_2(\mathbf{3.2})](SO_3CF_3)_2$: C, 14.00; H, 0.47; N, 9.80. Found: C, 14.01; H, 0.73; N, 9.53.

8.7.6. Complexes of 3.3

*$[Ag_2(\mathbf{3.3})](NO_3)_2$, **6.7***

Acetonitrile solution of silver(I) nitrate (0.010 g, 0.064 mmol) was added to a solution of **3.3** (0.010 g, 0.032 mmol) in methanol (1 mL). Slow evaporation of the solution over time resulted in red coloured crystals, which were collected, washed with dichloromethane and methanol, and dried *in vacuo*. Yield: 0.020 g (60%). M.p: 160 °C.

ESI–MS: Calc. for ($[Ag(\mathbf{3.3})_2]^+$): 727.0046, Found: 727.0055; Calc. for ($[Ag(\mathbf{3.3})\cdot(CH_3CN)]^+$): 457.9811, Found: 457.9812; Calc. for ($[Ag(\mathbf{3.3})]^+$): 416.9546, Found: 416.9551. **IR**: ν_{max} 1564, 1379, 1351, 1280, 1070, 1045, 1030, 968, 821, 793, 661, 551, 541, 407 cm^{-1}. **Analysis**: Calc. for $[Ag_2(\mathbf{3.3})](NO_3)_2\cdot CH_3CN$: C, 24.30; H, 2.18; N, 18.22. Found: C, 24.69; H, 2.11; N, 17.79.

*$[Ag_2(\mathbf{3.3})](ClO_4)_2$, **6.8***

Silver(I) perchlorate (0.013 g, 0.064 mmol) in acetonitrile (1 mL) was added to a solution of **3.3** (0.010 g, 0.032 mmol) in methanol (1 mL). The solution was left for evaporation at room temperature to give red crystals suitable for X–ray analysis. Yield: 9.0 mg (54%). M.p: decomposes at 240 °C.

ESI–MS: Calc. for ($[Ag(\mathbf{3.3})_2]^+$): 727.0046, Found: 727.0063; Calc. for ($[Ag(\mathbf{3.3})\cdot(CH_3CN)]^+$): 457.9811, Found: 457.9815; Calc. for ($[Ag(\mathbf{3.3})]^+$): 416.9546, Found: 416.9554. **IR**: ν_{max} 1567, 1419, 1385, 1352, 1317, 1102, 1074, 1054, 1017, 969, 929, 792, 619, 552, 540, 409 cm^{-1}. **Analysis**: Calc. for $[Ag_2(\mathbf{3.3})](ClO_4)_2$: C, 19.86; H, 1.67; N, 11.58. Found: C, 20.45; H, 2.02; N, 11.84.

8.7.7. Complexes of 3.4

*[Ag(**3.4**)](CO$_2$CF$_3$), **6.9***

Silver trifluoroacetate (0.015 g, 0.070 mmol) in acetonitrile (2 mL) was added to a hot solution of **3.4** (0.010 g, 0.035 mmol) in methanol/dichloromethane (1:1) (2mL). Slow evaporation of the solution over a period of time gave orange crystals. Yield: 0.012 g (68%). M.p: 221 °C.

ESI–MS: Calc. for ($[Ag(\mathbf{3.4})_2]^+$): 675.1169, Found: 675.1171; Calc. for ($[Ag(\mathbf{3.4})]^+$): 391.0107, Found: 391.0107. **IR**: ν_{max} 1651, 1501, 1459, 1174, 1129, 1020, 800, 785, 759, 719, 698, 435, 418, 408 cm^{-1}. **Analysis**: Calc. for $[Ag(\mathbf{3.4})](CO_2CF_3)$: C, 47.55; H, 2.39; N, 11.09. Found: C, 46.88; H, 2.56; N, 10.88.

*[Ag$_2$(**3.4**)](ClO$_4$)$_2$, **6.10***

Silver perchlorate (0.014 g, 0.070 mmol) in acetonitrile was added slowly to a warm solution of **3.4** in methanol/dichloromethane (1:1). Slow evaporation of the solution over a period of time gave red crystals. Yield: 8.0 mg (52%). M.p: > 300 °C.

ESI–MS: Calc. for ($[Ag(\mathbf{3.4})_2]^+$): 675.1169, Found: 675.1185; Calc. for ($[Ag(\mathbf{3.4})]^+$): 391.0107, Found: 391.0112. **IR**: ν_{max} 3515, 1698, 1615, 1502, 1380, 1055, 834, 784, 756, 617 cm^{-1}. **Analysis**: Calc. for $[Ag_2(\mathbf{3.4})](ClO_4)_2\cdot CH_3CN\cdot CH_3OH$: C, 32.67; H, 2.48; N, 9.07. Found: C, 32.75; H, 2.48; N, 8.34.

*[Ag(**3.4**)](SO$_3$CF$_3$)·H$_2$O, **6.11***

An acetonitrile solution of silver(I) triflate (0.014 g, 0.070 mmol) was added to a hot solution of **3.4** (0.010 g, 0.035 mmol) in methanol/dichloromethane. Slow evaporation solution resulted in red coloured crystals, which were collected, washed with

dichloromethane and methanol, and dried *in vacuo*. Yield: 0.020 g (quantitative). M.p: 250 °C.

ESI–MS: Calc. for ($[Ag(\mathbf{3.4})_2]^+$): 675.1169, Found: 675.1189; Calc. for ($[Ag(\mathbf{3.4})]^+$): 391.0107, Found: 391.0115. **IR**: ν_{max} 3457, 1504, 1435, 1222, 1159, 1024, 870, 844, 822, 779, 760, 628, 513 cm^{-1}. **Analysis**: Calc. for $[Ag(\mathbf{3.4})](SO_3CF_3)\cdot H_2O$: C, 40.80; H, 2.52; N, 10.02. Found: C, 40.25; H, 2.48; N, 9,78.

Appendix I

Crystallographic Tables

Appendix I – Crystallography

Table A1 –A12 list the crystal data and X–ray experimental details for the thirty six crystal structures discussed in this thesis. Selected bond lengths and bond distances are listed in the discussion of the structures, while the remaining distances and angles, as well as the atomic coordinates, anisotropic displacement parameters and hydrogen atom coordinates are available on request from the Department of Chemistry, University of Canterbury.

All the X–ray crystallographic data was collected on either a Bruker APEX–II instrument with graphite–monochromatised Mo Kα (λ = 0.71073 Å) radiation or on an Oxford–Agilent SuperNova instrument with focussed microsource Mo Kα (λ = 0.71073 Å) and Cu Kα radiation (λ = 1.5418 Å) and ATLAS CCD area detector. The structures were solved using direct methods with SHELXS[323] and refined on F^2 using all data by full–matrix least square procedures with SHELXL–97.[324] Multiscan absorption corrections were done using SADABS or SCALE3 ABSPACK. The non–hydrogen atoms were refined with anisotropic displacement parameters. All the hydrogen atoms were included in calculated positions with isotropic displacement parameters 1.2 or 1.5 times the isotropic equivalent of their carbon atoms.

Table A1. Crystal data and X–ray experimental data for complexes **2.7**, **2.8** and **2.10**.

Complex (Code)	**2.7** (3SRA01)	**2.8** (3SRA03)	**2.10** (3SRA11)
Identification Code	3s	3s	3SRA11_s
Empirical Formula	$C_{31.5}H_{27}F_{12}N_8O_{0.5}P_2Ru$	$C_{58}H_{52}F_{24}N_{16}P_4Ru_2$	$C_{32}H_{28}F_{12}N_8P_2Ru$
Formula weight	916.62	1755.17	915.63
Temperature (K)	110(2)	113(2)	120(1)
Crystal system	triclinic	triclinic	monoclinic
Space group	*P*–1	*P*–1	$P2_1/c$
a (Å)	11.5749(3)	11.1111(4)	10.9639(2)
b (Å)	12.0178(4)	12.1033(4)	13.8765(2)
c (Å)	14.8598(7)	13.7478(5)	23.8383(5)
α (°)	106.172(2)	90.518(2)	90
β (°)	93.502(2)	105.515(2)	102.449(2)
γ (°)	114.482(2)	111.168(10)	90
Volume / Å	1769.56(12)	1649.73(10)	3541.48(12)
Z	2	1	4
Density (calculated) mg/m^3	1.720	1.767	1.717
Absorption Coefficient mm^{-1} (Radiation)	0.636 (Mo)	0.677 (Mo)	0.635 (Mo)
F (000)	916	876	1832
Crystal size (mm^3)	0.49 × 0.29 × 0.05	0.43 x 0.21 x 0.12	0.27 × 0.10 × 0.08
2θ range for data collection (°)	2.914 to 53.6	4.86 to 55.1	5.388 to 55.0
Reflections collected	36586	38051	91998
Independent Reflections [R(int)]	7576 [0.0706]	7599 [0.0719]	8120 [0.0301]
Data/ restraints/ parameters	7576/1/516	7599/0/471	8120/0/498
Goodness–of–fit on F^2	1.209	0.917	1.092
Final R_1 indices [I>2sigma(I)]	R_1 = 0.0594, wR_2 = 0.1390	R_1 = 0.0388, wR_2 = 0.0675	R_1 = 0.0269, wR_2 = 0.0631
Final R indices [all data]	R_1 = 0.0705, wR_2 = 0.1572	R_1 = 0.0621, wR_2 = 0.0720	R_1 = 0.0296, wR_2 = 0.0649
Largest diff. peak/hole (e.Å^{-3})	0.95/–1.12	1.51/–0.71	0.65/–0.55

Table A2. Crystal data and X–ray experimental data for complexes **2.11**, **2.13** and **2.14**.

Complex (Code)	**2.11** (3SRA20)	**2.13** (3SRA41)	**2.14** (3SRA37)
Identification Code	3sra20	3sra41a	3sra37
Empirical Formula	$C_{62}H_{59}F_{24}N_{17}P_4Ru_2$	$C_{37.5}H_{37}Cl_2F_{12}N_8O_{2.5}P_2Ru$	$C_{62}H_{56}N_{18}F_{24}P_4Cl_2Ru_2$
Formula weight	1824.28	1101.66	1906.17
Temperature (K)	120(1)	120(2)	120(1)
Crystal system	orthorhombic	triclinic	monoclinic
Space group	$P2_12_12_1$	$P\text{–}1$	$P2_1/c$
a (Å)	13.8511(1)	12.7485(2)	11.68070(6)
b (Å)	21.2980(2)	12.7698(3)	22.22138(10)
c (Å)	23.7630(2)	15.1015(3)	13.93440(6)
α (°)	90	93.4048(15)	90
β (°)	90	111.6252(16)	94.7224(4)
γ (°)	90	101.7779(16)	90
Volume / Å	7010.08(10)	2212.68(7)	3604.55(3)
Z	4	2	2
Density (calculated) mg/m^3	1.729	1.654	1.756
Absorption Coefficient mm^{-1} (Radiation)	5.422 (Cu)	5.537 (Cu)	5.974 (Cu)
F (000)	3656	1108	1904
Crystal size (mm^3)	0.42 × 0.28 × 0.05	0.24 × 0.19 × 0.06	0.35 × 0.20 × 0.10
2θ range for data collection (°)	5.572 to 148.3	6.366 to 135.0	7.5 to 135.0
Reflections collected	94373	32409	145646
Independent Reflections [R(int)]	14148 [0.0665]	7978 [0.0388]	6480 [0.0387]
Data/ restraints/ parameters	14148/0/989	7978/0/600	6480/0/508
Goodness–of–fit on F^2	1.059	1.035	1.073
Final R_1 indices [I>2sigma(I)]	R_1 = 0.0357, wR_2 = 0.0944	R_1 = 0.0340, wR_2 = 0.0866	R_1 = 0.0253, wR_2 = 0.0629
Final R indices [all data]	R_1 = 0.0367, wR_2 = 0.0953	R_1 = 0.0379, wR_2 = 0.0899	R_1 = 0.0276, wR_2 = 0.0647
Largest diff. peak/hole (e.Å^{-3})	0.75/–0.78	1.12/–1.03	0.76/–0.53
Flack parameter	–0.015(3)	–	–

Table A3. Crystal data and X–ray experimental data for complexes **2.15**, **2.16** and **3.10**.

Complex (Code)	**2.15** (3SRA39)	**2.16** (3SRA63)	**3.10** (3SRA15)
Identification Code	3SRA39	3SRA63	3sra15
Empirical Formula	$C_{37.5}H_{37}Br_2F_{12}N_8O_{2.5}P_2Ru$	$C_{62}H_{56}Br_2F_{24}N_{18}P_4Ru_2$	$C_{54}H_{45}Cl_2F_{18}N_{17}P_3Ru_2$
Formula weight	1190.58	1995.08	1640.02
Temperature (K)	120(1)	120(1)	120(1)
Crystal system	triclinic	monoclinic	monoclinic
Space group	*P*–1	$P2_1/c$	$C2/c$
a (Å)	12.8070(2)	11.7699(2)	23.7676(2)
b (Å)	12.8963(2)	22.2200(3)	21.8027(1)
c (Å)	15.0747(3)	13.9621(3)	14.4797(1)
α (°)	93.8914(15)	90	90
β (°)	112.1769(17)	94.6873(16)	114.338(1)
γ (°)	101.9052(15)	90	90
Volume / Å	2226.62(7)	3639.23(11)	6836.50(11)
Z	2	2	4
Density (calculated) mg/m^3	1.776	1.821	1.593
Absorption Coefficient mm^{-1} (Radiation)	6.501 (Cu)	6.529 (Cu)	0.689 (Mo)
F (000)	1180	1976	3268
Crystal size (mm^3)	0.28 × 0.13 × 0.07	0.32 × 0.19 × 0.08	0.43 × 0.41 × 0.07
2θ range for data collection (°)	6.416 to 135.0	7.496 to 135.0	5.298 to 59.7
Reflections collected	49987	57196	254416
Independent Reflections [R(int)]	8040 [0.0342]	6550 [0.0659]	9553 [0.0518]
Data/ restraints/ parameters	8040/0/600	6550/0/508	9553/0/513
Goodness–of–fit on F^2	1.030	1.035	1.105
Final R_1 indices [I>2sigma(I)]	R_1 = 0.0270, wR_2 = 0.0645	R_1 = 0.0303, wR_2 = 0.0769	R_1 = 0.0582, wR_2 = 0.1752
Final R indices [all data]	R_1 = 0.0300, wR_2 = 0.0665	R_1 = 0.0340, wR_2 = 0.0793	R_1 = 0.0721, wR_2 = 0.1932
Largest diff. peak/hole (e.Å^{-3})	1.12/–0.86	0.62/–0.94	2.20/–0.75

Table A4. Crystal data and X–ray experimental data for complexes **3.12**, **3.13** and **3.14**.

Complex (Code)	**3.12** (3SRA49)	**3.13** (3SRA29)	**3.14** (3SRA08)
Identification Code	3SRA49	3SRA29	pjs
Empirical Formula	$C_{52}H_{42}Br_2F_{18}N_{16}P_3Ru_2$	$C_{32}H_{26}Cl_2F_{12}N_{10}P_2Ru$	$C_{60}H_{56}N_{18}P_4F_{24}Cl_2Ru_2$
Formula weight	1687.87	1012.54	1882.15
Temperature (K)	120(1)	120(1)	110(2)
Crystal system	triclinic	monoclinic	triclinic
Space group	*P*–1	$P2_1/c$	*P*–1
a (Å)	11.6038(2)	8.7251(1)	11.7445(8)
b (Å)	12.3877(2)	25.2174(4)	12.1239(7)
c (Å)	12.5279(2)	17.4010(3)	14.6963(10)
α (°)	100.0237(16)	90	101.783(4)
β (°)	115.6257(18)	92.7580(14)	110.670(4)
γ (°)	103.4110(15)	90	101.782(4)
Volume / Å	1500.14(5)	3824.22(11)	1827.40(2)
Z	1	4	1
Density (calculated) mg/m^3	1.868	1.759	1.710
Absorption Coefficient mm^{-1} (Radiation)	7.378 (Cu)	6.311 (Cu)	0.689 (Mo)
F (000)	831	2016	940
Crystal size (mm^3)	0.23 × 0.16 × 0.04	0.10 × 0.09 × 0.03	0.48 x 0.12 x 0.08
2θ range for data collection (°)	7.724 to 149.2	6.176 to 135.0	5.70 to 55.1
Reflections collected	44090	25537	36971
Independent Reflections [R(int)]	6084 [0.0407]	6770 [0.0354]	8430 [0.1306]
Data/ restraints/ parameters	6084/0/422	6770/0/536	8430/0/499
Goodness–of–fit on F^2	1.037	1.104	0.925
Final R_1 indices [I>2sigma(I)]	R_1 = 0.0361, wR_2 = 0.0913	R_1 = 0.0414, wR_2 = 0.1006	R_1 = 0.0636, wR_2 = 0.1532
Final R indices [all data]	R_1 = 0.0401, wR_2 = 0.0955	R_1 = 0.0469, wR_2 = 0.1036	R_1 = 0.1706, wR_2 = 0.1894
Largest diff. peak/hole (e.Å^{-3})	1.04/–1.17	0.88/–0.55	0.76/–1.38

Table A5. Crystal data and X–ray experimental data for complexes **3.15**, **3.16** and **3.17**.

Complex (Code)	**3.15** (3SRA02)	**3.16** (3SRA23)	**3.17** (3SRA61)
Identification Code	p21c	3sra23	3SRA61
Empirical Formula	$C_{41}H_{34}F_{12}N_8OP_2Ru$	$C_{70}H_{62}F_{24}N_{18}P_4Ru_2$	$C_{39}H_{32}F_{12}N_{10}OP_2Ru$
Formula weight	1045.77	1937.39	1047.75
Temperature (K)	113(2)	120(1)	120(1)
Crystal system	monoclinic	triclinic	monoclinic
Space group	$P2_1/c$	$P\bar{1}$	$P2_1/c$
a (Å)	17.7370(6)	11.6227(5)	17.30753(8)
b (Å)	14.3227(5)	11.6705(4)	14.29440(9)
c (Å)	16.9777(6)	16.0765(7)	16.77249(8)
α (°)	90	85.033(3)	90
β (°)	102.693(2)	79.967(4)	98.8354(5)
γ (°)	90	63.849(4)	90
Volume / Å	4207.6(3)	1927.37(15)	4100.29(4)
Z	4	1	4
Density (calculated) mg/m^3	1.651	1.669	1.697
Absorption Coefficient mm^{-1} (Radiation)	0.548 (Mo)	4.977 (Cu)	4.760 (Cu)
F (000)	2104	972	2104
Crystal size (mm^3)	0.46 x 0.18 x 0.05	0.28 × 0.17 × 0.06	0.13 × 0.11 × 0.04
2θ range for data collection (°)	4.918 to 55.1	5.582 to 135.0	8.062 to 135.0
Reflections collected	88085	13614	78359
Independent Reflections [R(int)]	9705 [0.1290]	6931 [0.0680]	7384 [0.0399]
Data/ restraints/ parameters	9705/0/588	6931/0/535	7384/0/588
Goodness–of–fit on F^2	0.732	1.027	1.051
Final R_1 indices [I>2sigma(I)]	R_1 = 0.0402, wR_2 = 0.0856	R_1 = 0.0516, wR_2 = 0.1339	R_1 = 0.0240, wR_2 = 0.0604
Final R indices [all data]	R_1 = 0.0909, wR_2 = 0.1005	R_1 = 0.0595, wR_2 = 0.1427	R_1 = 0.0262, wR_2 = 0.0618
Largest diff. peak/hole (e.Å^{-3})	0.73/–0.64	1.06/–0.93	0.99/–0.48

Table A6. Crystal data and X–ray experimental data for complexes **3.19**, **3.20** and **3.21**.

Complex (Code)	**3.19** (3SRA19)	**3.20** (3SRA09)	**3.21** (3SRA45)
Identification Code	3sra19	3sra9	3SRA45–Cu
Empirical Formula	$C_{76}H_{72}F_{24}N_{24}P_4Ru_2$	$C_{58}H_{42}F_{24}N_{14}P_4Ru_2$	$C_{42}H_{38}F_{12}N_{10}O_2P_2Ru$
Formula weight	2103.59	1717.07	1105.83
Temperature (K)	120(1)	120(1)	120(1)
Crystal system	monoclinic	monoclinic	monoclinic
Space group	*P*2/c	*C*2/c	$P2_1/c$
a (Å)	14.1578(2)	22.5647(3)	19.5939(2)
b (Å)	24.3485(3)	14.2744(2)	13.9284(1)
c (Å)	13.3280(1)	23.1050(4)	16.5234(2)
α (°)	90	90	90
β (°)	94.5387(11)	102.033(2)	101.0338(12)
γ (°)	90	90	90
Volume / Å	4580.04(9)	7278.6(2)	4426.08(9)
Z	2	4	4
Density (calculated) mg/m^3	1.525	1.567	1.660
Absorption Coefficient mm^{-1} (Radiation)	4.258 (Cu)	5.173 (Cu)	4.462 (Cu)
F (000)	2120	3408	2232
Crystal size (mm^3)	0.44 × 0.43 × 0.11	0.43 × 0.11 × 0.05	0.19 × 0.16 × 0.15
2θ range for data collection (°)	6.262 to 135.0	7.376 to 147.8	7.838 to 135.0
Reflections collected	92403	32209	46811
Independent Reflections [R(int)]	8251 [0.0511]	7215 [0.0464]	7974 [0.0372]
Data/ restraints/ parameters	8251/0/608	7215/0/518	7974/0/626
Goodness–of–fit on F^2	1.169	1.025	1.096
Final R_1 indices [I>2sigma(I)]	R_1 = 0.0548, wR_2 = 0.1392	R_1 = 0.0585, wR_2 = 0.1625	R_1 = 0.0612, wR_2 = 0.1995
Final R indices [all data]	R_1 = 0.0585, wR_2 = 0.1416	R_1 = 0.0660, wR_2 = 0.1727	R_1 = 0.0647, wR_2 = 0.2024
Largest diff. peak/hole (e.Å^{-3})	1.58/–1.02	2.12/–1.07	3.75/–1.08

Table A7. Crystal data and X–ray experimental data for complexes **3.22**, **4.3** and **4.4**.

Complex (Code)	**3.22** (3SRA65)	**4.3** (3SRA10)	**4.4** (3SRA13)
identification Code	3sra65	3sra10	3sra13
Empirical Formula	$C_{39}H_{32}F_{12}N_{10}OP_2Ru$	$C_{54}H_{42}F_{24}N_{14}P_4Ru_2$	$C_{42}H_{31}F_{12}N_9OP_2Ru$
Formula weight	1047.75	1669.03	1068.77
Temperature (K)	120(1)	120(1)	120(1)
Crystal system	monoclinic	triclinic	monoclinic
Space group	$P2_1/c$	$P\bar{1}$	$P2_1/n$
a (Å)	17.9790(5)	11.3568(4)	12.16186(9)
b (Å)	14.3523(3)	12.5932(8)	23.23128(15)
c (Å)	16.6077(4)	12.8533(7)	14.65098(9)
α (°)	90	69.457(6)	90
β (°)	103.611(2)	70.796(4)	93.1574(6)
γ (°)	90	64.750(5)	90
Volume / Å	4165.06(17)	1521.63(16)	4133.14(5)
Z	4	1	4
Density (calculated) mg/m^3	1.671	1.821	1.718
Absorption Coefficient mm^{-1} (Radiation)	4.686 (Cu)	0.728 (Mo)	4.732 (Cu)
F (000)	2104	828	2144
Crystal size (mm^3)	0.16 × 0.04 × 0.03	0.30 x 0.20 x 0.03	0.16 × 0.13 × 0.10
2θ range for data collection (°)	7.972 to 135.0	5.65 to 55.0	7.142 to 148.1
Reflections collected	28009	18933	132635
Independent Reflections [R(int)]	7479 [0.0641]	6989 [0.0310]	8353 [0.0661]
Data/ restraints/ parameters	7479/0/588	6989/0/443	8353/0/606
Goodness–of–fit on F^2	1.041	1.048	1.038
Final R_1 indices [I>2sigma(I)]	R_1 = 0.0432, wR_2 = 0.1109	R_1 = 0.0457, wR_2 = 0.1116	R_1 = 0.0345, wR_2 = 0.0850
Final R indices [all data]	R_1 = 0.0565, wR_2 = 0.1183	R_1 = 0.0563, wR_2 = 0.1213	R_1 = 0.0391, wR_2 = 0.0892
Largest diff. peak/hole (e.Å^{-3})	1.36/–1.20	2.40/–1.24	0.64/–0.60

Table A8. Crystal data and X–ray experimental data for complexes **4.5**, **5.7** and **5.8**.

Complex (Code)	**4.5** (3SRA26)	**5.7** (3SRA42)	**5.8** (3SRA50)
Identification Code	3SRA26	3sra42	3SRA50
Empirical Formula	$C_{58}H_{42}F_{24}N_{14}P_4Ru_2$	$C_{56}H_{48}F_{24}N_{14}P_4Ru_2$	$C_{62}H_{52}Cl_4N_{14}O_{16}Ru_2$
Formula weight	1717.08	1699.10	1593.11
Temperature (K)	120(1)	120(2)	120(1)
Crystal system	triclinic	triclinic	monoclinic
Space group	*P*–1	*P*–1	$P2_1/c$
a (Å)	11.2107(4)	12.1396(5)	14.3792(2)
b (Å)	12.8474(3)	12.6233(4)	13.1170(1)
c (Å)	12.9944(3)	12.8958(5)	17.9619(3)
α (°)	66.196(3)	76.863(3)	90
β (°)	70.410(3)	64.151(4)	110.9563(17)
γ (°)	71.275(3)	63.335(4)	90
Volume / Å	1575.35(8)	1588.08(13)	3163.74(8)
Z	1	1	2
Density (calculated) mg/m^3	1.810	1.777	1.672
Absorption Coefficient mm^{-1} (Radiation)	5.976 (Cu)	5.917 (Cu)	6.123 (Cu)
F (000)	852	846	1612
Crystal size (mm^3)	0.30 × 0.16 × 0.07	0.08 × 0.07 × 0.02	0.16 × 0.10 × 0.06
2θ range for data collection (°)	7.66 to 147.7	7.624 to 135.0	6.512 to 135.0
Reflections collected	27326	19557	42657
Independent Reflections [R(int)]	6273 [0.0534]	5711 [0.0584]	5685 [0.0438]
Data/ restraints/ parameters	6273/0/460	5711/0/452	5685/0/491
Goodness–of–fit on F^2	1.059	0.898	1.045
Final R_1 indices [I>2sigma(I)]	R_1 = 0.0397, wR_2 = 0.0998	R_1 = 0.0416, wR_2 = 0.0995	R_1 = 0.0356, wR_2 = 0.0840
Final R indices [all data]	R_1 = 0.0490, wR_2 = 0.1088	R_1 = 0.0559, wR_2 = 0.1044	R_1 = 0.0406, wR_2 = 0.0881
Largest diff. peak/hole (e.Å^{-3})	0.93/–0.81	1.38/–0.59	0.63/–1.04

Table A9. Crystal data and X–ray experimental data for complexes **6.1**, **6.2** and **6.3**.

Complex (Code)	**6.1** (3SRA12)	**6.2** (3SRA21)	**6.3** (3SRA34)
Identification Code	3sra12	3sra21	3sra34
Empirical Formula	$C_{11}H_8F_3N_4O_3SAg$	$C_{16}H_{12}F_6N_4O_4Ag_2$	$C_{10}H_6Cl_2N_5O_3Ag$
Formula weight	441.14	654.04	422.97
Temperature (K)	120(1)	120(1)	120(1)
Crystal system	monoclinic	monoclinic	tetragonal
Space group	$P2_1/n$	$P2_1/n$	$P4_2/n$
a (Å)	10.56992(7)	8.3028(7)	16.6435(1)
b (Å)	10.32936(6)	21.6575(2)	16.6435(1)
c (Å)	13.43872(8)	10.8491(8)	9.45138(7)
α (°)	90	90	90
β (°)	94.8075(6)	91.6315(8)	90
γ (°)	90	90	90
Volume / Å	1462.08(2)	1950.08(3)	2618.08(4)
Z	4	4	8
Density (calculated) mg/m^3	2.004	2.228	2.146
Absorption Coefficient mm^{-1} (Radiation)	1.574 (Mo)	2.098 (Mo)	1.965 (Mo)
F (000)	864	1264	1648
Crystal size (mm^3)	0.36 × 0.24 × 0.18	0.47 × 0.36 × 0.34	0.17 × 0.16 × 0.10
2θ range for data collection (°)	5.524 to 55.0	5.256 to 55.0	5.528 to 70.6
Reflections collected	181391	225517	130409
Independent Reflections [R(int)]	3360 [0.0375]	4465 [0.0699]	5825 [0.0367]
Data/ restraints/ parameters	3360/0/208	4465/0/291	5825/0/190
Goodness–of–fit on F^2	1.105	1.120	1.087
Final R_1 indices [I>2sigma(I)]	R_1 = 0.0180, wR_2 = 0.0421	R_1 = 0.0217, wR_2 = 0.0552	R_1 = 0.0234, wR_2 = 0.0553
Final R indices [all data]	R_1 = 0.0218, wR_2 = 0.0447	R_1 = 0.0242, wR_2 = 0.0570	R_1 = 0.0314, wR_2 = 0.0607
Largest diff. peak/hole (e.Å^{-3})	0.44/–0.37	0.61/–0.67	1.10/–0.56

Table A10. Crystal data and X–ray experimental data for complexes **6.4**, **6.5** and **6.6**.

Complex (Code)	**6.4** (3SRA14)	**6.5** (3SRA17)	**6.6** (3SRA51)
Identification Code	3SRA14	3SRA17	3sra51
Empirical Formula	$C_8H_4Cl_3N_6O_4Ag$	$C_{16}H_8Ag_2Cl_4N_{14}O_6$	$C_{27}H_{12}Br_6F_9N_{18}O_9S_3Ag_3$
Formula weight	462.39	849.90	1802.80
Temperature (K)	120(1)	120(1)	120(1)
Crystal system	triclinic	triclinic	triclinic
Space group	*P*–1	*P*–1	*P*–1
a (Å)	7.8494(2)	9.4905(1)	7.6952(3)
b (Å)	9.4897(2)	9.7663(1)	10.4683(4)
c (Å)	9.8974(2)	13.8808(2)	15.5297(4)
α (°)	96.542(2)	83.922(1)	79.690(3)
β (°)	99.529(2)	89.264(1)	84.543(2)
γ (°)	100.811(2)	78.294(1)	75.651(3)
Volume / Å	706.120(3)	1252.69(3)	1190.72(7)
Z	2	2	1
Density (calculated) mg/m^3	2.175	2.253	2.514
Absorption Coefficient mm^{-1} (Radiation)	2.021 (Mo)	2.058 (Mo)	6.492 (Mo)
F (000)	448	824	852
Crystal size (mm^3)	0.24 × 0.22 × 0.20	0.30 × 0.12 × 0.07	0.45 × 0.33 × 0.07
2θ range for data collection (°)	5.384 to 55.0	5.262 to 55.0	5.214 to 55.0
Reflections collected	52040	93166	29191
Independent Reflections [R(int)]	3232 [0.0387]	5745 [0.0389]	5459 [0.0821]
Data/ restraints/ parameters	3232/0/238	5745/0/405	5459/0/340
Goodness–of–fit on F^2	1.072	1.099	1.066
Final R_1 indices [I>2sigma(I)]	R_1 = 0.0317, wR_2 = 0.0756	R_1 = 0.0419, wR_2 = 0.1092	R_1 = 0.0444, wR_2 = 0.1165
Final R indices [all data]	R_1 = 0.0386, wR_2 = 0.0805	R_1 = 0.0510, wR_2 = 0.1181	R_1 = 0.0579, wR_2 = 0.1252
Largest diff. peak/hole (e.Å^{-3})	1.09/–0.58	3.07/–1.22	1.42/–1.12

Table A11. Crystal data and X–ray experimental data for complexes **6.7**, **6.8** and **6.9**.

Complex (Code)	**6.7** (3SRA32)	**6.8** (3SRA33)	**6.9** (3SRA56)
Identification Code	3sra32	3sra33	sra1
Empirical Formula	$C_{12}H_{12}Cl_2N_7O_3Ag$	$C_{12}H_{12}Cl_3N_6O_4Ag$	$C_{20}H_{12}F_3N_4O_2Ag$
Formula weight	481.06	518.50	505.21
Temperature (K)	120(1)	120(1)	120(1)
Crystal system	triclinic	triclinic	monoclinic
Space group	*P*–1	*P*–1	*C*2/*c*
a (Å)	8.1704(3)	8.0406(2)	17.0146(7)
b (Å)	9.6902(3)	9.8922(3)	8.2740(2)
c (Å)	11.2554(4)	11.7097(4)	14.5536(4)
α (°)	73.341(3)	71.402(3)	90
β (°)	86.035(3)	88.737(2)	115.629(4)
γ (°)	74.892(3)	78.666(2)	90
Volume / Å	824.20(5)	864.69(5)	1847.26(12)
Z	2	2	4
Density (calculated) mg/m^3	1.938	1.991	1.817
Absorption Coefficient mm^{-1} (Radiation)	1.576 (Mo)	1.662 (Mo)	1.147 (Mo)
F (000)	476	512	1000
Crystal size (mm^3)	0.44 × 0.26 × 0.08	0.13 × 0.07 × 0.04	0.20 × 0.18 × 0.06
2θ range for data collection (°)	5.952 to 55.0	6.104 to 70.6	5.594 to 66.2
Reflections collected	13754	30879	19546
Independent Reflections [R(int)]	3795 [0.0301]	7351 [0.0381]	3343 [0.0368]
Data/ restraints/ parameters	3795/0/230	7351/0/239	3343/0/151
Goodness–of–fit on F^2	1.052	1.090	1.094
Final R_1 indices [I>2sigma(I)]	R_1 = 0.0195, wR_2 = 0.0487	R_1 = 0.0277, wR_2 = 0.0614	R_1 = 0.0257, wR_2 = 0.0547
Final R indices [all data]	R_1 = 0.0214, wR_2 = 0.0500	R_1 = 0.0348, wR_2 = 0.0647	R_1 = 0.0308, wR_2 = 0.0576
Largest diff. peak/hole (e.Å^{-3})	0.50/–0.39	0.72/–0.58	1.04/–0.37

Table A12. Crystal data and X–ray experimental data for complexes **6.10** and **6.11**.

Complex (Code)	**6.10** (3SRA58)	**6.11** (3SRA57)
Identification Code	sra	sra2
Empirical Formula	$C_{36}H_{24}Cl_2N_8O_8Ag_2$	$C_{38}H_{26}F_6N_8O_7S_2Ag_2$
Formula weight	983.27	1100.53
Temperature (K)	120(1)	120(1)
Crystal system	monoclinic	monoclinic
Space group	*C*2/*c*	*Cc*
a (Å)	19.9456(5)	26.0608(10)
b (Å)	27.1458(5)	8.8435(2)
c (Å)	14.4557(3)	18.4677(5)
α (°)	90	90
β (°)	116.563(2)	111.409(3)
γ (°)	90	90
Volume / Å	7000.7(3)	3962.5(2)
Z	8	4
Density (calculated) mg/m^3	1.866	1.845
Absorption Coefficient mm^{-1} (Radiation)	1.339 (Mo)	1.184 (Mo)
F (000)	3904	2184
Crystal size (mm^3)	0.20 × 0.13 × 0.12	0.30 × 0.20 × 0.08
2θ range for data collection (°)	5.382 to 55.0	5.706 to 55.0
Reflections collected	44486	29631
Independent Reflections [R(int)]	8031 [0.0285]	9088 [0.0318]
Data/ restraints/ parameters	8031/0/506	9088/2/569
Goodness–of–fit on F^2	1.063	1.049
Final R_1 indices [I>2sigma(I)]	R_1 = 0.0244, wR_2 = 0.0621	R_1 = 0.0220, wR_2 = 0.0515
Final R indices [all data]	R_1 = 0.0300, wR_2 = 0.0654	R_1 = 0.0230, wR_2 = 0.0522
Largest diff. peak/hole (e.Å^{-3})	1.14/–0.28	0.42/–0.36
Flack parameter	–	0.002(8)

References

[1] V. Balzani, G. Bergamini, F. Marchioni, P. Ceroni, *Coordination Chemistry Reviews* **2006**, *250*, 1254–1266.
[2] L. De Cola, P. Belser, *Coordination Chemistry Reviews* **1998**, *177*, 301–346.
[3] R. J. Watts, *Journal of Chemical Education* **1983**, *60*, 834.
[4] V. Balzani, F. Scandola, *Supramolecular Photochemistry*, Ellis Horwood, West Sussex, UK, **1991**.
[5] A. Jablonska–Wawrzycka, P. Rogala, S. Michalkiewicz, M. Hodorowicz, B. Barszcz, *Dalton Transactions* **2013**, *42*, 6092–6101.
[6] V. Balzani, A. Juris, M. Venturi, S. Campagna, S. Serroni, *Chemical Reviews* **1996**, *96*, 759–834.
[7] V. Balzani, A. Juris, *Coordination Chemistry Reviews* **2001**, *211*, 97–115.
[8] R. T. F. Jukes, V. Adamo, F. Hartl, P. Belser, L. De Cola, *Coordination Chemistry Reviews* **2005**, *249*, 1327–1335.
[9] J. Otsuki, T. Akasaka, K. Araki, *Coordination Chemistry Reviews* **2008**, *252*, 32–56.
[10] V. Balzani, G. Bergamini, P. Ceroni, *Coordination Chemistry Reviews* **2008**, *252*, 2456–2469.
[11] A. C. Benniston, *Chemical Society Reviews* **2004**, *33*, 573–578.
[12] K. Kalyanasundaram, M. Grätzel, *Coordination Chemistry Reviews* **1998**, *177*, 347–414.
[13] D. L. Ashford, C. R. K. Glasson, M. R. Norris, J. J. Concepcion, S. Keinan, M. K. Brennaman, J. L. Templeton, T. J. Meyer, *Inorganic Chemistry* **2014**, *53*, 5637–5646.
[14] E. Zahavy, M. Seiler, S. Marx–Tibbon, E. Joselevich, I. Willner, H. Dürr, D. O'Connor, A. Harriman, *Angewandte Chemie International Edition in English* **1995**, *34*, 1005–1008.
[15] C. G. Garcia, J. F. de Lima, N. Y. Murakami Iha, *Coordination Chemistry Reviews* **2000**, *196*, 219–247.
[16] H. Dürr, S. Bossmann, *Accounts of Chemical Research* **2001**, *34*, 905–917.
[17] P. D. Beer, N. C. Fletcher, T. Wear, *Polyhedron* **1996**, *15*, 1339–1347.
[18] T. Duff, A. Grüßing, J.–L. Thomas, M. Duati, J. G. Vos, *Polyhedron* **2003**, *22*, 775–780.
[19] J. A. Kitchen, E. M. Boyle, T. Gunnlaugsson, *Inorganica Chimica Acta* **2012**, *381*, 236–242.
[20] C. D. Clark, M. Z. Hoffman, *Coordination Chemistry Reviews* **1997**, *159*, 359–373.
[21] H. Yersin, W. Humbs, J. Strasser, *Coordination Chemistry Reviews* **1997**, *159*, 325–358.
[22] K. Kalyanasundaram, M. K. Nazeeruddin, *Inorganic Chemistry* **1990**, *29*, 1888–1897.
[23] C. Creutz, N. Sutin, *Proceedings of the National Academy of Sciences of the United States of America* **1975**, *72*, 2858–2862.
[24] J. G. Vos, J. M. Kelly, *Dalton Transactions* **2006**, 4869–4883.
[25] J. R. Schoonover, K. M. Omberg, J. A. Moss, S. Bernhard, V. J. Malueg, W. H. Woodruff, T. J. Meyer, *Inorganic Chemistry* **1998**, *37*, 2585–2587.
[26] C. Niezborala, F. Hache, *The Journal of Physical Chemistry A* **2007**, *111*, 7732–7735.
[27] P. A. Anderson, G. B. Deacon, K. H. Haarmann, F. R. Keene, T. J. Meyer, D. A. Reitsma, B. W. Skelton, G. F. Strouse, N. C. Thomas, *Inorganic Chemistry* **1995**, *34*, 6145–6157.
[28] P. A. Anderson, F. R. Keene, T. J. Meyer, J. A. Moss, G. F. Strouse, J. A. Treadway, *Journal of the Chemical Society, Dalton Transactions* **2002**, 3820–3831.
[29] P. J. Steel, F. LaHousse, D. Lerner, C. Marzin, *Inorganic Chemistry* **1983**, *22*, 1488–1493.
[30] P. J. Steel, E. C. Constable, *Journal of the Chemical Society, Dalton Transactions* **1990**, 1389.
[31] C. Creutz, H. Taube, *Journal of the American Chemical Society* **1973**, *95*, 1086–1094.
[32] J. A. McCleverty, M. D. Ward, *Accounts of Chemical Research* **1998**, *31*, 842–851.
[33] K. Kalyanasundaram, M. K. Nazeeruddin, *Inorganica Chimica Acta* **1994**, *226*, 213–230.
[34] F. Barigelletti, L. Flamigni, *Chemical Society Reviews* **2000**, *29*, 1–12.
[35] M. D. Ward, *Chemical Society Reviews* **1997**, *26*, 365–375.

[36] W. R. Browne, R. Hage, J. G. Vos, *Coordination Chemistry Reviews* **2006**, *250*, 1653–1668.
[37] G. Giuffrida, S. Campagna, *Coordination Chemistry Reviews* **1994**, *135–136*, 517–531.
[38] W. R. Browne, J. J. D. de Jong, T. Kudernac, M. Walko, L. N. Lucas, K. Uchida, J. H. van Esch, B. L. Feringa, *Chemistry – A European Journal* **2005**, *11*, 6414–6429.
[39] D. M. D'Alessandro, F. R. Keene, *Dalton Transactions* **2004**, 3950–3954.
[40] E. A. Fellows, F. R. Keene, *Journal of Physical Chemistry B* **2007**, *111*, 6667–6675.
[41] S. Ernst, V. Kasack, W. Kaim, *Inorganic Chemistry* **1988**, *27*, 1146–1148.
[42] M. D. Ward, *Chemical Society Reviews* **1995**, *24*, 121–134.
[43] J. E. Sutton, H. Taube, *Inorganic Chemistry* **1981**, *20*, 3125–3134.
[44] P. J. Steel, *Coordination Chemistry Reviews* **1990**, *106*, 227–265.
[45] P. Belser, S. Bernhard, C. Blum, A. Beyeler, L. De Cola, V. Balzani, *Coordination Chemistry Reviews* **1999**, *190–192*, 155–169.
[46] J. A. Joule, K. Mills, *Heterocyclic Chemistry*, Fifth ed., John Wiley and Sons Limited, United Kingdom, **2010**.
[47] W. Kaim, *Angewandte Chemie International Edition in English* **1983**, *22*, 171–190 and references therein.
[48] W. Kaim, B. Sarkar, *Coordination Chemistry Reviews* **2007**, *251*, 584–594.
[49] E. Iengo, G. Mestroni, S. Geremia, M. Calligaris, E. Alessio, *Journal of the Chemical Society, Dalton Transactions* **1999**, 3361–3371.
[50] M. J. Powers, T. J. Meyer, *Journal of the American Chemical Society* **1980**, *102*, 1289–1297.
[51] R. W. Callahan, F. R. Keene, T. J. Meyer, D. J. Salmon, *Journal of the American Chemical Society* **1977**, *99*, 1064–1073.
[52] R. W. Callahan, G. M. Brown, T. J. Meyer, *Journal of the American Chemical Society* **1974**, *96*, 7829–7830.
[53] R. W. Callahan, G. M. Brown, T. J. Meyer, *Inorganic Chemistry* **1975**, *14*, 1443–1453.
[54] C. H. Londergan, C. P. Kubiak, *The Journal of Physical Chemistry A* **2003**, *107*, 9301–9311.
[55] W. Kaim, A. Klein, M. Glöckle, *Accounts of Chemical Research* **2000**, *33*, 755–763.
[56] U. Fuerholz, H. B. Buergi, F. E. Wagner, A. Stebler, J. H. Ammeter, E. Krausz, R. J. H. Clark, M. J. Stead, A. Ludi, *Journal of the American Chemical Society* **1984**, *106*, 121–123.
[57] U. Fuerholz, S. Joss, H. B. Buergi, A. Ludi, *Inorganic Chemistry* **1985**, *24*, 943–948.
[58] M. I. Frazão Barbosa, E. M. A. Valle, S. L. Queiroz, J. Ellena, E. E. Castellano, V. R. S. Malta, J. R. de Sousa, O. Piro, M. P. de Araujo, A. A. Batista, *Polyhedron* **2010**, *29*, 2297–2303.
[59] J. Y. Wang, W. Gu, W. Z. Wang, X. Liu, D. Z. Liao, *Journal of Coordination Chemistry* **2011**, *64*, 2321–2328.
[60] D. E. Richardson, H. Taube, *Journal of the American Chemical Society* **1983**, *105*, 40–51.
[61] M. J. Powers, T. J. Meyer, *Inorganic Chemistry* **1978**, *17*, 2955–2958.
[62] G. M. Tom, C. Creutz, H. Taube, *Journal of the American Chemical Society* **1974**, *96*, 7827–7829.
[63] S. B. Braun–Sand, O. Wiest, *The Journal of Physical Chemistry A* **2002**, *107*, 285–291.
[64] R. A. Pavinato, J. A. Walk, M. E. McGuire, *Inorganic Chemistry* **1993**, *32*, 4982–4984.
[65] D. M. D'Alessandro, F. M. Foley, M. S. Davies, P. C. Junk, F. R. Keene, *Polyhedron* **2007**, *26*, 216–221.
[66] M. Hunziker, A. Ludi, *Journal of the American Chemical Society* **1977**, *99*, 7370–7371.
[67] K. J. Brewer, W. R. Murphy, J. D. Petersen, *Inorganic Chemistry* **1987**, *26*, 3376–3379.
[68] N. C. Fletcher, P. C. Junk, D. A. Reitsma, F. R. Keene, *Journal of the Chemical Society, Dalton Transactions* **1998**, *0*, 133–138.

[69] N. C. Fletcher, F. R. Keene, *Journal of the Chemical Society, Dalton Transactions* **1999**, *0*, 683–690.
[70] C. M. Fitchett, P. J. Steel, *Polyhedron* **2008**, *27*, 1527–1537.
[71] M. Haga, T. Matsumura–Inoue, S. Yamabe, *Inorganic Chemistry* **1987**, *26*, 4148–4154.
[72] J. Yin, R. L. Elsenbaumer, *Inorganic Chemistry* **2007**, *46*, 6891–6901.
[73] G. Denti, S. Campagna, L. Sabatino, S. Serroni, M. Ciano, V. Balzani, *Inorganic Chemistry* **1990**, *29*, 4750–4758.
[74] I. G. Phillips, P. J. Steel, *Australian Journal of Chemistry* **1998**, *51*, 371–382.
[75] W. Kaim, *Coordination Chemistry Reviews* **2002**, *230*, 127–139.
[76] R. Hage, A. H. J. Dijkhuis, J. G. Haasnoot, R. Prins, J. Reedijk, B. E. Buchanan, J. G. Vos, *Inorganic Chemistry* **1988**, *27*, 2185–2189.
[77] A. J. Downard, G. E. Honey, L. F. Phillips, P. J. Steel, *Inorganic Chemistry* **1991**, *30*, 2259–2260.
[78] P. Didier, L. Jacquet, A. Kirsch–De Mesmaeker, R. Hueber, A. Van Dorsselaer, *Inorganic Chemistry* **1992**, *31*, 4803–4809.
[79] F. R. Keene, *Coordination Chemistry Reviews* **1997**, *166*, 121–159.
[80] F. R. Keene, *Dalton Transactions* **2011**, *40*, 2405–2418.
[81] T. J. Rutherford, D. A. Reitsma, F. R. Keene, *Journal of the Chemical Society, Dalton Transactions* **1994**, 3659–3666.
[82] J. A. Treadway, P. Chen, T. J. Rutherford, F. R. Keene, T. J. Meyer, *Journal of Physical Chemistry A* **1997**, *101*, 6824–6826.
[83] D. A. Reitsma, F. R. Keene, *Journal of the Chemical Society, Dalton Transactions* **1993**, 2859–2860.
[84] F. R. Keene, *Chemical Society Reviews* **1998**, *27*, 185–194.
[85] U. Knof, A. von Zelewsky, *Angewandte Chemie International Edition* **1999**, *38*, 302–322.
[86] P. Belser, S. Bernhard, E. Jandrasics, A. von Zelewsky, L. De Cola, V. Balzani, *Coordination Chemistry Reviews* **1997**, *159*, 1–8.
[87] X. Hua, A. von Zelewsky, *Inorganic Chemistry* **1995**, *34*, 5791–5797.
[88] B. Bosnich, F. Dwyer, *Australian Journal of Chemistry* **1966**, *19*, 2229–2233.
[89] T. J. Rutherford, M. G. Quagliotto, F. R. Keene, *Inorganic Chemistry* **1995**, *34*, 3857–3858.
[90] P. Hayoz, A. von Zelewsky, H. Stoeckli–Evans, *Journal of the American Chemical Society* **1993**, *115*, 5111–5114.
[91] H. Mürner, P. Belser, A. von Zelewsky, *Journal of the American Chemical Society* **1996**, *118*, 7989–7994.
[92] N. C. Fletcher, F. R. Keene, H. Viebrock, A. von Zelewsky, *Inorganic Chemistry* **1997**, *36*, 1113–1121.
[93] L. S. Kelso, D. A. Reitsma, F. R. Keene, *Inorganic Chemistry* **1996**, *35*, 5144–5153.
[94] T. J. Rutherford, F. R. Keene, *Inorganic Chemistry* **1997**, *36*, 2872–2878.
[95] T. J. Rutherford, O. Van Gijte, A. Kirsch–De Mesmaeker, F. R. Keene, *Inorganic Chemistry* **1997**, *36*, 4465–4474.
[96] B. T. Patterson, F. R. Keene, *Inorganic Chemistry* **1998**, *37*, 645–650.
[97] D. M. D'Alessandro, F. R. Keene, P. J. Steel, C. J. Sumby, *Aust. J. Chem.* **2003**, *56*, 657–664.
[98] C. Richardson, P. J. Steel, *Aust. J. Chem.* **2002**, *55*, 783–788.
[99] J. A. Zampese, F. R. Keene, P. J. Steel, *Dalton Transactions* **2004**, 4124–4129.
[100] J. W. Slater, D. M. D'Alessandro, F. R. Keene, P. J. Steel, *Dalton Transactions* **2006**, 1954–1962.
[101] U. S. Schubert, H. Hofmeier, G. R. Newkome, *Modern Terpyridine Chemistry*, Wiley–VCH,Weinheim, **2006**.
[102] C. M. Hartshorn, N. Daire, V. Tondreau, B. Loeb, T. J. Meyer, P. S. White, *Inorganic Chemistry* **1999**, *38*, 3200–3206.
[103] L. M. Vogler, B. Scott, K. J. Brewer, *Inorganic Chemistry* **1993**, *32*, 898–903.
[104] A. J. Prussin Ii, S. Zhao, A. Jain, B. S. J. Winkel, K. J. Brewer, *Journal of Inorganic Biochemistry* **2009**, *103*, 427–431.
[105] C. R. Arana, H. D. Abruna, *Inorganic Chemistry* **1993**, *32*, 194–203.

[106] L. M. Vogler, K. J. Brewer, *Inorganic Chemistry* **1996**, *35*, 818–824.
[107] P. Bonhote, A. Lecas, E. Amouyal, *Chemical Communications* **1998**, 885–886.
[108] D. M. Dattelbaum, C. M. Hartshorn, T. J. Meyer, *Journal of the American Chemical Society* **2002**, *124*, 4938–4939.
[109] S. Flores–Torres, G. R. Hutchison, L. J. Soltzberg, H. D. Abruña, *Journal of the American Chemical Society* **2006**, *128*, 1513–1522.
[110] N. Yoshikawa, S. Yamabe, N. Kanehisa, T. Inoue, H. Takashima, K. Tsukahara, *Journal of Physical Organic Chemistry* **2011**, *24*, 1110–1118.
[111] H. Jude, B. L. Scott, R. C. Rocha, *Acta Crystallographica Section E* **2013**, *69*, m81–m82.
[112] F. Barigelletti, L. Flamigni, V. Balzani, J. P. Collin, J. P. Sauvage, A. Sour, E. C. Constable, A. M. W. C. Thompson, *Journal of the American Chemical Society* **1994**, *116*, 7692–7699.
[113] L. Hammarström, F. Barigelletti, L. Flamigni, M. T. Indelli, N. Armaroli, G. Calogero, M. Guardigli, A. Sour, J. P. Collin, J. P. Sauvage, *The Journal of Physical Chemistry A* **1997**, *101*, 9061–9069.
[114] E. A. Medlycott, G. S. Hanan, *Chemical Society Reviews* **2005**, *34*, 133–142.
[115] E. A. Medlycott, G. S. Hanan, *Coordination Chemistry Reviews* **2006**, *250*, 1763–1782.
[116] M. I. J. Polson, F. Loiseau, S. Campagna, G. S. Hanan, *Chemical Communications* **2006**, 1301–1303.
[117] A. K. Pal, G. S. Hanan, *Chemical Society Reviews* **2014**, *43*, 6184–6197.
[118] E. C. Constable, M. J. Hannon, *Inorganica Chimica Acta* **1993**, *211*, 101–110.
[119] J.–P. Collin, M. Beley, J.–P. Sauvage, F. Barigelletti, *Inorganica Chimica Acta* **1991**, *186*, 91–93.
[120] C. J. Barrett, J. i. Mamiya, K. G. Yager, T. Ikeda, *Soft Matter* **2007**, *3*, 1249–1261.
[121] Y. Ogawa, C. Yoshiyama, T. Kitaoka, *Langmuir* **2012**, *28*, 4404–4412.
[122] C. Dugave, L. Demange, *Chemical Reviews* **2003**, *103*, 2475–2532.
[123] J. Zhang, J. Wang, H. Tian, *Materials Horizons* **2014**, *1*, 169–184.
[124] J. Yoshino, N. Kano, T. Kawashima, *Dalton Transactions* **2013**, *42*, 15826–15834.
[125] A. M. Breul, M. D. Hager, U. S. Schubert, *Chemical Society Reviews* **2013**, *42*, 5366–5407.
[126] A. Nisal, K. Trivedy, H. Mohammad, S. Panneri, S. Sen Gupta, A. Lele, R. Manchala, N. S. Kumar, M. Gadgil, H. Khandelwal, S. More, R. S. Laxman, *ACS Sustainable Chemistry & Engineering* **2013**, *2*, 312–317.
[127] J. Garcia–Amoros, M. C. R. Castro, P. Coelho, M. M. M. Raposo, D. Velasco, *Chemical Communications* **2013**, *49*, 11427–11429.
[128] B. L. Feringa, R. A. van Delden, N. Koumura, E. M. Geertsema, *Chemical Reviews* **2000**, *100*, 1789–1816.
[129] A. Krüger, M. Bernien, C. F. Hermanns, W. Kuch, *The Journal of Physical Chemistry C* **2014**, *118*, 12916–12922.
[130] X.–M. Liu, B. Yang, Y.–L. Wang, J.–Y. Wang, *Chemistry of Materials* **2005**, *17*, 2792–2795.
[131] W. Xiao, W.–H. Chen, X.–D. Xu, C. Li, J. Zhang, R.–X. Zhuo, X.–Z. Zhang, *Advanced Materials* **2011**, *23*, 3526–3530.
[132] W. Xiao, W.–H. Chen, J. Zhang, C. Li, R.–X. Zhuo, X.–Z. Zhang, *The Journal of Physical Chemistry B* **2011**, *115*, 13796–13802.
[133] M. Häckel, L. Kador, D. Kropp, H. W. Schmidt, *Advanced Materials* **2007**, *19*, 227–231.
[134] Y. Liu, N. Li, X. Xia, J. Ge, Q. Xu, J. Lu, *European Polymer Journal* **2011**, *47*, 1160–1167.
[135] A. S. Abd–El–Aziz, P. O. Shipman, P. R. Shipley, B. N. Boden, S. Aly, P. D. Harvey, *Macromolecular Chemistry and Physics* **2009**, *210*, 2099–2106.
[136] M. Tian, L. Liu, Y. Li, R. Hu, T. Liu, H. Liu, S. Wang, Y. Li, *Chemical Communications* **2014**, *50*, 2055–2057.
[137] I. A. Banerjee, L. Yu, H. Matsui, *Journal of the American Chemical Society* **2003**, *125*, 9542–9543.

[138] Y. Yang, X. Wang, L. Liu, X. Xie, Z. Yang, R. K. Y. Li, Y.–W. Mai, *The Journal of Physical Chemistry C* **2007**, *111*, 11231–11239.
[139] R. A. Krause, K. Krause, *Inorganic Chemistry* **1980**, *19*, 2600–2603.
[140] M. Shivakumar, K. Pramanik, P. Ghosh, A. Chakravorty, *Chemical Communications* **1998**, 2103–2104.
[141] M. Shivakumar, K. Pramanik, P. Ghosh, A. Chakravorty, *Inorganic Chemistry* **1998**, *37*, 5968–5969.
[142] R. Roy, P. Chattopadhyay, C. Sinha, S. Chattopadhyay, *Polyhedron* **1996**, *15*, 3361–3369.
[143] W. Y. Wong, S. H. Cheung, S. M. Lee, S. Y. Leung, *Journal of Organometallic Chemistry* **2000**, *596*, 36–45.
[144] S. Banerjee, S. Bhattacharyya, B. K. Dirghangi, M. Menon, A. Chakravorty, *Inorganic Chemistry* **2000**, *39*, 6–13.
[145] A. K. Deb, S. Choudhury, S. Goswami, *Polyhedron* **1990**, *9*, 2251–2255.
[146] A. H. Velders, K. van der Schilden, A. C. G. Hotze, J. Reedijk, H. Kooijman, A. L. Spek, *Dalton Transactions* **2004**, 448–455.
[147] G. K. Lahiri, S. Bhattacharya, S. Goswami, A. Chakravorty, *Journal of the Chemical Society, Dalton Transactions* **1990**, 561–565.
[148] M. N. Ackermann, C. R. Barton, C. J. Deodene, E. M. Specht, S. C. Keill, W. E. Schreiber, H. Kim, *Inorganic Chemistry* **1989**, *28*, 397–403.
[149] S. D. Ernst, W. Kaim, *Inorganic Chemistry* **1989**, *28*, 1520–1528.
[150] M. Krejcik, S. Zalis, J. Klima, D. Sykora, W. Matheis, A. Klein, W. Kaim, *Inorganic Chemistry* **1993**, *32*, 3362–3368.
[151] H. Bock, R. Dienelt, H. Schödel, T. H. Van, *Structural Chemistry* **1998**, *9*, 279–288.
[152] C. M. Fitchett, C. Richardson, P. J. Steel, *Org. Biomol. Chem.* **2005**, *3*, 498–502.
[153] A. Kirpal, E. Reiter, *Chemische Berichte* **1927**, *60B*, 664.
[154] D. A. Baldwin, A. B. P. Lever, R. V. Parish, *Inorganic Chemistry* **1969**, *8*, 107–115.
[155] W. Kaim, *Coordination Chemistry Reviews* **2001**, *219–221*, 463–488.
[156] W. Kaim, S. Kohlmann, *Inorganic Chemistry* **1987**, *26*, 68–77.
[157] C. Richardson, P. J. Steel, D. M. D'Alessandro, P. C. Junk, F. R. Keene, *Journal of the Chemical Society, Dalton Transactions* **2002**.
[158] C. Richardson, C. M. Fitchett, F. R. Keene, P. J. Steel, *Dalton Transactions* **2008**, 2534–2537.
[159] C. M. Fitchett, P. J. Steel, *Polyhedron* **2007**, *26*, 400–405, and references therein.
[160] N. S. Oxtoby, A. J. Blake, N. R. Champness, C. Wilson, *Proceedings of the National Academy of Sciences of the United States of America* **2002**, *99*, 4905–4910.
[161] J. A. R. Navarro, B. Lippert, *Coordination Chemistry Reviews* **2001**, *222*, 219–250.
[162] M. Bardaji, M. Barrio, P. Espinet, *Dalton Transactions* **2011**, *40*, 2570–2577.
[163] M. Camalli, F. Caruso, G. Mattogno, E. Rivarola, *Inorganica Chimica Acta* **1990**, *170*, 225–231.
[164] A. Dogan, B. Sarkar, A. Klein, F. Lissner, T. Schleid, J. Fiedler, S. Záliš, V. K. Jain, W. Kaim, *Inorganic Chemistry* **2004**, *43*, 5973–5980.
[165] L. Carlucci, G. Ciani, D. M. Proserpio, S. Rizzato, *New Journal of Chemistry* **2003**, *27*, 483–489.
[166] R. K. Golder, M. Sc. Thesis, University of Canterbury, **2012**.
[167] J. Burgess, J. R. A. Cottam, P. J. Steel, *Australian Journal of Chemistry* **2006**, *59*, 295–297.
[168] C. J. Sumby, P. J. Steel, *Inorganica Chimica Acta* **2007**, *360*, 2100–2114.
[169] P. J. Steel, C. J. Sumby, *Dalton Transactions* **2003**, 4505–4515.
[170] J. Burgess, P. J. Steel, *Coordination Chemistry Reviews* **2011**, *255*, 2094–2103.
[171] R. Puttreddy, P. J. Steel, *CrystEngComm* **2014**, *16*, 556–560.
[172] R. Puttreddy, J. R. A. Cottam, P. J. Steel, *RSC Advances* **2014**, *4*, 22449–22454.
[173] S. W. Kelemu, P. J. Steel, *Polyhedron* **2014**, *71*, 99–103.
[174] J. W. Steed, J. L. Atwood, *Supramolecular Chemistry*, Second ed., Wiley, New York, **2009**.
[175] J. M. Lehn, *Supramolecular Chemistry*, Wiley–VCH, Weinheim, **1995**.
[176] S. J. Dalgarno, *Annual Reports Section "B" (Organic Chemistry)* **2010**, *106*, 197–215.
[177] K. Müller–Dethlefs, P. Hobza, *Chemical Reviews* **1999**, *100*, 143–168.

[178] M. Nishio, Y. Umezawa, K. Honda, S. Tsuboyama, H. Suezawa, *CrystEngComm* **2009**, *11*, 1757–1788.
[179] T. Steiner, *Angewandte Chemie International Edition* **2002**, *41*, 48–76.
[180] G. R. Desiraju, *Accounts of Chemical Research* **1996**, *29*, 441–449.
[181] C. B. Aakeroy, K. R. Seddon, *Chemical Society Reviews* **1993**, *22*, 397–407.
[182] J. G. Planas, C. Masalles, R. Sillanpaa, R. Kivekas, F. Teixidor, C. Vinas, *CrystEngComm* **2006**, *8*, 75–83.
[183] E. C. Constable, *Chemistry and Industry* **1994**, *2*, 56.
[184] P. J. Steel, *Chemistry in New Zealand* **2003**, *67*, 57–60.
[185] B. J. Holliday, C. A. Mirkin, *Angewandte Chemie International Edition* **2001**, *40*, 2022–2043.
[186] A. G. Young, L. R. Hanton, *Coordination Chemistry Reviews* **2008**, *252*, 1346–1386.
[187] D. A. McMorran, *Inorganic Chemistry* **2007**, *47*, 592–601.
[188] R. P. Feazell, C. E. Carson, K. K. Klausmeyer, *Inorganic Chemistry* **2005**, *45*, 935–944.
[189] A. J. Blake, N. R. Champness, P. A. Cooke, J. E. B. Nicolson, C. Wilson, *Journal of the Chemical Society, Dalton Transactions* **2000**, 3811–3819.
[190] A. N. Khlobystov, A. J. Blake, N. R. Champness, D. A. Lemenovskii, A. G. Majouga, N. V. Zyk, M. Schröder, *Coordination Chemistry Reviews* **2001**, *222*, 155–192.
[191] G. F. Swiegers, T. J. Malefetse, *Coordination Chemistry Reviews* **2002**, *225*, 91–121.
[192] P. Thanasekaran, R. T. Liao, Y.–H. Liu, T. Rajendran, S. Rajagopal, K. L. Lu, *Coordination Chemistry Reviews* **2005**, *249*, 1085–1110.
[193] M. Fujita, K. Umemoto, M. Yoshizawa, N. Fujita, T. Kusukawa, K. Biradha, *Chemical Communications* **2001**, 509–518.
[194] P. J. Steel, *Molecules* **2004**, *9*, 440–448.
[195] P. J. Steel, *Accounts of Chemical Research* **2005**, *38*, 243–250.
[196] C. Kaes, A. Katz, M. W. Hosseini, *Chemical Reviews* **2000**, *100*, 3553–3590 and references therein.
[197] F. Robinson, M. J. Zaworotko, *Journal of the Chemical Society, Chemical Communications* **1995**, 2413–2414.
[198] A. J. Blake, N. R. Champness, M. Crew, S. Parsons, *New Journal of Chemistry* **1999**, *23*, 13–15.
[199] O. M. Yaghi, H. Li, *Journal of the American Chemical Society* **1996**, *118*, 295–296.
[200] M. Fujita, J. Yazaki, K. Ogura, *Journal of the American Chemical Society* **1990**, *112*, 5645–5647.
[201] S. Roche, C. Haslam, S. L. Heath, J. A. Thomas, *Chemical Communications* **1998**, 1681–1682.
[202] T. T. Yeh, J. Y. Wu, Y. S. Wen, Y. H. Liu, J. Twu, Y. T. Tao, K. L. Lu, *Dalton Transactions* **2005**, 656–658.
[203] P. J. Stang, B. Olenyuk, *Accounts of Chemical Research* **1997**, *30*, 502–518.
[204] D. W. Johnson, K. N. Raymond, *Supramolecular Chemistry* **2001**, *13*, 639–659.
[205] K.–i. Yamashita, K.–i. Sato, M. Kawano, M. Fujita, *New Journal of Chemistry* **2009**, *33*, 264–270.
[206] S. Goetz, P. E. Kruger, *Dalton Transactions* **2006**, 1277–1284.
[207] D. A. McMorran, P. J. Steel, *Angewandte Chemie International Edition* **1998**, *37*, 3295–3297.
[208] M. Albrecht, *Chemical Reviews* **2001**, *101*, 3457–3498.
[209] X.–D. Chen, T. C. W. Mak, *Dalton Transactions* **2005**, 3646–3652.
[210] M. Fujita, *Accounts of Chemical Research* **1998**, *32*, 53–61.
[211] J.–P. Sauvage, *Accounts of Chemical Research* **1998**, *31*, 611–619.
[212] P. L. Anelli, N. Spencer, J. F. Stoddart, *Journal of the American Chemical Society* **1991**, *113*, 5131–5133.
[213] S. R. Batten, R. Robson, *Angewandte Chemie International Edition* **1998**, *37*, 1460–1494.
[214] B. Moulton, M. J. Zaworotko, *Chemical Reviews* **2001**, *101*, 1629–1658.
[215] L. Carlucci, G. Ciani, D. M. Proserpio, A. Sironi, *Journal of the American Chemical Society* **1995**, *117*, 4562–4569.
[216] P. J. Steel, C. M. Fitchett, *Coordination Chemistry Reviews* **2008**, *252*, 990–1006.

[217] P.–X. Yin, J. Zhang, Z.–J. Li, Y.–Y. Qin, J.–K. Cheng, L. Zhang, Q.–P. Lin, Y.–G. Yao, *Crystal Growth & Design* **2009**, *9*, 4884–4896.
[218] B. Li, S.–Q. Zang, C. Ji, H.–W. Hou, T. C. W. Mak, *Crystal Growth & Design* **2012**, *12*, 1443–1451.
[219] S. E. D. H. Etaiw, M. M. El–Bendary, *Journal of Coordination Chemistry* **2010**, *63*, 1038–1051.
[220] R. Wang, M. Hong, J. Luo, F. Jiang, L. Han, Z. Lin, R. Cao, *Inorganica Chimica Acta* **2004**, *357*, 103–114.
[221] G. Marin, M. Andruh, A. M. Madalan, A. J. Blake, C. Wilson, N. R. Champness, M. Schröder, *Crystal Growth & Design* **2008**, *8*, 964–975.
[222] L. Qin, J.–S. Hu, Y.–Z. Li, H.–G. Zheng, *Crystal Growth & Design* **2011**, *12*, 403–413.
[223] Y. Yu, W. Zhan, T. E. Albrecht–Schmitt, *Inorganic Chemistry* **2007**, *46*, 10214–10220.
[224] N. Gimeno, R. Vilar, *Coordination Chemistry Reviews* **2006**, *250*, 3161–3189.
[225] R. Custelcean, *Chemical Society Reviews* **2010**, *39*, 3675–3685.
[226] B. L. Fei, W. Y. Sun, K. B. Yu, W. X. Tang, *Journal of the Chemical Society, Dalton Transactions* **2000**, 805–811.
[227] M. A. Withersby, A. J. Blake, N. R. Champness, P. Hubberstey, W.–S. Li, M. Schröder, *Angewandte Chemie International Edition in English* **1997**, *36*, 2327–2329.
[228] I. Bassanetti, F. Mezzadri, A. Comotti, P. Sozzani, M. Gennari, G. Calestani, L. Marchiò, *Journal of the American Chemical Society* **2012**, *134*, 9142–9145.
[229] H. Tsurugi, H. Tanahashi, H. Nishiyama, W. Fegler, T. Saito, A. Sauer, J. Okuda, K. Mashima, *Journal of the American Chemical Society* **2013**, *135*, 5986–5989.
[230] Y. Li, Z.–Y. Lin, W.–T. Wong, *European Journal of Inorganic Chemistry* **2001**, *2001*, 3163–3173.
[231] H. Hartmanna, T. Scheiringa, J. Fiedlerb, W. Kaim, *Journal of Organometallic Chemistry* **2000**, *604*, 267–272.
[232] D. Oyama, A. Asuma, T. Hamada, T. Takase, *Inorganica Chimica Acta* **2009**, *362*, 2581–2588.
[233] A. Dogan, C. Kavakli, M. Sieger, M. Niemeyer, B. Sarkar, W. Kaim, *Zeitschrift für anorganische und allgemeine Chemie* **2008**, *634*, 2527–2531.
[234] E. Corral, A. C. G. Hotze, D. M. Tooke, A. L. Spek, J. Reedijk, *Inorganica Chimica Acta* **2006**, *359*, 830–838.
[235] I. Ucar, F. Arslan, A. Bulut, H. Icbudak, H. Olmez, O. Buyukgungor, *Acta Crystallographica Section C* **2004**, *60*, m523–m525.
[236] A. Bencini, I. Ciofini, C. A. Daul, A. Ferretti, *Journal of the American Chemical Society* **1999**, *121*, 11418–11424.
[237] R. S. Srivastava, F. R. Fronczek, L. M. Romero, *Inorganica Chimica Acta* **2004**, *357*, 2410–2414.
[238] N. Prokopuk, A. Chafin, R. Gilardi, J. R. Deschamps, *Inorganica Chimica Acta* **2011**, *365*, 439–446.
[239] F. Baumann, W. Kaim, M. García Posse, N. E. Katz, *Inorganic Chemistry* **1998**, *37*, 658–660.
[240] M. Krejcik, A. A. Vlcek, *Inorganic Chemistry* **1992**, *31*, 2390–2395.
[241] M. Heilmann, S. Frantz, W. Kaim, J. Fiedler, C. Duboc, *Inorganica Chimica Acta* **2006**, *359*, 821–829.
[242] M. Heilmann, F. Baumann, W. Kaim, J. Fiedler, *Journal of the Chemical Society, Faraday Transactions* **1996**, *92*, 4227–4231.
[243] C. Richardson, P. J. Steel, *Australian Journal of Chemistry* **2000**, *53*, 93–97.
[244] C. M. Fitchett, F. R. Keene, C. Richardson, P. J. Steel, *Inorg. Chem. Commun.* **2008**, *11*, 595–598.
[245] Z. Gan, B. Hu, Q. Song, Y. Xu, *Synthesis* **2012**, *44*, 1074–1078.
[246] S. J. Nara, M. Jha, J. Brinkhorst, T. J. Zemanek, D. A. Pratt, *The Journal of Organic Chemistry* **2008**, *73*, 9326–9333.
[247] C. Richardson, P. J. Steel, *Dalton Trans.* **2003**, *0*, 992–1000.
[248] A. Das, T. M. Scherer, A. D. Chowdhury, S. M. Mobin, W. Kaim, G. K. Lahiri, *Inorganic Chemistry* **2012**, *51*, 1675–1684.

[249] A. Das, T. M. Scherer, S. M. Mobin, W. Kaim, G. K. Lahiri, *Chemistry – A European Journal* **2012**, *18*, 11007–11018.
[250] W. Kaim, S. Kohlmann, J. Jordanov, D. Fenske, *Zeitschrift für anorganische und allgemeine Chemie* **1991**, *598*, 217–234.
[251] E. C. Constable, R. W. Hay, L. A. P. Kane–Maguire, *Mechanisms of Inorganic and Organometallic Reactions* **1991**, *7*, 279–308.
[252] E. S. Dodsworth, A. B. P. Lever, *Chemical Physics Letters* **1985**, *119*, 61–66.
[253] E. S. Dodsworth, A. B. P. Lever, *Chemical Physics Letters* **1986**, *124*, 152–158.
[254] E. Brauns, S. W. Jones, J. A. Clark, S. M. Molnar, Y. Kawanishi, K. J. Brewer, *Inorganic Chemistry* **1997**, *36*, 2861–2867 and references therein.
[255] N. Doslik, T. Sixt, W. Kaim, *Angewandte Chemie International Edition* **1998**, *37*, 2403–2404.
[256] W. Kaim, N. Doslik, S. Frantz, T. Sixt, M. Wanner, F. Baumann, G. Denninger, H. J. Kümmerer, C. Duboc–Toia, J. Fiedler, S. Zališ, *Journal of Molecular Structure* **2003**, *656*, 183–194.
[257] H. Y. Ye, F. R. Dai, L. Y. Zhang, Z. N. Chen, *Inorganic Chemistry* **2007**, *46*, 6129–6135.
[258] R. Jana, F. Lissner, B. Schwederski, J. Fiedler, W. Kaim, *Organometallics* **2013**, *32*, 5879–5886.
[259] S. Goswami, S. Jana, S. Dey, A. K. Adak, *Australian Journal of Chemistry* **2007**, *60*, 120–123.
[260] W. Marckwald, E. Meyer, *Chemische Berichte* **1900**, *33*, 1885.
[261] G. M. Badger, R. G. Buttery, *Journal of the Chemical Society* **1955**, 2816–2818.
[262] C. L. Wang, X. X. Wang, X. Y. Wang, J. P. Xiao, Y. L. Wang, *Synthetic Communications* **1999**, *29*, 3435–3438.
[263] F. Kóródi, *Synthetic Communications* **1991**, *21*, 1841–1846.
[264] J. G. Rodríguez, C. de los Rios, A. Lafuente, *Tetrahedron* **2005**, *61*, 9042–9051.
[265] H. R. Bjørsvik, C. Gambarotti, V. R. Jensen, R. R. González, *The Journal of Organic Chemistry* **2005**, *70*, 3218–3224.
[266] X. Huang, H. Yang, H. Fu, R. Qiao, Y. Zhao, *Synthesis* **2009**, 2679–2688.
[267] C. Krieger, A. Koçak, Ö. Bekâroğlu, *Helvetica Chimica Acta* **1985**, *68*, 581–583.
[268] G. M. Fischer, M. I. Krondahl, I. G. Schnetmann, E. Daltrozzo, A. Zumbusch, *Chemistry – A European Journal* **2009**, *15*, 4857–4864.
[269] T. R. M. Rauws, C. Biancalani, J. W. De Schutter, B. U. W. Maes, *Tetrahedron* **2010**, *66*, 6958–6964.
[270] J. E. Campbell, M. C. Hewitt, P. Jones, L. Xie, WO 2011/150156 A2, Sunovion Pharmaceuticals Inc., USA . **2011**, pp. 1–233.
[271] K. B. Wiberg, D. Nakaji, C. M. Breneman, *Journal of the American Chemical Society* **1989**, *111*, 4178–4190.
[272] C. R. Johnson, R. E. Shepherd, *Inorganic Chemistry* **1983**, *22*, 2439–2444.
[273] C. Bhaumik, S. Das, D. Maity, S. Baitalik, *Dalton Transactions* **2012**, *41*, 2427–2438.
[274] E. C. Constable, A. M. W. C. Thompson, *Journal of the Chemical Society, Dalton Transactions* **1992**, 3467–3475.
[275] E. C. Constable, P. Harverson, C. E. Housecroft, E. Nordlander, J. Olsson, *Polyhedron* **2006**, *25*, 437–458.
[276] G. S. Hanan, C. R. Arana, J.–M. Lehn, D. Fenske, *Angewandte Chemie International Edition in English* **1995**, *34*, 1122–1124.
[277] A.–M. Stadler, F. Puntoriero, S. Campagna, N. Kyritsakas, R. Welter, J.–M. Lehn, *Chemistry – A European Journal* **2005**, *11*, 3997–4009.
[278] D. Brown, R. Zong, R. P. Thummel, *European Journal of Inorganic Chemistry* **2004**, *2004*, 3269–3272.
[279] J. Otsuki, I. Kurihara, A. Imai, Y. Hamada, N. Omokawa, *Bulletin of the Chemical Society of Japan* **2007**, *80*, 902–909.
[280] T. Akasaka, J. Otsuki, K. Araki, *Chemistry – A European Journal* **2002**, *8*, 130–136.
[281] D. B. Moran, G. O. Morton, J. D. Albright, *Journal of Heterocyclic Chemistry* **1986**, *23*, 1071–1077.
[282] J. Yin, B. Xiang, M. A. Huffman, C. E. Raab, I. W. Davies, *The Journal of Organic Chemistry* **2007**, *72*, 4554–4557.

[283] Y. Engel, A. Dahan, E. Rozenshine–Kemelmakher, M. Gozin, *The Journal of Organic Chemistry* **2007**, *72*, 2318–2328.
[284] A. P. Krapcho, J. B. Lanza, *Organic Preparations and Procedures International* **2007**, *39*, 603–608.
[285] E. C. Constable, N. Hostettler, C. E. Housecroft, P. Kopecky, M. Neuburger, J. A. Zampese, *Dalton Transactions* **2012**, *41*, 2890–2897.
[286] M. L. Scudder, H. A. Goodwin, I. G. Dance, *New Journal of Chemistry* **1999**, *23*, 695–705.
[287] J. McMurtrie, I. Dance, *CrystEngComm* **2005**, *7*, 216–229.
[288] J. McMurtrie, I. Dance, *CrystEngComm* **2010**, *12*, 2700–2710.
[289] E. C. Constable, G. Zhang, C. E. Housecroft, M. Neuburger, J. A. Zampese, *CrystEngComm* **2010**, *12*, 3733–3739.
[290] M. J. Hannon, C. L. Painting, E. A. Plummer, L. J. Childs, N. W. Alcock, *Chemistry – A European Journal* **2002**, *8*, 2225–2238.
[291] Z. Yu, A. Nabei, T. Izumi, T. Okubo, T. Kuroda–Sowa, *Acta Crystallographica Section C* **2008**, *64*, m209–m212.
[292] G. Dong, P. Ke–liang, D. Chun–ying, H. Cheng, M. Qing–jin, *Inorganic Chemistry* **2002**, *41*, 5978–5985.
[293] E. C. Kesslen, W. B. Euler, *Tetrahedron Lett.* **1995**, *36*, 4725–4728.
[294] R. Drozdzak, B. Allaert, N. Ledoux, I. Dragutan, V. Dragutan, F. Verpoort, *Coordination Chemistry Reviews* **2005**, *249*, 3055–3074.
[295] Y. Bai, G.–Q. Zhang, D.–B. Dang, P.–T. Ma, H. Gao, J.–Y. Niu, *CrystEngComm* **2011**, *13*, 4181–4187.
[296] Q. Wu, Y.–G. Li, Y.–H. Wang, R. Clerac, Y. Lu, E.–B. Wang, *Chemical Communications* **2009**, 5743–5745.
[297] A. R. Kennedy, K. G. Brown, D. Graham, J. B. Kirkhouse, M. Kittner, C. Major, C. J. McHugh, P. Murdoch, W. E. Smith, *New Journal of Chemistry* **2005**, *29*, 826–832.
[298] G. A. Broker, E. R. T. Tiekink, *Acta Crystallographica Section E* **2007**, *63*, m2420–m2420.
[299] N. Yoshida, K. Ichikawa, M. Shiro, *Journal of the Chemical Society, Perkin Transactions 2* **2000**, 17–26.
[300] F. Tuna, J. Hamblin, G. Clarkson, W. Errington, N. W. Alcock, M. J. Hannon, *Chemistry – A European Journal* **2002**, *8*, 4957–4964.
[301] Y. Parajo, J. Malina, I. Meistermann, G. J. Clarkson, M. Pascu, A. Rodger, M. J. Hannon, P. Lincoln, *Dalton Transactions* **2009**, 4868–4874.
[302] M. J. Hannon, C. L. Painting, A. Jackson, J. Hamblin, W. Errington, *Chemical Communications* **1997**, 1807–1808.
[303] G. Dong, H. Cheng, D. Chun–Ying, Q. Chun–Qi, M. Qing–Jin, *New Journal of Chemistry* **2002**, *26*, 796–802.
[304] R. Karmakar, C. R. Choudhury, S. R. Batten, S. Mitra, *Journal of Molecular Structure.* **2007**, *826*, 75–81.
[305] F. Tuna, G. Clarkson, N. W. Alcock, M. J. Hannon, *Dalton Transactions* **2003**, 2149–2155.
[306] Y. F. Yue, E. Q. Gao, S. Q. Bai, Z. He, C. H. Yan, *CrystEngComm* **2004**, *6*, 549–555.
[307] P. Cai, M. X. Li, C. Y. Duan, F. Lu, D. Guo, Q.–J. Meng, *New Journal of Chemistry* **2005**, *29*, 1011–1016.
[308] S. Chakraborty, P. Munshi, G. K. Lahiri, *Polyhedron* **1999**, *18*, 1437–1444.
[309] K. Marjani, J. Asgarian, M. Mousavi, V. Amani, *Zeitschrift für anorganische und allgemeine Chemie* **2009**, *635*, 1633–1637.
[310] N. M. Shavaleev, Z. R. Bell, G. Accorsi, M. D. Ward, *Inorganica Chimica Acta* **2003**, *351*, 159–166.
[311] L. Yang, D. R. Powell, R. P. Houser, *Dalton Transactions* **2007**, 955–964.
[312] E. C. Constable, C. E. Housecroft, B. M. Kariuki, N. Kelly, C. B. Smith, *Inorganic Chemistry Communications* **2002**, *5*, 199–202.
[313] P. Alborés, C. Plenk, E. Rentschler, *Inorganic Chemistry* **2012**, *51*, 8373–8384.
[314] V. Kokars, A. Yanishevskii, V. Kampars, *Chemistry of Heterocyclic Compounds* **2002**, *38*, 805–809.
[315] Y. O. Jang, S. W. Lee, *Polyhedron* **2010**, *29*, 2731–2738.

[316] Y. Nakabayashi, Y. Watanabe, T. Nakao, O. Yamauchi, *Inorganica Chimica Acta* **2004**, *357*, 2553–2560.
[317] E. C. Johnson, B. P. Sullivan, D. J. Salmon, S. A. Adeyemi, T. J. Meyer, *Inorganic Chemistry* **1978**, *17*, 2211–2215.
[318] M. J. Ridd, D. J. Gakowski, G. E. Sneddon, F. R. Keene, *J. Chem. Soc., Dalton Trans.* **1992**, 1949–1956.
[319] A. Kirpal, *Chemische Berichte* **1934**, *67B*, 70–71.
[320] N. Campbell, A. W. Henderson, D. Taylor, *Journal of the Chemical Society* **1953**, 1281–1285.
[321] M. Woźniak, M. Tomula, *Liebigs Annalen der Chemie* **1993**, *1993*, 471–475.
[322] H. J. W. Van den Haak, H. C. Van der Plas, B. Van Veldhuizen, *The Journal of Organic Chemistry* **1981**, *46*, 2134–2137.
[323] G. M. Sheldrick, *Acta Crystallographica Section A* **2008**, *64*, 112–122.
[324] G. M. Sheldrick, SHELXL97. Programs for crystal structure analysis, University of Göttingen, **1997**.